

---

# Dynamics of small interfering RNA

-

## FRET based integrity measurements of siRNA in the cuvette & inside cells

---

### Dissertation

zur Erlangung des Grades

“Doktor der Naturwissenschaften”

im Promotionsfach Pharmazie

am Fachbereich Chemie, Pharmazie und Geowissenschaften

DER JOHANNES GUTENBERG-UNIVERSITÄT

in Mainz

vorgelegt von

**Markus Hirsch**

geb. am 29.04.1983 in Feuchtwangen

Mainz, im September 2013

Dekan:

[REDACTED]

1. Berichterstatter:

[REDACTED]

2. Berichterstatter:

[REDACTED]

Datum der mündlichen Prüfung: 31.10.2013

*D77 (Dissertation Mainz)*



Die vorgelegte Dissertation wurde am Institut für Pharmazie und Biochemie der Johannes Gutenberg-Universität in Mainz zur Erlangung des Grades “Doktor der Naturwissenschaften”, unter Betreuung von [REDACTED] angefertigt.

Erstgutachter:

[REDACTED]  
Abteilung: Pharmazeutische Chemie  
Institut für Pharmazie und Biochemie  
Johannes Gutenberg-Universität in Mainz

Zweitgutachter:

[REDACTED]  
Abteilung: Biochemie  
Institut für Pharmazie und Biochemie  
Johannes Gutenberg-Universität in Mainz

---

Hiermit versichere ich eidesstattlich:

1. Ich habe die jetzt als Dissertation vorgelegte Arbeit selbst angefertigt und alle benutzten Hilfsmittel (Literatur, Apparaturen, Material) in der Arbeit angegeben.
2. Ich habe oder hatte die jetzt als Dissertation vorgelegte Arbeit nicht als Prüfungsarbeit für eine staatliche oder andere wissenschaftliche Prüfung eingereicht.
3. Ich hatte weder die jetzt als Dissertation vorgelegte Arbeit noch Teile davon bei einer anderen Fakultät bzw. einem anderen Fachbereich als Dissertation eingereicht.

---

Ort, Datum

Markus Hirsch







"Ich bin immer noch verwirrt, aber auf einem höheren Niveau."

*(Enrico Fermi, italienischer Physiker)*

# Danksagung

[Redacted text block containing multiple paragraphs of text, all obscured by black bars]







## Abstract

RNAi is a powerful tool for gene function analysis and promises high potential for therapeutic application. While in cell culture models efficient knockdown rates can be achieved, applications *in vivo* remain challenging. Especially the delivery of siRNA into the target tissue or cells and a progressing degradation of siRNA are the major hurdles for therapeutic application.

Labeled siRNA can be used for both, observing cellular localization and analyzing the integrity level of the applied siRNA. Two dyes attached to each strand of an siRNA duplex, i.e. the donor on the 3'-end of the sense strand and the acceptor on the 5'-end of the antisense strand, create a robust FRET system [1]. The ratio of FRET to donor emission, the R/G ratio, serves as a sensitive classifier to determine the integrity level of duplex siRNAs [2–4]. With this system, siRNA degradation of less than 5 % can be determined in either the cuvette or in living cells.

The presented research deals with the evaluation of potential FRET dye pairs regarding their suitability for *in vitro* and *in vivo* application. Several new FRET pairs have been evaluated covering the whole range of the visible light spectrum. This allows the selection of a FRET dye pair, compatible with other fluorescence labels or a certain test system.

On basis of Alexa555/Atto647N siRNA the successful formulation of liposomes containing siRNA was surveyed. A subsequent evaluation of different nanoparticulate delivery systems identified liposomes, nanohydrogels and cationic peptides as systems with an excellent protective effect. With these results those delivery systems can now be further optimized for successful cellular delivery.

Atto488/Atto590 siRNA proved to be ideal for integrity measurements in real-time in living cells. Enhanced photophysical properties, i.e. resistance to photobleaching and minimal spectral crosstalk, allowed the observation of transfected cells for up to 8 hours. With help of Atto488/Atto590 siRNA the delivery and the release process of cells transfected by cationic lipids was investigated in real-time, enabling the analysis of single release events, regarding release process and cellular distribution.

An initial strong release phase could be determined directly after transfection and was followed by a moderate and constant release rate over the rest of the observed time period. The average residence time of siRNA in the cytosol ranged around 24 and 58 min differentiating in long and short lasting release events. An import of siRNA into the nucleus could be observed, although, the time point of entrance was not yet determinable. The whole release process occurred spontaneously and changes in cellular distribution could be monitored within few minutes. Additionally, the released siRNA was cleared from the cytoplasm over time, leaving only small aggregates inside the cells that, however, displayed still siRNA at low integrity state.



## Zusammenfassung

RNAi ist ein bedeutendes Werkzeug zur Funktionsanalyse von Genen und hat großes Potential für den Einsatz in der Therapie. Obwohl effiziente Knockdowns in der Zellkultur erzielt werden, erweist sich eine *in vivo* Anwendung als schwierig. Die großen Hürden sind dabei der Transport der siRNA ins Zielgewebe und deren voranschreitende Degradierung.

Markierte siRNA kann sowohl zur eigenen Integritätsmessung als auch zur Lokalisierung verwendet werden. Zwei Farbstoffe an den jeweiligen 3'- bzw. -5'-Enden des Sense- bzw. Antisense-Stranges erzeugen ein robustes FRET-System [1]. Das Verhältnis von FRET- zu Donor-Signal, das R/G-Ratio, dient zur sensitiven Klassifizierung des Integritätslevels einer siRNA Probe [2–4]. Mit diesem System kann eine Degradierung von weniger als 5 % in der Küvette und in Zellen nachgewiesen werden.

Die vorliegende Arbeit beschäftigt sich mit der Evaluierung von potentiellen FRET Farbstoffpaaren hinsichtlich deren Eignung für *in vitro* und *in vivo* Anwendung. Verschiedenste FRET-Paare, die das gesamte sichtbare Spektrum abdecken, wurden evaluiert und ermöglichen nun die Auswahl eines geeigneten Paares für die jeweilige Anwendung oder Kombination mit anderen Farbstoffen.

Mit Hilfe von Alexa555/Atto647N siRNA wurde ein erfolgreicher Einschluss von siRNA in Liposomen beobachtet. Eine anschließende Evaluierung der RNase-Protektion ergab für Liposomen, Nanohydrogele und kationische Peptide hervorragende protektive Eigenschaften. Basierend auf den Ergebnisse können diese und andere Transportsysteme nun für eine zelluläre Aufnahme optimiert werden.

Atto488/Atto590 zeigte die besten Eigenschaften für Echtzeit-Integritätsmessungen in der Lebendzellmikroskopie. Verringerte Bleicheigenschaften und minimaler spektraler "Cross-Talk" ermöglichten es, transfizierte Zellen über einen Zeitraum von bis zu 8 Stunden zu beobachten. Mittels Atto488/Atto590 siRNA wurde die Einschleusung und Freisetzung in Zellen in Echtzeit untersucht. Dabei konnten Freisetzung und Verteilung in einzelnen Zellen beobachtet und analysiert werden.

Auf eine anfängliche Phase mit hoher Freisetzungsrates folgte eine Phase mit geringerer Rate für den restlichen Beobachtungszeitraum. Die durchschnittliche Verweildauer im Zytosol betrug 24 und 58 Minuten, wobei zwischen lang- und kurzanhaltenden Ereignissen unterschieden werden konnte. Obwohl ein Import von siRNA in den Zellkern beobachtet wurde, konnte kein Schema bzw. genauer Zeitpunkt, in Bezug auf den Transfektionszeitraum für diese Ereignisse bestimmt werden. Die beobachteten Freisetzungsprozesse fanden sporadisch statt und Änderungen in der zellulären Verteilung geschahen innerhalb von wenigen Minuten. Einmal freigesetzte siRNA verschwand mit der Zeit wieder aus dem Zytosol und es blieben nur kleine Aggregate von siRNA mit immer noch geringer Integrität zurück.



# Table of contents

<b>Abstract</b>	<b>III</b>
<b>Zusammenfassung</b>	<b>V</b>
<b>Table of contents</b>	<b>VII</b>
<b>List of figures</b>	<b>XI</b>
<b>List of tables</b>	<b>XV</b>
<b>Abbreviations</b>	<b>XVII</b>
<b>1 Introduction</b>	<b>1</b>
1.1 RNA interference . . . . .	2
1.1.1 RNAi pathways . . . . .	3
1.1.2 Argonaute proteins and RISC incorporation . . . . .	7
1.1.3 Towards siRNA based therapeutics . . . . .	9
1.2 siRNA delivery . . . . .	12
1.2.1 <i>in vitro</i> delivery systems . . . . .	12
1.2.2 <i>in vivo</i> delivery systems . . . . .	14
1.2.3 siRNA uptake and release . . . . .	17
1.2.4 Localization of released siRNA . . . . .	20
1.3 RNA labeling for microscopy . . . . .	21
1.3.1 RNA binding motifs . . . . .	21
1.3.2 Fluorescently labeled probes . . . . .	23
1.3.3 EGFP analog on basis of an RNA aptamer . . . . .	24
1.4 Fluorescence & FRET . . . . .	25
1.4.1 Fluorescence . . . . .	25
1.4.2 Fluorescence resonance energy transfer . . . . .	28
1.5 Microscopy . . . . .	31
1.5.1 Fluorescence microscopy . . . . .	31
1.5.2 Live cell imaging . . . . .	35
1.5.3 Advanced imaging methods . . . . .	37
<b>2 Goal of this work</b>	<b>41</b>
<b>3 Results &amp; Discussion</b>	<b>43</b>
3.1 Model for siRNA integrity . . . . .	43
3.1.1 Principles of the R/G-model . . . . .	43
3.1.2 Fluorescein/Tetramethylrhodamine siRNA . . . . .	44

3.1.3	Alternative for FL/TMR . . . . .	45
3.1.3.1	Criteria for an optimized siRNA FRET pair . . . . .	45
3.1.3.2	The siRNA dye candidates . . . . .	46
3.1.3.3	Preparation of siRNA duplexes . . . . .	47
3.1.3.4	Influence of hybridization on fluorescence . . . . .	48
3.1.3.5	FRET analysis of substitutes for FL/TMR . . . . .	49
3.1.4	Photostability of FL/TMR analogs . . . . .	51
3.1.4.1	Photostability of single labeled FL and TMR analogs . . . . .	52
3.1.4.2	Photostability of double labeled FRET analogs . . . . .	53
3.1.5	Promising FRET pairs for future applications . . . . .	55
3.1.5.1	Atto488/Atto590 siRNA envisaged for imaging . . . . .	55
3.1.5.2	Further siRNA FRET constructs . . . . .	57
3.2	Application of FRET siRNA <i>in vitro</i> . . . . .	61
3.2.1	Influence of labeling on silencing capability . . . . .	61
3.2.2	R/G calibration of FRET siRNA . . . . .	62
3.2.3	Degradation of FRET siRNA . . . . .	65
3.2.4	Utilization of FRET siRNA for survey of liposomal formulation . . . . .	67
3.2.4.1	Examination of the preparation process . . . . .	67
3.2.4.2	Stability of prepared liposomes . . . . .	71
3.2.5	Evaluation of nanoparticular delivery systems . . . . .	72
3.2.5.1	Determination of the optimal siRNA to particle ratio . . . . .	72
3.2.5.2	Analysis of RNase protection . . . . .	73
3.3	FRET siRNA in fixed cells . . . . .	76
3.3.1	Bleaching behavior under the microscope . . . . .	76
3.3.1.1	Excitation of matrix embedded siRNA . . . . .	76
3.3.1.2	Excitation of siRNA in fixed cells . . . . .	78
3.3.2	Verification of Atto488/Atto590 FRET in cells . . . . .	80
3.3.3	Principles of R/G ratio algorithm . . . . .	82
3.3.4	Integrity simulation inside cells . . . . .	84
3.3.4.1	Inspection of image data . . . . .	84
3.3.4.2	R/G value analysis . . . . .	86
3.3.5	FL/TMR siRNA integrity in fixed cells over time . . . . .	88
3.3.5.1	First indications of changings in localization . . . . .	88
3.3.5.2	Large-scale analysis of fixed cells . . . . .	92
3.4	Observation of siRNA and integrity measurements in living cells . . . . .	96
3.4.1	Cellular costaining of organelles . . . . .	96
3.4.1.1	Lysosomes and nucleus . . . . .	96
3.4.1.2	Short-time imaging with violet laser . . . . .	98
3.4.1.3	Long-term imaging without violet laser . . . . .	99
3.4.1.4	Manual segmentation of the nucleus . . . . .	101
3.4.2	R/G adaptation to live cell imaging . . . . .	103
3.4.2.1	Microscopy parameters for live cell imaging . . . . .	103
3.4.2.2	R/G adaptation . . . . .	104
3.4.3	Live cell imaging with labeled siRNA . . . . .	106
3.4.3.1	Transfection with single labeled siRNA . . . . .	107
3.4.3.2	Live transfection with Atto488/Atto590 . . . . .	110

---

3.4.3.3	Influence of fixation . . . . .	113
3.4.3.4	R/G ratio analysis in HeLa cells . . . . .	114
3.4.3.5	Test of the alternative Alexa555/Atto647N siRNA . . . . .	116
3.4.4	Observations made during live cell imaging . . . . .	117
3.4.4.1	Uptake and release from lipoplexes . . . . .	117
3.4.4.2	Formation of siRNA aggregates during and after release . . . . .	119
3.4.4.3	2 <sup>nd</sup> releases, cell death and cell division after release . . . . .	122
3.4.4.4	Transfer of siRNA into neighboring cells . . . . .	123
3.4.5	Detailed analysis of cellular release events . . . . .	125
3.4.5.1	Starting release process . . . . .	125
3.4.5.2	Fluorescence time of siRNA in cytosol . . . . .	128
3.4.6	Single cell analysis of siRNA release . . . . .	130
3.4.6.1	Workflow in single cell analysis . . . . .	130
3.4.6.2	Example of cellular release . . . . .	132
3.4.6.3	Example of nuclear import . . . . .	134
<b>4</b>	<b>Conclusion &amp; Outlook</b>	<b>139</b>
<b>5</b>	<b>Materials &amp; Methods</b>	<b>145</b>
5.1	Materials . . . . .	145
5.2	Instruments & software . . . . .	152
5.3	Methods . . . . .	156
	<b>Collaborations</b>	<b>173</b>
	<b>Bibliography</b>	<b>175</b>
	<b>Publications</b>	<b>191</b>
	<b>Appendices</b>	<b>195</b>
	<b>Curriculum Vitae</b>	<b>231</b>





# List of Figures

1.1	Central dogma in molecular biology . . . . .	2
1.2	RNAi mechanisms . . . . .	4
1.3	Argonaute and siRNA domains . . . . .	8
1.4	Delivery systems . . . . .	13
1.5	Cellular uptake mechanisms . . . . .	18
1.6	Localization of PTGS based RNAi . . . . .	20
1.7	RNA labeling strategies . . . . .	22
1.8	Principles of fluorescence . . . . .	26
1.9	Principles of FRET . . . . .	29
1.10	Fluorescence microscopy . . . . .	32
3.1	Scheme of FRET siRNA . . . . .	43
3.2	FL/TMR siRNA . . . . .	45
3.3	Spectral overlap in FRET siRNA . . . . .	46
3.4	Hybridization of siRNA strands . . . . .	48
3.5	Visualization of intensity values used for FRET evaluation . . . . .	50
3.6	Photostability of dyes . . . . .	53
3.7	Photostability of FRET pairs . . . . .	54
3.8	siRNA Atto488/Atto590 . . . . .	56
3.9	FRET pairs in the visible light range . . . . .	58
3.10	Further promising FRET siRNA . . . . .	59
3.11	Influence of labeling on RNAi . . . . .	61
3.12	Calibration of the Atto488/Atto590 system . . . . .	63
3.13	Dynamic range of FRET siRNAs . . . . .	64
3.14	Degradation of Atto488/Atto590 siRNA . . . . .	66
3.15	Liposomes via DAC . . . . .	68
3.16	Spectral analysis of siRNA liposomes . . . . .	70
3.17	Storage of liposomes . . . . .	71
3.18	Evaluation of delivery systems . . . . .	75
3.19	Microscopic bleaching of siRNA (agarose embedded) . . . . .	77
3.20	Microscopic bleaching of siRNA (fixed cells) . . . . .	79
3.21	Atto488/Atto590 in microscopy . . . . .	81
3.22	R/G algorithm in fixed cells . . . . .	83
3.23	Integrity simulation in fixed cells . . . . .	85
3.24	R/G distribution of cell simulation . . . . .	87
3.25	Temporal monitoring of siRNA integrity in fixed cells . . . . .	89
3.26	Nuclear accumulation sites after transfection . . . . .	91
3.27	In-detail analysis of FL/TMR transfected cells . . . . .	95
3.28	Organelle stains in RBE4 cells . . . . .	97

## List of Figures

---

3.29 siRNA with nuclear costaining Hoechst . . . . .	99
3.30 siRNA with cellular costaining RedDot . . . . .	100
3.31 RedDot in long-term observation . . . . .	101
3.32 Nuclear segmentation . . . . .	102
3.33 Settings for live imaging . . . . .	105
3.34 Release of Atto488/— and —/Atto647N siRNA . . . . .	107
3.35 Co-transfection of single labeled siRNA . . . . .	109
3.36 R/G in RBE4 cells over 6 h . . . . .	111
3.37 Release event in RBE4 . . . . .	112
3.38 Fixation of living cells . . . . .	113
3.39 R/G in Hela cells . . . . .	115
3.40 Release of Alexa555/Atto647N siRNA . . . . .	116
3.41 Release of siRNA direct after uptake . . . . .	119
3.42 Formation of speckles during release . . . . .	120
3.43 Cellular aggregates of transfected lipoplexes over time . . . . .	121
3.44 2 <sup>nd</sup> release, cell division and cell death of transfected cells . . . . .	123
3.45 Transfer of siRNA into neighboring cells . . . . .	124
3.46 Time point of release of FRET siRNA . . . . .	126
3.47 Fluorescence time of released siRNA . . . . .	129
3.48 Workflow of single cell analysis . . . . .	131
3.49 Example of a release event showing fate of siRNA in cells . . . . .	133
3.50 Single cell analysis data of siRNA release . . . . .	135
3.51 Nuclear import of intact siRNA after cellular release . . . . .	136
4.1 Schematics of triple FRET siRNA . . . . .	143
A.1 List of FRET pairs . . . . .	195
A.2 Example of siRNA modifications . . . . .	196
B.3 Fluorescent labels . . . . .	197
B.4 siRNA structure . . . . .	198
C.5 Photostability of ss and ds siRNA . . . . .	199
C.6 Bleaching of Atto488/acceptor and Alexa488/acceptor siRNA . . . . .	199
C.7 Bleaching of donor/TMR FRET siRNA . . . . .	200
D.8 Comparison of R/G calibration . . . . .	202
D.9 Dynamic range of R/G and 1 <sup>st</sup> deviation . . . . .	202
E.10 Comparison of FRET siRNA degradation . . . . .	203
F.11 Liposomes on PAGE . . . . .	204
G.12 Nanohydrogel uptake into cells . . . . .	205
G.13 Complexation study I . . . . .	206
G.14 Complexation study II . . . . .	206
H.15 Scheme of cross-talk & bleed-through by CLSM . . . . .	207
H.16 Schematics of R/G ratio algorithm . . . . .	207
I.17 FL/TMR in microscopy . . . . .	208
I.18 Integrity simulation in fixed cells . . . . .	209
I.19 Box-whisker analysis of FL/TMR . . . . .	210
I.20 Temporal changes in ROI of FL/TMR . . . . .	211

---

I.21	Localization of FL/TMR . . . . .	212
J.22	RedDot in long-term observation . . . . .	213
J.23	Release of Atto488/— siRNA . . . . .	214
J.24	Release of —/Atto647N siRNA . . . . .	215
J.25	Nuclear segmentation by siRNA signal . . . . .	216
K.26	Co-transfection of single labeled siRNA . . . . .	217
L.27	Release event of Atto488/Atto590 in RBE4 . . . . .	218
L.28	Release of Alexa555/Atto647N siRNA . . . . .	219
L.29	Cellular aggregates over time . . . . .	220
L.30	Transfer of siRNA into neighboring cells . . . . .	221
M.31	Time point of release of single experiments . . . . .	222
M.32	Fluorescent cells per time point . . . . .	223
M.33	Fluorescence time of released siRNA . . . . .	224
N.34	Example release event of Atto488/Atto590 - overlay . . . . .	226
N.35	Example release event of Atto488/Atto590 - R/G ratio . . . . .	227
N.36	Nuclear import of intact siRNA in detail - overlay . . . . .	228
N.37	Nuclear import of intact siRNA in detail - R/G ratio . . . . .	229



# List of Tables

3.1	Key data of siRNA ON panel . . . . .	47
3.2	Fluorescence intensity data of siRNA ON panel . . . . .	48
3.3	FRET data of various dye combinations . . . . .	51
3.4	Photobleaching stability of dye analogs . . . . .	52
3.5	Knockdown efficiency of labeled siRNA . . . . .	62
3.6	Comparison of R/G calibration . . . . .	64
3.7	siRNA integrity in DAC liposomes . . . . .	71
3.8	Nanoparticulate evaluation data . . . . .	74
3.9	Microscopy bleaching of agarose embedded and transfected siRNA . . . . .	77
3.10	Microscopic crosstalk of Atto488/Atto590 . . . . .	81
3.11	R/G algorithm settings . . . . .	84
3.12	R/G frequency of simulated siRNA samples . . . . .	87
3.13	Microscopy settings for live cell imaging . . . . .	104
3.14	Cellular release events . . . . .	118
3.15	Release events and more . . . . .	123
3.16	Phases in cellular release after transfection . . . . .	126
3.17	Maximal number of fluorescent cells . . . . .	127
3.18	Average fluorescence time inside cytoplasm of released siRNA . . . . .	129
5.1	Settings for PAGE analysis . . . . .	158
5.2	Microscopy parameters for FRET imaging . . . . .	166
5.3	Parameters for different dyes and stains . . . . .	166



# Abbreviations

2'-OMe	2'-O-methyl
% v/v	volume per volume percent
% w/v	mass per volume percent
IC <sub>50</sub>	concentration for 50 % inhibition
A	FRET acceptor
AFC	adaptive focus control
Ago	subfamily of Argonaute family
AGO1-4	human Argonaute
AMD	age-related macular degeneration
AOBS	acousto optical beam splitter
AOTF	acousto optical tunable excitation filter
APS	ammonium persulfate
as	antisense
bFGF	basic fibroblast growth factor
BHQ	black hole quencher
bp	base pair
CCD	charged coupled device
CDGS	chromatin dependent gene silencing
chol	cholesterol
CLSM	confocal laser scanning microscopy
CPP	cell penetrating peptide
D	FRET donor
DAC	dual asymmetric centrifugation
DAPI	4',6-diamidino-2-phenylindole
DEPC	diethylpyrocarbonate
DFHBI	3,5-difluoro-4-hydroxybenzylidene imidazolinone
DMSO	dimethyl sulfoxide
DNA	deoxyribonucleic acid
DNase	deoxyribonuclease
ds	double stranded
dsA	double stranded, single labeled siRNA —/Acceptor
dsD	double stranded, single labeled siRNA Donor/—
dsDA	double stranded, double labeled siRNA Donor/Acceptor
DSMZ	Deutsche Sammlung von Mikroorganismen und Zellkulturen
DSPE	1,2-distearoyl-sn-glycero-3-phosphoethanolamine-N
EDTA	Ethylenediaminetetraacetic acid
EGFP	enhanced green fluorescent protein
EPC3	hydrogenated egg phosphatidylcholin
EPR	enhanced permeability and retention
ER	endoplasmic reticulum

## Abbreviations

---

FACS	fluorescence activated cell sorting or flow cytometry
FBS	fetal bovine serum
FCCS	fluorescence cross-correlation microscopy
FCS	fluorescence correlation spectroscopy
FISH	fluorescence <i>in situ</i> hybridization
FLAP	fluorescence localization after photobleaching
FLIM	fluorescent lifetime imaging
FLIP	fluorescence loss in photobleaching
FRAP	fluorescence recovery after photobleaching
FRET	fluorescence resonance energy transfer
FSC	forward scatter
GBG	green background
GEEC	glycosyl phosphatidylinositol-anchored protein enriched early endosomal compartment
GFP	green fluorescent protein
HBI	4-hydroxybenzylidene imidazolinone
HEPES	4-(2-hydroxyethyl)-1-piperazineethanesulfonic acid
HyperCLDB	hypertext cell line data base
LB	lysogeny broth
LUT	lookup table
LUV	large unilamellar vesicle
m5U	5-methyluridine
MFI	mean fluorescence intensity
mic med	microscopy medium
mic TF med	microscopy medium for transfection
miRNA	micro RNA
miRNP	miRNA-containing ribonucleoprotein particle
MLV	multilamellar vesicle
MRI	magnetic resonance imaging
mRNA	messenger RNA
MVB	multi vesicular bodies
MWCO	molecular weight cut off
N.A.	numerical aperture
N/A	not available, not applicable
ncRNA	non-coding RNA
nd	not determined
neg	negative
nt	nucleotides
ODC	ornithine decarboxylase
ON	oligonucleotide
P-bodies	processing bodies
PAGE	polyacrylamide gel electrophoresis
PALM	photoactivated localization microscopy
PAMAM	polyamidoamine
PAZ	Piwi-Argonaute-Zwille
PBS	phosphate buffered saline



PCR	polymerase chain reaction
PEG	polyethylene glycol
PEI	polyethylenimine
Pen/Strep	penicillin streptomycin
PES	polyethersulfon
PET	positron emission tomography
piRNA	PIWI interacting RNA
Piwi	subfamily of Argonaute family
PKC	protein kinase C
PMT	photomultiplier
pos	positive
PR	proximity ratio
pre TF med	pre-transfection medium
pre-miRNA	precursor micro RNA
pri-miRNA	primary micro RNA
PRR	pattern recognition receptor
PS	phosphorothioate
PSF	point spread function
PTGS	post-transcriptional gene silencing
Qdot	quantum dot
RBE4	rat brain endothelial cells 4
RBG	red background
RGB	red green blue
RISC	RNA induced silencing complex
RITC	rhodamine iso-thio-cyanate
RITS	RNA induced transcriptional silencing
RLC	RISC loading complex
RNA	ribonucleic acid
RNAi	RNA interference
RNase	ribonuclease
ROI	region of interest
ROS	reactive oxygen species
rRNA	ribosomal RNA
RSV	respiratory syncytial virus
s	sense
SD	standard deviation
SELEX	systematic evolution of ligands by exponential enrichment
set1/set2	settings for FL/TMR R/G analysis
setA/setB	early settings for Atto488/Atto590 R/G analysis
setC/setD	final settings for Atto488/Atto590 R/G analysis
shRNA	short hairpin RNA
SIM	structured illumination microscopy
siRNA	small interfering RNA
SL	sterically stabilized liposomes
sRNA	small RNA
ss	single stranded

## Abbreviations

---

SSC .....	side scatter
SSL .....	sterically stabilized liposome
std med .....	standard medium
STED .....	stimulated emission depletion
STORM .....	stochastic optical reconstruction microscopy
SUV .....	small unilamellar vesicle
TE .....	transposable element
TF .....	transfection
TF med .....	transfection medium
TLR .....	Toll-like receptor
TMR .....	Tetramethylrhodamine
TRBP .....	HIV transactivating response RNA-binding protein
Tris .....	tris(hydroxymethyl)-aminomethan
tRNA .....	transfer RNA
Trolox .....	6-hydroxy-2,5,7,8-tetramethylchroman-2-carboxylic acid
UTR .....	untranslated region
V-ATPase .....	vacuolar proton pump ATPase
VPG .....	vesicular phospholipid gel
Wago .....	subfamily of Argonaute family
xxx BP yy .....	band pass filter, blocks light outside indicated band width
xxx LP .....	long pass filter, blocks light below xxx nm
xxx SP .....	short pass filter, blocks light above xxx nm

# 1 Introduction

Nucleic acids, such as DNA or RNA, play besides other macromolecules, like proteins and carbohydrates, probably the most important role in living organisms.

While proteins are involved in catalyzing biochemical reactions of the cell metabolism, replication or cell signaling, and function as scaffolds that maintain cell shape or cell to cell interaction sites, nucleic acids are the information storage for all cellular processes and thus basis for all living organisms. The diversity of function of proteins is based on the combination of the 20 canonical amino acids which are encoded by the 4 major nucleobases of DNA, which are Adenine (A), Guanine (G), Thymine (T), Cytosine (C). The transfer of the encoded information from the DNA level to the final protein takes place during protein biosynthesis. This process can be divided into two major phases, which are the transcription of genetic information from DNA to messenger RNA (mRNA) and the translation of the mRNA sequence into proteins. Thereby, sets of three bases (base triplets) are recognized by transfer RNAs (tRNA) that carry the amino acid according to the genetic code. The protein biosynthesis takes place at the ribosome where the nascent protein is formed by coupling each new amino acid to the C-terminus of the initiator amino acid or the already synthesized polypeptide chain. On the RNA level Thymine is replaced by Uracil (U).

This basic description of an information flow from DNA via RNA to proteins describes the classical “*central dogma in molecular biology*” (see Figure 1.1 A). This expression was first named by Crick in 1970 [5] and describes a one-way information flow. At this point of view DNA can be seen as kind of legislative, that determines cellular processes on the basis of genetic information, and proteins as a kind of executive that maintain cellular life.

The process, however, is more complex and strictly regulated (see Figure 1.1 B). Proteins, on one hand, are involved in both translational and transcriptional regulation in eukaryotic organism. Thereby, they act as key factors for a basic gene expression. On the other hand, RNA has been shown to be involved in the regulation of both translation and transcription, too. This RNA-based regulation is in principle based on non-coding RNAs (ncRNA) that are, besides mRNA, tRNA and ribosomal RNA (rRNA), products of cellular transcription. A look at the human genome reveals that only a little fraction of the entire genetic sequence is actual coding for proteins, whereas a huge part of

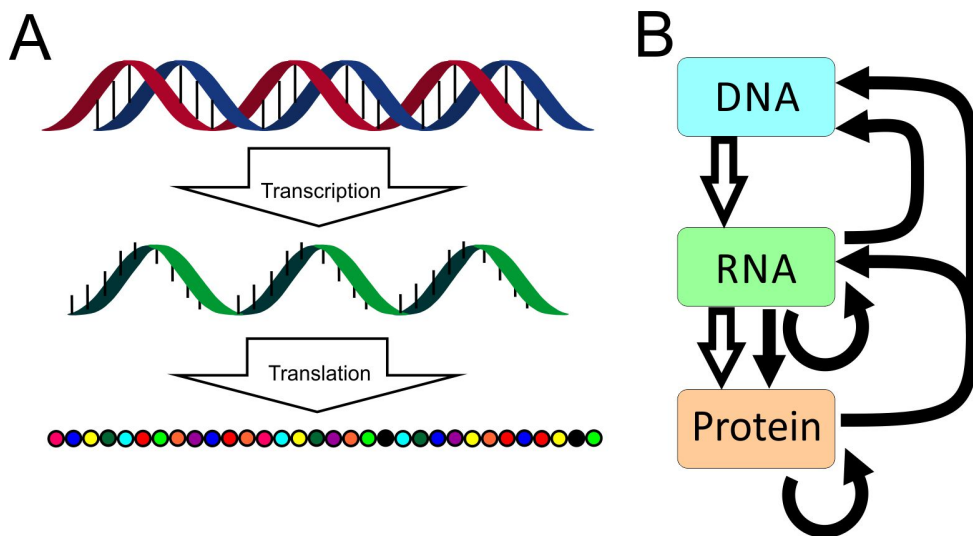


**Figure 1.1: Central dogma in molecular biology.** (A) classical concept of single information flow from DNA to RNA to proteins. (B) Adaptation of the central dogma to discovered regulation mechanisms during the last decades. Hollow arrows indicate classical dogma, whereas solid black arrows represent regulatory interactions of DNA, RNA and proteins. Modified illustration on basis of Thattai [6] and Ozomaro et al. [7].

the genetic information, i.e. introns, repetitive elements and intergenic space, is seen as non-coding material and was some years ago seen as a form of “junk DNA”. Today it is known that these non-coding DNA sequences and the corresponding transcripts play also an important role in regulation. After being transcribed, this genetic material forms the pool of ncRNA. One important player in the field of ncRNAs are small RNAs (sRNA) in the size about 20-30 base pairs (bp), to which the micro RNAs (miRNA), short interfering RNA (siRNA) and PIWI-interacting RNA (piRNA) belong. These sRNA can regulate gene expression on the post-transcriptional level by a process that is known as RNA interference (RNAi).

## 1.1 RNA interference

RNAi was first described by Fire and Mello in 1998 [8] and characterizes a mechanism in which small RNA duplexes lead to the downregulation of a specific gene depending on the sequence of the sRNA. Since then RNAi was observed in all mammals [9] and almost all other eukaryotic organisms [10], which makes RNAi very interesting for scientific research.

Shortly after the first description by Fire and Mello, Tuschl and co-workers could already elucidate the mechanics behind RNAi [11, 12] and made RNAi thus an applicable tool for research. The possibility to regulate gene expression on a post-transcriptional level made RNAi to an important research field and a standard technique in molecular biological research. The process of post-transcriptional gene silencing (PTGS) was then, and still is extensively studied and promises to be a source for plenty new strategies

to handle different diseases. The importance of the described regulative mechanism for the scientific society explains why already 7 years after the first description, Fire and Mello received the Nobel price in medicine for their discovery.

RNAi is based on sRNA localized in a multi-protein-complex, the RNA induced silencing complex (RISC), that guides the sRNA to the target site to perform a specific regulation. Especially siRNA and miRNA, two short RNA species, are of great interest. During the last years a third group emerged, the piRNA, which is in contrast to double stranded (ds) siRNA and ds miRNA (average length between 20-25 bp) a little longer (around 24-31 nt) and only single stranded (ss). While siRNAs originate from long ds RNA of intra- or extracellular RNA precursors that are cleaved by cellular endonucleases into the shorter siRNA duplexes, miRNAs have only an endogenous origin, like piRNAs do. It is obvious that such a diverse source of RNA species results in several different occurring cellular pathways.

sRNA, involved in RNAi, assemble in a complex with a family member of the Argonaute protein family (Ago). The Ago proteins recognize with help of the loaded small RNA species their target sequence. The most known regulatory effect involves the RNase H activity of some Ago proteins that lead to a enzymatic cleavage of the target RNA, this mechanism is basis for siRNA induced gene silencing, e.g. used for analyzing gene function. Other Ago proteins involve the recruitment of additional factors for different regulatory effects [13, 14].

RNAi is, in contrast to antisense technology, which had been first reported in the 1970s by Zamecnik and Stephenson [15], based on multiple turnovers of enzymatic cleavage, whereas classical antisense technology blocks translation via stoichiometric inhibition by hybridization to the target sense mRNA. Thus RNAi can achieve a stronger regulation with less oligonucleotide (ON) material than classical antisense technique and offers a much more potent drug [16].

### **1.1.1 RNAi pathways**

As mentioned above, there exist three different main pathways that are related to RNAi, i.e. the siRNA, miRNA and piRNA pathway (see Figure 1.2). In the following each pathway with its main downstream regulation will be briefly described. It is important to mention that a pathway is not unique to one species and that especially in the group of piRNA a set of different species dependent regulatory effects have been observed.

#### **1.1.1.1 siRNA pathway**

The origin of siRNA based RNAi lies probably in a cellular defense strategy against RNA viruses or transcripts of transposable elements (TE) [18]. Thereby, long ds RNA

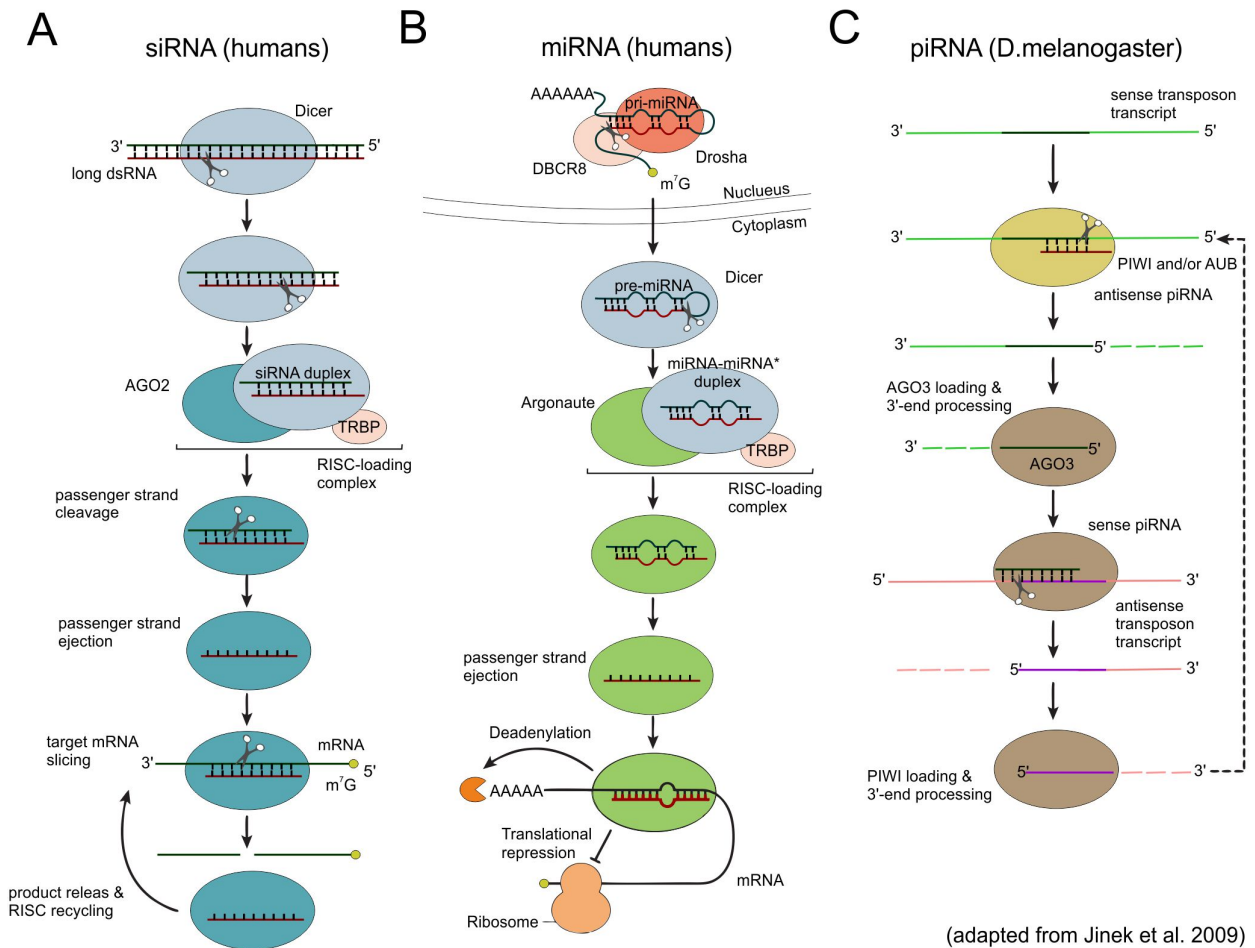


**Figure 1.2: Overview of RNAi mechanisms.** (A) ds RNA is cleaved by Dicer in short ds siRNA of 20-25 bp length and incorporated into RISC. The active RISC targets the mRNA and induces cleavage. (B) miRNA primary transcripts are cleaved into miRNA precursors inside the nucleus by the endonuclease Drosha. After export to the cytoplasm miRNA is formed by Dicer cleavage and incorporated into RISC which targets mRNA in the 3'-UTR with incomplete base pairing (bulge) and leads to translational inhibition. (3) piRNA are generated from single stranded transcripts of transposons. The initial step remains unclear, but once one piRNA is formed an amplification via a "ping-pong" mechanism occurs by association with Argonaute proteins (Ago or Piwi) and subsequent processing of target transposon transcripts into new piRNA. Adapted from Jinek and Doudna [17].

is the source of the formation of small RNA fragments, which serve as siRNA. With the discrimination of endogenous (TE based) or exogenous (RNA virus) ds RNA, siRNA can be divided in endo-siRNA or exo-siRNA [19]. The following cellular processes do, however, not discriminate between endo- or exo-siRNA.

Long ds RNA is recognized by a cellular type III nuclease, named Dicer, as foreign material and is cleaved into shorter fragments of around 20-25 bp [20]. This short duplexes contain two nucleotides (nt) overhang on each 3'-end, a 5'-phosphate and form the species of siRNA (see Figure 1.2 A). Besides the viral or TE dependent siRNA formation, siRNA can also be derived from short hairpin RNAs (shRNA) [21] that are introduced for therapeutic purposes either into the genome or by a transient plasmid. The most common approach used in research is, however, the direct transfection of chemically synthesized artificial siRNA duplexes, which then join the cellular siRNA

pathway.

After the cleavage or transfection into the cell, the siRNA duplex is incorporated in the RISC loading complex (RLC) which consists of Dicer, Argonaute and a cofactor named TRBP (transactivating response RNA-binding protein in HIV). In this complex the ds siRNA is unwound and one strand gets degraded (this strand is called the passenger or sense strand) whereas the other strand (called guide or antisense) remains associated with the multi-protein complex. After dissociation of Dicer and TRBP, the final RISC is formed. The RISC consists only of the guide siRNA strand and the Argonaute protein. After formation the RISC recognizes its target mRNA with the help of the guide siRNA and leads to target cleavage.

The term guide/passenger strand for the two strands of the siRNA are based on the function that one strand guides the RISC to the target mRNA whereas the other strand is more or less just a passenger of the siRNA duplex. The other terminology sense/antisense is based on the sequence of the single strands. The guide strand is actually complementary to the mRNA and can thus be seen as the antisense sequence to the mRNA whereas the passenger strand is identical to the mRNA sequence and thus called sense.

Besides RISC, siRNA can also be incorporated into the RNA induced transcriptional silencing (RITS) complex. The RITS complex is localized inside the nucleus, whereas RISC is localized in the cytoplasm. siRNA associated with RITS leads to methylation of euchromatin and histone modification which finally leads to the formation of transcriptional inactive heterochromatin. This process is also named chromatin dependent gene silencing (CDGS). The RITS complex and CDGS was similar to RISC based RNAi found in many organisms including mammals [22, 23].

Though in principle two effector pathways can be assigned to siRNA based RNAi, the cleavage of target mRNA by RISC is of major interest for potential drug development and silencing genes in cell studies.

### **1.1.1.2 miRNA pathway**

Different from the siRNA pathway, miRNAs originate exclusively from endogenous RNA which is transcribed as long primary micro RNA (pri-miRNA) transcript that forms multiple stem-loop structures (see Figure 1.2B). The pri-miRNA is then cleaved by the nuclear RNase Drosha into short stem-loop structures of around 70 nt which represent a precursor miRNA (pre-miRNA) [24]. The pre-miRNA can also be derived from introns of spliced mRNA which is called mirtron [19, 25]. miRNA precursors are then exported from the nucleus by Exportin-5 and join a similar pathway as siRNA that involve Dicer cleavage [24].

The mature miRNA is similar to siRNA between 20-25 bp long and has 3'-overhangs. In

contrast to siRNA, miRNA are characterized by incomplete basepairing with their target (see bulges in Figure 1.2 middle part) which results in different downstream regulatory effect.

Different from siRNA RISC, which triggers target mRNA cleavage, miRNA RISC, sometimes also referred as miRNA-containing ribonucleoprotein particle (miRNP) [14], results in a repression of translation by binding to the 3' untranslated region (UTR) of the target mRNA. Thereby the lack of sequence complementary inhibits the cleavage of the mRNA. The inhibition of translation is based on either deadenylation of the poly-A-tail of the messenger RNA, and thus a decomposition via cellular mechanisms in the processing bodies (P-bodies) [26], or interaction with the translation initiation complex. miRNA-RISC is also often found in P-bodies where mRNA is decomposed. Because of the incomplete basepairing and imprecise cleavage of Drosha and Dicer in the miRNA maturation, one miRNA gene locus generates multiple miRNAs and can regulate a complete set of mRNA [17, 27].

### 1.1.1.3 piRNA pathway

piRNA are the last class of sRNA that are associated with the RNAi pathway. Research indicates that piRNA are also probably the largest group of sRNA that is involved in fine-tuning of gene expression. The generation of piRNA is a non-Dicer-dependent pathway, which separates piRNAs from siRNA and miRNA [27–29]. Their name origins from the associated Argonaute protein, which belongs to the Piwi-subfamily of the Argonaute protein family. piRNA are, as indicated, slightly longer than siRNA and miRNA but consist of only one strand and are mainly located in germ cells. The function of piRNA is a kind of guardian of the germline by silencing transposon activity [28, 30] and thus maintaining the genome for the offspring.

piRNA originate from single stranded transcripts of TE or piRNA-gene-clusters [31]. In a primary generation process the mature piRNA is formed by cleavage by an endonuclease [32]. These primary piRNA can be amplified in an “ping-pong” mechanism (see Figure 1.2 C) which enhances the silencing capability. During this secondary generation process antisense piRNA-Piwi complexes bound to their target (mainly transposable RNA) lead to target cleavage and thereby to the formation of secondary sense piRNA. These sense piRNA associate again with a Piwi protein and produce antisense piRNA and so on. piRNAs can efficiently silence transposable elements and maintain genome integrity.



## 1.1.2 Argonaute proteins and RISC incorporation

The guide sRNA strand and the associated Argonaute protein are the driving force in PTGS based on siRNA. Therefore a closer look on the Argonaute protein family and the incorporation of sRNA especially siRNA is necessary.

### 1.1.2.1 Argonaute protein family

The Argonaute protein family displays a protein family that is essential for the regulatory effect of sRNA. The name originates from an *A.thaliana* knockout that resembles the tentacles of the octopus, *Argonauta argo* [14, 33].

Argonaute proteins can be found in many organisms, with the most studied being *C. elegans*, *Drosophila*, *Xenopus*, *Zebrafish*, mouse and human [32, 34]. So far, one Argonaute protein was also identified in the fission yeast *S. pombe*, whereas the model organism par excellence, i.e. the budding yeast *S. cerevisiae*, seems to lack the machinery of RNAi and Argonaute proteins [14, 35]. Even in some prokaryotes members of this protein family have been found, though their function remains unclear [17].

The family of Argonaute proteins can be divided in two subfamilies. On the one hand there are the *A.thaliana* analogs, named Ago, and on the other hand the Argonaute proteins that resemble the *drosophila melanogaster* Piwi protein. The Ago subfamily is mainly involved in the formation of miRNA and siRNA RISC whereas the Piwi subfamily associates with the piRNA group of sRNA [14, 34]. So far Piwi proteins are uniquely found in animals and not in plants, like the Ago subfamily [25]. In humans 4 Ago (AGO1-4) and 4 Piwi (HIWI1, HIWI2, HIWI3 and HILI) proteins have been found [14]. Common for all Argonaute protein is the structural similarity concerning the different protein domains, which are involved in sRNA and target recognition and a typical molecular weight of around 100 kDa. Basically, there are 4 conserved domains, which are the N-terminal, PAZ (Piwi-Argonaute-Zwille), MID and PIWI domain (see Figure 1.3 A). The three-dimensional structure reveals a bilobate structure with one lobe consisting of PIWI and MID domain and the other lobe of the N-terminal domain and PAZ [17] (see Figure 1.3 B).

The MID and PAZ domain are involved in the binding of sRNA, where PAZ recognizes the 3'-overhang by its free OH-site [38] and MID recognizes the 5'-end with its phosphate group [39, 40]. Though the 5'-phosphate is reported to be essential [17, 41], recent studies also indicate that the attachment of fluorescent dyes on the 5'-phosphate do only weakly interact with the silencing capability [42]. The actual cleavage of the target mRNA occurs by the PIWI domain which forms an RNase H-like structure and shows similar endonucleolytic activity [17]. The cleavage occurs at the opposite site of the antisense strand between position 10 and 11, counted from the 5'-end [43, 44], see

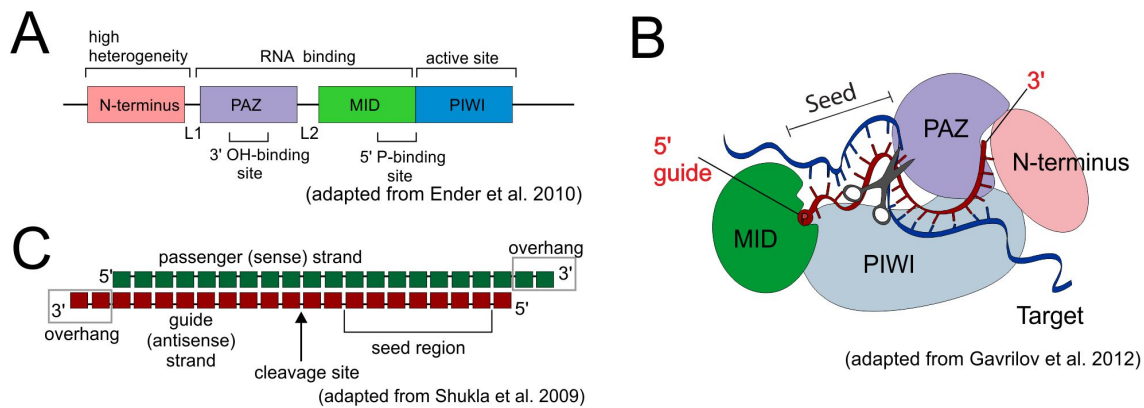


**Figure 1.3: Argonaute protein domains and siRNA structure.** (A) Protein domains of Argonaute proteins. N-terminal domain (blue), PAZ domain (violet) with 3'-binding site, MID domain (orange) with 5'-recognition site and PIWI domain (green) with RNase H activity. Adapted from Ender and Meister [14] (B) Schematics of Argonaute protein with bound guide strand and target mRNA. Indicated are the seed region, 5'- and 3'-recognition site of the guide strand. Adapted from Gavrilov and Saltzman [36] (C) Schematics of an siRNA with 3'-overhangs and indication of the seed region and substrate cleavage site. Adapted from Shukla et al. [37]

also Figure 1.3 C. AGO2 is the only human Ago protein that shows RNase H activity which is also called slicer activity [43]. Due to the catalytic active PIWI domain, AGO2 RISC loaded with siRNA leads to enzymatic cleavage of the target mRNA. The other human Ago protein lost the slicer activity due to mutations in the catalytic center of their PIWI domain. Nevertheless, the inactive PIWI domain still contains an RNA binding site, which is involved in target mRNA and ds siRNA binding [17], as is necessary for non-catalytic RNAi.

### 1.1.2.2 RISC incorporation of sRNA

After the siRNA duplex is recognized and bound by the MID and PAZ domain, the duplex is unwound and the strand with the less thermodynamically stable 5'-end in the duplex is selected as guide or antisense [45–47]. This selection process seems to be based on the fact that the more stable 5'-end does not interact with the MID domain and thus an asymmetry in strand selection occurs [48, 49]. The sense or passenger strand is either cleaved by the slicer activity of the PIWI domain or separates from the complex by an yet unknown process [44, 50–52]. The human AGO1,3,4, that lack the slicing activity, can still load miRNA and due to incomplete basepairing the sense strand gets more easily and without slicing separated from the complex [51].

Synthetic siRNA that lack a 5'-phosphate get phosphorylated by an endogenous kinase and are further recognized as Dicer products in the RNAi pathways [9].

The active silencing complex recognizes its target by basepairing with the guide strand and leads to a catalytic cleavage of the mRNA [53]. After the cleavage the RISC dissociates and is able to degrade further mRNA molecules [54].

A closer look at the complex and target RNA reveals that nucleotides 2 to 6 of the guide

strand are orientated in a way that allows free basepairing with target RNA [48, 49]. This region, that is according to crystal structures, responsible for target recognition lies within the so called 'seed region' which ranges from position 2 to 8 of the antisense strand. The seed region is seen as the most important sequence part of siRNA and miRNA as here the target specificity is defined [53, 55]. Thus, siRNA with an abundant seed region in the target genome probably will result in off-target effects by silencing other than the originally intended genes.

### 1.1.3 Towards siRNA based therapeutics

siRNA seems to be an ideal system for developing new efficient drugs. siRNA can be designed to almost every target mRNA and in cell culture efficient silencing can be achieved [56]. Over the last years, around 21 different clinical studies targeting around 12 different diseases, like cancer, viruses and genetic disorders have been performed [57]. In two detailed reviews on these ongoing or terminated clinical trials, Burnett et al. [57] and Burnett and Rossi [58] describe the different approaches and targets for potential siRNA therapeutics.

The major hurdles for a potential *in vivo* application are thereby [36, 57–60]:

- Delivery into the target tissue or organ
- Protection against blood and cellular RNases
- Renal clearance and circulation time in the blood system
- Delivery across the cellular membrane
- Immunostimulation by either siRNA or delivery vehicle
- miRNA-like off-target gene silencing
- Saturation of RNAi machinery

#### 1.1.3.1 Off-target effects

Unwanted side effects of siRNA application are also known as off-target effect. The most important off-target effects are either based on similarities to miRNA and thus the activation of miRNA pathway or the induction of the cellular innate immune system.

Due to the similarity of siRNA and miRNA a crossing over between the pathways can occur and might cause unwanted gene regulation. This off-target gene silencing [36] is based on similarities of mRNA sequences with the seed region of an designed siRNA [61]. The seed region is a region of around 6-7 nt and off-target effects with the miRNA pathway are most likely [62] (see Figure 1.3 C). This effect clarifies when remembering that for the miRNA pathway an incomplete base pairing is sufficient for targeting the 3'-UTR of mRNA. Additionally, one has to keep in mind that miRNA targets not only on mRNA level, which can be analyzed by real-time PCR and microarray, but also represses

translation without mRNA degradation. Thus mRNA screens might lack a potential translational repression that might cause severe side-effects during clinical studies [63]. Additionally, off-target effects can originate from sense strand incorporation, which might then also join the miRNA pathway [36]. In consequence a detailed bioinformatic screen of the genome and subsequent analysis on mRNA and protein level is essential.

On the other side, an activation of the immune system by siRNA [60] is another unwanted side effect. The induction of inflammatory cytokines or interferons was first reported only for long ds RNA. However, there are also some shorter siRNA duplexes that trigger an immune response, which can finally lead to cell death [64, 65]. The response is based on activation of pattern recognition receptors (PRR), like the Toll-like receptors TLR3 or TLR7, which recognize ss or ds RNA [66–68] and are found in the endosomes of eukaryotic cells. Another class of cytosolic PRRs, like PKR (a protein kinase) and RIG-I (an RNA helicase), mediate interferon response or inhibition of translation [67]. As siRNA delivery uses endocytotic pathway, siRNA is prone to be exposed to the TLRs in the endosomes and thus resulting in a potential immune response. Nevertheless the usage of short 20-24 bp long duplexes reduces the immunostimulatory potential significantly compared to Dicer-substrate siRNA precursor, which are in the range of 25-30 bp, or longer ds RNA [69, 70].

### 1.1.3.2 siRNA modifications

Extensive studies on siRNA modification were made to improve the siRNA efficiency for *in vivo* application [37] addressing the mentioned hurdles. The major intention of modifying siRNA is to reduce off-target silencing and immunostimulatory potential and to improve the nuclease resistance of the duplex, as naked siRNA gets degraded within minutes inside the blood stream [71]. These modifications can in principle be divided into three groups, which are the modification of the backbone, the ribose or the base itself (for an overview of siRNA modifications see Appendices A.2 or a review from Shukla et al. [37]).

One common backbone modification are phosphorothioates (PS) [72, 73]) where one oxygen of the phosphodiester bond is replaced by sulfur. The introduction of PS results in general in an enhanced nuclease stability but too excessive modification might on the other hand cause cytotoxicity.

On the ribose site 2'-OMe, meaning a methylation of the free 2'-OH-group is one major modification of interest. Similar to PS, 2'-OMe is reported to enhance nuclease stability [74] and furthermore reduce the innate immune response by preventing a TLR recognition in the endosome [75]. Additionally 2'-OMe or 2'-F increase the melting temperature of an RNA duplex and might be useful in guiding strand selection in the RISC [37].

Base modifications, such as 5-methyluridine (m5U) [76] and many more (see Appendices A.2), were tested for the modulatory effect on the melting temperature and thus the influence on the stability of the duplex which might again be useful in guide incorporation [37]. Modification of the siRNA sequence especially of the passenger strand might also be suitable for masking against nucleases.

### 1.1.3.3 Guidelines for siRNA duplex design

Based on several modification studies and the principle mechanism of siRNA mediated RNAi, the following guideline for the design of modified siRNA can be made [9, 37, 77]:

#### **Thermodynamical and structural considerations:**

- siRNA duplex consisting of single strands of  $\sim 21$  nt length
- double stranded region of  $\sim 19$  bp
- lower internal stability at 5'-end of antisense strand by U-/A-bases
- higher internal stability at 5'-end of sense strand by G-/C-bases
- GC content between 30-50% (enhanced unwinding)
- avoid internal repeats

#### **Sequence and base specific considerations:**

- preferably UU at 3'-end
- BLAST screen to avoid sequences with high similarity to other genomic sequences, especially within the seed region
- U at position 10 of sense strand (enhances RISC cleavage of target)
- no G at position 13 of sense strand (improved unwinding)
- presence of A and absence of G or C at position 19 of sense strand (strand selection)

#### **Modification considerations**

- avoid bulky modification in seed region and cleavage site of guide (reduced RNAi)
- modification preferably at 3'-overhang and after position 16 of guide as not involved in recognition
- modifications preferably in sense strand
- PS modification in 3'-overhang of sense might enhance nuclease resistance
- stabilizing modifications at 5'-end of sense
- a total of three 2'-OMe uridine in sense and antisense prevent immunostimulation
- sulfur modifications improve biodistribution

Besides modification of the naked siRNA a protection against nucleases can be achieved by the formulation into nanoparticulate delivery systems.

## 1.2 siRNA delivery

Delivery of nucleic acids is one of the major goals in ongoing RNAi research for a future therapeutic application. Thereby, the main focus lies on the transfer of nucleic acids inside cells and into the cytoplasm where siRNA based gene silencing occurs. This process can, in general, be referred to transfection [56], though the term “transfection” is more suitable for *in vitro* delivery in cell culture experiments. Nevertheless, *in vitro* or *in vivo* delivery face the same problem of transporting intact siRNA across the cellular membrane, as siRNAs are with around 14 kDa too large and too negatively charged for passive uptake by membrane diffusion [56].

One can divide the different delivery or transfection approaches into two basic categories. On the one hand the *in vitro* delivery systems that are not suitable for *in vivo* approaches and on the other the *in vivo* compatible approaches. In principle, every *in vivo* compatible approach can be used *in vitro*, too, but not vice versa.

### 1.2.1 *in vitro* delivery systems

The most studied systems are based on cell culture models and used for research purpose only to deliver nucleic acid, especially DNA like plasmids, into cells. The nucleic acids need to enter the cell to observe a certain effect. The most common techniques thereby are chemical or physical transfection systems.

#### 1.2.1.1 Chemical transfection

The group of chemical transfection agents contains cationic compounds, like the commercially available cationic lipids lipofectamine<sup>®</sup> or oligofectamine<sup>™</sup> and many more, or one of the first transfection agents used, calcium phosphate [78]. Now more and more new, also *in vivo* compatible chemical transfection agents, are excessively studied.

The principle of all chemical transfection approaches is to mask the negative charge of the nucleic acid, DNA or RNA, by positively charged molecules or build a fusogenic particle [79, 80] that is then easily taken up by cells via endocytosis (see Figure 1.4B upper part).

Whereas in case of calcium phosphate the charged DNA (usually plasmids) is masked by forming a precipitate with  $\text{Ca}_3(\text{PO}_4)_2$  [78], cationic lipids form more complex structures with DNA or RNA oligonucleotides (so called lipoplexes or polyplexes), that carry a positive net charge. The complexes sediment onto cell and adhere to the negatively charged cell membrane. After endocytosis the complex is located in endosomes and during the maturation process to lysosomes the complex or cargo gets released into the

cytoplasm [81–83]. In case of delivery of DNA material an import into the nucleus can occur, followed by integration into the genome or the expression of exogenous genes (in case of plasmids).

Though in cell culture cationic lipids enable an efficient transfection rate, a high cytotoxicity is disadvantageous for *in vivo* application [84].

In 2005 the Sczakiel group published another transfection approach by using phosphorothioates that stimulate a caveosomal based uptake of naked siRNA [85, 86]. In this approach high concentrations of PS stimulate an caveosomal uptake with a cotransport of siRNA.

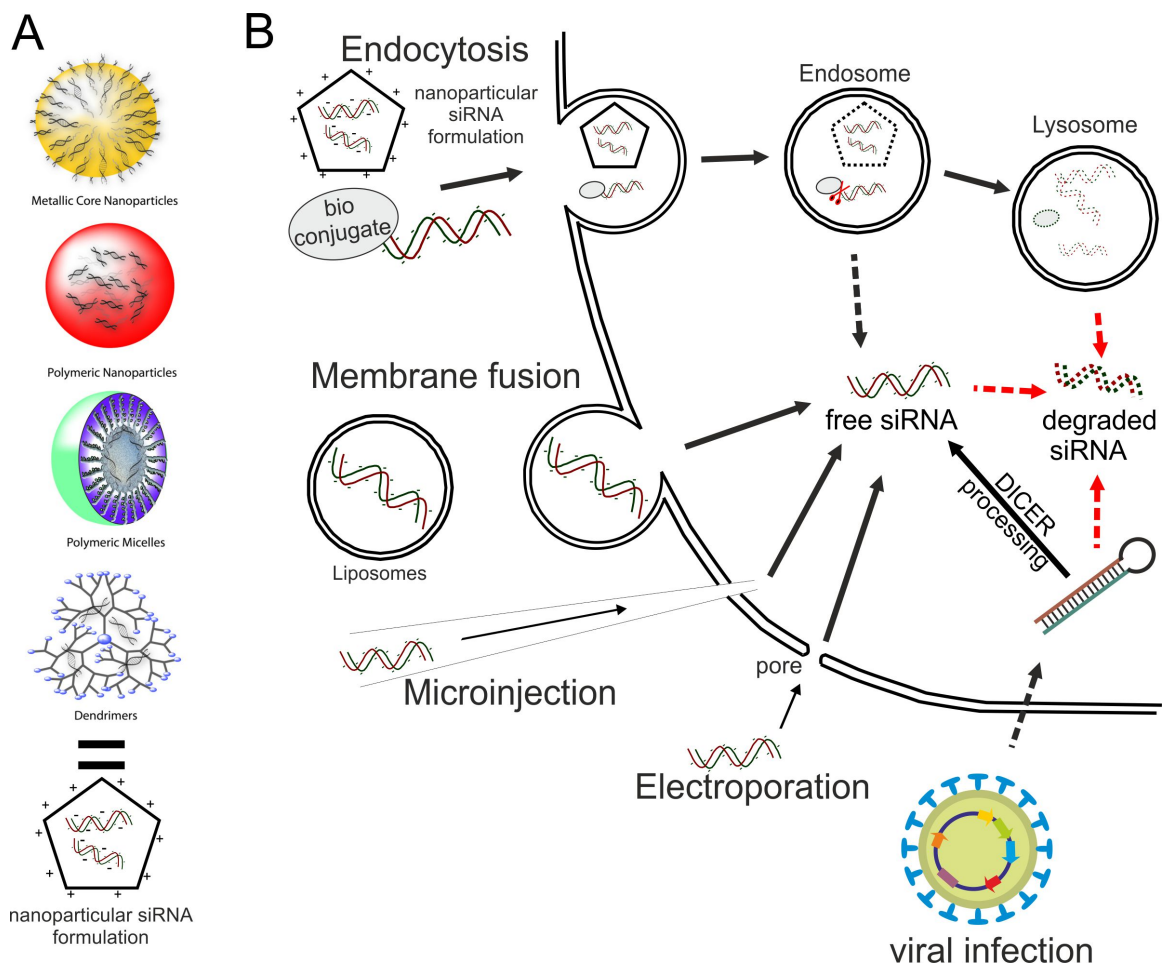


**Figure 1.4: Delivery of siRNA and siRNA formulations inside target cells.** (A) nanoparticulate delivery systems (pentagon with siRNA, bottom) with example of metallic core nanoparticle, polymeric nanoparticles, mycellar structures and dendrimers (from top). Adapted from Gavrilov and Saltzman [36] (B) different Delivery/Transfection methods of nucleic acid. Endocytosis of nanoparticulate formulations and bioconjugates (top) into endosomes. Release occurs during maturation process towards lysosomes. Membrane fusion of liposomes (upper middle part). passive diffusion after pore formation (e.g. electroporation) or direct injection (lower middle part) and viral delivery of shRNA coding vectors (lower part) and subsequent Dicer processing.

### 1.2.1.2 Physical transfection

Physical transfection methods are based on a disruption of the cell membrane followed by the delivery of DNA/RNA into the cytoplasm or nucleus. The most common techniques are electroporation and microinjection.

During electroporation, a high electric impulse disrupts the cell membrane and the DNA can enter the cytoplasm [87]. Microinjection is based on direct injection of DNA or RNA into the cytoplasm or the nucleus by ultrafine needles that deliver a small volume into a cell (see Figure 1.4 B middle part) [88].

The major disadvantage of physically based approaches is that they need special equipment (electroporator, microinjection device) which complicates an *in vivo* utilization. Nevertheless, these methods can be used to transfect cells *ex vivo*, for example blood stem cells. These cells can be harvested from patient blood and treated under *in vitro* conditions before administering them back in the blood donor.

### 1.2.2 *in vivo* delivery systems

As mentioned *in vivo* delivery systems faces many more hurdles than *in vitro* application. Besides the transport across the the cell membrane, *in vivo* delivery has to deal with:

- circulation time in the blood stream
- renal excretion
- unwanted uptake and binding to serum proteins
- degradation by blood RNases
- accumulation and toxicity of delivery vehicle

In general, again two different types of *in vivo* application can be distinguished. The local application, where siRNA is directly injected or applied into the target tissue, or a systemic application where the siRNA-delivery system circulates in the blood stream until it reaches the site of action in the distinct target tissue or cells.

The first approach can be used if the target site is limited to a small area, like lung or eye and no diffusion into other regions is desired. An example for a local administration in the eye is related to treatment of wet AMD (age-related macular degeneration) by intravitreal injection of the siRNA [89]. The targeting of the lung epithelial can be achieved by intranasal dosing and is currently under investigation by e.g. Alnylam Pharmaceuticals by the treatment of respiratory syncytial virus (RSV) [58, 90].

In most other cases a systemic delivery is the only way of administration facing the mentioned problems. One way to prevent siRNA from degradation is the encapsulation or complexation with the delivery material to form a shielded nanoparticle that enhances the circulation time of the siRNA in the blood and thus enables the delivery to the target site. PEGylation is one way to mask the particle and siRNA from defense



systems such as macrophages or nucleases [91, 92] and also prevents from binding to serum proteins or self-aggregation [93].

Potential *in vivo* delivery systems for systemic administration are nanoparticulate delivery systems, liposomes, viral systems or bioconjugates [36, 56, 59].

### 1.2.2.1 Liposomal based delivery

Liposomes are often confused with lipoplexes which represent a complexation of nucleic acids with the cationic lipid compound and thus show not the well defined liposomal structure. Consisting of a bilayer of lipids, liposomes are able to fuse with the cell membrane and release the entrapped substance into the cytoplasm [94]. Furthermore, cytotoxic side effects are minimized due to the architecture that mimics a cell membrane.

In contrast to micelles, liposomes consist of a lipid bilayer that surrounds an inner, entrapped space (see Figure 1.4 B middle part). There are different types of liposomes: multilamellar vesicles (MLV), large unilamellar vesicles (LUV) and small unilamellar vesicles (SUV). Furthermore, three groups are distinguished according to their net charge caused by the usage of different phospholipids: cationic liposomes (containing e.g. DOTAP or DOTMA), anionic liposomes (containing e.g. DPPC or DMPC) and neutral liposomes (containing e.g. the DOPE) [95, 96].

### 1.2.2.2 Viral delivery systems

Viral systems offer a high delivery efficiency, but may cause inflammation or other unwanted side effects, based on the host immune system [97, 98].

This kind of delivery is, or was, widely used in gene therapy. During the past, the severe side effect of viral based gene therapy, even causing the death of several trial participants [99], led to a field wide discussion about the suitability for *in vivo* application.

The experiences in gene therapy prove the viral approach not to be the best choice for siRNA delivery. Nevertheless, viral systems have their advantage in the *in vitro* delivery of genetic material into cell lines that are difficult to transfect, e.g. neurons, immune cells or stem cells.

### 1.2.2.3 Nanocarriers

The field of potential nanocarriers is large (see Figure 1.4 A). Several different approaches are made all seeking the omnipotent delivery system that can be modulated to target different cell types or tissues.

To give some short example, there are carriers based on complexation with nucleic acids to form polymeric nanoparticles like chitosan [100], peptides [101, 102]

or polyethylenimine (PEI) derivatives [103]. These aggregates show, however, an ill-defined size distribution which might be disadvantage for clinical studies. Liposomes can also be included into the group of nanocarriers.

Other systems are based on magnetic core nanoparticles of a homogenous size that integrate siRNA in their outer polyethylenglycol (PEG)-shell by ionic interactions [104]. Similar relatively well defined structures can be observed in case of dendrimers [105] that represent a porous system in which siRNA duplexes can be integrated and shielded. Another larger group is based on a micellar-like structure, that combines features of liposomes or polymeric nanocarriers. These structures are build by self assembly of single components and contain a hydrophobic core that complexes siRNA and hydrophilic shell that protects their payload from degradation [106].

### 1.2.2.4 Bioconjugates

The last approach to mention is the direct conjugation of siRNA to biomacromolecules [107] to facilitate their uptake into cells and facilitate a release from endosomes. In general only, the guide or antisense strand is necessary for gene silencing of the target mRNA and thus modifications on the sense strand are more tolerable, as already described. As potential conjugates different targeting ligands have been used, like cholesterol [108], folic acid [109], transportin [110], penetratin [110], galactoside derivatives [111], aptamers [112] or even antibodies [113].

### 1.2.2.5 Concluding remarks on *in vivo* delivery systems

The presented systems need all to be further enhanced to address all described hurdles and are so far only the first step in the development of an ideal delivery system. In a recently published mini review [59], a combination approach of multiple systems, like conjugates, siRNA modification and complexation or encapsulation, is suggested as a future efficient *in vivo* delivery system.

It is also to mention that the described systems themselves can cause side-effects like cytotoxicity or immunostimulation [114, 115]. This becomes clear when taking into account that usually the delivery compound is used in a mass excess over siRNA [116–118]. In most cases the reported effects are based on the cationic character of many delivery systems, that on the one hand facilitates the uptake, but on the other hand can cause toxicity by interferon response, creation of reactive oxygen species, destabilization of the cell membrane, interaction with protein kinase C (PKC) or rise in cellular calcium levels [67, 119–121]. The usage of neutral or anionic systems can diminish such side effect but also lowers the uptake efficiency. PEI [122] and oligofectamine<sup>TM</sup> or lipofectamine<sup>®</sup> [84] are known for severe side effects.

Another side effect that has to be considered is the overdosing of siRNA inside cells. Too high levels of delivered siRNA might interfere with the endogenous miRNA pathway and thus lead to misregulated gene function [97, 123].

The presented examples are only few of a complete field of toxicity studies of known and new established delivery systems. They indicate the necessity of a clear evaluation of all side effects before approaches *in vivo* can be made. So far, only few siRNA carriers were subjected to clinical trials [124] and none are on the market yet.

### 1.2.3 siRNA uptake and release

The presented nanocarriers are usually in the range of 50-200 nm and not capable to freely diffuse through the cell membrane. The most common or likely uptake mechanism is endocytosis, although membrane fusion, in case of liposomes liposomes [125], or cell penetration via cell penetrating peptides (CPP), by energy dependent translocation [126, 127], are possible. Furthermore, for each system two different modes of targeting cells are possible. An active targeting involves receptor-ligand interaction and should deliver siRNA only to distinct cells, whereas a passive targeting can be used to deliver siRNA and carriers into tumors by use of the enhanced permeability and retention effect (EPR effect) [128–131].

#### 1.2.3.1 Endocytotic pathways

Endocytosis means the uptake of extracellular material into the cytoplasm by an active process that leads to the formation of intracellular vesicles. These vesicles consist, like the cell itself, of a bilayer and surround extracellular material like fluids, bigger particles or membrane associated molecules and complexes. Thereby, different modes of endocytotic uptake can be distinguished depending on whether larger particles (phagocytosis) or fluids or soluble molecules are taken up (pinocytosis) [132].

The pinocytosis itself can be divided into different pathways:

- Macropinocytosis
- Clathrin dependent endocytosis
- Caveolin dependent endocytosis
- Clathrin and caveolin independent pathways

Phagocytosis and macropinocytosis are driven by the actin cytoskeleton and form larger vesicles, i.e. uptake of larger particles like pathogens or larger volumes of fluids (average diameter of membrane patches  $> 1 \mu\text{m}$ ) [134, 135], whereas the other endocytotic pathways are more specific and rely on coating proteins, that form cavities or pits, or on other pinch off mechanisms [132] (see Figure 1.5).

The most studied mechanism is thereby the clathrin mediated uptake pathway that

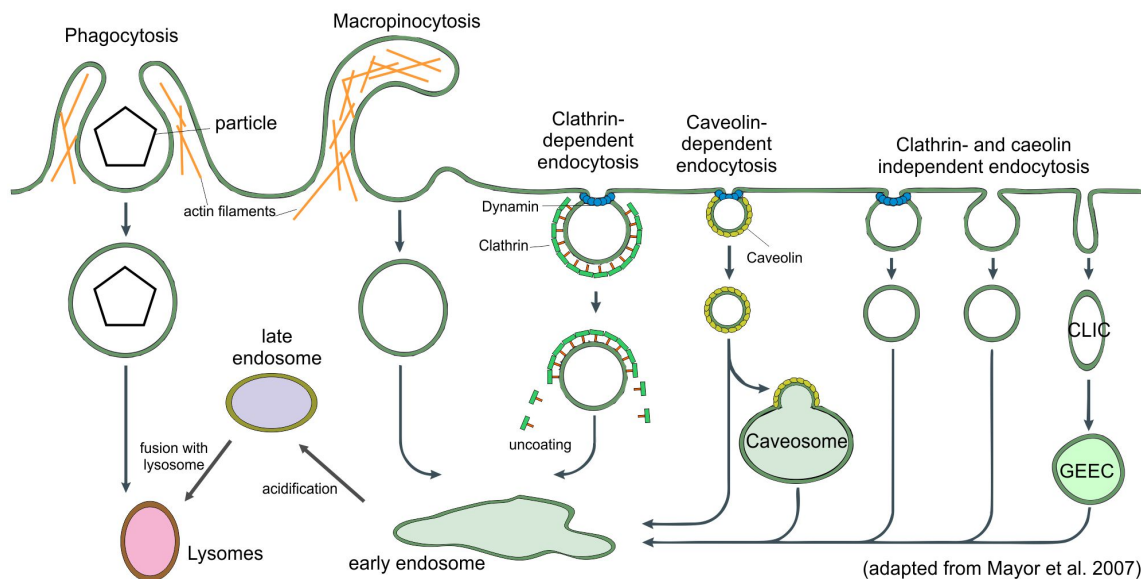


**Figure 1.5: Pathways of cellular uptake.** Larger particles are taken up by phagocytosis and larger volumes of fluids by macropinocytosis, both dependent on actin filaments. Further endocytotic uptake mechanisms are clathrin-dependent or caveolin-dependent uptake by the formation of pits and severing off by dynamin. Clathrin- and caveolin-independent pathways may involve dynamin for membrane separation. After vesicle formation fusion with the lysosome (phagocytosis), early endosome (most uptake mechanisms) or intermediate vesicles like the caveosome or GEEC occurs. The intermediate steps finally fuse with the early endosomes to be further matured into late endosomes by acidification and a final fusion with lysosomes. Adapted from Mayor and Pagano [133]

depends on the large GTPase dynamin, which severs the newly formed clathrin-coated vesicle from the cell membrane [136]. A similar mechanism has been reported to trigger the release of caveolae-mediated endocytotic vesicles from the membrane [137]. Besides these more or less well-studied endocytotic pathways, a number of clathrin- and caveolin-independent pathways have been reported [133].

The most endocytotic pathways form vesicles that deliver their content directly to early endosomes by fusion. Others take an intermediate step by delivering their payload into the caveosome or glycosyl phosphatidylinositol-anchored protein-enriched early endosomal compartment (GEEC) before a fusion with the early endosome occurs [133].

### 1.2.3.2 Endosomal escape

After the uptake and fusion with an early endosome, a maturation process occurs which finally leads to the formation of lysosomes where recycling processes take place. Via an acidification process that involves the vacuolar proton pump (V-ATPase), the neutral pH of the early endosome drops to pH 5-6 in the late endosome [138]. Further acidification and fusion with lysosomes results in organelles with an average pH of 4-5 [124]. During this maturation process, the cellular vesicle (i.e. early or late endosome and lysosome) are transported from the cellular periphery towards the nucleus by dynein and kinesin via the microtubule network [139, 140]. During this maturation and traveling process, the siRNA payload can escape the cellular vesicle and join the RISC for PTGS.

Nguyen and Szoka [124] claim that the time point of release of the nucleic payload is essential for finding the cellular target site. DNA, for example, needs to enter the nucleus and therefore a late release from the endosome or lysosome is favored [124]. In case of cytosolic RNAi the release can occur during the whole maturation process as the RNAi machinery can be found along the complete way from the periphery to perinuclear region (see Section 1.2.4).

Besides the release from the endosome or lysosome, also a release from the delivery system is required, which in most cases coincides with endosomal release or later in the cytoplasm. This process, however, is dependent on the ability of the delivery system to entrap or complex the siRNA payload.

**Polymeric based delivery systems** Polymeric cations use an effect called “proton sponge” to escape the endosome [141, 142]. Thereby due to the buffering capacity of some polycations the acidification of the endosomes and thus the proton influx leads to an increased influx of  $\text{Cl}^-$  and osmotic based swelling. Another synergistic effect is called the “umbrella hypothesis” which describes the volumetric expansion of polymers at lower pH values of 5-6, like in case of polyamidoamin (PAMAM) dendrimers, from a condensed state [83]. Both effects can cause endosomal rupture and release of the delivery payload.

**Lipid based delivery systems** For lipid based vectors, like cationic lipids or liposomes, an interaction with anionic phospholipids of the endosome membrane is considered to be responsible for endosomal escape. Thereby, the cationic lipoplexes in proximity to the endosome membrane form cationic-anionic ion pairs that have a cone shape and tend to form more likely micelles than a bilayer. This transfer from a lamellar to micellar structure leads to membrane destabilization by pore formation and the escape of the payload into the cytoplasm [143–145]. Neutral lipids, ionizable at lower pH are non-immunogenic since the cationic character that is responsible for immune recognition is lacking [146]

Vesicular transport is not only involved in endocytosis but also in the release of cellular material to the extracellular matrix or other cells by exocytosis. Thereby a repacking of delivered material in so called exosomes might occur [124, 147]. In consequence exosomes can be the source for deep tissue RNAi. siRNA might travel within exosomes via exo- and endocytosis from one cell to another and thus in otherwise not accessible tissue regions.

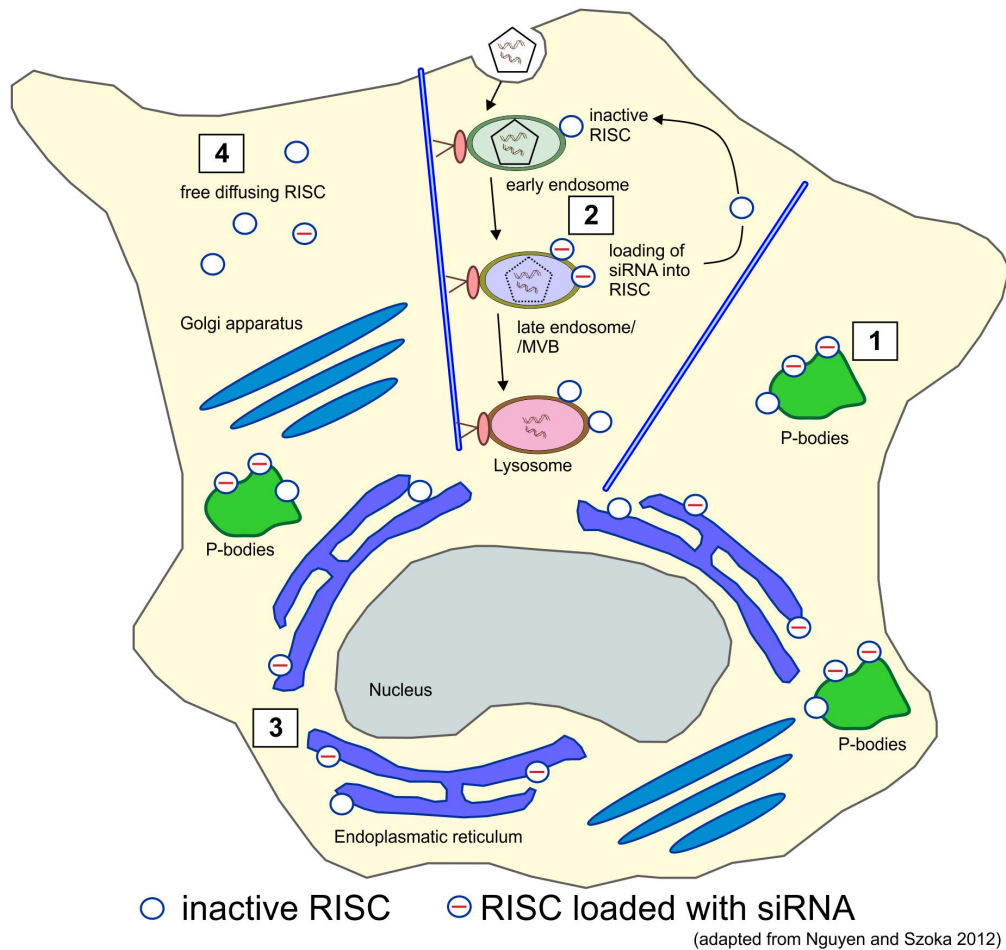


**Figure 1.6: Overview of cellular localization of PTGS related RISC.** After endocytotic uptake of siRNA delivery systems into early endosomes the maturation into lysosomes and transport from periphery to perinuclear region is depicted in the upper central part. siRNA release can occur from early or late endosomes and lysosomes. One of the major accumulation site of siRNA and miRNA based RNAi are the P-bodies where RISC loading or aggregation of loaded RISCs occurs (1). Released siRNA joins the RISC either directly at the release site from late endosomes and MVB (multi vesicular bodies) (2) or at the ER after an later release (3). Free diffusing siRNA can also be incorporated in free diffusing RISC (4). Adapted and modified from Nguyen and Szoka [124]

### 1.2.4 Localization of released siRNA

As one can already assume by the multiple different mechanisms that are involved in RNAi, the active site of the RISC differs between and within pathways. In general RNAi is seen to take place inside the cytoplasm as there the targets for PTGS are located (see Figure 1.6) but also nuclear RNAi based on CDGS has already been introduced.

A nuclear localization of RNAi is, of course, target dependent as in case of chromatin modulation or by Argonaute proteins that incorporate other small RNAs that are localized within the nucleus [32]. Additionally, piRNA tend to localize in the active complex inside the nucleus to target nascent transposable transcripts [32]. Nevertheless, the siRNA associated mammalian Ago2 was reported to be found in the nucleus, too [32, 148, 149].

Besides the reported pathways, the general localization of RNAi based on miRNA

and siRNA is the cytoplasm [51, 150]. Special aggregation sites in the cytoplasm are hereby P-bodies, which are processing sites for deadenylation, decapping and RNA degradation [151]. It is assumed that miRNA RISC accumulate in P-bodies for either mRNA silencing or as a storage site for assembled RISC [152]. Other aggregation sites for Argonaute proteins are reported to be multi vesicular bodies (MVB) that are related to the endocytotic pathway [153, 154]. These sites, which relate also to endosomes and lysosomes, have been reported to stimulate the loading of Ago complexes and thus be a center for assembly and disassembly of RISC [153, 154]. The localization of Ago proteins at the site of endocytotic pathways might also be explained with the delivery of artificial siRNA via those pathways and the release of siRNA from endosomes or lysosomes. Recently Stalder et al. [155] reported the rough endoplasmic reticulum (ER) as a central nucleation site for siRNA mediated gene silencing.

Though plenty research has been done to investigate single pathways, a clear localization, especially of siRNA related mechanisms, remains to be solved. Especially the dynamics behind siRNA based RNAi are of interest, as reports describe a duration of days or weeks after the application of exogenous siRNA in cell culture [156]. With longer incubation, RNAi is reported to be thinned out by cell division or siRNA decomposition [56].

Therefore, methods to visualize the cellular localization of nucleic acids especially siRNA are needed.

## 1.3 RNA labeling for microscopy

For studying the cellular fate of delivered siRNA fluorescent labels are the method of choice as they are easy to monitor via fluorescence microscopy. Alternative approaches that avoid fluorescent labels are based on isolation of cellular organelles or extracts, like nuclei [157] or endosomes [158], and further *in vitro* analysis to verify the presence of the delivered siRNA. Other approaches use the immunoprecipitation of RISC or better Argonaute proteins to study bound RNA species [159]. These procedures are rather laborious and lack the direct cellular visualization which can be achieved by labeling of the siRNA. In the following, a short overview of RNA labeling methods will be discussed.

### 1.3.1 RNA binding motifs

For studying the dynamics of cellular proteins, the classical approach is to introduce a plasmid coding for a tagged protein into the cell to produce fluorescently labeled proteins. The basis for this approach was the discovery of the green fluorescent protein (GFP) and variants by Shimomura et al. [161] and Heim et al. [162]. Unfortunately,

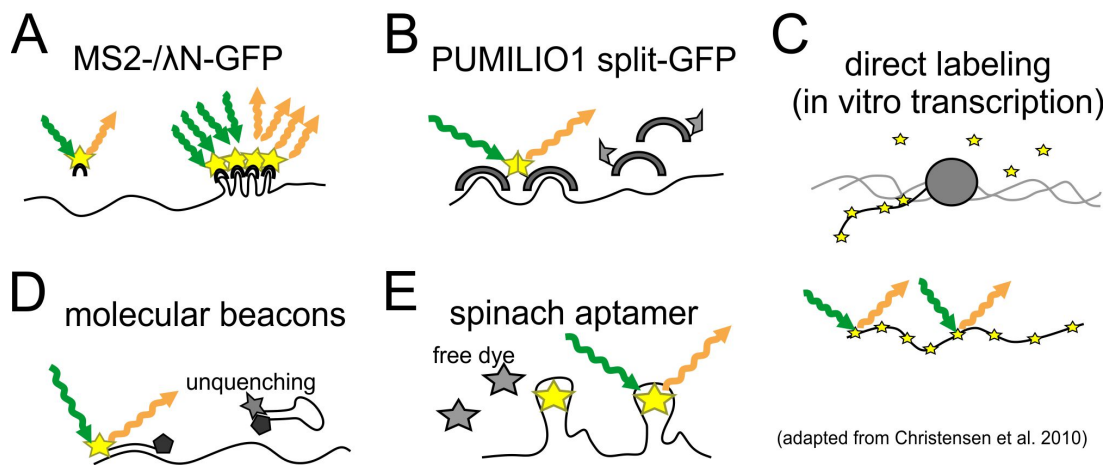


**Figure 1.7: Strategies for labeling RNA for *in vivo* visualization.** (A) MS2 or  $\lambda_N$  system. GFP-tagged binding protein binds to RNA-motif. (B) Split GFP approach with PUMILIO1. Two inactive halves of GFP, attached to different PUMILIO1 variants, assemble in proximity to create an active GFP. (C) Direct labeling of RNA by incorporation of fluorescently labeled nucleotides. (D) Molecular beacons fluoresce upon binding to target RNA as dye and quencher dissociate. (E) Spinach aptamer that induces fluorescence to non-fluorescent precursor dyes upon binding. Adapted from Christensen et al. [160]

this system can not be directly used to label RNA, too.

Therefore, proteins that bind to RNA or specific RNA-motifs were used and altered by introduction of a fluorescent protein tag to label RNAs, i.e. mRNAs, that contain these specific sequences. As a result, GFP or the enhanced green fluorescent protein (EGFP) can be attached to the target RNA. One molecule EGFP is, however, not sufficient to detect the signal of a single RNA and thus multiple repeats of the RNA-motifs have to be introduced in one mRNA. [163]. Furthermore, the system relies on a two step approach. First, the introduction of the RNA motif into the target RNA and second, the expression of tagged binding protein.

**MS2 system** One example of such an RNA-binding protein is the coat protein of the bacteriophage MS2, that binds to a unique RNA-hairpin structure (see Figure 1.7 A). For sufficient labeling multiple copies of the motif have to be introduced in the UTR region. This is necessary because the tagged protein itself results in a strong background signal and multiple copies of the binding motif and thus bound tagged proteins enable to discriminate between free and bound form [163, 164]. In a similar way, the lambda  $\lambda_N$  system from the bacteriophage  $\lambda$  [165] or Poly(A)-binding protein [166] can be used to image altered mRNA.

**PUMILIO1 system** To circumvent the background fluorescence of unbound tagged proteins split GFP approaches have been developed [167] where two inactive halves of GFP have to bind close to each other to form an active GFP. One system uses PUMILIO1



that, in contrast to other RNA-binding proteins, binds to a specific sequence and not to a secondary structure as for most other systems [168]. PUMILIO1 can be adjusted to bind to specific sequences. By designing two different PUMILIO1 proteins the inactive halves of GFP can be combined on one mRNA and form a stable GFP protein (see Figure 1.7B). This stability of the formed complex is the drawback in this method as even a release from the binding sites does not disrupt the active GFP [163].

The problem of this systems is that the compounds for detection, meaning fluorescently tagged proteins and adjusted RNA with binding motifs, have to be stable integrated into the cell line to be observed.

### 1.3.2 Fluorescently labeled probes

Besides the natural occurring fluorophore systems in fluorescent proteins (FP), small fluorescent organic dyes can be used to label RNA, too. Therefore, the dyes need to be covalently attached to the base or sugar of the RNA molecule, intercalate or bind direct to the RNA molecule or be attached to specific fluorescent hybridization probes.

**Labeling of RNA transcripts** The direct labeling of RNA transcripts involves fluorescently labeled nucleotides that are incorporated during the transcription of genomic DNA (see Figure 1.7 C). As these nucleotides are not cell permeable, an *in vitro* transcription followed by cellular delivery, like microinjection, is the method of choice [169]. Thus, the fate of a distinct RNA species can be followed inside the cells. For long RNA, like mRNA, the transcription approach is the method of choice. Another approach uses 5-ethynyluridine that can migrate through cell membranes and be incorporated instead of uridine in nascent RNA and later be modified by “the click reaction” with azido dyes [170]. This approach, however, involves a fixation of the cells to allow the dye and the cofactors, i.e. ascorbic acid and CuSO<sub>4</sub>, to enter the cell.

**RNA staining dyes** An alternative staining approach uses the affinity of some organic dyes to bind to nucleic acids. There are different dyes available that can bind to both DNA and RNA, like DAPI [171], or selective to one group. A broad spectrum of such dyes are offered by several manufactures, like the cyanine dye series of Molecular Probes (Life Technologies GmbH, Darmstadt, Germany), with SYTO<sup>®</sup>RNASelect<sup>™</sup>, that specifically binds to RNA [172] or the classical Hoechst dyes that bind only to ds DNA [173]. RNA stains and the incorporation of labeled nucleotides are methods to label the entire, or newly formed, mRNA and are not useful for selective imaging of a certain mRNA species or sRNA.

**Short fluorescent probes** Shorter RNAs, like siRNA or hybridization probes, can be chemically synthesized with a fluorescent label and transfected into cells like previously described. Examples for the use of fluorescently labeled siRNA are single dye labeled oligonucleotides [174, 175] or FRET probes [2, 176, 177], which will be the focus of this work to study the dynamics of siRNA. Besides the direct tracing of labeled siRNA, short RNA probes can be used as hybridization probes to label RNA in cells in a manner similar to fluorescence *in situ* hybridization (FISH). Classical FISH, however, requires the fixation of cells to wash away unbound probes. The principles thereby are that a probe hybridizes with its complementary sequence which can thus be analyzed by microscopy. Hybridization probes used for imaging in living cells, need to be non-fluorescent until bound to the target RNA (see Figure 1.7 D). This can be achieved by so called “molecular beacons” that are basically double labeled RNA hairpins, that use fluorescence resonance energy transfer (FRET) to quench the fluorescence of a dye by a second dye, called quencher (see Chapter 1.4) [163, 178]. These molecular beacons or other hybridization probes face, however, the same problem of cellular delivery as potential siRNA therapeutics.

### 1.3.3 EGFP analog on basis of an RNA aptamer

Aptamers are short sequences of nucleic acids, that can bind small molecules on basis of their 3D-structure. In 2011, Paige et al. [179] published an RNA aptamer, named spinach, that can bind to a small organic non-fluorescent molecule that mimics the EGFP fluorophore moiety.

The EGFP fluorophore consists of Ser-Tyr-Gly, also named HBI (4-hydroxybenzylidene imidazolinone), and is only fluorescent in the the folded barrel structure of the EGFP which induces the fluorescence [180]. Paige et al. designed a similar fluorophore (DFHBI: 3,5-difluoro-4-hydroxybenzylidene imidazolinone) and evolved an RNA aptamer by SELEX (systematic evolution of ligands by exponential enrichment) [181] that induces a bright fluorescence to the non-fluorescent free dye (see Figure 1.7 E) [179, 182, 183]. The advantage of the spinach system is that modified RNA that contains the aptamer sequence can bind to the cell-permeant fluorophore and thus induces fluorescence in the aptamer tagged nascent RNA.

The presented systems are basically useful to label or detect longer RNA sequences like mRNA. The only way to trace and label siRNA is by direct attachment of a traceable tag like fluorescent dyes (fluorescence imaging), radioisotopes (PET: positron emission tomography) or magnetic nanoparticles (MRI: magnetic resonance imaging) directly to the siRNA [184]. An additional labeling approach for miRNA is desirable, which is due to the short sequence and lacking sequence specificity not available yet.

## 1.4 Fluorescence & FRET

The tracing of RNA or other macromolecules inside cells can most easily be achieved by using fluorescent labels. Fluorescent labels are easy to handle and detectable upon excitation and detection of their emission.

### 1.4.1 Fluorescence

#### 1.4.1.1 Principles of fluorescence

The term fluorescence was first introduced by G.G. Stokes in the middle of the 19<sup>th</sup> century [185] and describes a process in the area of photoluminescence. Luminescence is defined as “a spontaneous emission of radiation from an electronically excited species (or from a vibrationally excited species) not in equilibrium with its environment” [186, 187].

Besides fluorescence, phosphorescence describe processes of photoluminescence that are based on a direct photoexcitation of the emitting molecule [187]. Thereby, an electron of the ground state  $S_0$  absorbs a photon of a certain energy, defined by its wavelength  $\lambda$  ( $E = h \cdot \nu$  with  $\lambda = \frac{c}{\nu}$ ;  $\nu$ : frequency,  $c$ : speed of light,  $h$ : Planck's constant) and gets into an excited state  $S_1$  (see Jablonski diagram in Figure 1.8 A). From there it can drop back to ground state by emitting its energy as visible light, meaning fluorescence. Due to internal conversions in the excited state, the emitted light is of less energy, meaning shifted to the red.

However, an excited electron can undergo a so called forbidden transition from the singlet state ( $S_0, S_1, \dots$ ) to the triplet state  $T_1$  by a process called intersystem crossing. If the electron drops then back into the ground state  $S_0$  the process is called phosphorescence. As the triplet state has a longer lifetime  $\tau$  than the excited singlet state, phosphorescence usually continues after the excitation source has been removed, whereas fluorescence will immediately stop. The lifetimes of the excited singlet states are in the range of nanoseconds and microseconds for triplet states. [188]

Substances that show fluorescence are called fluorescent probes, dyes or fluorophores. They can be organic molecules (classical fluorescent dyes), inorganic ions (e.g. lanthanide ions of Yb), fluorescent proteins (e.g. EGFP), atoms (like mercury gas in lamps) or inorganic semiconductor nanoparticles *quantum dots*:  $Qdot^{TM}$  (a core shell architecture of two semiconductors that leads to emission of absorbed energy at a wavelength depending on the size of the  $Qdot^{TM}$ ). Organic dyes usually display a broad conjugated  $\pi$ -electron system that can easily be excited. If the energy is lost by vibrational and rotational conversions without the emission of photons the substance just shows chromaticity by absorbing a part of the light spectrum. [188]

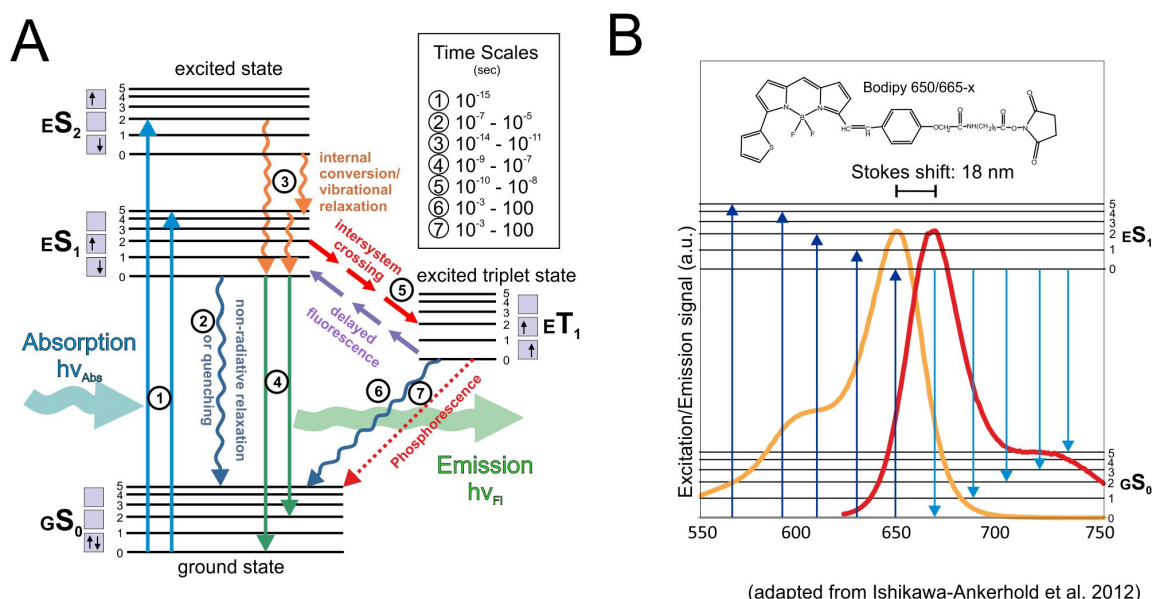


**Figure 1.8: Principles of fluorescence and phosphorescence.** (A) Jablonski diagram depicting fluorescence and phosphorescence. Electrons from the ground state are excited (1) into the excited singlet state. From there either internal conversions (3), fluorescence (4), quenching by non-radiative relaxation (2) or crossing to the triplet state (5) can occur. From the triplet state again a drop to the ground state by radiation-free (6) or light emitting phosphorescence (7) occurs. (B) Absorption and emission spectra of Bodipy650 dye with excitation processes resulting in different vibration levels (0-5) creating the absorption spectrum. Fluorescence from lowest excited vibrational level to different ground state vibration-levels results in emission spectrum. Indicated is the Stokes shift between absorption and emission maximum. Adapted from Ishikawa-Ankerhold et al. [188]

### 1.4.1.2 Fluorescence spectra

The most important feature of a fluorescent dye is its spectral characterization, meaning the absorption and emission profile. A dye usually is not only excitable at one distinct wavelength but at a certain spectrum. This can be explained by multiple vibration states in each singlet state ( $S_x$ ) and thus multiple possibilities to bring a photon in the  $S_1, S_2, \dots$  state. The resulting spectrum of absorption defines the absorption spectrum of a dye (see Figure 1.8 B dark blue arrows). The absorption spectrum corresponds more or less to the excitation spectrum, where a fixed emission wavelength is recorded by changing excitation wavelength. [188]

After internal vibration, relaxation or internal conversions, which are radiation free (wavy arrows in Figure 1.8 A), fluorescence can be emitted by dropping back into one of multiple ground state vibrational levels resulting in the emission spectrum (see Figure 1.8 B light blue arrows).

The internal conversion at the excited state result in the lowest vibrational level (see Figure 1.8 A yellow wavy arrows). In consequence, fluorescence is in a way independent from the exciting wavelength (as long as the energy leads to an excited state) as fluorescence occurs always from the same excited energetic level to the multiple levels in the ground state (Kasha's rule [189]).

In consequence, the emission spectra is often a mirror of the absorption spectra (mirror

rule) as from the lowest excited vibration level the electron can drop to each ground state vibration level (see Figure 1.8 B light blue arrows). [188]

### 1.4.1.3 Fluorescence characteristics

Besides the already named characteristics of fluorescence, some other important properties are necessary to understand or know when dealing with fluorescence [188]:

**quantum yield** The quantum yield or efficiency  $\Phi$  is the number of emitted photons in relation to absorbed photons:  $\Phi = \frac{\# \text{ of emitted photons}}{\# \text{ of absorbed photons}}$ . As not every absorbed photon results in fluorescence emission, due to internal non radiative decay processes,  $0 < \Phi < 1$ .

**extinction coefficient** The molar extinction coefficient  $\epsilon$  defines the proportion of absorbed light ( $E = -\log_{10} \frac{I}{I_0}$  with  $E$  being the extinction,  $I$  transmitted intensity and  $I_0$  irradiation intensity of light) at molar concentration ( $c$ ) in a cuvette of 1 cm path length ( $d$ ):  $\epsilon = \frac{E}{c \cdot d}$ . The extinction coefficient gives no clue on the quantum yield, but the higher  $\epsilon$  the higher the fluorescence at similar quantum yields.

**fluorescence life time** The fluorescent life time  $\tau$  defines the average time an electron stays in an excited state before returning into the ground state.

**stokes shift** The shift in absorption and emission maximum is called Stokes shift and was first described by Stokes [185] who observed a red-shift in the emission in fluorescence. Due to internal energy decay processes at the excited state emitted photons have less energy than excitation photons and appear thus red shifted.

**fluorescence quenching** Describes the effect of reducing the quantum yield of a fluorophore by interactions with other molecules. Quenching can be subdivided in:

- **self quenching** by close proximity to another fluorophore that absorbs the energy by radiation free energy transfer
- **color quenching** by the presence of a colorful substance that absorbs the emission
- **static quenching** by formation of non-fluorescent complexes
- **dynamic quenching** by collision with molecules that absorb the energy

**blinking or fluorescence intermittency** Random switching of a fluorophore between a fluorescent “on” and a non-fluorescent, dark “off” state in the microsecond timescale.

**photobleaching** Describes a process during which a fluorophore loses the ability to enter repetitive excitation/emission cycles. Photobleaching, also called “fading”, can be induced by destruction or irreversible modification of the fluorophore.

Especially excited fluorophores, that may also enter the triplet state, are prone to react with reactive oxygen species (ROS), thereby losing their ability to fluoresce. Scavenger systems can bind ROS and slow photobleaching.

**autofluorescence** Several cellular molecules show an intrinsic low background fluorescence that competes with the desired fluorescence of the used fluorophore (like NADPH, flavins or components of the extracellular matrix). Autofluorescence occurs in a window between 350-600 nm with lower value at less energetic, far-red excitation.

**environmental effects** The fluorescence of many dyes shows a dependency of the used solvent, the temperature or pH.

### 1.4.2 Fluorescence resonance energy transfer

Fluorescence resonance energy transfer (FRET), describes the non-radiative energy transfer from one excited fluorophore to another fluorophore or molecule. First described by Theodor Förster [190] it is sometimes also called Förster resonance energy transfer.

#### 1.4.2.1 Principles of FRET

An excited donor dye (FRET donor, D) transfers its energy in a non-radiative way, achieved by a long range dipole-dipole coupling mechanism, to an acceptor dye, the so-called FRET acceptor A (see Jablonski diagram, figure 1.9A). During FRET the energy of excited electrons of the donor is transferred to a less energetic excited state of an acceptor-electron, without emitting and reabsorbing photons. The excited acceptor can, after internal conversions, either fluoresce or the energy is lost by further internal conversions, which would make the acceptor a quencher. A quencher can thus be used to suppress donor emission without showing fluorescence.

For efficient FRET, donor and acceptor need to fulfill three key features [193]:

##### ***Spatial proximity of the donor and acceptor dyes***

In typical FRET experiments donor and acceptor dye are separated by a distance in the range of few nanometers ( $< 10$  nm) [194]. The Förster radius  $R_0$  characterizes the distance with half maximum FRET efficiency (see Figure 1.9C). For fluorescein and tetramethylrhodamine, a known FRET-pair, the Förster radius is approximately 55 Å [195].

##### ***Orientation of donor emission and the acceptor absorption dipole***

When the dipole moment of donor and acceptor are oriented parallel, FRET will be maximized, while perpendicular orientation leads to a minimized or rather no FRET effect (see Figure 1.9D).

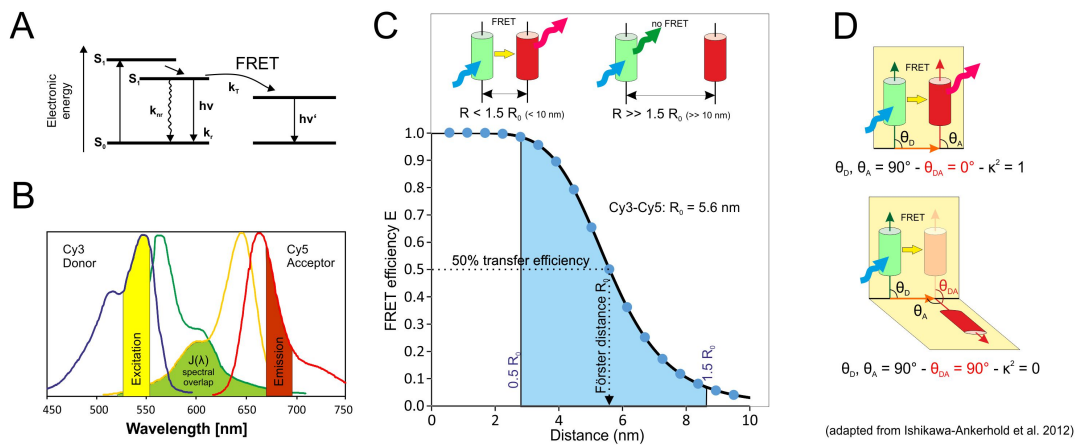


**Figure 1.9: Principles of FRET.** (A) Jablonski diagram depicting the principles of FRET. Adapted from Padilla-Parra and Tramier [191]. (B) Excitation and emission spectra of Cy3 and Cy5 depicting the spectral overlap and excitation and emission band. Adapted from [192] (C) Distance dependency of FRET efficiency in relation to Förster radius. [188] (D) FRET and dipole orientation influence. Adapted from Ishikawa-Ankerhold et al. [188]

### Spectral overlap of the donor and acceptor

Though FRET occurs without radiation, an overlap of donor emission and acceptor absorption is essential to transfer energy from one to another (see figure 1.9 B). [188]

The FRET efficiency, meaning the amount of energy transferred from the donor to the acceptor dye, is dependent on the Förster radius  $R_0$  and the distance  $r$  of the two fluorophores [188, 193] (see Figure 1.9 C left part).

$$E_{FRET} = \frac{1}{1 + \left(\frac{r}{R_0}\right)^6} \quad (\text{Eq. 1.1})$$

The Förster radius  $R_0$  itself is dependent on the spectral overlap  $J(\lambda)$ , the donor quantum yield  $\phi_D$ , the extinction coefficient of the acceptor  $\epsilon_A$  and the dipole orientation factor  $\kappa^2$  [188, 193]:

$$R_0 = \left[2.8 \times 10^{17} \cdot \kappa^2 \cdot \Phi_D \cdot \epsilon_A \cdot J(\lambda)\right]^{\frac{1}{6}} \quad (\text{nm}) \quad (\text{Eq. 1.2})$$

The orientation factor can range from 0 to 1 and in case of freely rotating dyes it can be approximated  $\kappa^2 = \frac{2}{3}$  (see Figure 1.9 D).

Due to the spectral overlap, which is essential for FRET to take place, one side effect, the spectral cross-talk, goes hand in hand (see Figure 1.9 B), which needs to be considered when calculating FRET efficiencies.

#### 1.4.2.2 Calculation of FRET efficiency

Equation (Eq. 1.1) shows the dependency of the FRET efficiency in relation to the distance, which is used to calculate distances on bases of FRET. Several methods to

calculate FRET efficiencies have been reported. In solution, FRET can easily be calculate by using (Eq. 1.3) by measurement of the donor emission in presence  $D_D(DA)$  and absence of an acceptor  $D_D(D)$  (with  $X_Y(Z)$ ; X representing donor or acceptor intensity at corresponding wavelength, Y representing donor or acceptor excitation wavelength, Z representing the used dye combination, which donor only, acceptor only or both FRET dyes) [196]:

$$E_{FRET} = 1 - \frac{D_D(DA)}{D_D(D)} \quad (\text{Eq. 1.3})$$

Another approach is to measure the donor ( $D_D(DA)$ ) and acceptor ( $A_D(DA)$ ) emission upon donor excitation of one sample. An additional factor has to be taken into account which addresses the properties of the respective dyes and the detection unit ( $\gamma$ ). Ignoring the characteristic system variable  $\gamma$  one obtains the proximity ratio PR [197]:

$$E_{FRET} = \frac{A_D(DA)}{A_D(DA) + \gamma \cdot D_D(DA)} \quad (\text{Eq. 1.4})$$

$$PR = \frac{A_D(DA)}{A_D(DA) + D_D(DA)} \quad (\text{Eq. 1.5})$$

The PR can be used to relatively compare samples without the necessity to calculate absolute distances which would imply to determine  $\gamma$ .

#### 1.4.2.3 FRET pairs

Literature reports a huge set of FRET dye pairs (see Appendices A.1). Very common are combinations of FP that are attached on different proteins to study their interactions. The first combination used was YFP and CFP, the yellow and blue variant of GFP [198]. Now several other combinations with more photostable FP and other colors emerged. Nevertheless, organic dyes, though they have to be synthetically attached on the target molecule, have in most cases higher quantum yields, extinction coefficients and offer variants in the far-red excitation range, where autofluorescence is lower [188]. Common organic dye FRET pairs that have been used to study nucleic acids are e.g. Cy3/Cy5 [199] or fluorescein/tetramethylrhodamine [2]. Additionally, organic dyes can function as quenchers, like the black hole quenchers (BHQ), that are used, for example, in molecular beacons, as described earlier.

#### 1.4.2.4 Applications of FRET

Usually FRET is used to determine whether two fluorescence labels are close to each other. This can be used to determine the dissociation or formation of biomolecule complexes, as in the case of real-time PCR or to study the integrity of siRNA duplexes as



earlier and recently described by Jarve et al. [2] and Holzhauser et al. [200] as indicator for siRNA integrity.

Other approaches use FRET to detect colocalization of labeled proteins or lipids inside the cells [192, 201, 202]. Plenty other applications for FRET are reported in literature, but will not be here. The advantage of FRET for such studies is the distance dependency (see Figure 1.9 C). With increasing distance, the FRET efficiency ( $E_{\text{FRET}}$ ) decreases with the inverse sixth power of the distance of the two dyes.

## 1.5 Microscopy

Fluorescently labeled molecules or biomacromolecules can not only be studied *in vitro* in the cuvette but also in cells under fluorescence microscopes. In the last years microscopy has become very important to study cellular processes and the distribution or localization of proteins, nucleic acids or labeled drugs. Thereby, fluorescently labeled probes allow a better signal to noise ratio than stains that only enhance the contrast by higher absorption rates.

### 1.5.1 Fluorescence microscopy

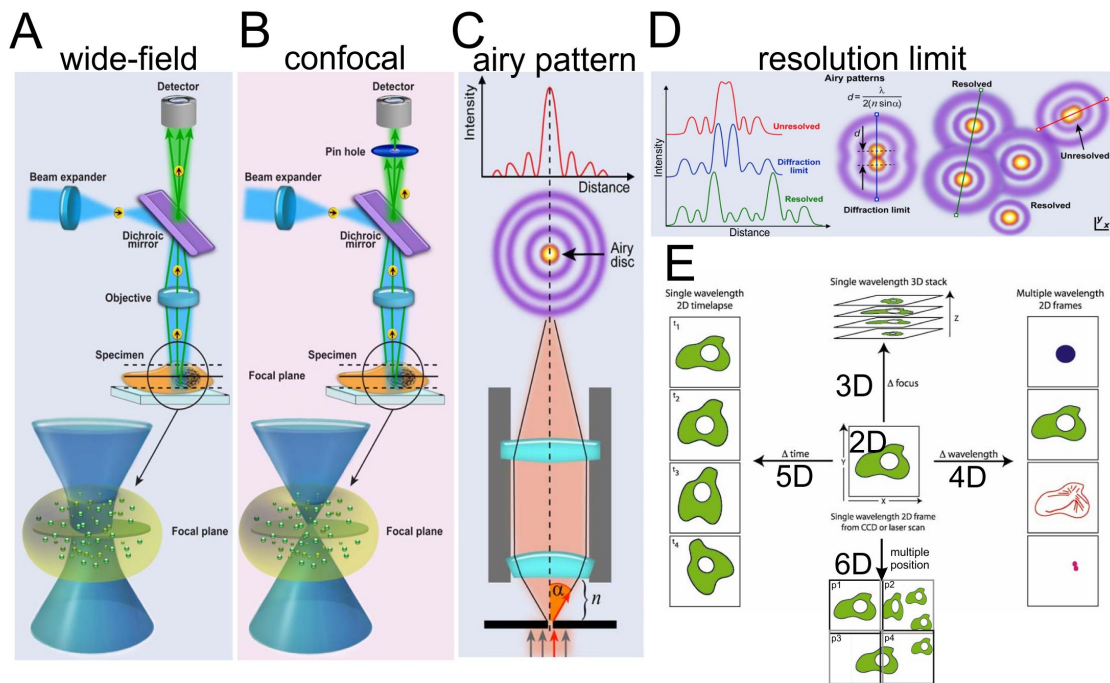
#### 1.5.1.1 Basic concepts of fluorescence microscopy

Fluorescence microscopy was first invented in the early 20<sup>th</sup> century by August Köhler and Oskar Heimstädt [188, 203]. Since then, a lot of improvements concerning resolution, magnification, illumination, fluorescence and detection were made. Today fluorescence microscopes use epi-illumination which means exciting and emitting light are collected at the same side of the specimen. Thereby, only emitted and reflected light are collected by the objective avoiding excitation rays in the detection optical path (see scheme of objective in Figure 1.10 A+B).

To improve the weak autofluorescence of biomolecules, staining with fluorophores that display high quantum yields and extinction coefficients became the method of choice. FPs and selective stains for cellular organelles are the state of the art allowing to simultaneously image multiple colors by usage of the right filter systems for excitation, dichroic mirror and emission [188].

A fluorescent microscope consists of the following main components [188](see Figure 1.10 A+B):

**lightsource** As light sources, metal lamps, e.g. mercury or xenon lamps, or lasers offer the required intense light to excite fluorophores. Common laser lines are 405 nm/488 nm/561 nm/633 nm.



(adapted from Ishikawa-Ankerhold et al. 2012 and Andrews et al. 2002)

**Figure 1.10: Fluorescence microscopy.**(A) Schematics of wide-field fluorescence microscope with excitation source, dichroic mirror, objective and detector. Specimen depicts broad hourglass shaped focus. Green rays depict fluorescence above, below and from the focus. (B) Confocal microscope with pinhole blocks fluorescence from above and below the focus. Focus is sharp and smaller than in wide-field microscopy. (C) Opening angle  $\alpha$  and diffraction that leads to formation of airy disc and pattern. (D) Resolution limit demonstrated on basis of airy patterns. (E) Multi-dimensional microscopy with one dimension for time  $t$ , color or wavelength,  $z$ -position and scanned region  $p$ . (A-D) from Ishikawa-Ankerhold et al. [188] and (E) adapted from Andrews et al. [204].

**filter unit** Defines exciting and emitted light bandpass by blocking other wavelengths. The dichroic mirrors separates excitation and emission light pass by reflecting lower wavelength and letting longer wavelength, i.e. the emission, pass. Besides standard bandpass, longpass or shortpass filter, prisms are used to split the visible light and select emission ranges by slits that block certain wavelengths.

**objective** Serves to focus the illuminating and collect the emitted rays to and from the specimen. In principle, air and immersion objectives are available with oil immersion objective being used for higher resolution.

**scanning unit** Specimen holder with XY-scanning unit to direct the beam path to the focus, in case of confocal microscopy. For fast image acquisition resonance scanner with up to 8000 Hz scanning speed can be used.

**detector** For detection either CCD cameras or photomultiplier (PMT) are used. A PMT can be adjusted by gain (amplification of the input signal) and offset (threshold for detected signal) whereas in CCD chips the exposure time is responsible for the signal strength. New hybrids of classical PMT and avalanche photo diodes can achieve an ideal signal to noise ratio by increased sensitivity.

### 1.5.1.2 Confocal microscopy

Besides the wide-field microscopy (see Figure 1.10 A), the confocal laser scanning microscopy (CLSM) has become very popular (see Figure 1.10 B), which was invented by Minsky in 1957 [205]. A pinhole in the excitation light pass enables to selectively collect light that is emitted from the focus and thus enhancing the resolution of the system. Thereby light rays from above or below the focal plane are blocked creating an optical z-section. [188]

Confocal microscopes scan the specimen pixel by pixel and use PMTs for signal detection. In consequence, as each image has to be created pixel by pixel CLSM using PMTs have a certain scanning speed that is defined by pixel number and time for collecting photons in each pixels (pixel dwell time). The adjustments in the light path are done by the scanning unit.

A small pinhole results in small z-sectioning and thus enhanced z-resolution by cost of signal intensity as out-of-focus emission is blocked.

### 1.5.1.3 Resolution limit

With the improvements of the last decades, fluorescence microscopes have a resolution limit of approximately 200 nm. The resolution limit defines the distance below which two separated fluorophores can not be resolved, meaning distinguished. Though fluorophores allow even to detect single molecules of much lower sizes, the resolution limit is caused by diffraction that occurs when light hits small objects. To enhance the contrast and thus resolution power, as much light as possible has to be collected from the objective. Ernst Abbe defined therefore the numerical aperture  $N.A.$  which describes the capability of an objective to collect light [206]:

$$N.A. = n \cdot \sin(\alpha) \quad (\text{Eq. 1.6})$$

With  $n$  being the refractive index of the surrounding medium and  $\alpha$  half of the opening angle of the objective. Oil objectives usually have  $N.A.$  of around 1.4 whereas air objectives have  $N.A.$  below 1. [188]

The resolution limit is defined according to Abbe as the minimal distance between two spots that can be detected on the basis of their contrast to the background. Each point signal causes a blurring defined by the point spread function (PSF), which is a function that defines the extend of blurring. The PSF resembles a 3D-Gaussian function and displays a point light source as a bright spot (Airy disc) with surrounding diffraction rings (Airy pattern) [188, 207]. In Figure 1.10 C diffraction an the formation of the Airy pattern is displayed.

On the basis of the Airy pattern and the Rayleigh-Criterion resolution ( $d$ ) can be defined

on the possibility to distinguish between two maxima of the blurred signal (see Figure 1.10 D) [208–210]:

$$d_{wide-field} = \frac{1.22 \cdot \lambda}{2 \cdot N.A.} = \frac{0.61 \cdot \lambda}{N.A.} \quad (\text{Eq. 1.7})$$

$$d_{confocal} = \frac{0.4 \cdot \lambda}{N.A.} \quad (\text{Eq. 1.8})$$

Abbe stated that in general the limit of resolution is half of the excitation wavelength, which is true for wide field microscopy and objectives with a *N.A.* of 1.2 (see (Eq. 1.7)). Taken visible light as potential excitation light source, ranging from 400 to 700 nm, the resolution limit lies between 200 and 350 nm. For confocal microscopy, due to smaller PSF the resolution is slightly higher (see (Eq. 1.8)). This, however, is only true for the lateral resolution, meaning in the x-y-plane. The axial resolution is worse due to a stronger blurring along the z-axis and is defined by [210]:

$$d_{axial} = \frac{1.4 \cdot \lambda \cdot n}{(N.A.)^2} \quad (\text{Eq. 1.9})$$

Additional to the resolution, the sampling rate is important for an ideally resolved image. The sampling rate describes the number of pixels per resolved distance *d* and thus the *pixelsize*. According to the Nyquist theorem, the sampling rate should exceed twice the distance to be resolved [209]:

$$\text{pixelsize} \leq \frac{d}{2.3} \quad (\text{Eq. 1.10})$$

To break down the resolution limit stimulated emission depletion microscopy (STED), photoactivated localization microscopy (PALM), stochastic optical reconstruction microscopy (STORM) and structured illumination microscopy (SIM) have been developed and are counted to super resolution microscopy techniques. They either rely on narrowing the excitation spot by inactivation of surrounding fluorophores or single molecular detection upon activation of the fluorophores. In principle, a 4-5-fold improvement of the diffraction barrier can be achieved [188].

#### 1.5.1.4 Multi-dimensional imaging

On basis of confocal microscopes, a multi-dimensional imaging can be performed (see Figure 1.10 E) [204]. In standard microscopy, only the x-y-axis is scanned resulting in a 2D-image. An additional optical sectioning expands the acquired data in the z-direction creating a 3D-image. Usually, image data consist of only grayscale images where the acquired intensity is stored in a range defined by the bit-depth (8-bit  $\hat{=}$   $2^8 = 256$  intensities). As it is possible to acquire multiple fluorophores a next dimension of the

acquired image can be defined in which the different fluorophore signals are stored (4D). The fifth dimensions can be assigned to time series of the same image resulting in time-lapse movies (5D). To increase the scanned area tile-scans can be performed which is, in fact, the acquisition of multiple regions that overlap at the edges thereby enlarging the scanning field by the same resolution. These multiple regions are stored as separate 5D-images resulting in a sixth data dimension (6D).

As the acquisition of a 6D-imaging is based on multiple imaging steps the acquisition time of 6D images is increased which results in lower temporal resolution. In consequence, one has to decide whether the focus lies on fast imaging for good temporal resolution (averaging, xyz-resolution etc.), spatial resolution (pixel and z-slice size) or sensitivity (averaging, dwell time). Usually, the enhancement of one causes a loss in the other two. In a lecture script from the university of Zurich, this is called the “triangle of frustration” [211] which describes the problematic pretty well.

## 1.5.2 Live cell imaging

For analyzing the whereabouts of material, like labeled nucleic acids, delivered inside cells, in principle, two approaches can be followed. On the one hand, there is the time-point analysis approach by stopping one of multiple simultaneously performed experiments, or a constant observation of one experiment under live-cell conditions.

The first approach requires the fixation or harvesting of the analyzed cells, which allows to perform excessive *in vitro* studies like determination of protein or RNA amount in the sample or isolated organelle. But the process of fixation (for imaging) or harvesting and isolation of cellular components can falsify the experimental data as cells are killed and might show a different behavior as cells that are analyzed under optimal growth conditions. Therefore the second approach of live-cell imaging might be an approach to elucidate the fate of applied substances inside cells.

### 1.5.2.1 Maintaining live conditions

The most critical step in live-cell imaging of mammalian cells is to maintain cell culture conditions to prevent cell stress and death [212, 213]:

#### *temperature*

For temperature maintenance the complete microscope or just the culture vessel needs to be put in an incubation unit to maintain temperature of 37°C. To put the complete microscope in an incubation unit is probably the easiest way to image cells under living conditions but also the most expensive. Due to the housing the complete system has the same temperature and focal drifts due to temperature changes are minimized. A negative aspect however is the long equilibration time

for the system to reach the right temperature. Alternatively, heated incubation chambers can be used that cover only the culture vessels and are placed directly on the stage. These stage-top incubation units are designed for special culture vessels and surround the complete dish or multi-well chamber to create an isolated incubation chamber. To reduce focal drift and prevent immersion oil or water evaporation a heating ring for the objective is recommended. [212, 213]

### ***pH control***

To maintain a physiologic pH at around 7.2-7.4 cell culture media needs to be buffered. In normal cell culture the pH is maintained by a carbonate buffer system which is in equilibrium with the surrounding CO<sub>2</sub> of the atmosphere. To keep the pH constant at 7.4 an increased CO<sub>2</sub> atmosphere of 5% has to be maintained. Alternatively if CO<sub>2</sub> supplementation is not possible HEPES can be used in 25 mM concentration as supplement in the media to maintain the pH. [212]

The incubation in 5% CO<sub>2</sub> saturated air containing still approximately 21% of oxygen usually results in oxygen concentration of 200  $\mu$ M in the medium and inside the cells [214].

### ***osmolarity***

It is also necessary to maintain the osmolarity inside the medium by avoiding evaporation. This can be achieved by applying a water saturated airstream in proximity to the cultured cell. Usually a bubbling of the CO<sub>2</sub> saturated air through water is sufficient.

## **1.5.2.2 Experimental consideration**

Besides the cell culture conditions it is also necessary to choose the right experimental setup [212, 213]:

### ***glass/plastic ware***

In order to perform confocal live-cell imaging, chambers with thin glass or plastic bottoms ( $\sim$ 0.17 mm) are required. The material should display low autofluorescence as the excitation and emission has to pass the culture vessel bottom. Glass is due to its low fluorescence ideal for imaging but needs to be treated by e.g. collagen to let cells efficiently attach and grow on the slide. Alternatively the Ibidi GmbH invented a low fluorescent and cell culture treated plastic surface that is also optimal for confocal imaging and cultivation.

### ***phenol red***

The use of phenol red should be avoided. Phenol red is the standard pH indicator in most cell culture media and allows easily to check the pH in a culture. Due to the red color at physiological pH the dye absorbs light, similar to other fluorophores

or chromophores, and can thus interfere with the detected fluorescence signals or cause phototoxicity.

#### ***photobleaching & phototoxicity***

Photobleaching is one major problem in live cell imaging. Upon excitation some fluorophores undergo the transition to the triplet state and can react with cellular oxygen. These fluorophores can not further undergo excitation and emission cycles and are thus photo-bleached. During this reaction, reactive oxygen species (ROS) are formed (like singlet oxygen) that can further induce phototoxicity [188, 215]. Besides reactive species, an increase in temperature upon excitation can also induce phototoxic effects. Phototoxicity manifests in the induction of morphological changes like vacuolation, blebbing or cell death [212] by excessive excitation. Scavenger systems, like Trolox [216], or anti-oxidants, like ascorbic acid [217], might be used to reduce the effects of ROS and thus slow bleaching.

#### ***laser intensity***

Confocal microscopes need powerful excitation sources, like lasers, but if the samples are excited at too high intensities dyes may bleach and phototoxicity might lead to cell death. Tan et al. [212] advise low laser intensities of 10 % for 488 nm laser and 10-15 % for the red lasers at 561 nm. Additionally, photostable dyes, like Alexa or Atto dyes, allow long-term imaging.

#### ***focus control system***

For short term imaging or single time-point imaging the described considerations are sufficient. But in case of longer time-lapse studies a focal drift might occur that interferes with the acquisition. The microscopy setup especially the z-axis adjustment can change over time by either temperature or physical changes, like vibrations or gravitational movement of the specimen. Thus a specimen drift is produced that leads over time to lose the focus. To prevent focal drift, temperature changes need to be reduced (e.g. by placing the microscope into an incubation unit) or an automatic adjustment of the z-position needs to be applied. Such systems use far-red lasers that are deflected from the bottom of the cover slip and used to determine the z-positions. In case of an increased or decreased distance, the system automatically readjusts to keep the specimen in focus.

### **1.5.3 Advanced imaging methods**

With the availability of fluorescent proteins, photostable organic fluorophores and superresolution microscopy a bundle of different advanced imaging methods have been evolved to study cellular processes, i.e. FRAP, FLIP, FLAP, FCCS or FRET microscopy [188].

**FRAP & FLIP** Fluorescence loss in photobleaching (FLIP) and fluorescence recovery after photobleaching (FRAP) describe methods to analyze diffusion processes inside cells. Basis for the analysis are fluorescently labeled proteins that are expressed in a cell. In case of FRAP a region of the cells is rapidly bleached at high laser intensity. Afterwards, the back-diffusion into the bleached region is analyzed to determine the diffusion constant of a labeled protein. In case of FLIP a fluorescent cells is permanently bleached at one region and the overall loss in fluorescence in the entire cell is observed. [188]

**FLAP** Fluorescently labeled proteins are permanently expressed in a cell and thus a certain population cannot be discriminated from surrounding proteins. Fluorescence localization after photobleaching (FLAP) uses a two color labeled protein in which one fluorophore is bleached. The “semi-bleached” protein can then be localized by the missing signal in a pool of double labeled proteins. Further developed techniques use photo-convertible or photo-activatable fluorescent proteins that can be activated by or change their color upon excitation at a distinct wavelength to follow single proteins inside a cell. [188]

**FCS or FCCS** Fluorescence correlation spectroscopy (FCS) or fluorescence cross-correlation microscopy (FCCS) are methods to study single molecules and complexes of two differently labeled species inside a small confocal volume, even inside cells. Thereby, the diffusion of labeled molecules (FCS) or complexes of double labeled molecules or complexes (FCCS) through the confocal volume is analyzed and allows to determine concentration, mobility, binding affinities or stoichiometries, enzyme kinetics and colocalization. [218]

**FRET microscopy** As already described, FRET allows to analyze the interaction of different biomolecules by proximity interaction. While in the cuvette the FRET efficiency can more or less easily be calculated by (Eq. 1.1) or (Eq. 1.4) an intracellular microscopic approach is more demanding and different approaches have been developed:

### ***Ratiometric FRET***

On the basis of measuring the donor and acceptor signal in a molecule or complex, the ratio of FRET to donor signal can be used to determine the FRET ratio. The system is very easily applicable, fast and thus suitable for live-cell imaging with known stoichiometry of donor and acceptor [191].

$$FRET_{ratio} = \frac{A_D(AD)}{D_D(AD)} \quad (\text{Eq. 1.11})$$



**3-cube FRET**

3-cube FRET or sensitized emission relies on a sequential acquisition of donor, acceptor and FRET emission in donor only, acceptor only and FRET samples. The recorded data is used to calculate the real FRET intensity  $FRET_{corr}$  by subtraction of donor bleed-through and acceptor cross-excitation [219]:

$$FRET_{corr} = FRET_{measured} - Donor_{corr} - Acceptor_{corr} \quad (\text{Eq. 1.12})$$

**Acceptor bleaching**

Similar to (Eq. 1.1), the FRET efficiency is determined by measuring the donor emission one time in presence and one time in absence of the donor. Thereby after an initial recording ( $D_D(DA)$ ) the acceptor is bleached by a high laser intensity to result in the  $D_D(D)$  [220]. This system however is not suitable for live cell application as the acceptor has to be bleached and thus allows no ongoing observation.

**FLIM**

Fluorescent life-time imaging uses the change in fluorescence lifetime  $\tau$  when an acceptor is in proximity of the donor dye [221]. However, FLIM measurement need a special equipment with pulsed lasers to measure decay rates and delay times.

$$E_{FRET} = 1 - \frac{\tau_{DA}}{\tau_D} \quad (\text{Eq. 1.13})$$



## 2 Goal of this work

RNAi, based on siRNA, is a wide spread tool in biological research for studying gene function and shows also high potential for new, selective therapy approaches for the treatment of misguided gene expression. Although efficient gene silencing is observed *in vitro* and in first *in vivo* studies, the question of the whereabouts of delivered siRNA remains unclear. Thereby, the uptake, release and the cellular fate of applied siRNA, including the question of siRNA stability, availability and localization, are of special interest.

The goal of this work was to establish a FRET siRNA system that allows the investigation of delivered siRNA in real-time in living cells. On the basis of fluorescence signals and occurring FRET, the integrity level inside living cells and a localization of the siRNA were investigated.

An earlier published FRET siRNA system, on the basis of fluorescein (FL) and tetramethylrhodamine (TMR) [2], has successfully been used in fixed cells, but lacks an efficient application in living cells. Due to photobleaching and cross-talk of the dyes used, a sensitive and reliable quantification was shown to be problematic. Especially, for long time-lapse observation, dyes that are prone to photobleaching are of no use. In addition, the described FL/TMR system shows only little spectral separation, in combination with a strong cross-talk of the single dyes, which is problematic for microscopy. Alternative dyes with a more narrow emission profile would reduce cross-talk, and a shift of the FRET siRNA system to the blue or red spectral range would also allow the use of common organelle labeling strategies to evaluate the localization of delivered siRNA populations.

According to the above defined problems, the work presented here is displayed in four sections, which deal with FRET dye pair evaluation, *in vitro* application, application in fixed cells and live cell observation of siRNA transfection.

In a first step, new photostable FRET pairs were investigated with respect to their suitability and capability to result in FRET.

In a next step, the identified FRET pairs were then calibrated for integrity quantification and tested *in vitro* in the cuvette. Thereby, the FRET siRNA system was shown to be useful for investigation and surveying of the formulation process of potential new delivery systems addressing the integrity level of the siRNA. Additionally, the protective

effect of different delivery systems was investigated by RNase degradation.

A next question, that has already been addressed earlier by the Helm lab [2], was the cellular fate of delivered siRNA. First impressions of the cellular distribution were obtained with the published FL/TMR pair and an ongoing detailed analysis in fixed cells was performed. Additionally to the ongoing research, the newly developed FRET system was evaluated in fixed cells for a proof of concept.

In a final extensive live cell study, the cellular dynamics in living cells were investigated. Therefore, the system was adapted to live cell imaging conditions and transfections by cationic lipids were monitored in real-time. A detailed analysis of release events was performed to elucidate time point of release, duration and cellular localization, i.e. cytoplasm or nucleus.

# 3 Results & Discussion

## 3.1 Model for siRNA integrity

### 3.1.1 Principles of the R/G-model

The basis of the presented thesis is an siRNA construct that enables the measurement of the integrity state of this siRNA duplex by FRET. FRET can be measured between two fluorophores attached to each strand of this siRNA duplex. In the presented case a donor dye (D) is attached via an amide bond to a C6-linker connected directly to the 3'-end of the RNA sequence. The acceptor dye (A) is similarly attached to the 5'-phosphate of the antisense strand (see Appendices B.4). This combination allows to observe FRET as described in Section 1.4. A suitable FRET pair, in following named as Dye-1/Dye-2 (where the first dye is always attached to the 3'-end of sense strand and the second dye to the 5'-end of the antisense strand, e.g. donor/acceptor or D/A), can be excited at the donor excitation wavelength ( $D_{ex}$ ) and will emit at the corresponding acceptor emission wavelength ( $A_{em}$ ) (see Figure 3.1).

The used siRNA is designed against the sequence of the enhanced green fluorescent protein (EGFP) [222] and allows an easy *in vitro* read-out of its silencing capability (see Chapter 3.2.1).

As both dyes are in proximity of each other [2] and in the range of the common Foerster radii, which are around  $\sim 50 \text{ \AA}$ , FRET can be detected at the  $A_{em}$  wavelength upon

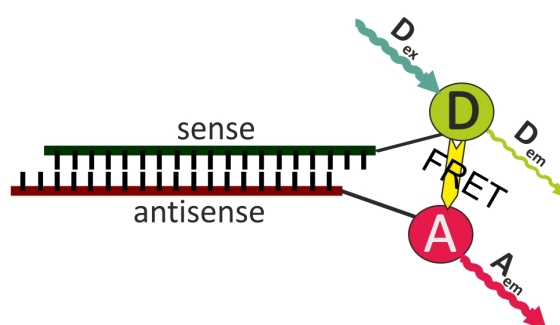


**Figure 3.1: Scheme of FRET siRNA.** Schematic drawing of the siRNA labeled with two dyes capable of FRET used for integrity measurements. siRNA is represented as a duplex with sense and antisense strand. The sense strand carries a fluorescent donor dye (D) that can be excited at the donor excitation wavelength ( $D_{ex}$ ) and emits a little fraction of its energy at the donor emission wavelength ( $D_{em}$ ). The other part is transferred via FRET to the acceptor dye (A) and is emitted at the corresponding acceptor emission wavelength ( $A_{em}$ ). Figure similar published in Hirsch et al. [1]

donor excitation (as indicated in Figure 3.1 by the yellow arrow). For the chemical structure of the siRNA duplex see Appendices B.4.

For calculating the integrity level of the duplex, the ratio of acceptor emission, meaning FRET emission, to donor emission is calculated (as earlier published by Jarve et al. [2]). The obtained ratio is named R/G-ratio as it is in fact a ratio of the less energy-rich, and thus redder, emission to the higher energy-rich, and thus greener, emission. For the already described FL/TMR system the red and green emission values are visualized in Figure 3.2 with  $I_A = I_{590}$  and  $I_D = I_{520}$ .

$$R/G = \frac{\text{fret emission}}{\text{donor emission}} = \frac{I_{\text{acceptor}}}{I_{\text{donor}}} = \frac{I_A}{I_D} \quad (\text{Eq. 3.1})$$

### 3.1.2 Fluorescein/Tetramethylrhodamine siRNA

Earlier data, published by Jarve et al. [2], are based on fluorescein and tetramethylrhodamine labeled siRNA, i.e. FL/TMR. Then, the system was a standard FRET pair which was described in literature by Wu and Brand [195] and a common labeling for RNA oligonucleotides (ON) and siRNA, respectively. The FL/TMR siRNA has the advantage that the dyes show a bright fluorescence and can be excited with common fluorimeters and microscopes that offer excitation at 488 nm or 543 nm, respectively. Furthermore these dyes are standard labels that are easy to handle and attached to the newly synthesized ON. The ss strands can then be hybridized to double stranded (ds) siRNA.

Figure 3.2 A+B depict the excitation and emission wavelengths of the FL/TMR FRET siRNA and the fluorescence spectra of the single and double labeled duplexes upon excitation at 488 nm. One can nicely observe the influence of the presence of the acceptor by the vanishing of the fluorescein emission peak at around 520 nm. The donor emission decreases from  $\sim 190$  AU to less than 20 AU. This quenching of the donor emission is the first sign of FRET between the both dyes. Additionally an increase in acceptor emission, which corresponds to FRET, of the double labeled construct can be observed, compared to the single acceptor labeled siRNA.

Nevertheless, one can also see that the acceptor itself shows weak fluorescence upon excitation at 488 nm. This fluorescence, also called cross-excitation, is one of the major drawbacks of the FL/TMR system. Due to the proximity of the excitation and emission spectra of the dyes, spectral crosstalk occurs. Besides cross-excitation a bleed-through of the FL emission into the TMR emission can also be observed. As for integrity analysis the ratio of acceptor to donor fluorescence is used, the occurrence of crosstalk is rather counterproductive. A closer look at the FRET siRNA emission profile also shows that the increase in TMR emission is only marginal. An adequate FRET pair should result in a

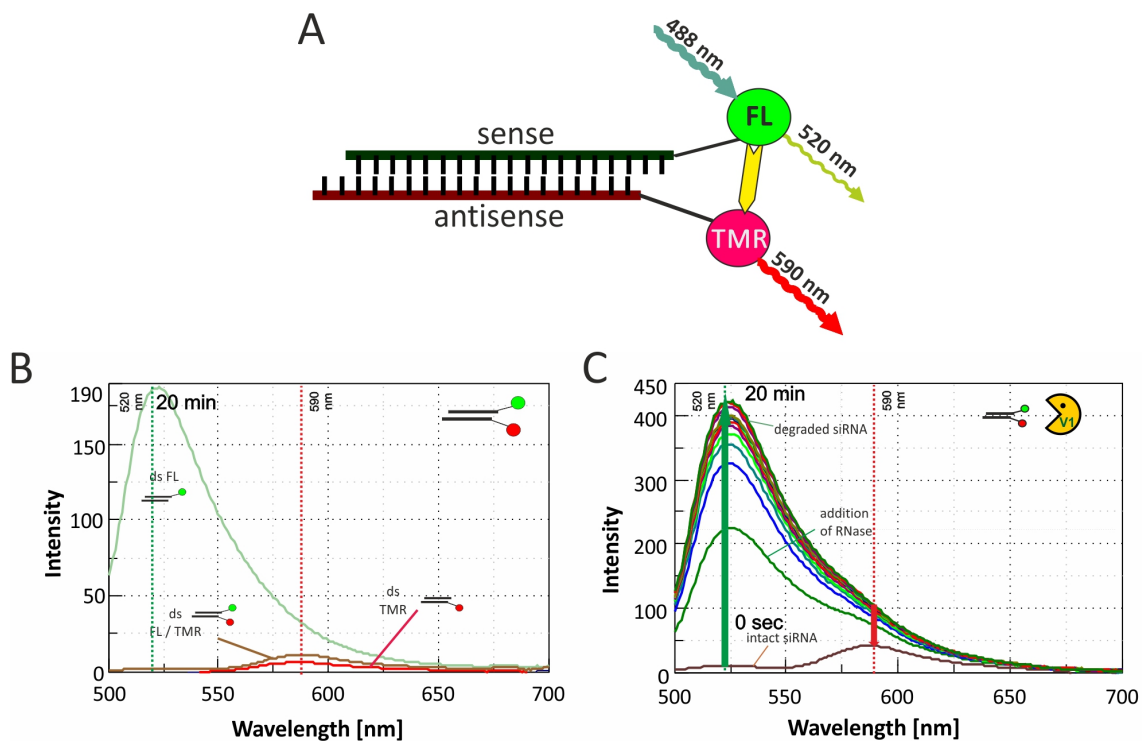


**Figure 3.2: FL/TMR siRNA system.** (A) Scheme of the FL/TMR siRNA with excitation at 488 nm, donor emission at 520 nm and FRET emission, which is detectable at 590 nm. (B) The fluorescence spectra upon 488 nm excitation show the interaction between donor and acceptor. Single fluorescein labeled siRNA (green) shows stronger donor fluorescence, than double labeled siRNA (brown). The acceptor only labeled siRNA (red) shows emission at 590 nm which indicates cross-excitation. (C) FL/TMR-labeled siRNA degraded by RNase V1. The emission spectra before the addition of RNase V1 (brown), right after addition (lower green curve), and at the end of degradation (upper green curve) are indicated. The lines at 520 nm and 590 nm indicate the emission intensities used for R/G ratio calculation. Part C published in a modified version in Hirsch et al. [1].

significant increase of the acceptor signal in case of FRET. Sometimes TMR is therefore also only used as quencher [223] without regard to the acceptor signal, which coincides with this behavior.

The other major drawback of the FL/TMR pair is the susceptibility to photobleaching. Under excitation FL is prone to bleaching which results already in decreasing fluorescence signals under repetitive excitation in the cuvette (see also Chapter 3.1.4).

### 3.1.3 Alternative dyes for FL/TMR and their evaluation of their suitability as FRET siRNA

#### 3.1.3.1 Criteria for an optimized siRNA FRET pair

Fluorescein/Tetramethylrhodamine show, as already indicated, unfavorable photophysical properties, i.e. photostability. But a good photostability is a necessity for live cell observations, as during such long-term observation the fluorescent dyes will be excited several times (up to 500, see Chapter 3.4.2). Therefore the development of a system that is not prone to photobleaching, as it is the case for FL/TMR, is

indispensable.

In addition to the enhanced photostability, an improved FRET pair would ideally also show minimal crosstalk and thus no falsification based on the measuring of a wrong FRET-signal. For this purpose a better spectral separation of donor and acceptor dye might also be considered.

### 3.1.3.2 The siRNA dye candidates

Based on the specifications for more suitable FRET dye pairs a panel of labeled single stranded siRNAs with the same sequence against the EGFP reporter gene was chosen. This panel includes mainly substitutes for either FL, i.e. Atto488 and Alexa488, or TMR, i.e. Alexa555, Atto550, and Atto590. For expansion of the FRET-siRNA system in the blue or deeper red range, Atto390 and Atto647N were also included in the panel. An overview of the dyes and the labeling position on the single strands can be seen in Table 3.1.

Based on the spectral profile of each dye, meaning the excitation and emission spectrum, a potential FRET can be assumed if there is spectral overlap of donor emission and acceptor excitation. Of course a validation in the cuvette is necessary as for efficient energy transfer additional criteria need to be fulfilled. Figure 3.3

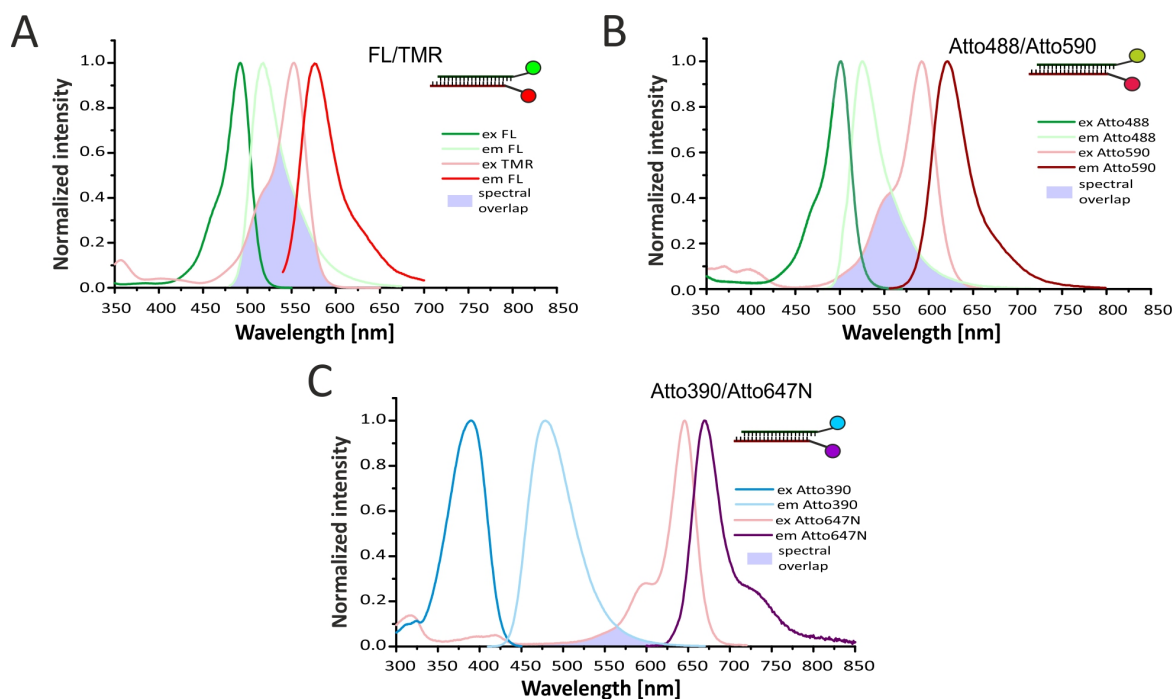


**Figure 3.3: Spectral overlap in FL/TMR, Atto488/Atto590 and Atto390/Atto647N.** Theoretical spectral data of FL/TMR (A), Atto488/Atto590 (B) and Atto390/Atto647N (C) siRNA. The spectra referring to the donor (green and blue) and the one referring to the acceptor (red and violet) are depicted. Donor emission (light green or blue) and acceptor excitation (light red) show the spectral overlap (blue-gray). In case of FRET, the donor excitation (dark green or blue) and acceptor emission (dark red or violet) are the important spectra to address, as they represent the excitation and the FRET emission.



Table 3.1: Key data of siRNA ON panel

ON	Type	Mod. site	Modification	Absorption max [nm]	Emission max [nm]	FRET	Quenching	Emission channel
MH151	s	3'	Atto390	390	479	N/A	Atto550/Atto590/ Atto647N	blue
MH330	as	5'	TMR	546	576	FL/ (Atto488/Alexa488)	N/A	red
MH331	s	3'	FL	496	516	TMR	N/A	green
MH533	as	none	none	N/A	N/A	N/A	N/A	N/A
MH534	s	none	none	N/A	N/A	N/A	N/A	N/A
MH540	s	3'	Atto488	501	523	TMR/Atto550/ Atto590/Atto647N	N/A	green
MH541	as	5'	Atto550	554	579	Atto488/Alexa488	Atto390	red
MH542	as	5'	Atto590	594	624	Atto488/Alexa488	N/A	dark red
MH543	as	5'	Atto647N	644	669	Atto488/Alexa488/ Alexa555	Atto390	far red
MH544	s	3'	Alexa488	495	519	TMR/Atto550/N Atto590/Atto647	N/A	green
MH545	s	3'	Alexa555	555	565	Atto647N	N/A	red

N/A: not applicable; TMR: Tetramethylrhodamine; FL: Fluorescein; s: sense strand; as: antisense strand. (Data published in Hirsch et al. [1])

shows the theoretical spectral profiles of the FL/TMR siRNA and the potential new candidate Atto488/Atto590 or Atto390/Atto647N. It is obvious that the already published construct shows the broader spectral overlap and thus might have the greater FRET potential. The second system shows a smaller spectral overlap, but the combination of Atto488/Atto590 is still capable of sufficient FRET for integrity analysis. The last of the three exemplary constructs, i.e. Atto390/Atto647N, shows almost no spectral overlap, but still FRET can be observed (see again Section 3.1.3.5). In case of FRET, the important data for performing measurements, are the donor excitation, basis for the excitation of the FRET system, and the acceptor emission, which corresponds to the FRET signal. The donor emission will be quenched on the basis of the energy transfer to the acceptor.

### 3.1.3.3 Preparation of siRNA duplexes

With this panel of potential single stranded siRNAs (ss siRNA) hybridizations were made to verify the duplex formation. As an example Figure 3.4A shows the hybridization of the Atto488/Atto590 siRNA with the single labeled double stranded (ds) siRNA as control in an electrophoretic mobility shift assay. One can clearly see the shift from ss to ds siRNA and also the double labeled ds siRNA showing the same migration pattern as the single labeled ds form. Additionally one can see that the hybridization process is not complete at a ratio of sense to antisense strand of 1:1. This means that the concentration determination by UV absorption is not precise enough to guarantee complete hybridization. A frequent consequence of this imprecise quantification is an excess of either of the strands which results in the presence of residual ss siRNA in the preparation. Therefore an optimization of hybridization ratio for each siRNA became a necessity. This optimization compensates inaccuracies in the quantification process or

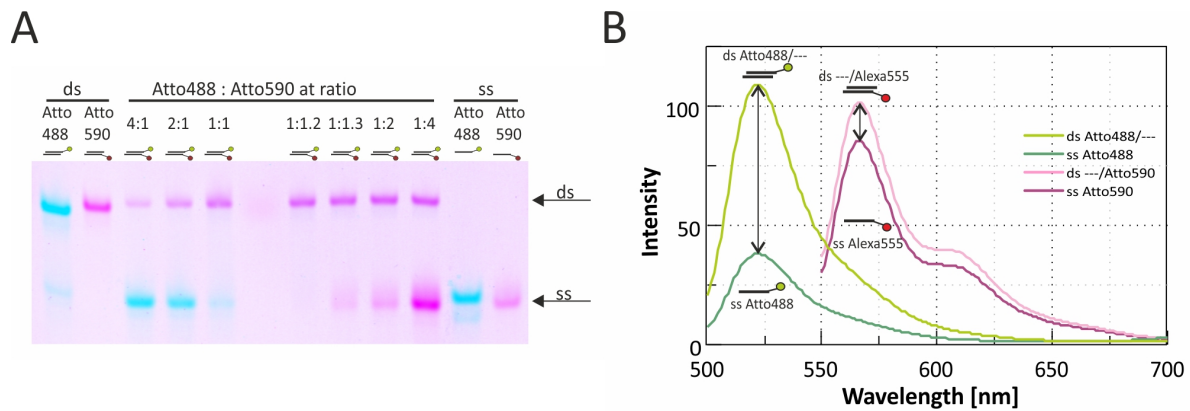


**Figure 3.4: Hybridization of siRNA strands.** (A) Optimization of the hybridization of Atto488 and Atto590 labeled siRNA duplex on non-denaturing PAGE. Donor and acceptor labeled ON were hybridized at different ratios (as indicated) to determine complete hybridization. Constructs with only one dye serve as control and size marker. The display is an adjusted inverted color picture where purple color indicates Atto590 fluorescence upon 532 nm excitation and blue color indicates Atto488 fluorescence upon 488 nm excitation. (B) Effects of hybridization on fluorescently labeled oligonucleotides. Atto488 (green spectra) and Alexa555 (red spectra) are depicted exemplarily. For both labels, the emission profile of ss (darker color) and ds (lighter color) constructs are presented at 488 or 543 nm excitation, respectively. ss and ds siRNA were analyzed at same concentrations of the respective dye. Arrows indicate changes in fluorescence due to hybridization. Data published in Hirsch et al. [1]

addresses the possibility of formation of triple helices. The latter could be eliminated due to the fact, that the range of the determined hybridization ratio is close to one (see Table 3.2), which points to inaccurately quantified RNA samples. Additionally no third band above the duplex band can be observed by titration of one strand in excess. In the presented example the optimal hybridization ratio for Atto488/Atto590 is 1 : 1.2 of sense siRNA (with Atto488) to antisense siRNA (with Atto590) (see Figure 3.4A).

### 3.1.3.4 Influence of hybridization on fluorescence

Upon investigation of the potential FRET combinations and the hybridization process of the siRNA panel, an observation concerning the fluorescence intensity of single labeled ds or ss siRNA was made. A closer investigation showed that the hybridization of a labeled ss siRNA strand enhances the fluorescence, resulting in ds siRNA being brighter in fluorescence than ss siRNA.

**Table 3.2: Fluorescence intensity data of siRNA ON panel**

Oligo	Type	Modification	excitation wavelength cuvette [nm]	emission wavelength cuvette [nm]	ratio of ds / ss intensity	brightness of ss siRNA relative to FL	brightness of ss siRNA relative to TMR
MH151	s	Atto390	405	470	1.2	N/A	N/A
MH331	s	FL	488	520	3.5	1	N/A
MH540	s	Atto488	488	520	2.9	1.22	N/A
MH544	s	Alexa488	488	520	1.7	1.39	N/A
MH545	s	Alexa555	561	590	1.4	N/A	1.85
MH330	as	TMR	561	590	3.3	N/A	1
MH541	as	Atto550	561	590	2	N/A	1.84
MH542	as	Atto590	561	625	4.1	N/A	0.87
MH543	as	Atto647N	633	665	1.8	N/A	N/A

N/A: not applicable; s: sense strand; as: antisense strand; ss: single stranded; ds: double stranded. (data published in Hirsch et al. [1])

The effect of an increased fluorescence in hybridized siRNA duplexes can easily be determined by measuring fluorescence intensities of ss siRNA and single labeled siRNA duplexes at same concentration in the cuvette. An increase in fluorescence was observed regardless of whether the label was on the 3'-end of the sense strand or the 5'-end of the antisense strand. Figure 3.4 B demonstrates this for single labeled ss and ds Atto488 and Alexa555 siRNA. Under the same conditions the ds form showed a 1.4-fold higher fluorescence for Alexa555 and 2.9-fold higher fluorescence for Atto488. The complete data set is displayed in Table 3.2 and shows changes in fluorescence intensity upon hybridization ranging from very little, i.e. by a factor of 1.2 for Atto390, to a more than 4-fold increase in case of Atto590. These results suggest that hybridization might influence the fluorescence properties of any attached dye as a general rule.

Double-stranded solutions of the potential substitutes for FL on one hand and TMR on the other hand range in their relative brightness between 0.9 and 1.8-fold of the respective reference. Table 3.2 displays relative brightness compared with FL and TMR as measured in a 1  $\mu$ M solution of single stranded ON.

### 3.1.3.5 FRET analysis of substitutes for FL/TMR

Cross-excitation of the acceptor dye, i.e. red acceptor emission upon excitation at green wavelength, contributes to an increased R/G value in the absence of actual donor dye, without FRET. In R/G imaging, which is the final goal of the search for new FRET siRNAs, this is akin to false positive simulation of intact siRNA. Although this effect is compensated in the calibration process of R/G imaging, it lowers accuracy and sensitivity of detection of intact siRNA.

A numerical classifier  $C_f$  was defined which allows the classification of cross-excitation potential of certain dye combination.  $C_f$  is calculated as the ratio of cross-excitation to FRET-based emission of the acceptor dye. This allows a direct assessment and comparison of the suitability of different dye pairs for R/G imaging. Table 3.3 gives an overview of the various combinations tested in detail. The meaning of a particular high  $C_f$  value is demonstrated in Figure 3.5 A where acceptor emission of the —/Atto647N siRNA ( $A_D(ds A)$  red curve) and Atto390/Atto647N siRNA ( $A_D(ds DA)$  brown curve) are depicted upon donor excitation. The emission of Atto647N in both constructs is of identical intensity, corresponding to a  $C_f$  value of 1 which leads to a constant acceptor signal.

Another example demonstrating a low  $C_f$  can be seen in Figure 3.5 B. Here  $A_D(—/Atto590)$  is much lower than  $A_D(Atto488/Atto590)$  resulting in a  $C_f$  of 0.16. As obvious, the lower the  $C_f$  value the better the FRET pair concerning cross-excitation and thus sensitivity for quantification.

Besides cross-excitation, the bleed-through of the donor emission into the detection of

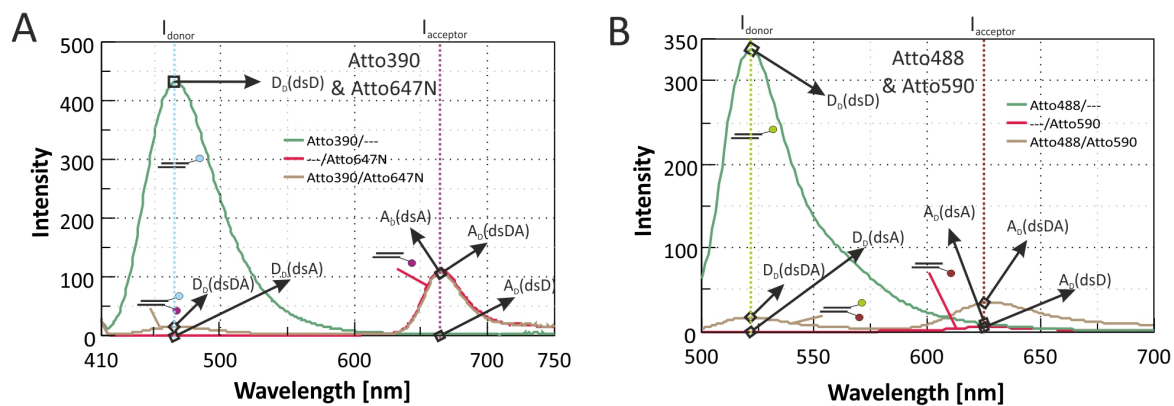


**Figure 3.5: Visualization of intensity values used for FRET evaluation.** Exemplarily the Atto390/Atto647N pair (A) and Atto488/Atto590 (B) are depicted at the corresponding donor excitation wavelength to visualize the intensity values used to calculate  $C_f$  and  $B_f$ . (A) The constructs of the Atto390/Atto647N dye pair are excited at 405 nm (corresponding to Atto390) and those for the Atto488/Atto590 dye pair are excited at the corresponding Atto488 wavelength, i.e. 488 nm (B). In both graphs the intensity used for R/G calculation is indicated by either  $I_{donor}$  or  $I_{acceptor}$ . Additionally extracted intensities are named according following parameters: excitation type (subscript letter; e.g. D for donor), emission (capital letter; e.g. D or A for donor or acceptor emission) and siRNA type (in parentheses; e.g. ss or ds for single or double stranded and D, A or DA for donor labeled, acceptor labeled or donor and acceptor labeled). Data published in Hirsch et al. [1]

the acceptor dye is of interest as this also effects the R/G calculation. In analogy to  $C_f$ , a bleed-through factor  $B_f$  was established which quantifies the contribution of donor emission to acceptor emission and thus increasing the fluorescence caused by FRET on its own.  $B_f$  is calculated as ratio of acceptor emission from donor only siRNA  $A_D(dsD)$  and acceptor emission of double labeled siRNA  $A_D(dsDA)$ .  $B_f$  values for the various FRET-pairs are given in Table 3.3, and Figure 3.5 B shows the Atto488/Atto590 pair as an example of low bleed-through, reflected by a  $B_f$  value of 0.24. The conventional FL/TMR pair exhibits a particularly unfavorable  $B_f$  value of 3. The most favorable dye pairs according to these parameters display  $C_f$  and  $B_f$  values below 0.3.

One problem with high crosstalk is, that on the basis of one single scan under the microscope one can not classify a complete population of siRNA. There is the possibility that the signal arises from either one homogenous population or as combination of a degraded or intact siRNA populations and additional free acceptor or donor label. This can be observed when the labels of degraded siRNA localizes in cellular compartments where still intact siRNA is present or a population of siRNA is to be degraded. In such a case the signal of the siRNA population of interest would be in a way contaminated or falsified by cross-excited acceptor or the bleed-through of donor signals. The described case is true for FL/TMR siRNA where high crosstalk, i.e. bleed-through and cross-excitation, can be observed. In case of the Atto488/Atto590 construct almost no bleed-through and less cross-excitation occurs. In consequence the measured FRET signals of Atto488/Atto590 give a direct hint whether intact siRNA is present or not (see also Chapter 3.4.4.2).

In addition to the  $C_f$  and  $B_f$  parameters, the R/G ratio of a given dye pair is an

Table 3.3: FRET data of various dye combinations

donor dye	acceptor dye	donor wavelength for R/G [nm]	acceptor wavelength for R/G [nm]	R/G ratio	Cross-excitation factor $C_f$	Bleed-through factor $B_f$
Atto390	Atto550	470	590	1.29	1.17	0.51
Atto390	Atto590	470	625	0.7	3.62	0.08
Atto390	Atto647N	470	665	7.4	1.04	0.01
FL	TMR	520	590	2.05	0.6	3.19
Atto488	TMR	n.d.	n.d.	n.d.	n.d.	n.d.
Atto488	Atto550	520	590	13.58	0.17	0.54
Atto488	Atto590	520	625	5.41	0.16	0.24
Atto488	Atto647N	520	665	9.09	0.05	0.07
Alexa488	TMR	520	590	n.d.	n.d.	n.d.
Alexa488	Atto550	520	590	6.95	0.16	0.61
Alexa488	Atto590	520	625	3.94	0.1	0.17
Alexa488	Atto647N	520	665	6.14	0.01	0.02
Alexa555	Atto647N	590	665	5.18	0.09	0.07

n.d.: not determined. (published in Hirsch et al. [1])

important parameter for the effective discrimination of intact from degraded siRNA. As shown in Table 3.3, several dye pairs exhibit values over 2, which is the value formerly used with the FL/TMR pair. Of particular interest are pairs including Atto550, like the Atto488/Atto550 and Alexa488/Atto550 pairs that show R/G values of 7 and 10, respectively. These high values are presumably related to Atto550's particular brightness (compare Table 3.2). However, this advantage is partially compensated by increased  $B_f$  values.

The criteria summarized in Table 3.3 identified several FRET pairs as promising, many of which include Atto647N as an acceptor. This dye and corresponding FRET pairs might offer suitable properties for other applications than the analysis of siRNA integrity.

The idea of using the product of  $C_f$  and  $B_f$  to identify potential FRET pairs, with low product values being favorable, turn out to be unsuitable. In case of one parameter being close to zero, like it is the case for  $B_f$  of Atto390/acceptor constructs, the negative classification by the other value ( $C_f$  for Atto390/acceptor  $> 1$ ) would be reversed and thus imply an ideal FRET combination.

### 3.1.4 Photostability of FL/TMR analogs

On the basis of data from testing the FRET suitability (see Table 3.3) the next step was to analyze the photostability of the candidates. As the initial intention was to find a replacement for FL/TMR which is suitable for live cell microscopy studies, the photostability of the new dyes is crucial. Since in live cell observations imaging is performed over hours or days, resulting in hundreds or thousands of scanning cycles, photostable dyes are essential.

The composition of the dye panel was designed for this purpose and the Atto390 and Atto647N dyes were included to test if combinations with these dyes were suitable for FRET studies or not. Therefore only FL and TMR analogs, i.e. Atto488 and Alexa488 or

Atto550, Alexa555 and Atto590, respectively, were further investigated concerning their photobleaching resistance.

Because the numerous parameters involved in fluorescence and photobleaching make an absolute measurement of standardized photostability extremely challenging, the best way to analyze the different dyes is a comparative analysis for similar dyes. Furthermore, to test the dyes in a system that resembles the microscopic laser setup, 488 nm for donor excitation and 561 nm for acceptor excitation was chosen.

Thus two groups, the FL-analogs (excitation at 488 nm and emission at 520 nm) and the TMR-analogs (excitation at 561 nm and emission at 590 nm) were first analyzed as single labeled siRNA (see Section 3.1.4.1) and later as FRET-labeled siRNA duplexes (see Section 3.1.4.2).

### 3.1.4.1 Photostability of single labeled FL and TMR analogs

Starting with ss siRNA, the samples were excited in the cuvette at a broad excitation bandwidth, and emission intensity was recorded over 10 h of continuous excitation. Alexa488 and Atto488 have been evaluated as potential substitute of FL because of their similar spectral properties including a maximum absorption at around 488 nm (see Table 3.1). In measurements of the emission in the cuvette over a period of 10 h, the known sensitivity of FL to bleaching becomes obvious, as it suffers a substantial loss of fluorescence already during the first hours, ultimately leading to almost complete (98%) photobleaching (see Figure 3.6 A). The Alexa and Atto analogs instead show a lower reduction of fluorescence. After 10 h of excessive irradiation Alexa488 still showed 70% of its initial fluorescence intensity and the Atto488 still 56%. The bleaching behavior was very similar in double-stranded and single-stranded RNA containing analogs of fluorescein (see Appendices C.5).

As potential acceptor dyes, the corresponding TMR alternatives from the Atto and Alexa dye series, i.e. Atto550 and Alexa555, respectively, were analyzed. The more red-shifted Atto590 variant was also included in this acceptor series, as it appeared compatible with the FL-analogs and additionally showed a reduced cross-excitation at 488 nm as compared with, e.g., TMR. As excitation wavelength, 561 nm was chosen, as this

**Table 3.4: Photobleaching stability of dye analogs**

	% of initial fluorescence after 10 h of excitation	
	ss	ds
FL	2	2
Atto488	56	57
Alexa488	70	72
TMR	14	n.d.
Atto550	35	n.d.
Alexa555	49	n.d.
Atto590	67	n.d.

n.d.: not determined

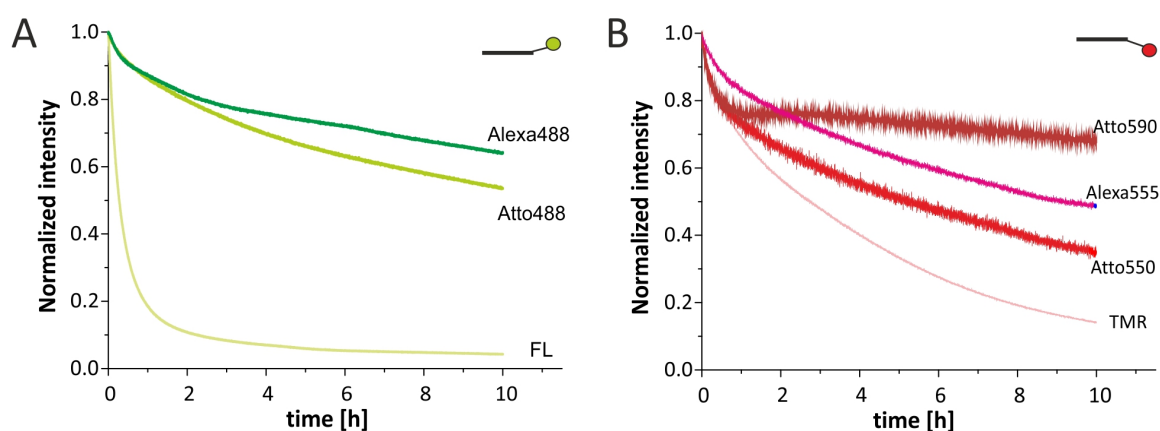


**Figure 3.6: Photostability of fluorescently labeled ss siRNA in the cuvette.** siRNA constructs were excited permanently over 10 h. (A) Normalized emission of green dyes like FL, Atto488, Alexa488 at 520 nm emission over 10 h by 488 nm excitation. (B) Normalized emission of red dyes like TMR, Atto550, Alexa555, Atto590 at 590 nm emission over 10 h by 561 nm excitation. Published in Hirsch et al. [1].

corresponds to the wavelength of laser excitation by confocal imaging. The emission was recorded at 590 nm, though this wavelength corresponds not to the maximum of e.g. Alexa555 and Atto590. The reason why one can still compare the obtained bleaching results is based on the Kasha rule [189] and the fact, that a reduction of a certain percentage at the maximum emission wavelength accompanies a reduction of the whole emission profile intensity by the same percentage.

While the reference dye TMR lost 86 % of its initial fluorescence intensity within 10 h, resulting in 14 % of the initial intensity (see Figure 3.6 B) the TMR-analogs show better photostability of up to 67 % of the initial fluorescence intensity. The most promising dye of the acceptor-analog panel is Atto590 as it still retained around around 67% of the initial fluorescence after the 10 h of permanent excitation. This predestinates Atto590 for a potential use in long-term imaging. On the other hand, Atto550 and Alexa555 are more prone to photobleaching which can be seen by only 35% and 49 % of initial fluorescence intensity (see also Table 3.4).

Based on the data from the bleaching in the cuvette, Atto590 was chosen for further investigation of a photostable FRET pair acceptor for future confocal imaging as it additionally shows the lowest cross-excitation potential. On the donor side Alexa488 shows the most promising behavior.

#### 3.1.4.2 Photostability of double labeled FRET analogs

With Atto590 being the first choice as FRET acceptor and Alexa488 and Atto488 both showed to act as a photostable donor, a detailed analysis of the behavior of the FRET pairs was performed. For this purpose combinations of FL, Atto488 or Alexa488 and TMR, Atto550 or Atto590 siRNA were hybridized yielding 3'-sense labeled and 5'-antisense labeled siRNA duplexes. Alexa555 could not be used as an acceptor as it

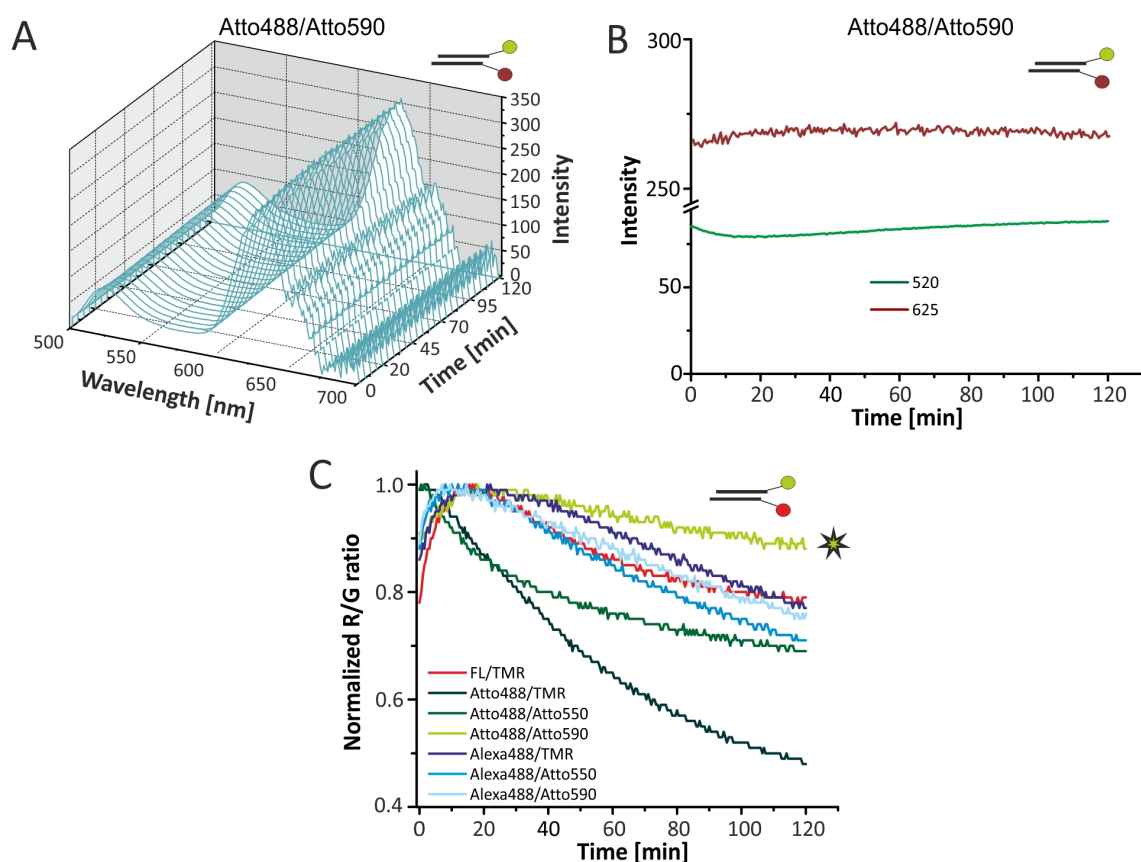


**Figure 3.7: Photostability of double-labeled siRNA constructs.** (A) Emission spectra of Atto488/Atto590 siRNA at continuous excitation at 488 nm over 120 min. (B) Donor and acceptor emission at 520 nm and 625 nm at continuous excitation at 488 nm over 120 min. (C) Behavior of the R/G ratio of double-labeled siRNA over time. Combinations of red and green dyes were analyzed as double-labeled siRNA duplexes over time, and the R/G ratio was calculated. Besides the reference of FL and TMR (red) combinations of Alexa488 (blue) and Atto488 (green) with TMR (dark color), Atto550 (medium color) or Atto590 (light color) as potential acceptor has been analyzed. The combination Atto488 and Atto590 is marked by an asterisk. Published in Hirsch et al. [1].

is attached on the 3'-end of the sense strand.

The hybridized constructs were continuously excited at 488 nm ( $D_{ex}$ ) in the cuvette, and the whole emission spectra were recorded over a period of 2 h at 2 min intervals. In Figure 3.7A the 3D-spectrum of Atto488/Atto590 is depicted as an example. From the recorded data the donor and acceptor intensities ( $I_{donor}$  and  $I_{acceptor}$ ) were extracted and used for the calculation of the R/G ratio. In Figure 3.7B the extracted donor and acceptor intensities are shown for the Atto488/Atto590 siRNA. One can see that over the whole time the intensities of donor and acceptor remain in a narrow corridor, meaning no strong changes in intensities over time.

Based on these traces the R/G-ratio was calculated according to (Eq. 3.1) with the corresponding emission wavelength for the donor  $I_D$  and acceptor  $I_A$  as listed in Table 3.3. The summary of the calculated R/G-values is shown in Figure 3.7C. Looking closer at the single R/G-traces one can see that in all cases the R/G ratio increases in the beginning before they decay over the exposure time of 2 h. This initial increase is almost not present in the Atto488/Atto550 and Atto488/TMR siRNA, whereas those two pairs



also show the strongest decay over the observed period. This behavior makes them less suitable for the purpose of live cell imaging.

It appears that this initial increase is most distinct for the FL and Alexa488 FRET pairs. As illustrated for the Atto488/Atto590 construct in Figure 3.7 B, the initial increase in the R/G-value is apparently due to some donor bleaching which causes the donor intensity to decrease and thus results in a higher R/G value. However, the cause for the subsequent recovery of the donor emission is unclear, though a decrease in FRET can be ruled out as the FRET signal stays constant.

In Figure 3.7 C one can also see, that the Atto488/Atto590 combination (indicated by an asterisk) is the most resistant to changes in the R/G ratio over time. It ranges in a narrow corridor of 100 % to 90 % of the determined maximal R/G value, whereas the other constructs display a drop in their respective R/G value to almost 15 % of the initial value.

Having the most stable R/G ratio of all tested FRET siRNAs over the observed time period and also ranked high in the evaluations of FRET efficiency, crosstalk, and bleed-through, Atto488/Atto590 was chosen as the siRNA FRET construct for live cell observations to investigate uptake and release in living cells (see Section 3.4).

Another observation that was made by permanently exciting the FRET siRNAs was that especially for FRET pairs that contain TMR as acceptor a change in the emission profiles was observed. This drift of the donor and/or acceptor emission maximum was most pronounced in the FL/TMR construct (see Appendix C.7) and not visible in other constructs (see Appendix C.6). A change of the emission maxima under permanent excitation suggests that changes of the chemical structure of the dyes occur which lead to the formation of a new kind of fluorophore that shows different spectral properties. These changes might however also influence the FRET efficiency, as intensities decrease due to that drift, and thus the possibility to use the FRET pairs with TMR as acceptor for long-term integrity measurements is unfavorable.

### 3.1.5 Promising FRET pairs for future applications

#### 3.1.5.1 Atto488/Atto590 siRNA envisaged for imaging

Because of good results in the photobleaching experiments and the much better spectral separation of Atto488/Atto590 to FL/TMR, see  $B_F$  Table 3.3 and Figure 3.8, the Atto488/Atto590 FRET pair offers the best qualification for accurate long-term live cell microscopy.

In Figure 3.8 A the schematic of the Atto488/ATTo590 siRNA is depicted and the adequate excitation and emission wavelength are shown in the FRET-cartoon. This siRNA can easily be excited at 488 nm which corresponds to the standard green laser in

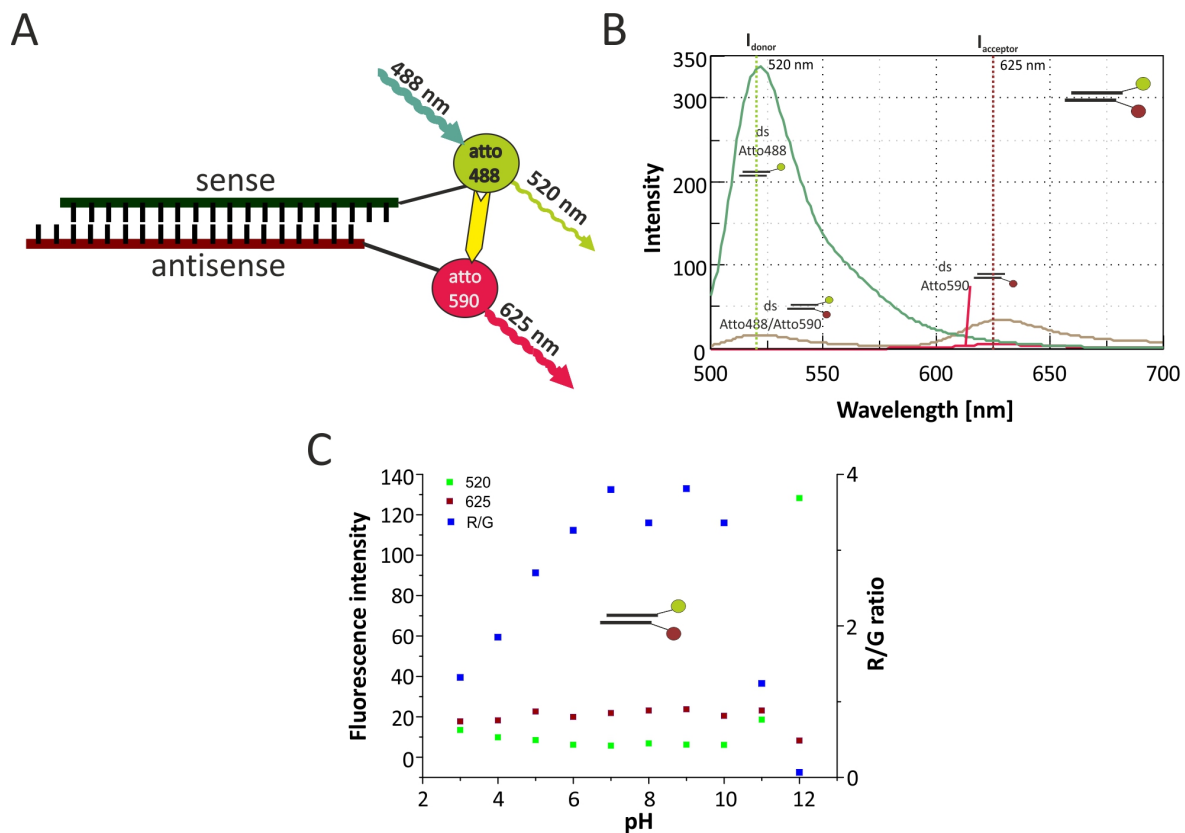


**Figure 3.8: Scheme of FRET siRNA Atto488/Atto590.** In (A) a scheme of the FRET construct is depicted which shows the excitation wavelength of the donor dye (Atto488) and the recorded emission of donor, i.e. 520 nm, and acceptor dye, i.e. 625 nm. The yellow arrow indicates FRET that occurs between the donor and acceptor. (B) The graph depicts the fluorescence spectra of the ds donor Atto488 (green), the ds acceptor Atto590 (red) and the ds FRET siRNA (brown). Dashed light green and dark red line indicate recorded emission wavelength for measurements in the cuvette. (C) pH dependency of the Atto488/Atto590 siRNA. Emission intensity of the donor signal at 520 nm (green) and FRET signal at 625 nm (dark red) are determined at different pH-values (left axis). The resultant R/G-ratio (blue) is indicated on the right axis. Part C published in Hirsch et al. [1].

most commercial available microscopes, which is also true for the acceptor, Atto590, and the excitation at 561 nm (red laser in many microscopes). As summarized in Table 3.3 the important emission wavelength for the donor is 520 nm and 625 nm for the acceptor. In case of microscopy studies, these distinct emission wavelengths are extended to emission bands of 30 nm, ranging from 510 nm to 540 nm for Atto488 and 605 nm to 635 nm for Atto590.

The observed R/G ratio in the cuvette is around 5.4 which is higher than for the FL/TMR pair analyzed in this work. Though one can see batch-to-batch changes in the R/G ratio the average value was above 4. A detailed analysis of this FRET siRNA for microscopic purpose can be found in Section 3.3.2.

An additional interesting question, concerning the application in cells, is the behavior of the dye, or the FRET pair, at different pH values. This is an important question, as during a cellular uptake process, which probably involves an endocytotic pathway, the siRNA, formulated in lipoplexes with cationic lipids, will pass different compartments, i.e. endosome, lysosome and cytosol, which includes changes in the pH. Normal

physiological pH is around 7.4 whereas during endocytosis and lysosomal delivery the pH drops to around 4.5. More basic pH levels above 8 are uncommon in eukaryotic organisms and only observed in the intestine or pancreatic juice.

Measurements in the cuvette at different pH (see Figure 3.8 C) show that the overall change in fluorescence intensity of the FRET pair stays rather constant in the range of a pH of 3 to 10, with a slight decrease in donor emission from lower to higher pH (see pH of donor (green) from 3 to 6, Figure 3.8 C). At pH values of 11 and higher the donor signal suddenly increases with a decrease of the FRET signal. This is obviously due to a strand separation and degradation of the construct at high pH. The resulting R/G value however, shows stronger changes than the fluorescence indicates. The maximum R/G can be observed close to neutral and weak basic pH, i.e. between 6 and 10. At lower pH values, i.e. from 5 to 4, the R/G drops to a ratio of 2. Below a pH of 4 and above a pH of 10 the R/G ratio is below 2, which is not useful for integrity determination. Looking at R/G values above 2 in a range from pH 5 to 10 and an R/G-ratio of 1.9 at the pH of 4, the described Atto488/Atto590 FRET pair is still suitable for intracellular classification. An R/G of 1.9 still indicates more than 97% intact siRNA in the sample (according to R/G calibration model in Section 3.2.2).

The pH behavior of Atto488/Atto590 allows an application in the physiological range with inaccuracies starting at very low pH of 4 or less as the duplex probably faces degradation.

#### **3.1.5.2 Further siRNA FRET constructs as extension of the FRET siRNA panel**

Besides the unfavorable properties of the FL/TMR siRNA, i.e. crosstalk and sensibility toward photobleaching, and the promising Atto488/Atto590 siRNA, which is spectrally better separated and more photostable, a set of plenty different FRET siRNA pairs can be combined (see Table 3.1).

The most interesting are Atto390/Atto647N, Atto390/Atto550, Alexa488/Atto550 and Alexa555/Atto647N. With the already described Atto488/Atto590, the whole range of the visible light range is covered (see Figure 3.9 and 3.10). This offers many possibilities to choose an adequate siRNA FRET system tailored to the desired application system.

The Atto390/Atto647N system shows one unique characteristic, which is a constant acceptor or FRET signal at 405 nm excitation indifferent to the presence of Atto390 as potential donor dye (see Figure 3.10 A+B). Nevertheless, the system (or other systems with Atto390 as donor) might offer the possibility to use an additional dye with emission in the range of 500-600 nm that lies in between the respective emission range of donor and acceptor dye. These dyes, like FITC or the fluorescent protein EGFP, are very common for organelle staining used in microscopy. This feature of the Atto390/Atto647N construct might somehow resemble to dyes with extreme large

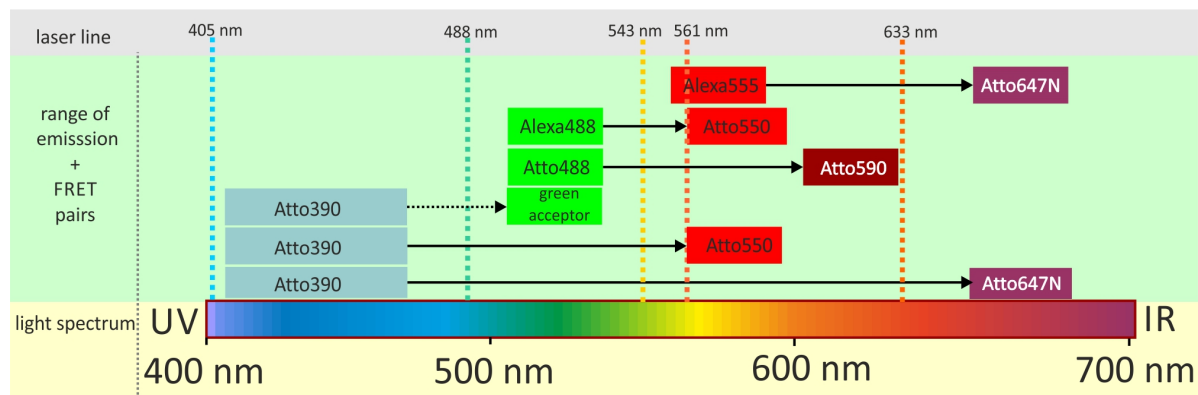


**Figure 3.9: FRET pairs in visible light range.** Position of the interesting siRNA FRET pairs in the visible light range from 400 nm to 700 nm. Shorter wavelengths correspond to the UV-range and longer wavelengths to the Infrared-range as indicated. Dotted lines indicate the common laser lines used in laser scanning microscopy. Colored boxes represent emission band of each dye. FRET is symbolized by black arrows between a donor dye (left dye) and acceptor dye (right dye). The construct Atto390/"green acceptor", indicates an imaginable FRET pair on basis of Atto390.

Stoke's Shifts, like the MegaStokes dyes that are offered by Dyomics.

Alternatives like Atto390 with a green acceptor might offer the possibility to place the FRET system in the blue/green-range of the visible light, enabling to use the yellow to red range for additional labels. The other mentioned alternative Atto390/Atto550 shows one improvement compared to the green acceptor, i.e. a better spectral separation as Atto390 shows a relatively broad emission bleeding through into the green and orange range.

As the studies indicate, the Atto390 based FRET systems display a constant signal of the acceptor in presence or absence of the donor. This means that potential acceptor dyes, like Atto550, act rather as a quencher than a FRET acceptor and show strong cross-excitation at 405 nm (see Figure 3.10 C+D). The Atto390 emission, however, is efficiently quenched in presence of the acceptor. Though a quenched system might, on the first look, not be useful for the desired purpose of integrity measurement on the basis of FRET, the system might be used as an labeling system to detect strand separation inside cells. After strand separation the system will collapse and thus result in a strong donor fluorescence. The acceptor presence can either be measured by excitation at 405 nm, as it shows a high cross-excitation (see also Table 3.3) or by excitation at the corresponding acceptor excitation, which is 633 nm for Atto647N.

Alexa488/Atto550 (see Figure 3.10 E+F) or the isospectral substituted system Atto488/Atto550 are a direct replacement of FL/TMR system with similar emission maxima of the acceptor dye. Though the spectral separation is similar, and thus an application in microscopy might be problematic, an application in the cuvette is still possible. In the cuvette, single wavelength emissions are recorded or extracted reducing the effect of broader emission spectra, which might be problematic in microscopy. In addition, the determined crosstalk factors  $C_f$  and  $B_f$  are much lower than in the case of FL/TMR siRNA. Due to the relatively narrow spectral separation, additional red emitting

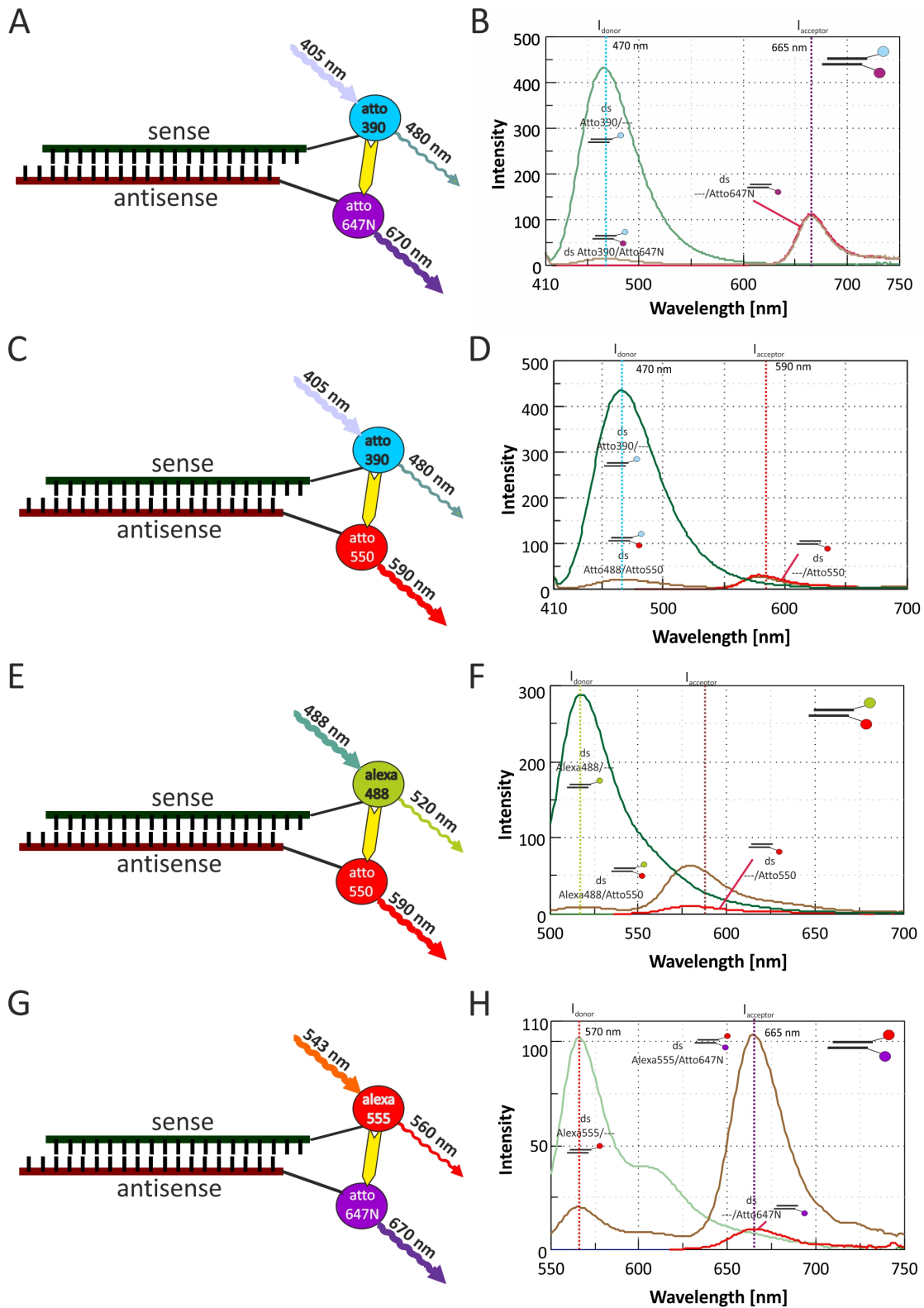


**Figure 3.10: Promising FRET siRNA.** Scheme of FRET siRNA consisting of Atto390/Atto647N (A+B), Atto390/Atto550 (C+D), Alexa488/Atto550 (E+F) and Alexa555/Atto647N (G+H). In (A, C, E and G) the excitation and recorded emission wavelength of each FRET pair are indicated. The yellow arrow indicates occurring FRET between each donor and acceptor. (B, D, F and H) The graphs depict the fluorescence spectra of the ds donor (here Atto390/—, Alexa488/— or Alexa555/—, respectively, in green), the ds acceptor (here —/Atto647N, —/Atto550 or —/Atto647N, respectively, in red) and the ds FRET siRNA (here Atto390/Atto647N, Atto390/Atto550, Alexa488/Atto550 or Alexa555/Atto647N, respectively, in brown). Dotted lines in the emission spectra indicate recorded wavelength for measurements in the cuvette.

dyes can be combined with these constructs. Thus being not optimal for accurate R/G imaging donor/Atto550 siRNA might be useful with microscopes that are not equipped with variable emission filters (like the spectrophotometer detection system of Leica) but with fixed filter cube combinations. The system might also be a basis for a triple-FRET construct with a far-red dye as third acceptor.

Besides these more or less disadvantageous spectral properties, the observed R/G ratio is rather high, i.e. 7 for the Alexa488 variant and 13.6 for the Atto488 variant (see Table 3.3). This high R/G ratio makes these combinations very sensitive to small changes in FRET efficiency and thus distance of donor and acceptor dye. For further analysis and comparison the Alexa488/Atto550 siRNA was used as a direct replacement for FL/TMR with better crosstalk properties and photostability.

The last FRET siRNA that will be discussed is the Alexa555/Atto647N siRNA, which represents a red shifted variant of the complete system (see Figure 3.9 and 3.10 G+H). Again like in the case of Atto390/Atto647N, this system offers a similar possibility, namely the combination with green fluorescent dyes. Thus one can imagine a simultaneous use with a green fluorescent protein or common fluorescent dyes, like fluorescein or OregonGreen (see Section 3.2.5.2).

## 3.2 Application of FRET siRNA *in vitro*

### 3.2.1 Influence of labeling on silencing capability

One main question arises when using labeled siRNA for tracing and integrity measurements, which is the remaining gene silencing capability.

As already described in Section 1.1.2.2 the recognition of the 5'-end and phosphate of the antisense strand is essential for effective gene silencing[17, 41]. With the acceptor label on the 5'-end of antisense strand the silencing capability might be influenced.

In earlier studies the activity of the FL/TMR system has already been evaluated in HEK293T cells by using an EGFP reporter gene assay and FACS evaluation (see master thesis [224]). The data of this previous work is shown in Figure 3.11 A.

In a more recent study [42] the gene silencing potential of the optimized Atto488/Atto590 siRNA system has already been analyzed in comparison to other labeled siRNA duplexes with label on the 5'-end of the antisense strand. The relevant experiments for gene silencing were conducted by [redacted] and kindly provided for the presented work (see Figure 3.11 B).

Both systems show similar results concerning the labeling position (see Table 3.5). As expected the unlabeled form is the most active, though the donor only labeled duplex shows a slightly higher average activity. This difference is caused by variations in the assay and is probably not due to changes in activity. Concerning these discrepancies as significant, one might assume that the label on the 3'-end of the sense strand destabilizes the duplex and might thus facilitates the incorporation of the active siRNA strand into the RISC.

Regarding the label on the 5'-end of the antisense strand, which is either TMR in the already described FL/TMR system [2] or Atto590 in the earlier published examination

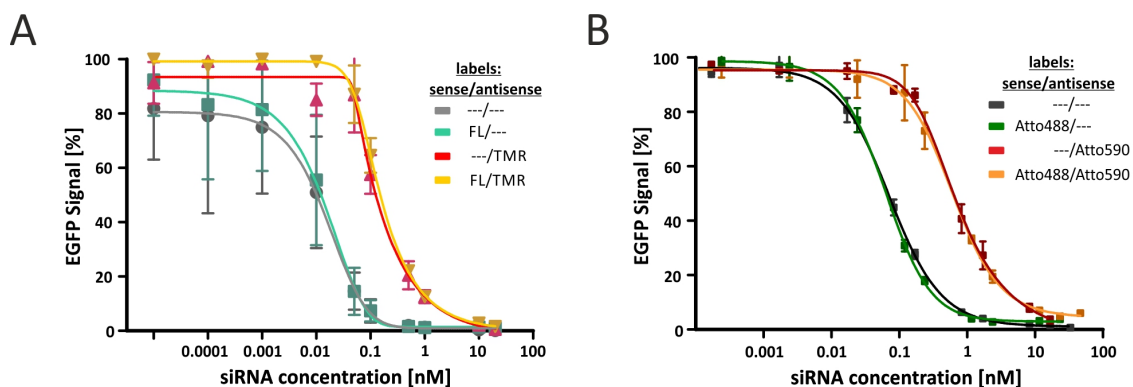


**Figure 3.11: Gene silencing efficiency of labeled siRNA constructs.** Different siRNA concentration were used to determine the  $IC_{50}$  value in an EGFP reporter gene assay in HEK293T cells. The test covered the unlabeled siRNA duplex, single labeled duplexes with donor or acceptor only and the double labeled FRET constructs. (A) previous work of master thesis [224] with FL/TMR siRNA (n=3). (B) previous work of [redacted] (n=3), published in Seidu-Larry et al. [42].

**Table 3.5: Knockdown efficiency of labeled siRNA**

	label at 3'-end of sense	label at 5'-end of antisense	FL / TMR IC <sub>50</sub> [pM]	Atto488 / Atto590 IC <sub>50</sub> [pM]
unlabeled	-	-	27	72
donor only	X	-	25	62
acceptor only	-	X	238	710
FRET labeled	X	X	255	610

parts of data published by Seidu-Larry et al. [42], Hirsch [224]

by Hirsch et al. [1], Seidu-Larry et al. [42], a 10-fold decrease in activity, meaning the IC<sub>50</sub> value can be observed. This means the influence on this position and label is much higher than the one of the donor dye on the sense strand. This observation agrees with the common opinion that the 5'-end is indeed important for efficient RNAi. From the single labeled duplexes the step to the double labeled FRET constructs results in a similar behavior as with an unlabeled donor only labeled siRNA. This means no decrease in activity but rather a slightly higher gene silencing capability. Nevertheless, the obtained data suggests a certain tolerance to modifications at the 5'-phosphate of the guide siRNA strand as earlier published by Shah and Friedman [225].

By comparing the data of FL/TMR to the recently published data [42] a lower overall activity of the Atto488/Atto590 siRNA in the range of 2.3- to 3-fold higher IC<sub>50</sub> values can be found. This is true for both labeled and unlabeled duplexes. These changes can be explained by different experimental conditions and equipment for the whole test since the examination of FL/TMR (new batch of siRNA ON, new established research lab and new equipment).

In addition, the referred data was obtained in a cotransfection experiment of a plasmid coding for EGFP and the respective siRNA [222]. At present, [REDACTED] studies knockdown efficiencies in a new established system that uses cells that constantly express an unstable variant of EGFP [226] that does not require a cotransfection with the EGFP-plasmid. This cell line, i.e. a subtype of HeLa cells, permanently expresses EGFP that is attached to a proline-glutamate-serine-threonine rich sequence (PEST) and thereby enhances the proteasomal decomposition of EGFP via an ornithine decarboxylase (ODC) [226]. Thus biased results due to insufficient cotransfection can be excluded.

### 3.2.2 R/G calibration of FRET siRNA

The most important step for classifying the integrity level of siRNA is to relate the integrity level of an siRNA to the R/G value (see (Eq. 3.1)).

For this purpose samples that simulate different siRNA integrity levels were prepared. This was done by mixing three different siRNA samples that represent intact and degraded siRNA. In case of the Atto488/Atto590 siRNA system this is the double



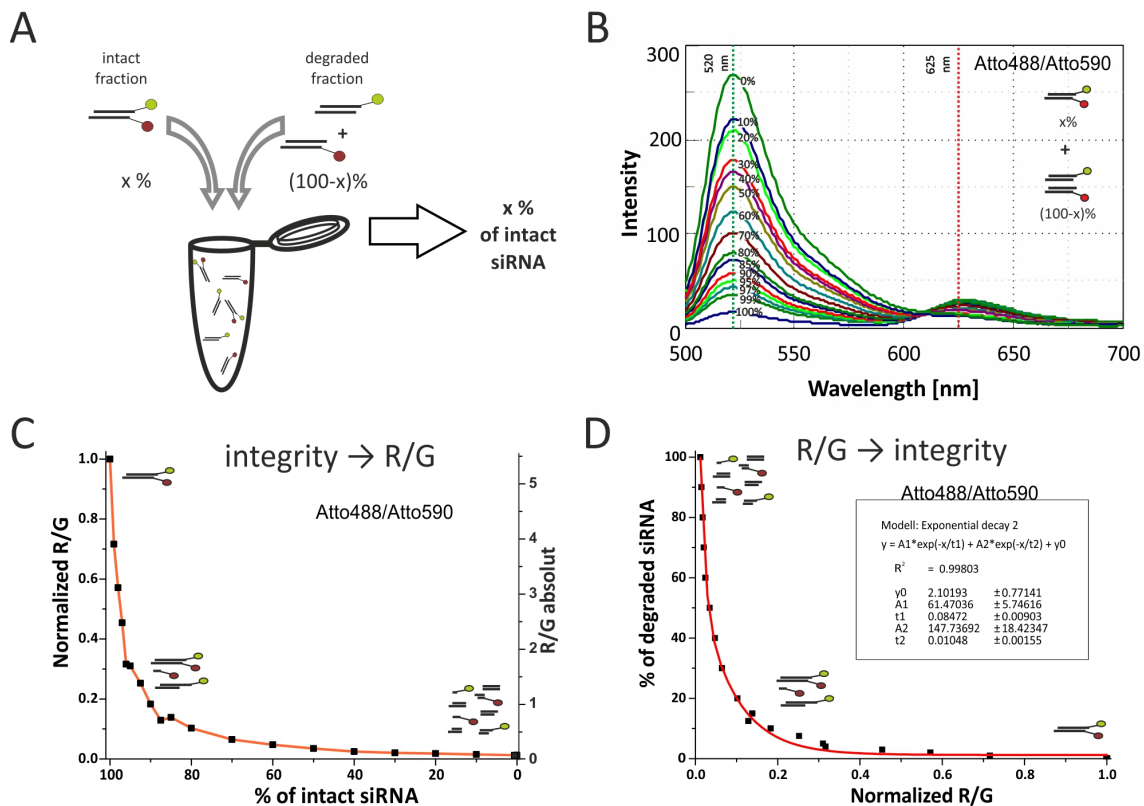


**Figure 3.12: Calibration of the Atto488/Atto590 system for the determination of siRNA integrity.** (A) siRNA integrity levels were simulated by mixtures that contain X % of the double labeled Atto488/Atto590 siRNA and (100-X) % of a mix containing the single Atto488 and single Atto590 labeled siRNA. (B) Emission spectra of samples with different integrity levels of the Atto488/Atto590 siRNA system. Emission intensity at 520 nm (green line) and 625 nm (red line) are used to calculate the R/G ratio. Numbers indicate the fraction of intact siRNA and thus the integrity level. (C) R/G ratio relation to different integrity simulations. (D) Model fit on the basis of the R/G values and corresponding degradation level that allows to classify unknown samples.

labeled Atto488/Atto590 siRNA and the single labeled donor only and acceptor only construct, i.e. Atto488/— duplex and —/Atto590 labeled duplex, respectively. When these components are mixed in a distinct ratio, one obtains a sample in which a certain fraction of siRNA is double labeled and another part is only single labeled simulating degraded siRNA (see Figure 3.12 A). In this case, degradation means either the siRNA is cleaved in single nucleotides and free dye by nucleases, high pH or temperature that destroy the RNA structure, or strand separation, as it occurs during RISC incorporation. All possibilities lead to a destruction of the siRNA duplex. The advantage of the used method is, that the different siRNA types are already hybridized and a rehybridization at ambient temperatures is unfavorable.

Samples that were prepared according to the scheme in Figure 3.12 A, were analyzed by excitation at the donor excitation wavelength (see Table 3.2) of 488 nm for the Atto488/Atto590 system. Figure 3.12 B depicts the retained emission profiles of samples simulating integrity levels ranging from 100 % intact, corresponding to only double labeled ds siRNA, to 0 % intact, corresponding to a mixture of exclusively single labeled siRNA duplexes. For comparability the concentration of the donor, i.e. Atto488, was kept

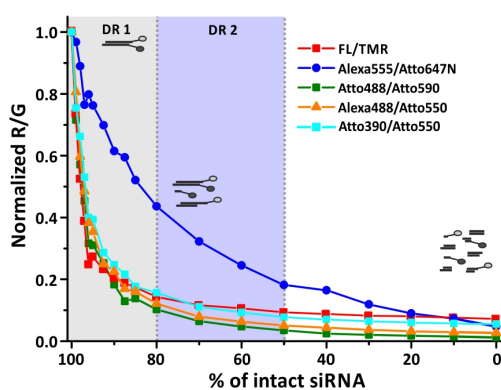


**Figure 3.13: R/G calibration of different siRNA systems.** Comparison of the different evaluated FRET siRNAs, i.e. FL/TMR (red), Atto488/Atto590 (green), Alexa488/Atto550 (orange) and Alexa555/Atto647N (blue). Normalized R/G values of simulated siRNA integrity states with indication of the dynamic range for quantification of siRNA integrity. The dynamic range DR 1 ranging from 100 % to 80 % (gray box) and DR 2 ranging from 100 % to 50 % (gray and blue box) are indicated.

constant and the acceptor only siRNA amount was adjusted according to the optimized hybridization ratios (see Chapter 3.1.3.3) to guarantee equal concentration of donor and acceptor dye in all samples.

Without any further calculation one can see that already little amounts of single labeled siRNA, i.e. 1 %, lead to an increase in donor emission to the same intensity level of the acceptor emission. Looking at the normalized R/G values (see Figure 3.12 C) these strong changes in R/G can be seen in the steep decrease in R/G value from 100 % to 80% of intact siRNA samples. In this range the system has the highest overall performance and sensitivity.

Based on the extracted R/G values a model was fitted that allows to calculate the integrity level of a sample on the basis of R/G measurements. Figure 3.12 D depicts the exponential decay model which best describes the simulated data. For classifying unknown samples it is necessary to determine the R/G ratio and normalize it to the siRNA reference or the reference that best describes the intact siRNA. Thus one obtains the level of degradation, which can easily be transformed into the integrity level.

On the basis of the described siRNA FRET pairs (see Chapter 3.1.5) R/G models were also simulated and fitted for Atto390/Atto550, Alexa488/Atto550, Alexa555/Atto647N and the published FL/TMR system (see Appendices D.8). All systems show a similar

**Table 3.6: Comparison of R/G calibration**

	ex [nm]	em <sub>D</sub> [nm]	em <sub>A</sub> [nm]	DR from 100 % to	R/G max in calibration	R/G before V1	R/G after V1	application
Atto390/Atto550	405	470	580	80 %	2.19	3.21	0.16	none
FL/TMR	488	520	590	80 %	2.75	5.7	0.25	<i>in vitro</i> tests -cuvette/ fixed cells ([2, 224, 227])
Alexa488/Atto550	488	520	580	80 %	7.44	6.68	0.21	none
Atto488/Atto590	488	520	625	80 %	5.42	4.01	0.06	live cell imaging
Alexa555/Atto647N	543	565	665	50 %	3.55	1.85	0.16	nanoparticle evaluation

potential to classify siRNA between an integrity level of 100 % intact to 80 %. For the Alexa555/Atto647N system an extension towards 50 % can be made as in this system the decrease of the R/G ratio was not so strong compared to the other systems (see Table 3.6). Thus the dynamic range for the Alexa555/Atto647N range is broader than for the other constructs (see Figure 3.13). As classifier for the determination of the dynamic range, the first derivative of the change in the R/G ratio was chosen. A first derivative larger than 0.01 enables still an adequate classification, though R/G values below the dynamic range can still be assigned an integrity level. This might be more inaccurate compared to higher R/G values, as little changes in R/G result in a large change in integrity state (see Appendix D.9 B).

Different to the analysis presented in 3.1.5, slightly different emission wavelengths for donor and acceptor were used (see Table 3.6). During the bleaching analysis an emission wavelength of 590 nm acceptable for the complete set of acceptor dyes was used. For the individual calibration of each siRNA system adapted emission wavelengths were used. Nevertheless, the results in Chapter 3.1.4.2 are still valid as the measured intensity, some nanometers below the actual emission maximum, should behave in the the same way as the maximal intensity.

The presented FRET siRNA systems offer thus a possibility to use a FRET system suitable for a distinct purpose or in combination with other dyes. Additionally, all the described systems have, at least in the cuvette, the power to analyze the integrity state of an siRNA sample.

### 3.2.3 Degradation of FRET siRNA

The integrity simulation represents an artificial approach which needs to be compared to an actual degradation of intact siRNA. This was achieved by degrading siRNA with RNase V1, an RNase that degrades double stranded RNA. The degradation leads to a fragmentation of the intact siRNA duplex into single nucleotides or fragments. The fragmentation leads to a collapse of the FRET system since the FRET dyes can now diffuse freely in solution at distances higher than the Förster radius of 60 nm (data provided by the supplier ATTO-TEC [228]). The collapse of the FRET signal over time is depicted in Figure 3.14.

Here the change in donor emission  $D_{em}$  and FRET emission  $A_{em}$  upon excitation at 488 nm can be demonstrated. Before the addition of RNase V1, the intact bulk sample shows a high R/G value of around 4 (see also Table 3.6) and a final degraded value of 0.06 after 20 min. In this case after 20 min no further change in the emission profile was observed which is apparently indicating a complete degradation of the siRNA in the sample.

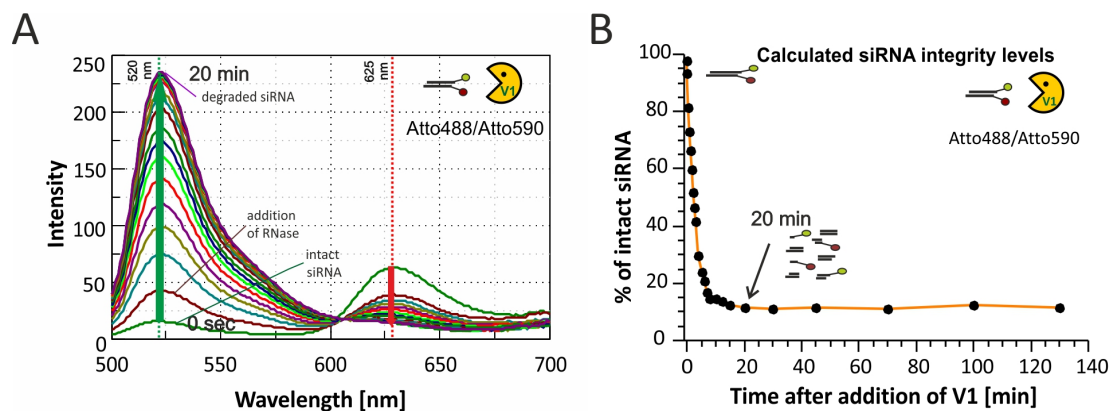


**Figure 3.14: Degradation of Atto488/Atto590 siRNA duplexes by RNase V1.** FRET siRNA was incubated with RNase V1 and emission upon excitation at 488 nm was recorded. Indicated are emission profiles before addition of V1 (first from below at 520 nm, green), the first scan after the addition of V1 (second from below at 520 nm, brown) and the final profile when no further changes within some minutes are observed (top at 520 nm, violet). Emission wavelength used for R/G calculation are indicated as dotted lines, i.e. at 520 nm (green) and 625 nm (red). (B) Calculated integrity levels on basis of the integrity simulation model fit.

The analysis of the degraded siRNA also shows some limitations. Though the FRET has collapsed and the R/G dropped to a minimum after already 20 min of degradation, a recalculation of the integrity states resulted still in 15 % intact siRNA (see Figure 3.14 B). The basis for the calculation was the integrity simulation and the fitted exponential decay model for converting R/G values into degradation levels (see Figure 3.12). This discrepancy of calculated integrity state to the obvious degraded siRNA sample is based on inaccuracies in the fitted model with lower integrity states. At low integrity levels the R/G changes are only marginal as depicted by a first derivative below 0.01 in the integrity simulation (see Appendix D.9 B) and a correct or absolute quantification is difficult or impossible. This fortifies the dynamic range for the quantification of integrity states in the range from 100 % intact to 80 % (for most of the siRNA evaluated) and down to 50 % for the Alexa555/Atto647N siRNA.

Similar to the degradation of Atto488/Atto590 siRNA the Atto390/Atto550, Alexa488/Atto550 and Alexa555/Atto647N siRNA were tested in the degradation assay (see Appendices E.10). The R/G values of the systems before and after degradation can be found in Table 3.6. The analysis shows that all tested siRNA constructs are rapidly degraded by RNase V1 resulting in complete degradation with no further changes in the emission profile after 20-60 min.

Regarding the calculated endpoint R/G values, one can see that there are differences between the systems. The Atto488/Atto590 systems shows the lowest R/G (below 0.1) which might also indicate the least crosstalk interaction. Whereas the other systems, that show either bleed-through or cross-excitation (i.e. Alexa488/Atto550 or Alexa555/Atto647N), result in final R/G values of 0.16 to 0.25.

The degradation of FRET siRNA samples will be used in following sections to analyze the integrity state, i.e. either for protective effects or surveillance of preparation processes.

### 3.2.4 Utilization of FRET siRNA for survey of liposomal formulation

With a FRET siRNA that allows to determine the integrity state of a sample, the preparation process of liposomes was surveyed. The idea was to monitor the success of encapsulation of intact siRNA into liposomes and to investigate the influence of the formulation procedure on the siRNA integrity. As method of choice for the preparation of siRNA liposomes the earlier published dual asymmetric centrifugation approach (DAC) was used (Hirsch et al. [229]).

#### 3.2.4.1 Examination of the preparation process

With the establishment of DAC for liposomal preparation, small amounts of siRNA liposomes with high siRNA concentrations can be prepared [229]. The system is basically a modification of a standard centrifuge that includes a second rotational axis that creates a backspin during centrifugation (see Figure 3.15 A+B). For preparation a viscous lipid mixture consisting of around 40% dried lipid film (depending on the composition of the liposome type) was incubated with the desired sample solution (~60%) to be encapsulated. The lipid / sample composition is depending on the respective formulation. Here, for the sterically stabilized liposomes (SSL) a ratio of 35% lipid with 65% siRNA solution was used. SSL contain pegylated phospholipids for stabilization in solution. For better homogenization small beads were added to standard screw cap reaction vial. Due to the described back-rotation and the beads in the reaction vial, the shear forces appearing homogenize the sample very efficiently to form a highly concentrated vesicular phospholipid gel (VPG) [229]. This VPG consists mainly of small unilamellar liposomes in the range of approximately 100  $\mu\text{m}$ . The VPG can then be redispersed into a liposomal suspension. After purification via inverted spin filters with a MWCO of 30 kDa free siRNA was removed resulting in samples of concentrations of around 1  $\mu\text{M}$ . The quantification of encapsulated Alexa488/— siRNA resulted in an entrapping efficiency of 51% which was lower than earlier reported 50-80% encapsulation efficiencies for FL/TMR by Hirsch et al. [229].

The big advantage of using FRET labeled siRNA is the possibility to determine the integrity state. For this purpose SSL were loaded with different FRET siRNA constructs, i.e. the old FL/TMR siRNA and the new Atto488/Atto590 and Alexa555/Atto647N siRNA. Figure 3.15 C depicts the average size distribution of the prepared liposomes before and after purification by dynamic light scattering. The sizes of empty liposomes containing only PBS, and siRNA loaded liposomes are in the same range of around 120 nm. The liposomes containing siRNA resulted in a slightly smaller diameter. Except the liposomes containing FL/TMR no changes in size after purification were observed. The change in FL/TMR liposomes size probably originates from aggregate formation

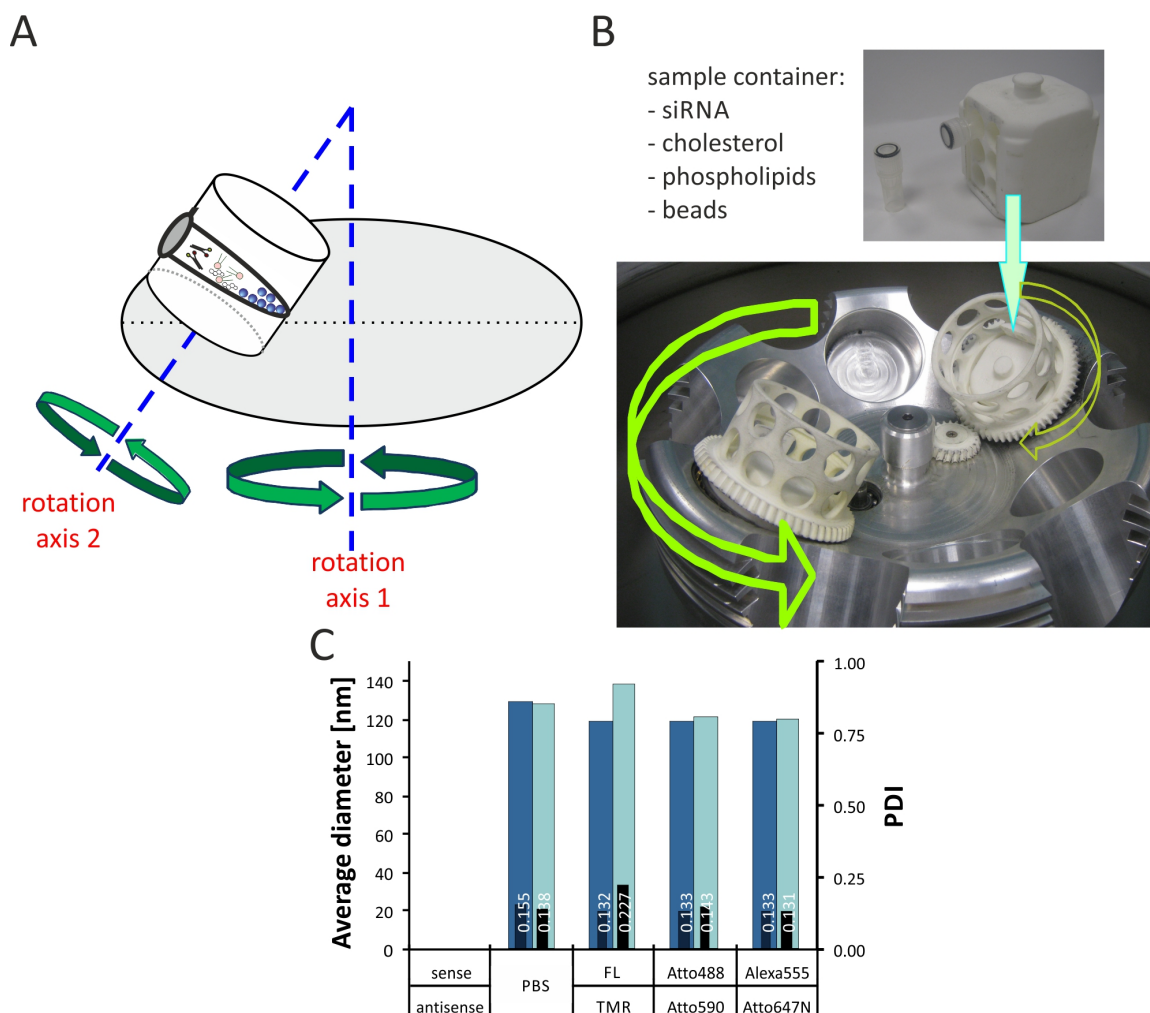


**Figure 3.15: Liposomes prepared by dual asymmetric centrifugation.** (A) Scheme of the dual asymmetric centrifugation system. Rotation around axis 1 results in centrifugation of the probe to the edge of the sample container. Rotation around axis 2 results in a back-rotation. With the beads in the sample container shear forces homogenize the liposomal mixture (phospholipid, cholesterol and sample, e.g. siRNA) to form a vesicular phospholipid gel. (B) sample container and sample holder inserted in the centrifugal device. (C) Measured size distribution of sterically stabilized liposomes (SSL) containing labeled siRNA or just PBS (empty liposomes). The liposome size was measured before (dark blue) and after (light blue) purification (left axis). Black bars inside the blue size columns indicate the PDI value (right axis).

during the purification process, in which the suspension was filtered by centrifugation for several hours. The results are in consistency with the earlier published loading of liposomes with FL/TMR siRNA [229].

The analysis of the size distribution of prepared liposomal formulations resulted in a polydispersity index (PDI) below 0.2 (see Figure 3.15 C black bars within colored bars). The value indicates that the liposomal formulations have a rather narrow size distribution which is essential for therapeutic application to guarantee a certain kind of uniformity.

Looking at the size distribution of the liposomes prepared by DAC, promising candidates for further applications were obtained. Subsequent cell studies were not performed, as earlier work with unmodified liposomes did not show an efficient cellular uptake.

Previous data [224] showed that uptake only occurred by incubation of cells in almost pure liposomal formulation. In consequence, modified liposomes, that contain targeting moieties for a specific uptake, like receptors agonists or cell penetrating properties (cationic charge), are of interest for future evaluation.

Ongoing research in the Helm group addresses this problem by using hyperbranched polyglycerol-based cholesterol [230] (provided by the group of Prof. Frey) that contain terminal alkyne groups that should allow a further modification with an targeting moiety via the *Copper catalyzed azide-alkyne 1,3-dipolar cycloaddition (CuAAC)* [231]. The reaction of a terminal alkyne with a terminal azide to an triazole represents an easy way to permanently post-modify alkyne groups with various azide-bearing molecules (dyes, macromolecules and other).

An other important question is of course, how the integrity of the encapsulated siRNA looks like. For this purpose purified siRNA liposomes were analyzed by fluorimetry upon excitation at the respective donor excitation wavelength. Figure 3.16 depicts the profiles of the three different encapsulated FRET siRNA. As the liposome itself has a strong autofluorescence that is high in the proximity to the excitation and at longer wavelengths (see gray curves in 3.16), one cannot simply compare the liposome profile with earlier described free siRNA profiles. To achieve comparability, empty liposomes were analyzed at the same lipid concentration and the spectra were subtracted from the siRNA liposome profiles. The obtained data (blue spectra in Figure 3.16) can now be compared with the intact siRNA spectra.

These calculated theoretical siRNA spectra match the original siRNA profile. No difference between calculated and measured spectra can be observed for Alexa555/Atto647N liposomes (see Figure 3.16 C). For Atto488/Atto590 and FL/TMR siRNA the donor signal almost doubled (see Figure 3.16 A+B). Nevertheless the R/G ratio is in all three preparations still above 2 which indicates an almost complete intact siRNA population. A detailed analysis with the respective calibration data of each FRET system showed no more than 1 % of degraded siRNA (see Table 3.7).

Another approach to investigate the integrity level of encapsulated siRNA is the visual inspection of the siRNA population using a non-denaturing PAGE. Degraded siRNA, which can result from either strand separation or from phosphodiester hydrolysis of the RNA chain, should result in additional or smeared bands on PAGE analysis. Strand separation would result in faster migrating ss siRNA and degradation in a smeared band below the band referring to intact ds siRNA. As the prepared liposomes do not migrate by PAGE (see Appendix F.11, fluorescence remaining in pocket) a prior disruption of the liposomal bilayer (called cracking) by incubation with Triton X-100 was performed as earlier described by Hirsch et al. [229].

Faint bands in case of the FL/TMR set, which consisted of the reference siRNA,



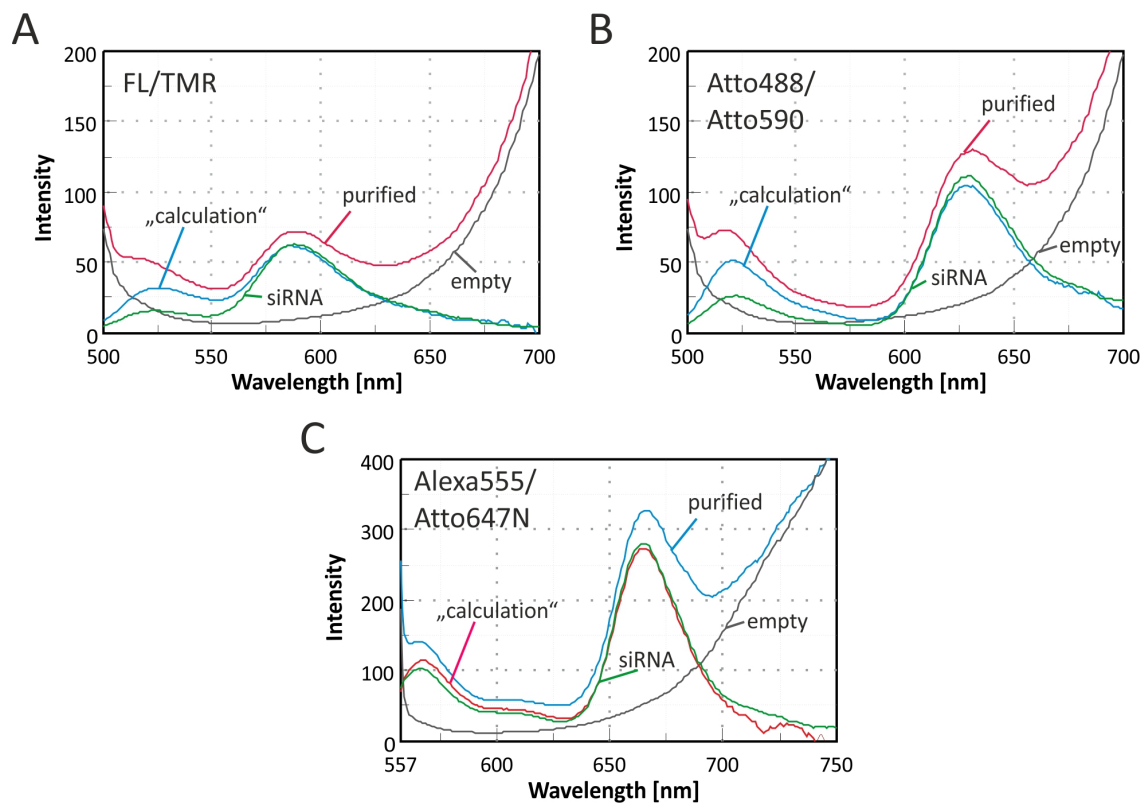


**Figure 3.16: Spectral analysis of liposomes.** Emission of liposomes containing FRET siRNA is determined under donor excitation. Liposomes containing FL/TMR siRNA (A), Atto488/Atto590 siRNA (B) and Alexa555/Atto647N (C) were analyzed. Graphs show spectra of purified liposomes (red), the profile of the siRNA alone (green), empty liposomes (dark gray) and calculated siRNA only spectra of the liposomes samples (blue).

purified liposomes and cracked liposomes were observed. This faint band was present in both siRNA and treated liposome, which indicates an incomplete hybridization at the beginning. In case of Alexa555/Atto647N a weak smeared band was observed at the height of ss siRNA. This indicates that the measured integrity loss of 1% (see Table 3.7) is caused by RNA decomposition, which might be due to higher temperatures and shear forces during preparation.

In addition to the fresh prepared liposomal formulations, an earlier preparation of Atto488/Atto590 containing liposomes was also analyzed to investigate whether decomposition occurs upon storage over longer periods. The analysis revealed an additional band for the 1.5 year old sample which indicates a loss of at least some bases of the siRNA duplex during the storage process. It can be ruled out that this additional band is single stranded siRNA, as this band migrates at a similar level as the bromphenol blue band, whereas single stranded siRNA migrates in the proximity of the xylene cyanol band (see Appendices F.11).

Nevertheless, the analyzed samples showed FRET in both PAGE fluorescence scans and in the fluorescence emission scans in the cuvette indicating the proximity of both dyes and thus intact siRNA.



**Table 3.7: Surveillance of siRNA integrity during liposomal preparation**

	R/G of reference	R/G of purified liposome	integrity loss upon formulation
FL/TMR	4.1	2.0	0.40 %
Atto488/Atto590	4.2	2.0	0.21 %
Alexa555/Atto647N	2.7	2.4	0.95 %

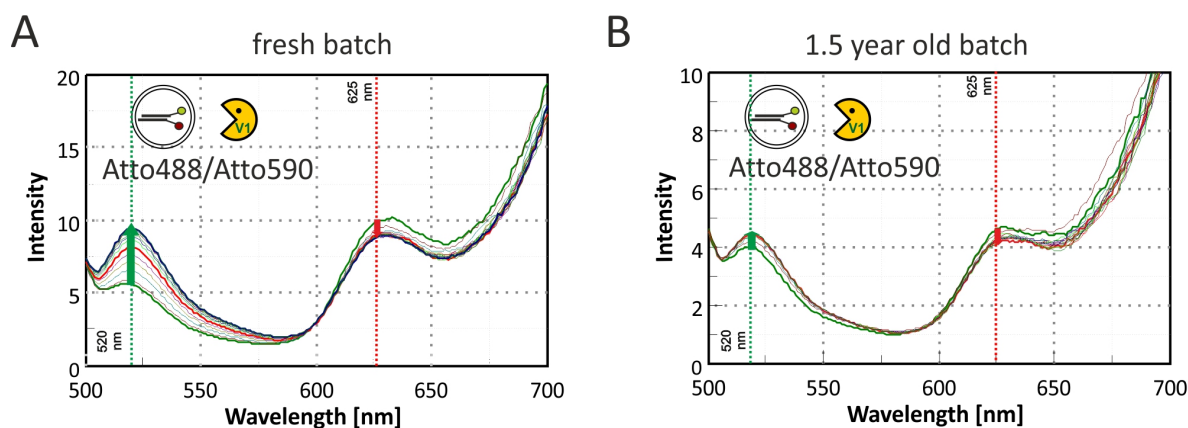


**Figure 3.17: Storage of liposomes.** Liposome containing siRNA Atto488/Atto590 was analyzed before (A) and after storage for 1.5 years at 4°C (B). Samples of each batch were treated with RNase V1 and analyzed over time. Spectra refer to original profile before addition of V1 (1<sup>st</sup> from below at 520 nm, green), during incubation with observable changes and at the end point (top at 520 nm, blue). Changes over time are indicated with red and green arrows.

R/G analysis showed that besides FL/TMR [229] also Atto488/Atto590 and Alexa555/Atto647N siRNA can be used to survey the preparation of liposomes containing intact siRNA duplexes.

### 3.2.4.2 Stability of prepared liposomes

Another question that arises with respect to formulation concerns storage properties of prepared liposomes. To address this question 1.5 year old liposomes were analyzed by RNase V1 treatment. Similar to the previous study with the pure intact siRNA, liposomes with FRET siRNA were incubated with the ribonuclease and changes were monitored by fluorescence emission scans.

The data depicted in Figure 3.17 A+B indicate the presence of a small fraction of free siRNA in the purified liposomes which was subject to degradation. In case of the fresh batch this led to an increase in the donor emission and a slight decrease in acceptor emission (Figure 3.17 A). The stored liposomes showed less changes in donor and FRET signal indicating less free siRNA. This difference of old and new prepared liposomes could probably be caused by a less efficient removal of free siRNA in the newer sample. An additional observation was, that the stored samples showed similar fluorescence intensities for both donor and a FRET intensity whereas the fresh prepared liposomes showed a higher initial FRET intensity.

It seems that the storage of the liposomes leads to some changes in the siRNA integrity, though R/G ratios above 1 indicate still almost complete intact siRNA samples (with

more than 99 % intact siRNA). This change in the siRNA population can also be observed by PAGE analysis in which an additional band appears (see Appendix F.11).

Apart from the observation that free siRNA is decomposed, the largest part of the siRNA remains intact and thus unaffected. This proves the concept of liposomal encapsulated siRNA being shielded from exterior influences like nucleases. Additionally, the 1.5 year old sample indicates also that the encapsulated siRNA does not escape the liposome and remains in the interior.

### 3.2.5 Evaluation of nanoparticular delivery systems

In another *in vitro* approach, the presented Alexa555/Atto647N siRNA integrity model was used to validate a panel of different nanoparticular delivery systems, that were provided by several collaboration partners. The purpose of the analysis was to determine the protective effect of each delivery system against RNases, which is essential for *in vivo* application.

#### 3.2.5.1 Determination of the optimal siRNA to particle ratio

The panel of potential delivery systems consists of nanohydrogels [232] (i.e. smaller nanohydrogels, larger nanohydrogels and Oregon green labeled nanohydrogels), a poly-L-lysine brush [233], liposomes prepared by DAC (see Chapter 3.2.4), cationic peptides [101], magnetic core-shell particles [104, 234] (RITC-labeled and unlabeled) and commercially available cationic lipids, i.e. Oligofectamine (Ivitrogen) as reference system. An overview of collaboration partners that provided the different particles can be found in Materials & Methods 5.1.5. These compounds are still in the developmental phase and the evaluation is ongoing. However, some results are already promising for potential *in vivo* studies.

There are some differences in the nanohydrogels as already indicated. One hydrogel is labeled by Oregon Green, which enables tracing inside cells, whereas the other two represent unlabeled hydrogels with different average diameters. Uptake studies with the labeled particles were performed in collaboration with Prof. Zentel and were already published (see Appendices G.12) [232].

In a first step the minimum ratio of particles per siRNA was determined by agarose gel shift assays, by titrating a constant amount of siRNA with increasing amounts of particles. This was necessary to achieve optimal loading of the particles with siRNA. This work was mainly done by a [REDACTED]. She kindly provided her data (see Appendices G.13) that was used to determine the optimal ratio of siRNA to particle for one part of the tested delivery systems (i.e. cationic peptide, labeled hydrogel, smaller hydrogel and poly-L-lysine brush). The data of the other evaluated nanoparticles (i.e. the larger

hydrogel, RITC-labeled and unlabeled magnetic particle) are shown in Appendices G.14. The second part of the evaluated particles faced the problem of reproducibility in synthesis or the obtained batch decomposed at 4°C over time. As far as a constant production or storage of these particles cannot be guaranteed no future experiments can be performed due to a lack of sufficient material.

The evaluation of optimal siRNA to particle ratio for liposomes was not necessary as they were prepared in advance and did not need an additional complexation step before usage.

Most particles showed complete complexation at an acceptable siRNA to particle ratio, which demonstrates their applicability for cellular uptake studies. The magnetic core-shell particles that also face the problems of a reproducible production showed no complete complexation of the siRNA. This resulted in a band of free siRNA or a smear that indicates release from the complex upon analysis by electrophoresis. Higher complexation ratios could not be tested due to lack of material and low concentration of provided material. On basis of the complexation assay for each particle a ratio that results in complete complexation or the highest possible ratio, in case of magnetic particles, was used for further analysis (see Table 3.8). Oligofectamine was used at the same siRNA to particle ratio as used for transfection, which is 1:14.

### 3.2.5.2 Analysis of RNase protection by siRNA integrity measurements

Besides the capability of complexation or encapsulation of siRNA or the capability of releasing the payload at the target site, the protective effect of the respective formulation is essential for *in vivo* application.

To verify the protective effect of the different delivery system siRNA/particle complexes were formed with constant amounts of Alexa555/Atto647N siRNA (ratios according to Table 3.8) and incubated with RNase V1 in a degradation assay. The exposure was monitored over a period of 2 h which allows to analyze if siRNA was released from the complex as degradation of free siRNA occurs within minutes (see Section 3.2.3).

The emission at 565 nm and 665 nm was determined to calculate the respective R/G value (according to Table 3.6). On the basis of the calibration of the FRET siRNA, normalized R/G values were used to determine siRNA integrity in the respective sample at each time point of observation. After standardizing the data (see Materials & Methods Section 5.3.9), the calculated integrity levels were used to fit an exponential decay model (see Figure 3.18). On the basis of the decay model, the decay rate  $\lambda$  was determined (see Table 3.8).

As control experiment free siRNA was treated with RNase V1 (see Figure 3.18) presumably showing the maximal degradation rate. Within 10 minutes the siRNA was completely degraded and no FRET between the two labels could be observed (see Table

Table 3.8: Nanoparticle evaluation data - Complexation and protective effect

particle	particle to siRNA ratio (mass:mass)	% of intact siRNA after			decay rate $\lambda$ (exponential fit)	Protective effect
		10 min	25 min	2 hours		
liposome	N/A	100	100	100	0	excellent
cationic peptide	1:10	100	100	100	0	excellent
nanohydrogel (Oregon Green)	1:50	100	100	100	0	excellent
cationic lipid (Oligofectamine)	TF $\cong$ 1:14	96.2	92.9	76.2	$< < 0.01$	very good
polymer brush	1:4	65.3	66.5	69.3	0.03	not classifiable
magnetic particle (FITC)	1:10	89.8	66.8	28.3	0.02	medium
nanohydrogel (small)	1:50	69.1	54.8	31.2	0.05	medium
nanohydrogel (large)	1:100	21.0	25.2	12.1	0.17	poor
magnetic particle (unlabeled)	1:20	1.8	0	0	0.30	poor
siRNA	NA	1.7	0.6	0	1.14	none

N/A: not applicable; TF: transfection conditions; excellent:  $\lambda = 0$ , very good:  $\lambda < 0.01$ , medium:  $\lambda < 0.1$ , poor:  $\lambda < 1$

3.8). This demonstrates the necessity of the protection of siRNA in *in vivo* delivery approaches.

Under the same conditions the complete panel of transport systems was tested and analyzed as described. A complete summary of the different integrity states at 10 min, 25 min and 2h of exposure to RNase V1 is shown in Table 3.8). One can distinguish between four different groups: Excellent protection (no degradation detectable, decay rate  $\lambda = 0$ ), very good protection ( $> 50\%$  intact siRNA after 2h,  $\lambda < < 0.01$ ), medium protection ( $> 25\%$  intact siRNA,  $\lambda < 0.1$ ) and no or poor protection at all (see colored categories in Table 3.8)

The first group, that showed no siRNA degradation at all, contains the liposomes, the labeled nanohydrogel and cationic peptide. This data identifies these systems as well suited for protection of formulated siRNAs against degradation by RNases. These particles guarantee a shielding of the siRNA from RNases and also show that, at least over a period of 2h, no siRNA can escape from the particle.

The standard transfection agent oligofectamine showed a good protection against RNases, though some degradation occurred over time. The cationic lipid was used as gold standard as all other transfection experiments were so far performed with the commercially available oligofectamine.

The poly-L-lysine brush is one exception in the analyzed set of particles. Data implies that after 2 hours still  $\sim 70\%$  of siRNA is intact and thus a very good protection can be assigned. Nevertheless the complexed siRNA and brush showed one anomaly, which indicates very strong interaction with the siRNA and the attached dyes. Upon complexation the measured R/G drops to a level which can be quantified as partly degraded siRNA sample. After RNase addition, no further changes can be observed over time. The data suggests that the brush itself somehow disrupts the siRNA integrity or interferes with the FRET dyes resulting in lower FRET intensities as expected from intact free duplexes. Nevertheless, no additional degradation can be observed which indicates a good protection against RNase at the cost of duplex integrity in the complex.

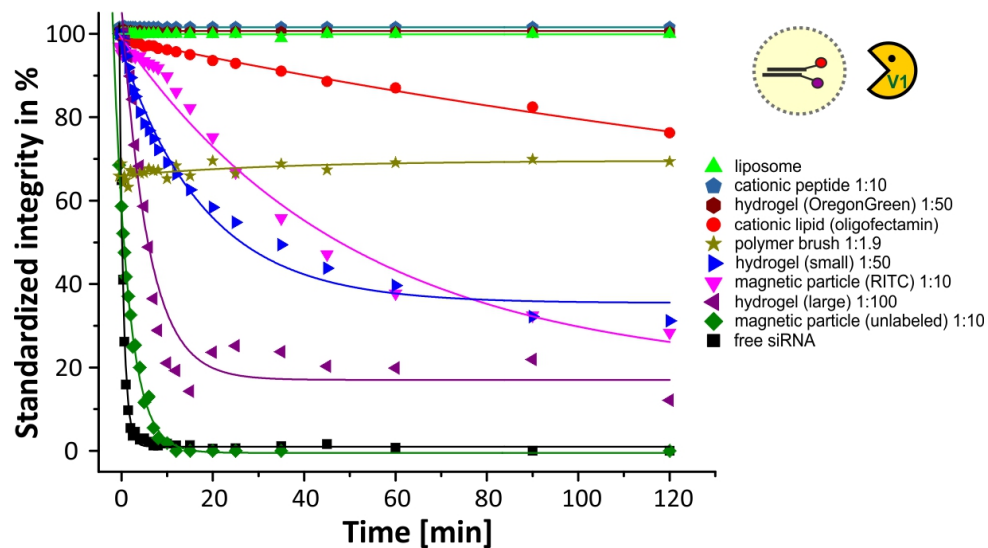


**Figure 3.18: Analysis of the protective effect of several nanoparticular delivery systems against RNase.** As nanoparticular delivery systems liposomes, cationic lipids, cationic peptides, nanohydrogels (labeled with Oregon Green, smaller and larger unlabeled), magnetic core-shell particles (labeled with RITC or unlabeled) and poly-L-lysine brush were tested. Liposomes were prepared in advance, whereas the other delivery systems were freshly loaded or complexed with the Alexa555/Atto647N siRNA in the indicated ratio right before the addition of RNase V1. Emission upon donor excitation at 543 nm is recorded up to 120 min and R/G values are calculated. Data is normalized to the integrity level of intact siRNA and standardized. Curve correspond to fitted exponential decay model.

Whether a real protection or the interaction of the FRET dyes with the polymer are responsible for these observations should be further investigated. An examination of siRNA released from the poly-L-lysine brush might give a hint whether the duplex is indeed degraded or whether the intact duplex can be rebuilt. First studies on this were done by [REDACTED] who could recover intact siRNA by heparin displacement.

The third group of tested particles showed a medium protective effect compared to free siRNA, but over time a release and thus successive degradation was observed. This effect was more pronounced as in case of cationic lipids. In this second group one finds the RITC labeled magnetic particle and the smaller nanohydrogel.

For the magnetic particle the results indicate that the interaction of short terminal amino-functionalized PEG that is masked by longer PEG-residues has not the best properties for shielding siRNA though a delayed degradation could be observed.

Besides the larger nanohydrogel, which has to be assigned to the group of non-protective particles, the unlabeled magnetic particle and of course free siRNA are degraded within few minutes.

### 3.3 FRET siRNA in fixed cells

#### 3.3.1 Bleaching behavior under the microscope

With Atto488/Atto590 an adequate FRET pair which is very suitable to identify the integrity state of siRNA in the cuvette has been evaluated. As mentioned earlier, the difference to microscopic analysis is the time of irradiation, meaning the number of scans per region, and the recorded emission band.

While in the cuvette a single scan to record an emission spectrum takes approximately 20 seconds, a scan in the confocal laser scanning microscope (CLSM) takes only some ms, depending on the size of the scan region. Nevertheless, the intensity of the laser used is much higher than the intensity of a Xenon lamp in a fluorimeter, so that a comparison from cuvette data with the microscopy is difficult. In addition, imaging of living cells faces problems of photobleaching and light induced phototoxicity by reaction with ROS or singlet oxygen that were not present, or only at lower levels, in the cuvette. For this purpose the Atto488/Atto590 construct was also tested in long-term or repetitive excitation in microscopy, respectively.

##### 3.3.1.1 Excitation of matrix embedded siRNA

In a first approach, chamber slides, which are also used for live cell imaging (see Chapter 3.4.2), were filled with the free FRET siRNA Atto488/Atto590 either as single labeled duplexes or double labeled FRET construct. To prevent diffusion inside the chamber the siRNA was embedded in agarose. For this purpose 2% agarose with one type of siRNA duplex at 1  $\mu\text{M}$  were prepared and scanned under the laser scanning microscope. The analysis showed for both single labeled duplexes a loss in fluorescence over time as indicated in Figure 3.19 A.

It can not be ruled out, that diffusion of siRNA influences the actual bleaching behavior, meaning an attenuation of the bleaching. There are different possibilities for diffusion. Temperature gradients that occur upon excitation, like it is used in thermophoresis [235], can either cause an accumulation or displacement of siRNA in the scanning region. Another possibility might be the diffusion of intact fluorophores into the scanning region due to a concentration gradient which occurs after bleaching of fluorophores. This is similar to the technique of FLIP, where the bleaching of a center region leads to diffusion of intact fluorophores from unbleached regions to compensate the loss [188]. An increase of intact fluorophore without bleaching can be ruled out as the overall scanned intensities drop. Nevertheless the observed bleaching behavior might be weakened by the processes described.

Over a period of 2000 scans the intensity decreases only 19% in case of the donor,

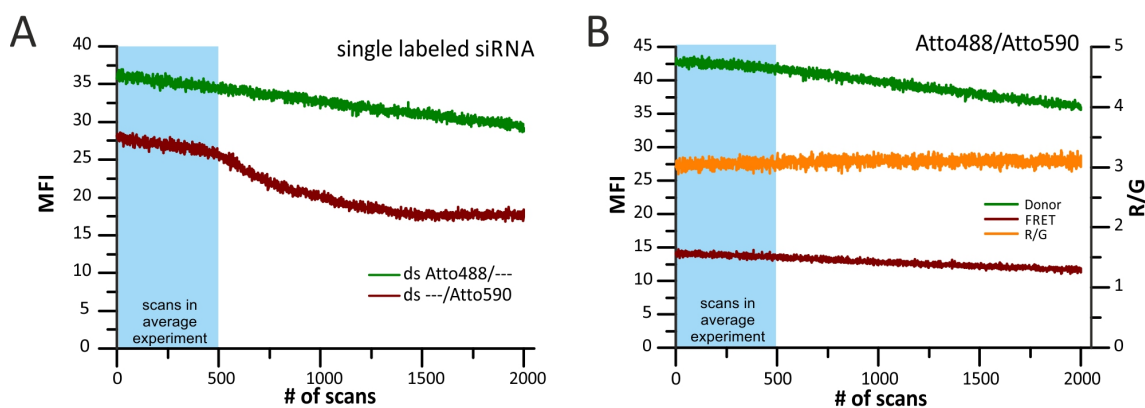


**Figure 3.19: Analysis of bleaching behavior of agarose embedded siRNA.** Atto488/—, —/Atto590 and Atto488/Atto590 siRNA embedded in 1 % agarose excited with CLSM at identical settings. (A) Atto488/— siRNA at 488 nm excitation and emission around 520 nm (green) and —/Atto590 duplex at 561 nm excitation and emission at 625nm (red) scanned for 2000 times at similar settings. Blue box indicates standard range for planned live cell experiments. (B) Atto488/Atto590 FRET siRNA excited at 488 nm for 2000 scans in a CLSM. Emission of donor (green) recorded at around 520 nm and of acceptor, meaning the FRET signal, at 625 nm (red). The calculated R/G value is depicted in orange on the right axis. Blue box indicates maximal scan number in microscopy observations.

Atto488/—, and 37 % in case of the acceptor, —/Atto590, for respective excitation at 488 nm or 561 nm. These 2000 scans would correspond to 33 hours of imaging of the same focal plane at 1 minute scan intervals. Within 500 scans, which represents an average experiment with up to 8 hours of observations in single scan and single plane mode, only 5-10 % intensity loss are observed.

For the FRET siRNA, i.e. Atto488/Atto590, the loss of donor and FRET signal, was similar to the donor only construct, meaning 2-4 % within 500 scans and 15-17 % within 2000 scans (see Figure 3.19 B and Table 3.9). Concerning the R/G, no change could be observed over time. In consequence the calculated R/G ratio is not affected as both dyes exhibit a similar bleaching behavior. This observation supports the suitability of the Atto488/Atto590 system for cellular observations.

In consequence, one can assume that free or released siRNA is not strongly affected by photobleaching during the planned observations times of  $\sim 500$  scans or up to 6 hours. If a diffusion of intact siRNA from unbleached regions occurred and in consequence lowered the bleaching effect, further investigations with non-diffusing samples need to be made.

**Table 3.9: Microscopy bleaching of agarose embedded and and transfected siRNA**  
[%] of initial signal

		Agarose embedded		Fixed cells	
		500 scans	2000 scans	500 scans	2000 scans
Atto488/— —/Atto590	Donor	95	81	62	32
	Acceptor	91	63	65	19
Atto488/Atto590	Donor	96	83	116	129
	FRET	98	85	86	57
	R/G	102	103	74	44

### 3.3.1.2 Excitation of siRNA in fixed cells

To further address the bleaching behavior of Atto488/Atto590 siRNA, RBE4 cells [236] were transfected with FRET siRNA using cationic lipids as transfection agent. The cells were subsequently fixed by formaldehyde treatment to prevent diffusion. Cell samples were, similar to agarose embedded samples, excited for up to 2000 times with the CLSM. Figure 3.20 A-C depicts the cellular bleaching behavior of Atto488/—, —/Atto590 and Atto488/Att590 siRNA. In all cases a decrease in intensity over time can be observed indicating a bleaching of the respective dye or FRET combination.

For Atto488/— siRNA a decrease of 38 % within 500 scans and 68 % within 200 scans can be observed (see Table 3.9 and Figure 3.20 A). This decrease is much stronger than observed in agarose embedded siRNA or in the cuvette. As indicated before, the agarose embedded samples might be influenced by diffusion effects from surrounding areas, whereas the fixed samples represent dye molecules that are covalently linked by formaldehyde cross-link to cellular macromolecules and thus remain immobile. This suggests that partial immobilization by embedding siRNA in agarose does not sufficiently describe fixed microscopy samples as used in standard microscopy analysis. The usage of fixed samples allows to analyze the behavior of siRNA that is located in a defined region, like lysosome or other cell compartment, that are not connected to a larger pool of intact fluorophores that may recover potential loss upon photobleaching. Though in live cell microscopy the fluorophores, meaning siRNA, can freely diffuse inside a cellular compartment, the scanned region is usually chosen in way that the whole cells gets excited and thus diffusion from the outside into the cell, or vice versa, can be excluded.

The approach presented here, with fixed molecules and excitation in only a small fraction of the actual scanning field, accurately represents the planned observations in live cell microscopy. Here the whole cell will be excited and thus effects from diffusion of molecules from outside the cell into the focal plane can be excluded. Regarding the results of the bleaching experiment one can state that after 2000 scans the fluorescence of Atto488 is almost lost and a detection is difficult. However, after 500 scans still 60 % of the initial signal strength can be detected, which is in the same range as the 10 hour excitation in the cuvette experiment (see Chapter 3.1.4). Therefore after 500 scans or estimated 6 hours of imaging the initial signal can still be detected.

For the acceptor only labeled siRNA, i.e. —/Atto590, a similar behavior can be observed (see Figure 3.20 B), though the overall loss in fluorescence is a slightly higher (35 % loss after 500 scans and 81 % loss after 2000 scans, see Table 3.9).

The behavior of the FRET siRNA, Atto488/Atto590, however, is different (see Figure 3.20 C). Here an initial increase of donor intensity can be observed, resulting in a 16 %



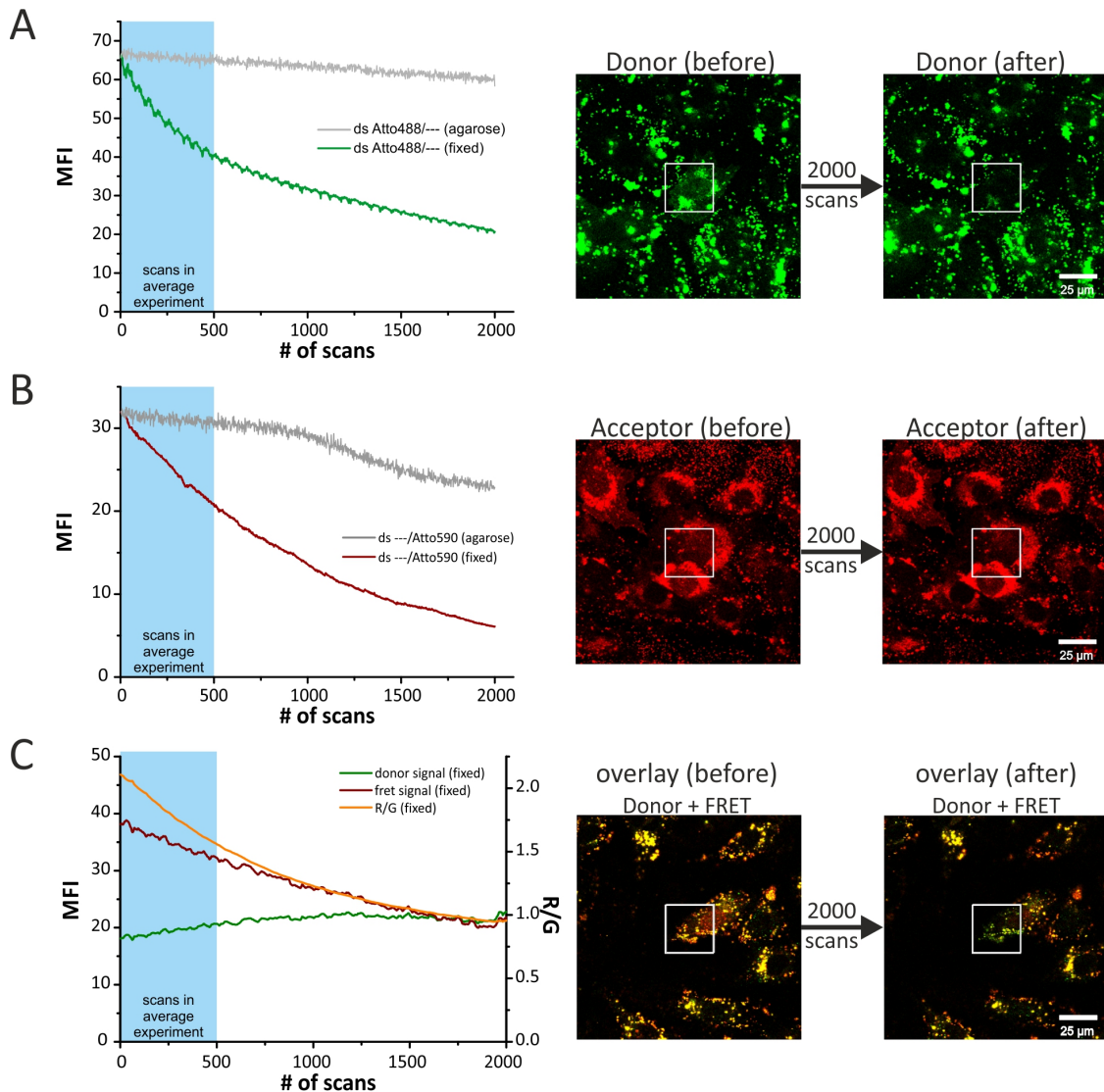


**Figure 3.20: Analysis of bleaching behavior of transfected Atto488/Atto590 siRNA.** RBE4 cells are transfected with Atto488/-, -/Atto590 and Atto488/Atto590 siRNA fixed after 11 hours of incubation. Depicted are intensity changes during scanning by CLSM (left diagram) and cell picture showing scanned area (white box) before (picture in the middle) and after 2000 scans (right pictures). (A) Atto488/- duplex at 488 nm excitation and emission around 520 nm (left diagram, green) upon excitation with CLSM. For comparison agarose embedded data is displayed in gray (normalized to fixated data). Microscopy image correspond to donor channel at 520 nm emission. (B) -/Atto590 duplex at 561 nm excitation and emission at 625 nm (left diagram, red) upon CLSM excitation. For comparison agarose embedded data is displayed in gray (normalized to fixated data). (C) Intensity changes of Atto488/Atto590 FRET siRNA over time (left). Depicted are donor emission (green), FRET signal (red) and calculated R/G ratio (orange, right axis) during 2000-fold excitation. Donor and FRET signal are depicted as overlay. Red-orange color indicates stronger FRET, whereas green-yellow pixels correspond to donor dominated signals.

gain of fluorescence after 500 scans and a final gain of 29% after 2000 scans. The trend of the recorded donor intensity suggest however a subsequent drop below the initial intensity upon extended excitation (a maximum can be observed around 1000 scans). This is comparable to the analysis of FRET siRNA in the cuvette (see Chapter 3.1.4.2) where the donor signal showed an increase upon excitation of the double labeled siRNA. But different to experiments in the cuvette the change in R/G in fixed microscopy samples is larger over time. Starting with an average R/G ratio of 2.14, which represents almost 100% intact siRNA, the R/G value drops to 1.6 after 500 scans, which corresponds to 75% of the initial value observed in the scanned region. After 2000 scans the R/G ratio drops even further to 0.95 corresponding to similarly intense donor and FRET signals. According to the simulation and calibration in the cuvette this corresponds to 97% still intact duplexes.

These results show that the changes observed are not too strong over a shorter time or few number of scans, but over longer observations times the integrity level measured might be influenced by the scan.

### **3.3.2 Verification of FRET between Atto488 and Atto590 inside fixed cells**

In order to rule out unfavorable behavior of Atto488/Atto590 siRNA inside cells control experiments with single labeled siRNA duplexes were conducted. For this purpose Atto488/— and —/Atto590 siRNA were transfected into RBE4 cells and fixed after 11 hours of incubation. Upon excitation of the donor dye at 488 nm, the emission of both, donor at 510-540 nm and acceptor at 605-635 nm, dyes was recorded (for emission bands see Appendices H.15). Additionally the acceptor signal was recorded using 561 nm excitation to confirm the presence of the acceptor dye. The signal of the acceptor dye upon donor excitation  $I_D(A)$  will in the following referred to as FRET signal, whereas acceptor emission upon acceptor excitation  $I_A(A)$  will be referred to as acceptor signal. Similarly the donor signal represents the signal around 520 nm upon excitation at 488 nm, i.e.  $I_D(D)$ .

Analysis of the single labeled siRNA did not show any bleed-through or cross-excitation in the respective detection channels (see 3.21 2<sup>nd</sup> column for bleed-through and 3<sup>rd</sup> column for cross-excitation and Table 3.10). In contrast the same analysis for FL/TMR (see Appendices I.17) showed bleed-through and cross-excitation values of 39% and 36%, respectively (see Table 3.10). These values were calculated as percentage of the donor only signal.

A closer look at the the FRET siRNA for both systems showed a stronger FRET signal for the FL/TMR construct and a lower donor signal, whereas the Atto488/Atto590

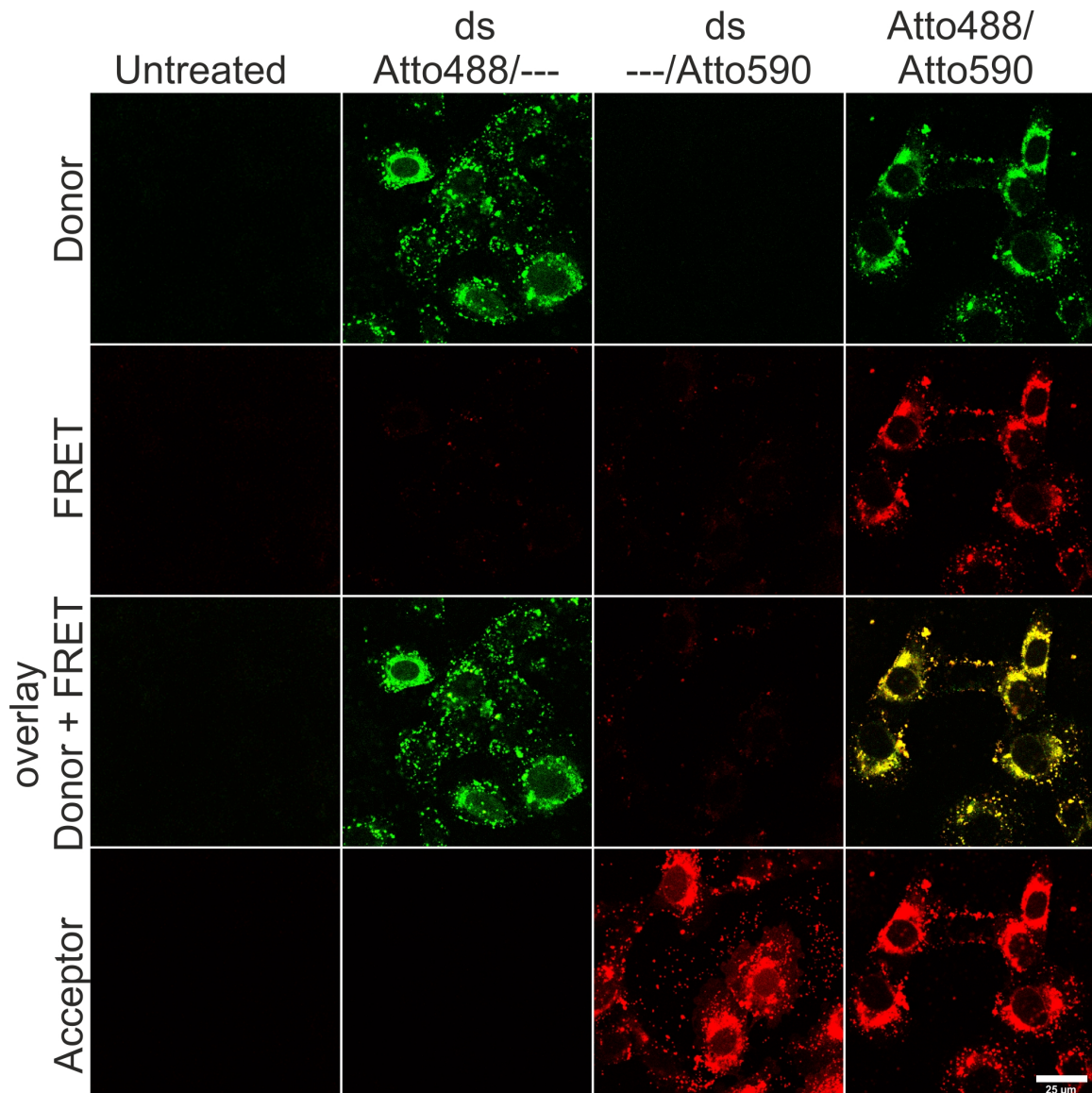


**Figure 3.21: Suitability of Atto488/Atto590 for microscopy.** RBE4 cells transfected with Atto488/— (2<sup>nd</sup> column), —/Atto590 (3<sup>rd</sup> column) and Atto488/Atto590 siRNA (4<sup>th</sup> column) to verify crosstalk and bleed-through. Untreated cells (1<sup>st</sup> column) are shown as reference. Cells were excited at 488 nm and emission recorded for donor signal at 510-540 nm (1<sup>st</sup> row) and FRET signal at 605-635 nm (2<sup>nd</sup> row). 3<sup>rd</sup> row depicts an overlay of donor and FRET signal. The last row represents the acceptor signal at 561 nm excitation and emission at 605-635 nm.

	background corrected MFI signal [%] of			background corrected MFI signal [%] of		
	Atto488/—	—/Atto590	Atto488/Atto590	FL/—	—/TMR	FL/TMR
Donor-channel †	100	1	58	100	13	16
FRET-channel †	0	0	59	39	36	78
Acceptor signal ‡	—	100 of —/Atto590 signal	91	—	100 of —/TMR signal	97

† normalized to donor only signal; ‡ normalized to acceptor signal

donor and FRET signals were almost the same (see Table 3.10 and Figure 3.21 4<sup>th</sup> column and Appendices I.17). With regard to the strong crosstalk detected, the FRET signal of FL/TMR is strongly influenced by bleed-through and cross-excitation of donor and acceptor, respectively. For control purpose the acceptor signal for both dyes was compared with the single labeled duplex. In both cases the acceptor signals show similar intensities, meaning approximately same concentration of acceptor dyes in the respective area.

Consequently detected FRET signals of the Atto488/Atto590 siRNA are actual real FRET signals that are not biased by crosstalk, whereas in case of FL/TMR detected FRET signals are influenced by crosstalk.

### 3.3.3 Principles of R/G ratio algorithm

The R/G ratio algorithm was kindly provided by the group of ██████████, Department of Biomedical Computer Vision of the German Cancer Research Center (DKFZ) in Heidelberg, and was programmed by ██████████ [2–4] in cooperation with the Helm group. In the beginning the algorithm was established with the help of ██████████ [227] and further optimized in the previous master thesis [224] (both members of the Helm lab). The algorithm was tailored towards the double labeled FL/TMR siRNA construct and the detailed principle is described in Appendices H.16. A more intuitive representation of the algorithm is depicted in Figure 3.22 B.

In principle the algorithm uses the green (donor signal) and red (FRET signal) channel of the microscopy analysis of FRET siRNA transfected cells. In order to prevent saturation, which would lead to inaccurate R/G ratios, fixed cells are imaged at at least three different PMT-Gains, i.e. 830 V, 750 V and 600 V (an additional gain of 500 V might be also included). On basis of the highest donor and FRET intensity image the R/G ratio is calculated for each pixel according to (Eq. 3.2).

$$R/G = \frac{I_{red} - BG_{red}}{I_{green} - BG_{green}} \quad (\text{Eq. 3.2})$$

The R/G calculation starts with the highest intensity of the donor/FRET image pair. In case of saturation the next lower intensity pair is used to calculate the R/G ratio (see Figure 3.22 A), thus the effect that saturated pixel return wrong R/G values is prevented. For example an R/G of 1 would result from two saturated red and green values as both are assigned the maximum intensity. By using the next lower intensity image pair the saturation effect can be circumvented. The resulting ratio image is colored with a lookup table (LUT) that assigns pixels below the minimum R/G value ( $rg_{\min}$ ) a green and above the maximum R/G value ( $RG_{\max}$ ) red color. R/G ratios between the minimum and

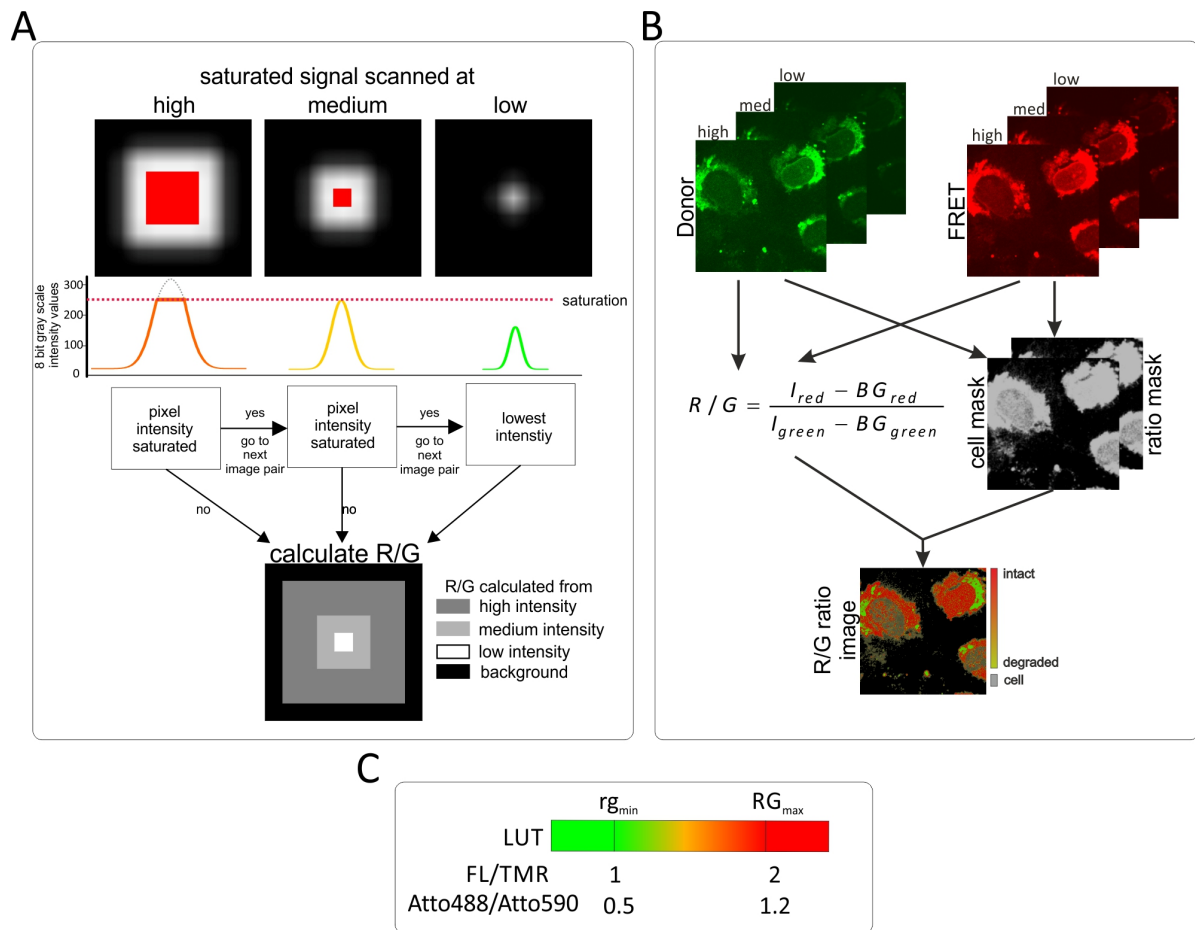


**Figure 3.22:** (A) top: Cartoon of saturated signal (red color indicates saturation,  $I < 255$ ) scanned at three different gains (high, medium, low). Intensities of a point signal are represented by Gaussian intensity distributions (orange, yellow, green), based on a theoretical Gaussian PSF. On reaching the saturation level, the top of signal is cut off and set to 255 (middle part). If saturated pixels are recorded the corresponding values of the next lower intensity pair is used for R/G calculation. The R/G ratio image may consists of R/G ratios calculated from each intensity acquired (white, light gray, dark gray in lower R/G image). (B) R/G algorithm in fixed cells. Donor and FRET signals are acquired at at least three different intensities, i.e. high, medium and low (upper part). Based on both signals the R/G ratio is calculated using a background correction (middle left). Additionally a ratio mask and cell mask is calculated on the basis of the fluorescence of the donor and FRET channel (middle right). In a final visualization step the R/G ratio image is created with green pixels representing degraded and red pixels intact siRNA populations. Besides siRNA populations, cell regions with low fluorescence are colored gray (lower part). (C) Color coding of integrity representation in R/G ratio image.

maximum range are assigned a transition from green to red color (see Figure 3.22 C). Additionally two different masks are calculated that are used for the final representation of the R/G ratio image, which is the ratio mask and the cell mask. R/G ratio and mask images are then used to visualize the R/G ratio image in which green pixels ( $R/G < rg_{min}$ ) represent degraded and red pixels ( $R/G > RG_{max}$ ) still intact siRNA (see Figure 3.22 B+C). A more detailed description of the algorithm can be found in the method section (see Methods 5.3.15).

With the basic algorithm an adaptation of the original settings for FL/TMR processing was made. Manually chosen threshold values, allowed the analysis of experiments with very weak intensities, too (see Table 3.11 set1). Nevertheless, the automatic thresholding was used as the default setting for FL/TMR analysis (set2 in Table 3.11).

Table 3.11: R/G algorithm settings

	FL/TMR		Atto488/Atto590			
	set1	set2	setA	setB	setC	setD
threshold mode	auto	manual	auto	manual	auto	manual
$rg_{\min}$	1	1	0.5	0.5	0.9	0.9
$RG_{\max}$	2	2	1.2	1.2	1.7	1.7
manualRatioMaskThreshold	N/A	150	N/A	90	N/A	90
manualCellMaskThresholdRed	N/A	75	N/A	50	N/A	50
manualCellMaskThresholdGreen	N/A	75	N/A	50	N/A	50

N/A: not applicable

For the new Atto488/Atto590 construct different settings were used. For microscopy analysis, the overall R/G ratio in observed cells was slightly lower so that the  $rg_{\min}$  and  $RG_{\max}$  were adjusted to 0.9 and 1.7 (setC and setD). Adaptation to new technical equipment required additional adaptation of the parameter (see Table 3.11 setA as default and setB for weaker signals).

This initial setting was later dismissed to obtain a better visualization by using sets with  $rg_{\min}$  and  $RG_{\max}$  of 0.5 and 1.2. setA and setB refer to R/G algorithm settings used for live-imaging (see R/G adaptation for live cell imaging in Chapter 3.4) with enhanced visualization. The changes in the R/G borders for visualization does not interfere with the calculation itself, but facilitates fast interpretation of the data.

### 3.3.4 Integrity simulation inside cells

Similar as in the cuvette, Atto488/Atto590 siRNA was transfected at different integrity states into RBE4 cells. Integrity levels ranging from 100% to 0% were simulated as earlier described (see Section 3.2.2 Figure 3.12). After transfection and fixation cells were imaged either on a Leica TCP SP5 equipped with a 405 nm laser or on a Leica STED CW with incubation unit and Adaptive Focus Control (AFC) but no 405 nm laser. The latter is the microscope of choice for live cell imaging due to the possibility of imaging under cell culture conditions.

For the fixed samples, three different PMT gains of 830 V, 700 V and 600 V were scanned. Donor and FRET channels were further processed with the R/G ratio algorithm using setB. Figure 3.23 depicts the acquired and R/G processed data (see Appendices I.18 for detailed data with acceptor control).

#### 3.3.4.1 Inspection of image data

In all samples, except the untreated controls, a measurable donor signal can be detected, indicating the presence of Atto488 labeled siRNA. Additionally the acceptor signal of Atto590 can be detected in all samples (see Appendices I.18) which shows a constant level of acceptor dye present in all samples. The signal of Atto488 increases from the completely intact sample towards the complete degraded sample, giving the first hint of



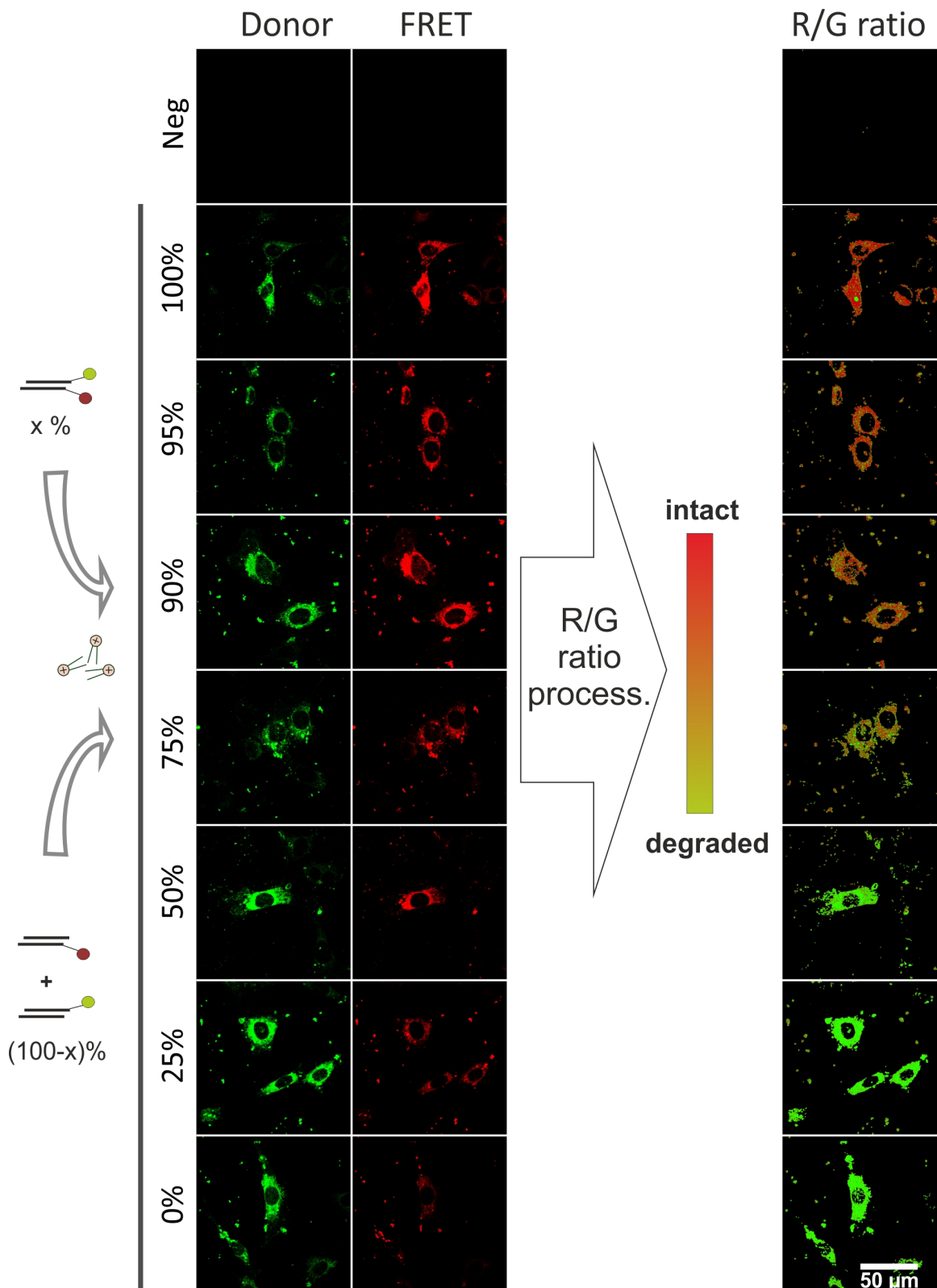


**Figure 3.23: Integrity simulation and R/G processing inside fixed cells with Atto488/Atto590.** Depicted are the donor (first column) and FRET (second column) signal of RBE4 cells transfected with samples referring to different siRNA integrity states of Atto488/Atto590 siRNA. Different integrity levels of siRNA are obtained by mixing different amounts of single labeled duplexes (simulating degraded siRNA) and double labeled (referring to intact siRNA) duplexes (see scheme on the left). On the right (third column) the R/G ratio image is depicted with red pixels refer to intact siRNA and green to degraded siRNA. R/G processing was performed with setA.

reduced FRET and thus disruption of the siRNA integrity. Additionally the FRET signal shows maximum intensity in the 100 % to 90 % samples. As expected from the cuvette this represents samples that result in a high FRET with approximately similar donor and FRET intensities. At the low integrity samples, the FRET signal diminishes indicating the spatial distance of donor and FRET dye.

The R/G ratio image depicts this loss in integrity or rather the spacial separation of donor and acceptor dye. While at the 100 % intact sample almost all detectable signals refer to intact siRNA, meaning R/G ratio over 1.2, the samples that represent partly degraded siRNA population show more and more dark-green or orange-brown pixels that indicate the drop in R/G value. At around 75 % of simulated intact siRNA the R/G analysis results in almost exclusively R/G values below 0.5, which is represented by bright green color. The lowest integrity levels, i.e. 50 % and less intact siRNA, are classified in very bright green based on values below 0.5.

The presented data is based on transfection and subsequent fixation of the samples after 4 h of incubation. In consequence the transfected siRNA could already have faced degradation processes by RNases. Nevertheless, the data clearly shows that the simulated integrity states can be detected after transfection by different R/G distribution.

It needs to be mentioned, that the decrease of integrity in a population of siRNA leads to a superposition of the lower donor emission of an intact duplex by the high donor emission of degraded siRNA. With respect to the poor crosstalk of Atto488/Atto590 (see Figure 3.21) the relative high FRET signal in the 0 % sample might indicate a rehybridization of the single labeled siRNA duplexes. Otherwise this strong signal would not be plausible.

### **3.3.4.2 R/G value analysis**

Based on the R/G ratio analysis of the simulated integrity samples an R/G distribution analysis in the R/G ratio image was performed. The distribution of R/G ratio values can be seen in Figure 3.24. Here one can nicely see the shift of intact classified pixels in the 100 % sample to degraded pixels in the 0 % sample. Looking at the distribution the chosen minimal and maximal R/G values for visualization seem to be justified, as the mean, modal and median R/G value for the 100 % sample are all above 1.2 (see Table 3.12). With increasing amount of separated siRNA these values shift first to an intermediate range between 0.5 and 1.2 (for 95 % to 75 %) and for samples with more than 50 % degraded siRNA the values drop into the degraded state. All analyzed histograms can be classified as positive skewed distribution as mean > median > modal, meaning a sharp increase from R/G of 0 to the maximum and soft decline to larger R/G values. This also shows that each distribution contains pixels with higher R/G values



and thus maybe indicate an accumulation of intact duplexes at distinct locations inside the cells. These region might be either lysosomes or the mRNA processing foci, called P-bodies [237].

Additionally the overall analysis shows that in the 100 % sample around 72 % of the positive classified pixels represent siRNA populations with a FRET signal at least as high as the donor signal. This fraction, as already mentioned, refers to area in the cell with almost completely intact siRNA populations. Again this higher fraction of intact

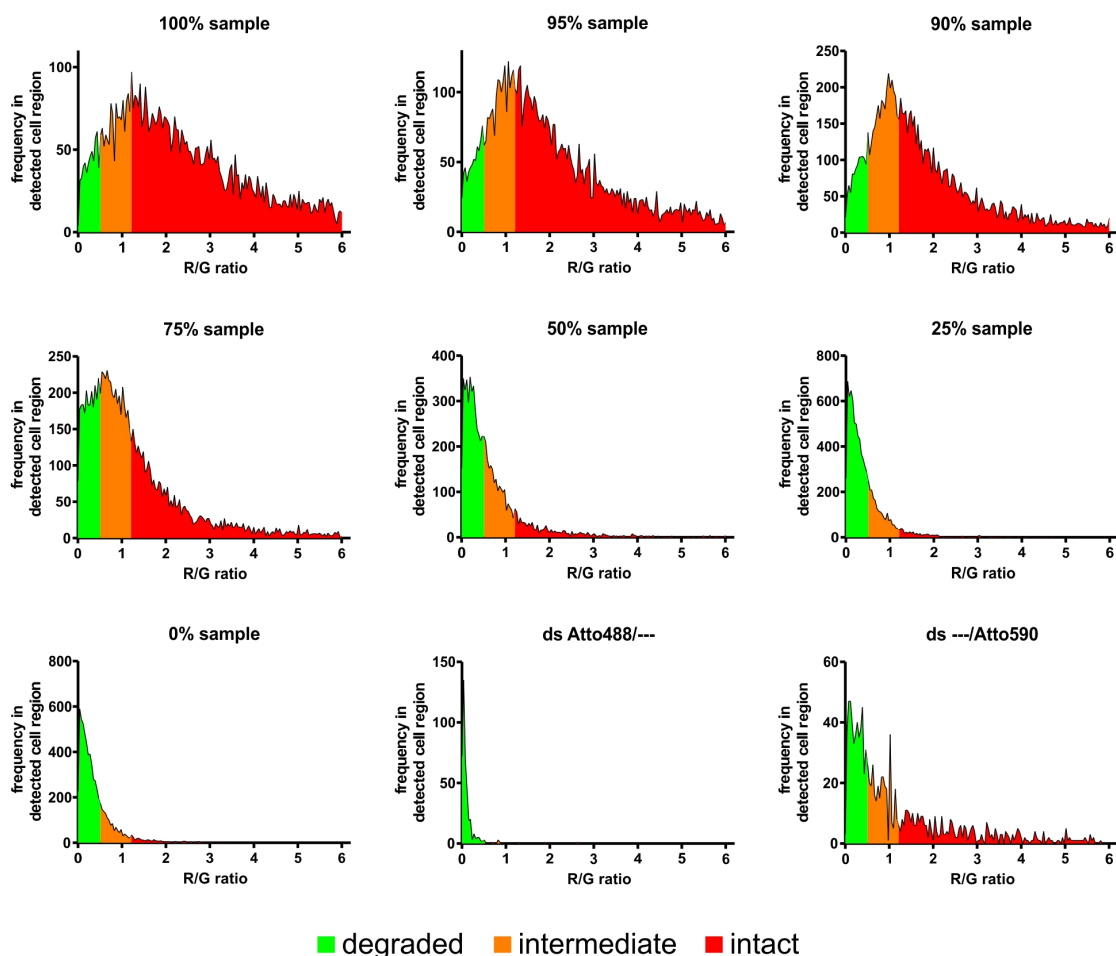


**Figure 3.24: R/G distribution in fixed cells.** R/G value distribution in integrity simulation data of Atto488/Atto590 in fixed cells. For each sample referring to 100 %, 95 %, 90 %, 75 %, 50 %, 25 % and 0 % intact siRNA and single donor and acceptor only samples the R/G distribution was determined on the basis of R/G ratio processing. In each histogram the green area refers to R/G values below 0.5, the red area to R/G values above 1.2 and the orange to intermediate R/G values.

**Table 3.12: R/G frequency of simulated siRNA samples**

	simulated integrity level of Atto488/Atto590 siRNA						
	100 %	95 %	90 %	75 %	50 %	25 %	0 %
intact [%]	72	65	58	37	13	6	6
intermediate [%]	19	25	30	36	29	21	19
degraded [%]	9	10	12	27	57	72	76
modal R/G	1.2	1.1	1.0	0.7	0.2	0.1	0.1
mean R/G	2.3	2.0	1.8	1.3	0.7	0.5	0.4
median R/G	2.0	1.6	1.4	0.9	0.4	0.3	0.2

classified pixels can be found in all samples with at least 75 % intact siRNA.

Having a closer look at the single labeled siRNA controls, one can see in case of the Atto590 only construct, that in absence of the donor high R/G ratios are calculated also. It is important to keep in mind that with the automated thresholding in absence of a donor signal the threshold is lowered and thus autofluorescence or the little cross-excitation present (see Figure 3.21) results in higher R/G values and thus mimics intact populations of siRNA. The fraction of false classified pixels is nevertheless very small and almost not visible in the R/G ratio image (see Appendices I.18).

Nevertheless, the analysis presented here shows that it is possible to transfer the cuvette data to cell experiments. During the incubation of transfected siRNA and uptake a fraction of siRNA might be degraded by cellular nucleases and thus resulting in lower R/G ratios. But still, even if the applied siRNA might be degraded by RNases the fixed cell analysis still shows a large proportion of intact duplexes in the complete 100 % siRNA samples. This indicates that the siRNA is protected by cationic lipids used for transfection until a release of those lipoplexes occurs inside a cell.

An alternative method to analyzed the integrity state of the simulated samples inside a cell is probably the use of microinjection followed by an immediate fixation, as performed by Jarve et al. [2]. What cannot be eliminated but reduced, is the possibility of degradation of the microinjected samples by nucleases inside the cytoplasm. From the cuvette studies one knows that degradation can be really fast and thus even with microinjection degradation might occur within minutes until image acquisition is performed. In consequence the method used to verify siRNA integrity inside cells seem suitable and the results indicate, that at least intact siRNA is present in the cells analyzed.

### **3.3.5 Investigation of siRNA integrity over time in fixed cells transfected with FL/TMR**

Before the idea of an photostable alternative to FL/TMR was considered, first extensive cell tests with the published FRET pair were performed.

#### **3.3.5.1 First indications of changings in localization**

One of the first experiments with FRET siRNA was the analysis of different incubation times after transfection with cationic lipids into RBE4 cells. The idea was to analyze whether there were changes in localization of the siRNA over time. In the preceding master thesis [224] the first approach to address the question of the whereabouts of administered siRNA to cells was made by incubating cells up to 2 days before fixations. The extended observations up to 10 days can be seen in Figure 3.25. Also a longer

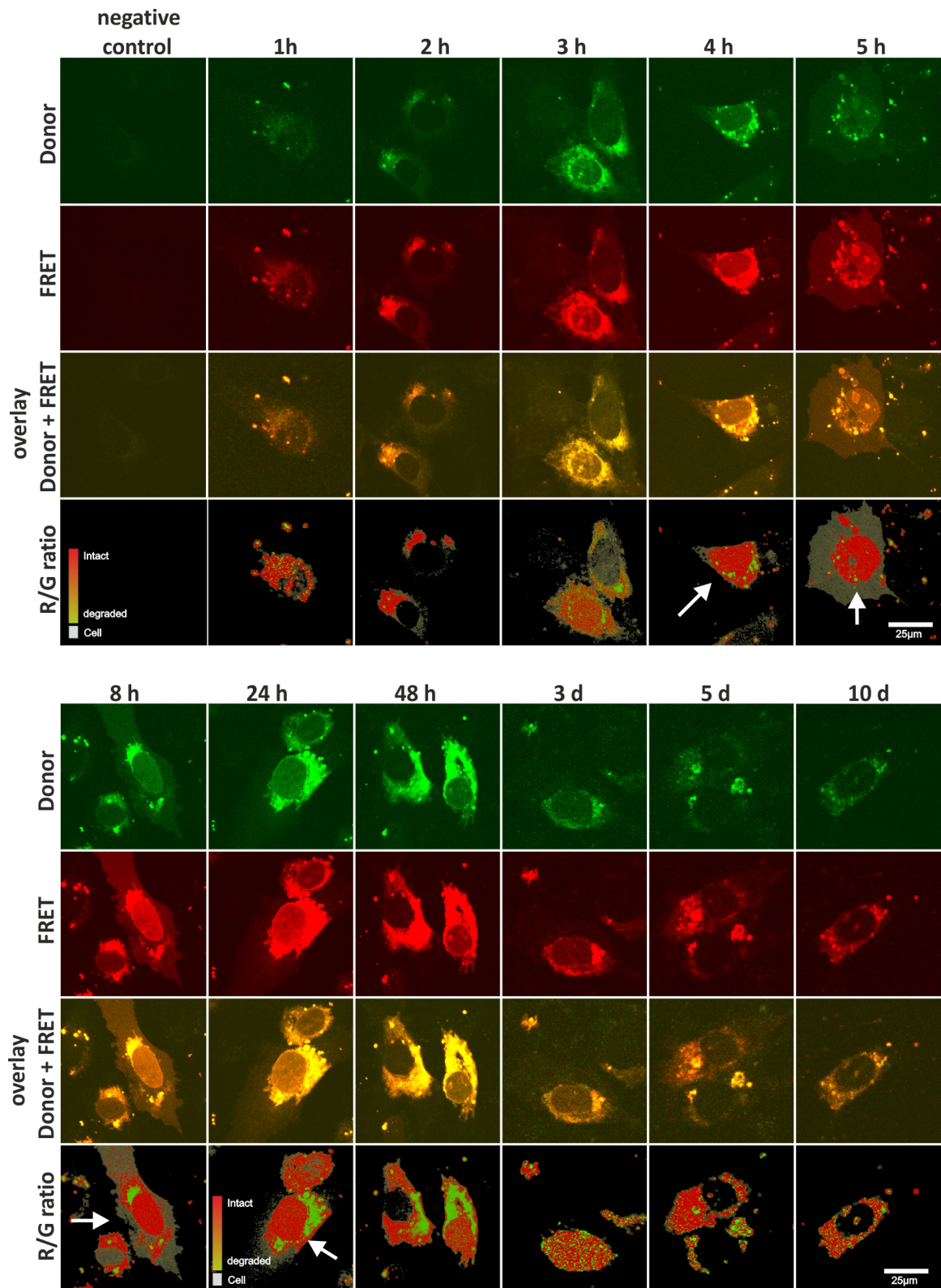


**Figure 3.25: RBE4 cells transfected with FL/TMR siRNA incubated for different periods after transfection.** Cells are incubated for 1 h, 2 h, 3 h, 4 h, 5 h, 8 h, 24 h, 48 h, 3 d, 5 d and 10 d after transfection before fixation. The donor emission of FL (row 1 and 5), FRET emission of TMR (row 2 and 6), the overlay of donor and FRET signal (row 3 and 7) and the R/G ratio image using set1 (row 4 and 8) are depicted for a representative sample of each incubation time. White arrows indicate intact siRNA population inside the nucleus. (parts of the data are part of the preceding master thesis [224])

incubation up to 15 days was tested but unfortunately only background signals could be detected (data not shown).

The observation that can be made is that labeled siRNA accumulates over time inside the cell. Already after 1 hour of incubation larger areas of fluorescence can be seen indicating the beginning uptake process. Cells that are incubated longer show an increase in overall fluorescence with a maximum at around 24 h of incubation. Longer incubation times, i.e. 2 days and more, lead to a decrease of detectable fluorescence. Additionally, due to cell growth the longer incubation times show higher cell densities which leads to compression of the cells and even the formation of different growing layers. This condensation, cell division and growing in multilayers leads to a dilution of the transfected siRNA.

Nevertheless, it was possible to detect cells that show fluorescence even after 10 days of growth after the initial transfection. Of course the question arises, whether this fluorescence is just the cleaved label, i.e. FL or TMR in the presented data, or if still intact siRNA is present. The first can be ruled out as the R/G analysis shows only red pixels, which is according to set1 for FL/TMR referred to an R/G over 2. One might now argue that, due to the unfavorable crosstalk of FL and TMR the R/G classification might be biased by cross-excited TMR emission. This argument can be diminished by having a closer look at the donor signal, i.e. FL channel, that also shows a high signal for all scanned pixels. This means, that at least FL and TMR are similar distributed inside the cell, without TMR dominated regions, which would be visible by red areas in the overlay image (row three and seven in Figure 3.25).

The analysis of the R/G ratio image also shows, that over the whole period monitored intact siRNA is present in the depicted cells. It can also be seen, that starting at 3 h larger pixel areas begin to be classified in the intermediate state indicating strand separation or degradation. A stronger degradation can be seen at around 24 and 48 hours in the area around the nucleus, the perinuclear region [86]. Later Stalder et al. [155] reported the rough endoplasmic reticulum as a nucleation site of siRNA-mediated RNAi. In some cells incubated longer than 3 days the most common color is red, meaning R/G ratios still higher than 2 and thus intact siRNA. It is to mention that after longer incubation, the siRNA signal is diluted so that most cells did not show any fluorescence at all.

An additional interesting observation was the presence of intact siRNA inside the nucleus, which can especially be seen at 4 h, 5 h, 8 h and 24 h. At these time points the siRNA mainly seems to be localized inside the nucleus and the surrounding perinuclear region.

A nuclear localization of siRNA was first reported by Ohrt et al. [175], Guang et al. [238] who could observe labeled siRNA inside the nucleus and nucleolar regions after microinjection. Later Ohrt et al. [239] also demonstrated that siRNA with nuclear target,

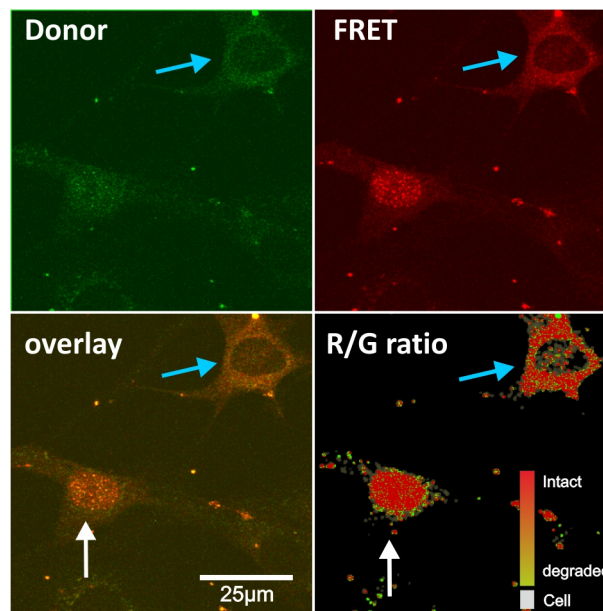


**Figure 3.26: Nuclear accumulation of FL/TMR siRNA.** Observation of nuclear accumulation of FL/TMR after transfection in fixed cells. RBE4 cells after transfection showing siRNA accumulation mainly in the cytoplasm (light blue arrow) or in the nucleus (white arrows). Nuclear siRNA shows accumulation in small distinct foci. R/G processing was performed using set1.

like small nuclear RNA, accumulates due to a process of shuttling of the loaded RISC into the nucleus and a retention due to target recognition.

One special observation in this context was the presence of small aggregation sites inside the nucleus. This observation however could not be assigned to a distinct incubation time and was only observed randomly (as an example see Figure 3.26 white arrow). These nuclear accumulations in distinct foci may be referred to nuclear speckles [240] or Cajal bodies [241], which are known to be involved in RNA processing, or other nuclear accumulation sites meaning nuclear bodies [242–244]. The example also shows the two different distribution states observed, one with mainly fluorescence in the cytoplasm and one mainly in the nucleus. It has to be mentioned, that in these nuclear sites the siRNA still remains intact, as high FRET signal can be detected.

Another possibility which so far was not investigated is whether siRNA, that gets released into the cytoplasm, somehow undergoes a maturation process during which the siRNA is imported into the nucleus, which would correspond to the shuttling reported by Ohrt et al. [239], and subsequent release into the cytoplasm by an active export that might involve Exportin-5 [175].

Based on these observations several theories emerged, like the one that transfection stress triggers the uptake of cytoplasmic siRNA into the nucleus. Attempts to analyze re-transfection in fixed cells did not succeed so far and a switch to live cell imaging is necessary to validate these hypotheses. One approach might be the transfection of different labeled siRNA populations at a different time point to address the distribution behavior. The attempt of these investigations are addressed in Chapter 3.4.

Another question that arises, concerning the detection of intact siRNA after 10 days, is the duration of its activity meaning RNAi based gene silencing. In cell culture experiments knockdown durations based on siRNA have been reported ranging up to 2-4 weeks [11, 245–249] which indicates the need of intact siRNA in some kind of cellular reservoir for later activity or release. It is also unclear, whether siRNA once released is active over the whole period or if there are multiple releases inside the cytoplasm, each resulting in active RISC that in sum result in permanent knockdown up to the reported 4 weeks.

An elongation of the observation time to intervals longer than 10 day did not succeed. RBE4 cells show division cycles of about 24 h and confluency is reached within one week of incubation. With a lower cell density at the time of transfection one gains 1-3 days but at longer incubation periods the cells start to grow in multilayers and due to high number of cell divisions fluorescent cells are diminished in the culture. Maybe labeled siRNA is not only thinned out by division but also causes reduced division rates in transfected cell compared to healthy cells. An approach of using slow-dividing cell lines (like a melanoma cell line from a collaboration partner, Prof. Jonuleit University medical center in Mainz) did not show the desired effect of prolonged observation times as the difference in division rate was not so high as expected.

In another approach it was attempted to cultivate transfected cells for longer times by passaging them after the transfection to keep the cell density at a moderate level. However, passaged cells did not show any fluorescence which again indicates that untransfected cells show an advantage over cells with high levels of labeled siRNA. Whether this is due to the transfection process itself or due to the presence of fluorophores is not clear.

This might raise the question of toxicity of the dyes used. So far, no study of cell compatibility with the chosen FRET dyes was made and at least for up to some days of cultivation no toxic effects could be observed in standard cell culture.

### **3.3.5.2 Large-scale analysis of fixed cells**

On the basis of the observations made by investigating different incubation times after transfection an extended analysis was performed. For this purpose new transfections with FL/TMR were made and this time more image data of each transfection experiment acquired. This lead to at least 30 different scanning regions for each cover slip and incubation time. The scanning points were equally distributed over the whole cover slip containing cells with fluorescence. It was also attempted to avoid a biased selection of cells that show a special type of siRNA distribution.

After collection of the data, cells were manually analyzed and nucleus, cell outline and the perinuclear region were marked. Up to 4 cells were selected resulting on average in



more than 50 analyzed cells per incubation time. In case of the RBE4 cell this selection can be done by visual inspection of the cells, as they present a clearly visible nucleus without the usage of a counterstain like DAPI or another nuclear stain.

The perinuclear region, which was reported as the area surrounding the nucleus by Detzer et al. [86], was also manually selected. This area was previously reported to be the localization site of phosphorothioate stimulated uptake of siRNA via the caveosome [86]. The perinuclear region represents the highly structured area around the nucleus, mainly consisting of ER and parts of the Golgi network. Again a manual selection was possible, as in case of RBE4 cells this area showed a highly structured and contrast rich appearance in the transmission channel of each acquired image. For a more detailed description how the different regions were selected see Chapter 3.4.1.4.

After highlighting the different regions, the mean fluorescence intensity (MFI) of each region of interest (ROI) was extracted using the *measurement function* in ImageJ [250] and MFI values for the perinuclear & cytoplasm, nucleus, perinuclear, cytoplasm and nucleus & perinuclear ROI were calculated (for details in processing of the data see Methods 5.3.16.1). This was done for the donor, FRET, acceptor and merged overlay (donor + FRET), here named RGB, image. An attempt to analyze the data was made by first separately analyzing each incubation time. Therefore a box-whisker-plot was created that allows to compare the different distributions in each cell region by using the overlay data (RGB). The overlay data was used since this set of data combines the overall fluorescence that is recorded upon 488 nm excitation. As an example Figure 3.27 A depicts the data for the control and 2 h, 4 h, 8 h and 24 h of incubation. A complete set of data referring to the RGB MFI values can be seen Appendices I.19. The data did not reveal a change in localizations over time. In fact in all analyzed time points the same distribution pattern between the different regions can be found. This means the highest fluorescence is being detected in the perinuclear region, whereas the nucleus shows only slightly higher average intensity than the complete cell (data normalized to total cell fluorescence, which was set to 1).

For better comparison the whole experimental data was plotted in an MFI over incubation time plot as depicted in Figure 3.27 B. On the left the averaged and normalized fluorescence in all analyzed nuclei and the extranuclear region (meaning the cytoplasm and perinuclear ROI) is shown. The data suggests that over the complete time the average fluorescence inside the nucleus (meaning the mean fluorescence intensity in the selected region per pixel) is higher than in the extranuclear region. As the fluorescence surrounding the nucleus is very high in most cases this result can be explained by the fact that this high fluorescence is masked by averaging over the complete cell. Thus a selective approach with distinguishing between nuclear, perinuclear and the remaining rest (here named cytoplasm) was conducted (see Figure

3.27B right). In this case one again can clearly see the overall high fluorescence intensities in the perinuclear region and a lower signal inside the nucleus, but still a higher signal than the complete cell. Finally inside the remaining cytoplasm the intensity is lower than the complete cells. The data shows again the same behavior for all analyzed time points.

As a third possible representation an MFI vs. ROI plot was chosen, with line graphs for each incubation time. The data is depicted in Figure 3.27C. Here one can clearly see the same distribution behavior for all analyzed states.

Common to all analysis approaches is the big variation inside each population of analyzed cells at each incubation time. This is especially true for the perinuclear and nuclear region, and is observed in the donor, FRET, acceptor and merged signal (see Appendices I.21 and I.20). A clear localization of siRNA inside the nucleus can be claimed without regard to the incubation time. This nuclear presence confirms earlier reports of several groups [2, 175, 238, 239]. What could not be verified is a time related presence of siRNA inside the nucleus and a later localization outside the nucleus meaning extranuclear.

Important to mention again are the large variations in each representation. Maybe a more sophisticated statistical analysis in which the relationship between the respective ROIs for each cell is included might result in more insight in the distribution behavior (including multidimensional principle component analysis). However, this single cell analysis was not possible so far and it is questionable whether more information can be obtained by analyzing the fixed cell data. This conclusion is supported by ongoing experiments in living cells that indicate a release behavior independent from the incubation time (see Chapter 3.4).

Another special observation has to be mentioned, which is the comparison of donor, FRET, RGB and acceptor data. In Appendices I.21 one can observe an overall higher donor fluorescence in the extranuclear region compared to the other signals. This might lead to the conclusion that the donor dye, meaning the sense siRNA strand or free dye, is favorably localized in the cytoplasm after duplex disintegration.

Summarizing, the analysis shows all different kinds of distribution patterns in the single cells for each timepoint, which does not result in any trend when averaging the complete population of recorded cells. An additional R/G analysis was not performed due to increasing complexity and already mentioned switching to live cell analysis for further information.



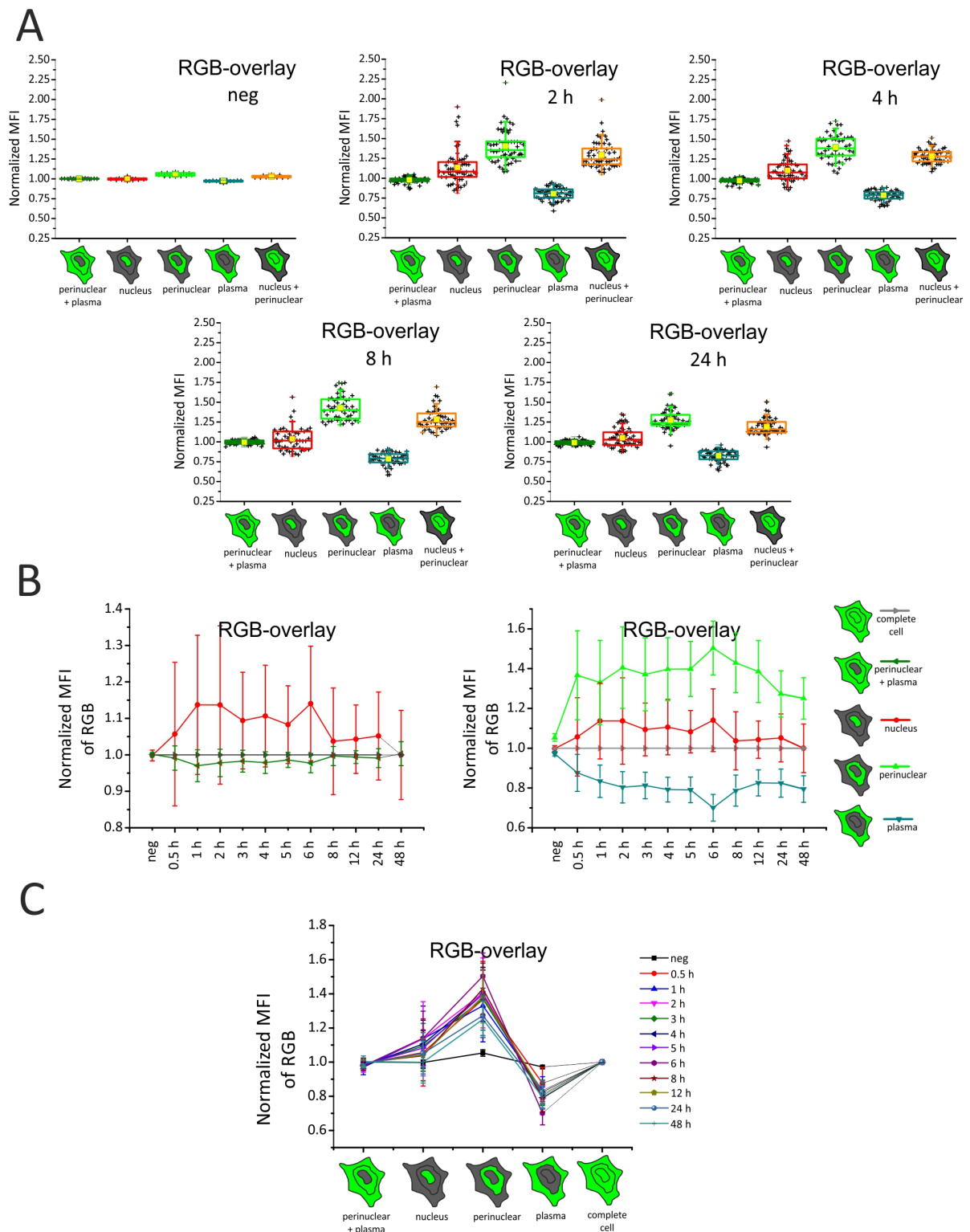


**Figure 3.27: In-detail analysis of FL/TMR transfected cells.** RBE4 cells transfected with FL/TMR and incubated for different time points before fixation, were manually segmented into nucleus, perinuclear, perinuclear&cytoplasm, cytoplasm and perinuclear&nucleus. For each ROI of an cell the MFI value was determined and normalized to the overall cell fluorescent. In average each data set contains at least 50 analyzed cells from around 30 different scanning areas. (A) Box whisker analysis for control, 2, 4 h, 8 h and 24 h incubation after transfection. Box represent upper and lower quartile, the line inside the box the median value and the whiskers the standard deviation. In yellow the mean value is depicted and in black all measured data points. (B) Normalized MFI values compared over time, ranging from 0.5 h to 48 h. Depicted are nuclear ROI (red) and extranuclear (dark green) ROI (left diagram). Right diagram shows nuclear (red), perinuclear (light green) and cytoplasm (blue-gray) ROI. (C) Normalized MFI values in different cellular ROIs. Each graph represents one incubation time.

## 3.4 Observation of siRNA and integrity measurements in living cells

The analysis of fixed cells lacks one major aspect: the possibility of analyzing the actual release event of labeled siRNA into the cell. Due to fixation only an endpoint analysis can be performed which seems not to be adequate for the investigation of the whereabouts of siRNA inside cells. The experimental results (see section 3.3.5) shows a non-synchronized behavior of the analyzed fixed cells. This means each cell shows uptake and release at different stages resulting in an inhomogeneous population of cells. To address this asynchronous behavior live cell imaging might give a hint to the uptake and cellular release of exogenous siRNA applied by transfection with classical cationic lipids. The usage of classical transfection agents will help to establish a system which can later be used to test a group of different delivery systems. (see Section 3.2.5).

### 3.4.1 Cellular costaining of organelles

To further evaluate the behavior of internalized siRNA and the cellular localization a simultaneous costaining is indispensable. Observations of fixed cells indicate the localization of siRNA to the nucleus and the perinuclear region, which is composed of endoplasmic reticulum and parts of the cis-Golgi network Detzer et al. [86]. Additionally the endocytotic pathway, which involves endosomes, phagosomes or caveosomes are the first organelles to face siRNA containing lipoplexes during the uptake process [251–253]. Eventually, complexes end up in the lysosome, where the delivered material is either decomposed or a final release can occur. Whether a release occurs from the late endosome or the transition to the decomposing lysosome is not clear yet.

#### 3.4.1.1 Lysosomes and nucleus

To address the uptake mechanism a lysosomal staining with LysoTracker Blue, Green or Red was considered. Since no laser for the excitation of the blue dye was available on the Leica STED microscope only the red and green variant were used.

As an alternative a microscope without incubation unit can be used for short-term imaging. The evaluation of the blue stain on a microscope without incubation unit showed only weak staining potential upon excitation at 405 nm, i.e. by the violet laser. Figure 3.28 A+B depict living RBE4 cells that are stained with the green and red LysoTracker variant. In both cases one can see the dots of lysosomal staining in the cytoplasm. It is also visible that the green variant shows a stronger background in the entire cells, which makes it difficult to detect signals correctly.

In addition to lysosomes, the nucleus is of interest in presented work. Therefore ,

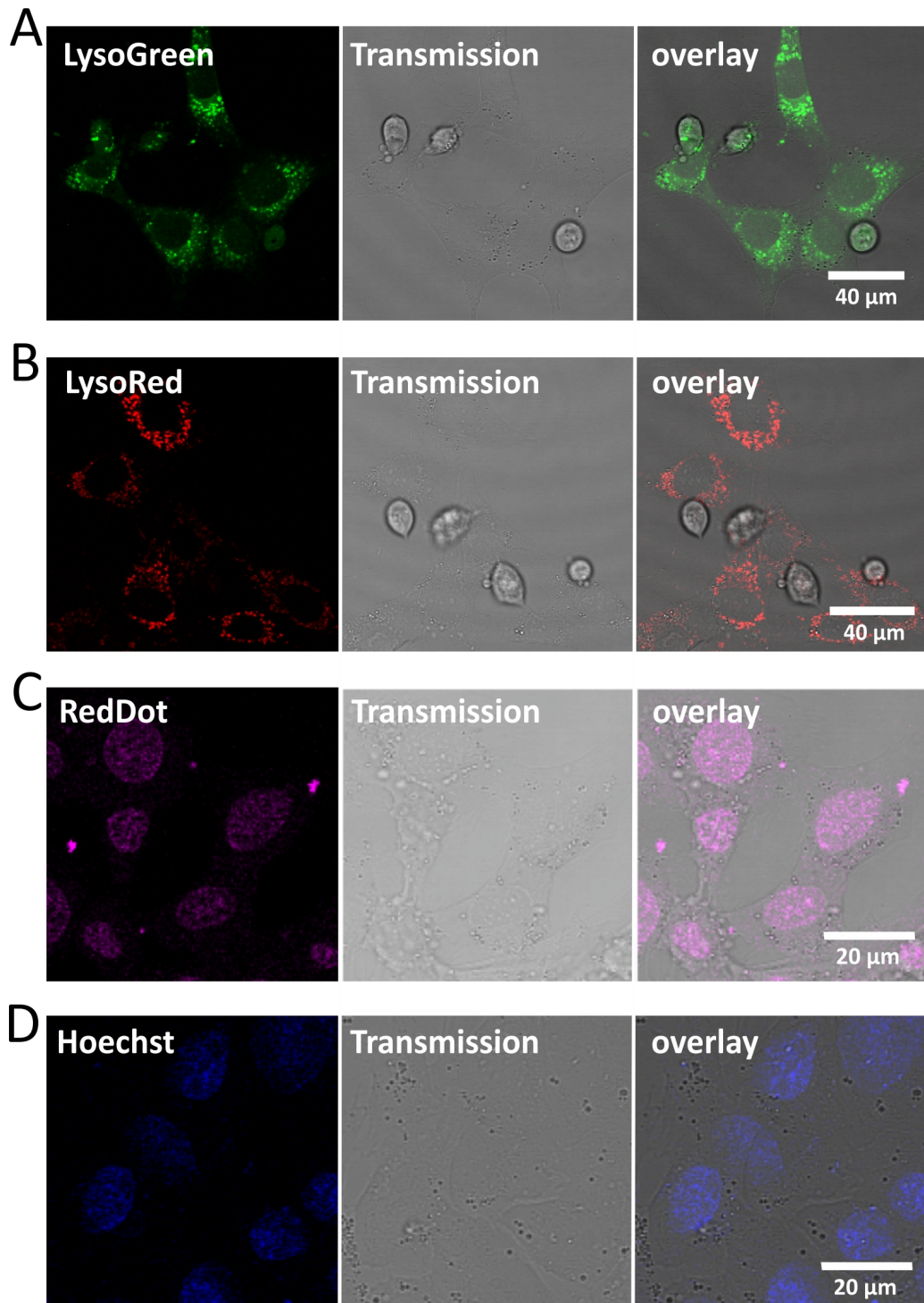


**Figure 3.28: RBE4 cells stained for different organelles.** Lysosomal staining by LysoTracker Green at 488 nm excitation (A) and LysoTracker Red at 561 nm excitation (B). C and D depict nuclear staining by either RedDot™<sub>1</sub> (excitation at 633 nm) or Hoechst 33258 (excitation at 405 nm).

the classical nuclear stain, Hoechst 33258, and the new live cell compatible far-red dye RedDot<sup>TM</sup> 1 were used. DAPI or Hoechst dyes are not suitable for the live cell experiments as the microscopy setup allows no excitation at 405 nm. The switch to a far-red nuclear dye, e.g. RedDot<sup>TM</sup> 1, is a necessity for simultaneous Atto488/Atto590 and nuclear detection, though nuclei in RBE4 cells can already be discriminated in the transmission channel (see section 3.4.1.4). The recorded data (see Figure 3.28 C+D) suggests that in principle both nuclear dyes might be used in a simultaneous staining with the Atto488/Atto590 siRNA in living cells, with respect to the availability of the right excitation wavelength.

### **3.4.1.2 Costaining of labeled siRNA with organelle staining for short-time imaging and use of violet laser**

In a first approach a confocal microscope with violet laser was used and a costaining of labeled siRNA with nuclear stain or lysosomal staining was performed. To prevent a bleed-through the image acquisition was performed by sequential excitation of each label.

In Figure 3.29 A RBE4 cells show transfected aggregates of Atto488/— siRNA inside the cytoplasm and in the surrounding medium. Additionally, a colocalization with red labeled lysosomes can be seen (white arrows in Figure 3.29 A). A release of Atto488/— into the cytoplasm was not observed. Nevertheless, the colocalization of lysosomes and the Atto488 signal indicates the presence of either the siRNA or at least of the label of decomposed siRNA. A clear statement whether the siRNA or just the label is inside the lysosome cannot be made.

The LysoTracker Red can not be used with Atto488/Atto590 siRNA but may be used in combination with an siRNA consisting of an Atto488 or Alexa488 combined with a far-red dye like Atto647N (see Table 3.3).

The second approach of using —/Atto590 siRNA with LysoTracker Green shows similar results (see Figure 3.29 B). Again transfected lipoplexes can be found inside and outside of the cells and a colocalization of the acceptor signal, i.e. Atto590, can be seen (indicated by white arrows). A potential usage of LysoTracker Green combined with integrity measurements would be possible by using the earlier described red shifted FRET siRNA construct Alexa555/Atto647N.

In combination with the Atto488/Atto590 siRNA and the Hoechst nuclear stain an interesting observation was made. In Figure 3.29 C the white arrow indicates a connection of two cellular aggregates that contain the FRET siRNA. Whether this is related to a release into the cytoplasm or a communication between the aggregates is not clear. Over the recorded 10-20 minutes no fluorescence in the complete cytoplasm was detected indicating no cytosolic release. Compared to later live experiments, in

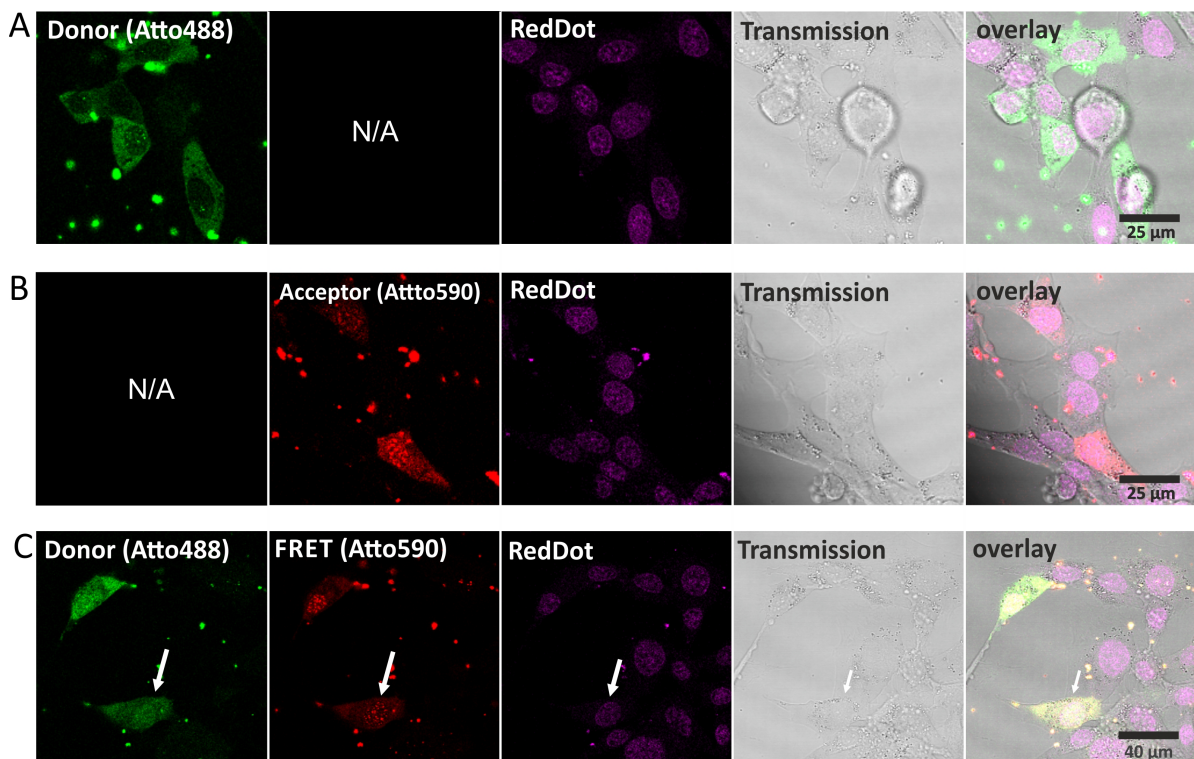


**Figure 3.29: Costaining of transfected cells with blue nuclear dye.** RBE4 cells transfected with single or double labeled siRNA by simultaneously staining of the nucleus with Hoechst and of lysosomes. (A) Atto488/— siRNA with costaining of lysosomes by LysoTracker<sup>®</sup>RED. White arrows indicate yellow spots that show colocalization of siRNA and lysosome. (B) —/Atto590 siRNA with costaining of lysosomes by LysoTracker<sup>®</sup>Green. White arrow indicate colocalization. (C) Atto488/Atto590 siRNA by simultaneous labeling of the nucleus. White arrows indicate a connection of two cellular aggregates.

which a microscope with incubation unit and HyD-PMTs was used, the photomultipliers in this setup were only standard PMTs that show a lower sensitivity and signal to noise discrimination. Additionally, it has to be mentioned that recently LysoTracker Deep Red got available which might be combined with the Atto488/Atto590 siRNA.

### 3.4.1.3 Costaining of labeled siRNA with organelle staining for long-term imaging with an incubation unit

In order to circumvent the lack of an UV laser, RedDot<sup>™</sup>1 dye was evaluated for long-term imaging.

Similar to the evaluation with the Hoechst nuclear stain, RedDot<sup>™</sup>1 was incubated with single and double labeled siRNA duplexes (see Figure 3.30). The imaging was performed in an incubation unit that allowed long-term imaging and viable cells during the examination.

In contrast to the experiments with Hoechst dye, free siRNA was observed within the cytoplasm for all three kind of transfected siRNA, i.e. Atto488/—, —/Atto590 and Atto488/Atto590. Whether this is related to the new microscope setup, with incubation unit and the more sensitive HyD-PMTs, remains unclear. All further presented data were



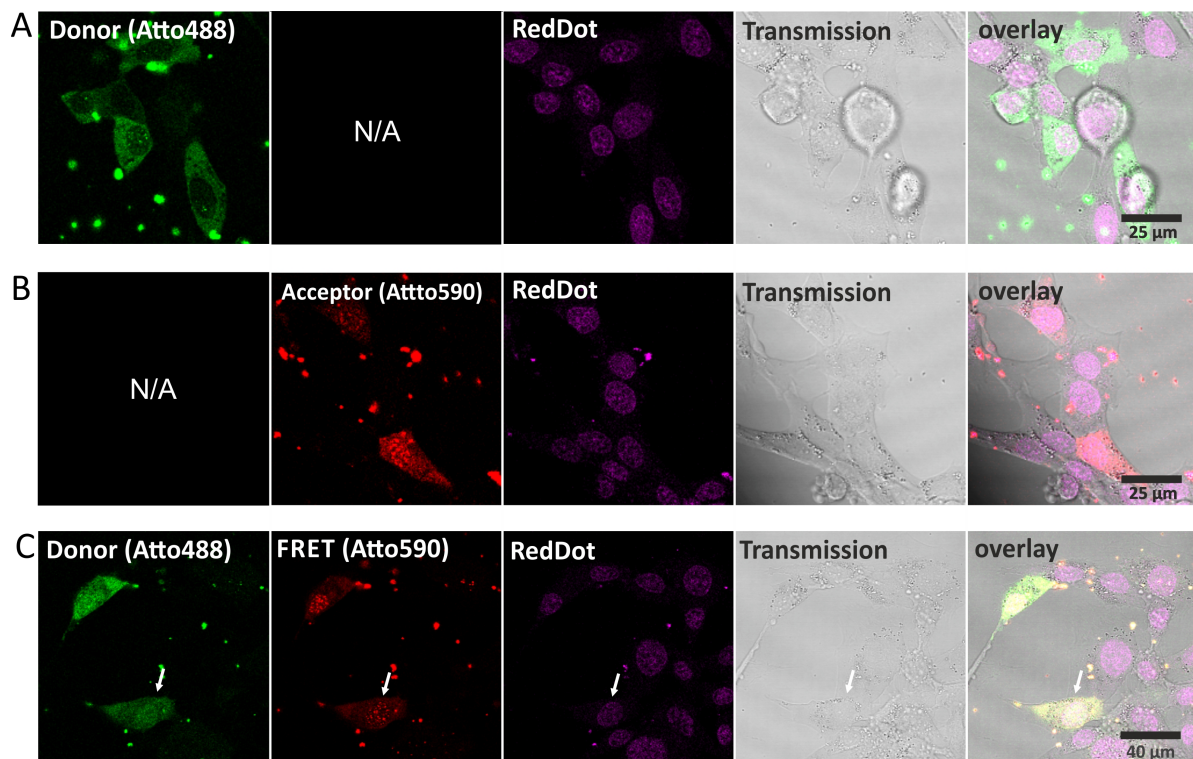


**Figure 3.30: Costaining of transfected cells with far-red nuclear dye.** RBE4 cells transfected with single or double labeled siRNA by simultaneously staining of the nucleus with RedDot™ 1. (A) Atto488/— single labeled siRNA (green) with costaining of RedDot™ 1 (magenta). (B) —/Atto590 single labeled siRNA (red) with costaining of the nucleus by RedDot™ 1 (magenta). (C) Double labeled Atto488/Atto590 siRNA by simultaneous labeling of the nucleus. Donor (Atto488 in green) and FRET signal (Atto590 in red) were recorded simultaneously. White arrows indicate a small aggregates inside the nucleus.

acquired on the Leica STED microscope. It offers the possibility of using the incubation unit to simulate conditions similar to a cell incubator.

Figure 3.30 A shows the localization of green fluorescence mainly in aggregates outside the cell or in the complete cytoplasm of the cells. Aggregates inside the cell were also detected but not as common as in case for Hoechst stained cells. Whether there is a connection can so far not be concluded. The Atto488/— siRNA can, nevertheless, be observed within the whole cytoplasm and also inside the nucleus, though the nuclear signal is much weaker.

In case of —/Atto590 labeled siRNA cellular aggregates of transfected lipoplexes can be observed (see Figure 3.30 B red dots). Additionally, cytoplasmic and nuclear localization of the acceptor signal can be seen. The presented data also shows cells in which a stronger fluorescence is observed inside the nucleus than in the cytosol. This stronger fluorescence is accompanied with the detection of small aggregation sites inside the nucleus.

In part C of Figure 3.30, the FRET siRNA was incubated with RedDot 1 stained cells. Here, lipoplexes were again visible inside the cells and outside in the medium. The presented region depicts one cell that shows FRET and thus intact siRNA inside the

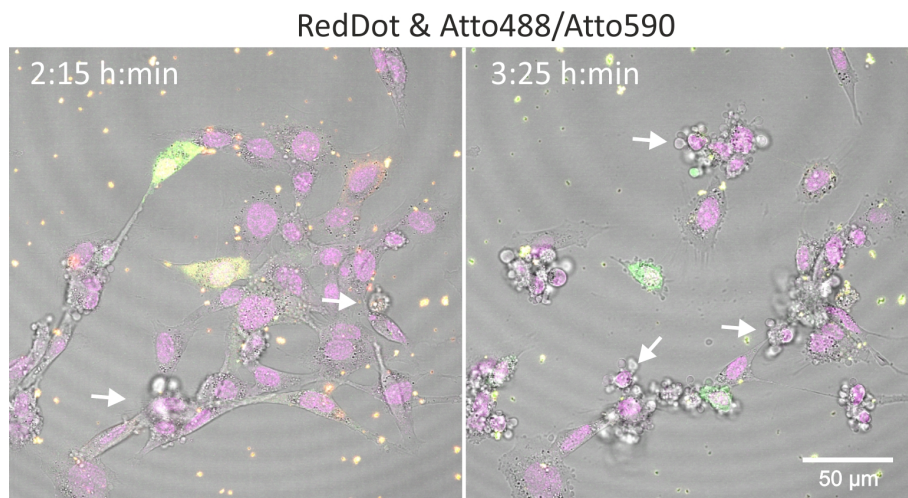


**Figure 3.31: Nuclei of RBE4 cells stained by RedDot™ 1 in long-term incubation.** Left: RBE4 cells after 2 h 15 min incubation and staining with the nuclear stain RedDot™ 1. Right: same region after additional 70 min of constant imaging at 1 min intervals. White arrows indicate blebbing of dying cells.

cytoplasm, whereas another cell shows mainly donor signal indicating degraded siRNA. Additionally, aggregates inside the nucleus with a strong FRET signal were observed. A similar observation was made with —/Atto590 siRNA and with FL/TMR siRNA in fixed cells (see Figure 3.26). It seems that intact siRNA tends to locate at some time point after cellular release inside the nucleus and thereby sometimes sublocalized in these aggregates or speckles.

During the experiments with RedDot 1 stained cells another observation was made. It seems that this nuclear stain leads to cell death upon longer incubation times and exposure to laser irradiation. Figure 3.31 depicts cells 2 h 15 min after the incubation with RedDot 1 and after additional 70 min of imaging (see Appendices J.22 for detailed sequence). One can clearly see dead cells that show blebbing as a first indicator of apoptosis [254, 255]. Additionally, the organelles around the stained nuclei show a much higher contrast, indicating stress by interaction of RedDot 1 with cellular mechanisms. The blebbing of cells and the changes in cellular organelles occurred not only in the scanned regions but also in other areas of the incubation chamber. Thus, phototoxicity caused by permanent excitation can be ruled out. Based on this observation a staining by RedDot 1 was not further conducted. Alternatively a visual segmentation of the nucleus was performed.

#### 3.4.1.4 Manual segmentation of the nucleus

The tested nuclear stains are either not compatible with the microscope (Hoechst stain) or cause cell death (RedDot 1). Thus an alternative way to detect or segment the nucleus had to be found.

The RBE4 used in this study display a large cellular volume with a well defined round

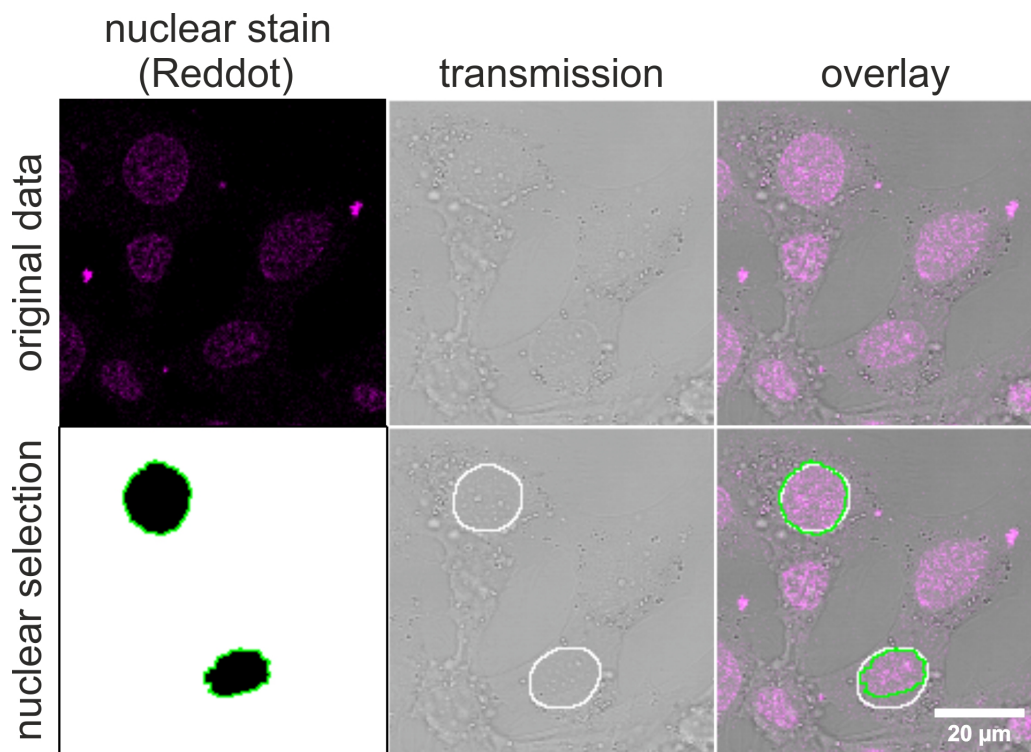


**Figure 3.32: RBE4 cells stained with RedDot™ 1 for nuclear segmentation.** Row 1 depict recorded data and row 2 the segmented nucleus of the nuclear stain (first column), transmission channel (second column) and the overlay (last column). Green outline indicates the nucleus based on signal of the nuclear stain, whereas white outline represents the visual and manual segmented nucleus.

shaped nucleus surrounded by a large cytoplasmic compartment. This allowed the segmentation of the nucleus without any further staining just by using the contrast of the recorded transmission channel.

To prove the possibility of a visual nucleus detection, reference images with either RedDot 1 nuclear stain, or released siRNA were evaluated. In Figure 3.32 the nuclear staining by RedDot 1 and the recorded transmission channel of freshly incubated cells is depicted. On the basis of the nuclear stain a segmentation of the nuclei was performed using ImageJ (see Materials & Methods 5.3.14).

In Figure 3.32 an example of manual and RedDot 1 based segmentation is depicted.

The manual selection is based on the described feature of RBE4 cells displaying the nucleus as a round shaped, larger disc in the cell center of the cell surrounded by a large cytoplasm. The nucleus shows a homogenous structure that can be distinguished from the cytoplasm with the other organelles. Either the nuclear envelope, as a contrast richer line, or contrast rich granules and regions surrounding the nucleus can be used for segmentation. This contrast rich structures probably refer to the perinuclear region, which consist of the endoplasmic reticulum and parts of the cis-Golgi network.

The described procedure works well on isolated cells that do not grow at high confluency. A comparison of the ImageJ-segmented nuclei and the manually chosen nuclei show more or less similar shapes (see Figure 3.32), though the manual chosen



nuclei tend to be slightly larger. Nevertheless, the described method can be used to verify whether fluorescence is present inside the segmented nucleus or not.

#### **3.4.2 R/G adaptation to live cell imaging**

For live cell imaging the imaging procedure used for fixed cells is not applicable (see Figure 3.22).

Due to cellular changes between different scans, neither averaging nor multiple acquisitions that represent the exact same cellular state are advisable. In consequence the acquisition of four images of the exact same condition with different PMT settings, as used for the R/G algorithm, cannot be used to determine the optimal integrity level for each pixel as used for fixed cells.

In addition, first live cell imaging studies indicated very fast cellular dynamics which require very fast scanning cycles to achieve a adequate time-resolution.

##### **3.4.2.1 Microscopy parameters for live cell imaging**

For observing living cells, the same region is scanned repeatedly. The delay time specifies the time of one scanning cycle and the interval length in temporal resolution. A fast scanning speed combined with the acquisition of the necessary data to apply the R/G algorithm is therefore required.

With a scanning area of  $246\ \mu\text{m} \times 246\ \mu\text{m}$  only few cells can be analyzed at the same time. An expansion of the scanning region by reducing magnification would also increase the acquisition time (at same pixel size, more pixels have to be scanned) or reduce resolution (at same pixel number of  $512 \times 512$  pixels). An adaptation of the scanning field is not favorable as the R/G algorithm relies on  $512 \times 512$  pixel images and lower resolution is not useful for cell analysis. Therefore an alternative approach was used by performing a tile-scan acquisition (see Figure 3.33 B). Four neighboring regions are scanned in a  $2 \times 2$  tile scan. This allows to distribute the acquisition time for the whole area to four different smaller areas with a shorter acquisition time for one image of each region. In this way an area of approximately  $500\ \mu\text{m} \times 500\ \mu\text{m}$  can be scanned. Additionally, a z-stacking was performed to acquired data from different layers within the cell. As a z-stacking again increases the interval length of the complete scanning cycle 5 z-slices at a thickness of  $1\ \mu\text{m}$  spanning a range of  $5\ \mu\text{m}$  were acquired (see Figure 3.33 C). A complete overview of different scan settings can be seen in Table 3.13.

With the Leica STED microscope the acquisition of one image with  $512 \times 512$  pixels takes approximately 0.85 s, one full scan of the  $2 \times 2$  tiles at 5 z-slices would take in theory approximately 17 seconds. Due to repositioning and a focus correction in each cycle,

**Table 3.13: Microscopy settings for live cell imaging**

	high speed mode	advanced mode	acceptor mode
tiles	2x2	2x2	2x2
z-stack	5	5	5
scanning speed	600 Hz	600 Hz	600 Hz
focus correction	1 per cycle	1 per cycle	1 per cycle
acquired signal	donor/FRET @ 1 intensity	donor/FRET @ 2 intensities	donor/FRET + acceptor
scans per slice	1	2	2
setting changes per slice	0	0	1
scanning speed	~35 seconds	~55 seconds	~90 seconds

the scan time ranges between 30 and 35 seconds. This is the minimal time resolution that can be acquired with the described setup by scanning only 1 image. This setting was named high-speed setting due to the minimal time between two scanning cycles (see Figure 3.33 D left).

To address the question of saturation a second scan with a much lower laser gain was performed to prevent saturation. With a delay of around 0.85 seconds slight changes inside the cell might occur until the second scan. This little delay time is probably too short to have a strong influence on the R/G processing. Therefore the acquisition of two very fast performed scans at different laser gains is favored and the used method of choice to analyze live cell uptake of transfected particles. This advanced speed mode takes approximately 55 to 60 seconds for on complete scanning cycle (see Figure 3.33 D middle and Table 3.13).

An additional approach was tested including a scan of the acceptor signal at excitation at 561 nm, which leads to a much higher scanning time due to changes within the microscope for the other laser excitation. This combination results in final scanning cycle of ~ 90 seconds and was named acceptor mode.

In the following live cell experiments, the advanced mode was chosen as standard acquisition setting as it allows to perform relatively fast imaging with reducing saturation effects. In case of long-term observations with an additional staining like LysoTracker or a second siRNA the acceptor mode setting was be used.

### 3.4.2.2 R/G adaptation

The most favored setting was the high-speed mode as with this setting the highest time resolution was obtained. The drawback however was the problem with saturated pixels in both, the donor and FRET channel. Saturation in both channels leads to an R/G ratio of 1 ( $\frac{I_{\text{saturated}}}{I_{\text{saturated}}} = \frac{255}{255} = 1$ ) and a calculated integrity of the siRNA of 92 % (according to the Atto488/Atto590 calibration model in Section 3.2.2). Based on the visualization of the FL/TMR optimized R/G ratio this value would be colored in bright green.

Nevertheless, as Atto488/Atto590 showed almost no signs of crosstalk, compared to FL/TMR siRNA, an R/G of 1 is still a sign of a large amount of intact siRNA present in the analyzed region. Otherwise no saturated FRET signal could be measured. Thus,

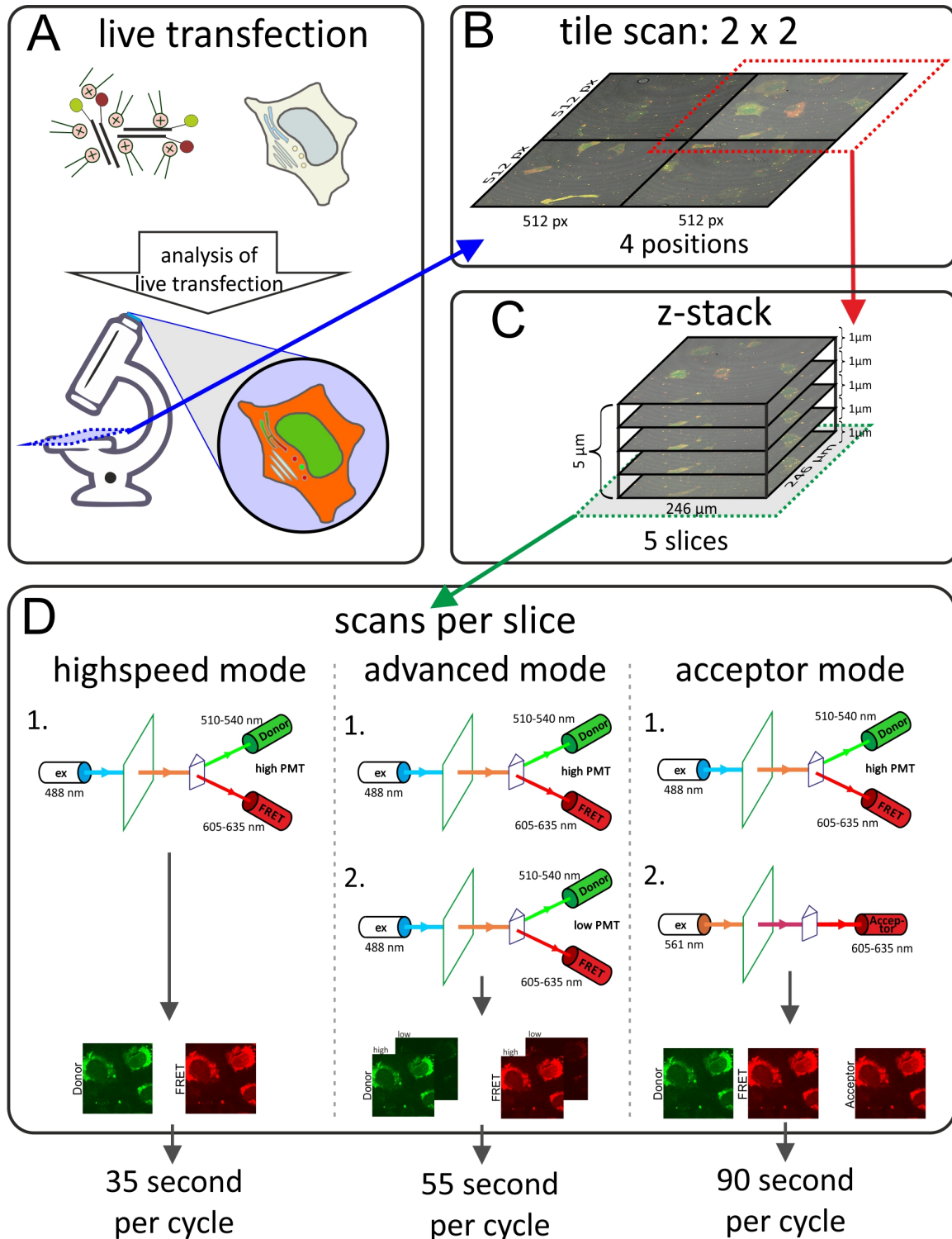


**Figure 3.33: Schematic representation of settings for live cell imaging.** (A) Setup for the 2x2 tile scan with 4 scanning positions each at 512x512 pixels. (B) z-stack acquisition over 4  $\mu\text{m}$  distance with 5 slices at 1  $\mu\text{m}$  section thickness and X x Y dimension of 246 x 246  $\mu\text{m}$ . (C) Microscopy setting for *highspeed mode* (left) with one acquisition at donor excitation and donor and FRET detection at high PMT gain. The middle, *advanced mode* setting, with two similar scans at different PMT settings (i.e. high and low). On the right the *acceptor mode* setting with detection of donor and FRET signal in the first scan and the additional scan for the acceptor at the respective excitation wavelength.

the assignment of bright green color to an R/G of 1 seems misleading. Therefore lower thresholds  $rg_{\min}$  and  $RG_{\max}$  for the R/G ratio image were chosen, which are 0.5 and 1.2 (setA and setB in Table 3.11).

According to the calculations in the cuvette, an R/G of 0.5 corresponds to still 80% of intact siRNA. Thus, in the obtained R/G ratio images green pixels refer to less than 80% intact siRNA populations whereas red pixels refer to siRNA with an integrity state higher than 95%. These thresholds for  $rg_{\min}$  of 0.5 and for  $RG_{\max}$  of 1.2 do not interfere with the R/G calculation itself but only support the visual representation. (see settings in Table 3.11) .

Another approach tested, was to modify the calculated R/G ratio images by applying a mean filter on the R/G values originated from two saturated values in the source images. The idea was to recalculate the color value in the ratio image in case of an R/G of 1. Such an R/G is the result of a ratio of two saturated and thus maximum intensity values of 255 (8-bit image range from 0 to 255). To prevent a recalculation of R/G values from unsaturated data, an additional inclusion of the source data was considered. If both source images show a maximum intensity of 255 and an R/G of 1, the color code for the ratio image should be averaged by the surrounding values.

Though the idea seemed promising, problems occurred in case of highly saturated aggregates. These refer to lipoplexes that were just delivered and therefore contain a high concentration of both dyes and usually do not show a lot unsaturated source pixels surrounding the saturated spot (meaning a broad Gaussian intensity distribution). In consequence the idea of post-modification was discarded and the adaption of  $rg_{\min}$  and  $RG_{\max}$  from 0.9 and 1.7 (setC and setD) to 0.5 and 1.2 (setA and setB) was favored.

In the following, R/G ratio analysis was performed with the lowered R/G thresholds of 0.5 and 1.2.

### 3.4.3 Live cell imaging with labeled siRNA

After having analyzed fixated cells and concluding an asynchronous behavior of the different cells the investigation of living cells to study single release events was further proceeded. In a first step observations made with single labeled siRNA will be described and later a focus on FRET labeled siRNA that is used to determine the integrity state of the delivered siRNA.

### 3.4.3.1 Transfection with single labeled siRNA

In a first approach single labeled siRNA duplexes were transfected into RBE4 cells and observed up to 4 hours on the LEICA-STED microscope with incubation at standard cell culture conditions. In Figure 3.34 A an exemplary release of Atto488/— transfected siRNA is shown which has been monitored  $\sim 30$  min after the addition of the transfection mixture. The costaining with LysoTracker Red can indicate the origin of the release (for the complete data set of each recorded channel see Appendices J.23). The white arrow indicates a colocalization of siRNA with a lysosome at the beginning of the image sequence at 0 min (defined as the starting of the release event) from which the green fluorescence spreads over the whole cytoplasm. The round shaped area in the middle of the cell can be identified as the nucleus (see above). The green fluorescence on the left, before the actual release event, originates from a transfected cell that grew partly over the cell of interest. Over time, it seems that the siRNA also enters the nucleus for a short time (blue arrow). After prolonged observation the fluorescence is then again mainly located in the cytoplasm. The diffuse spot inside the nucleus at around 8 min can be explained by blurred fluorescence at the edge of the section and thus does not represent a nuclear accumulation.

Earlier observation led to the idea that the transfection itself may trigger a release

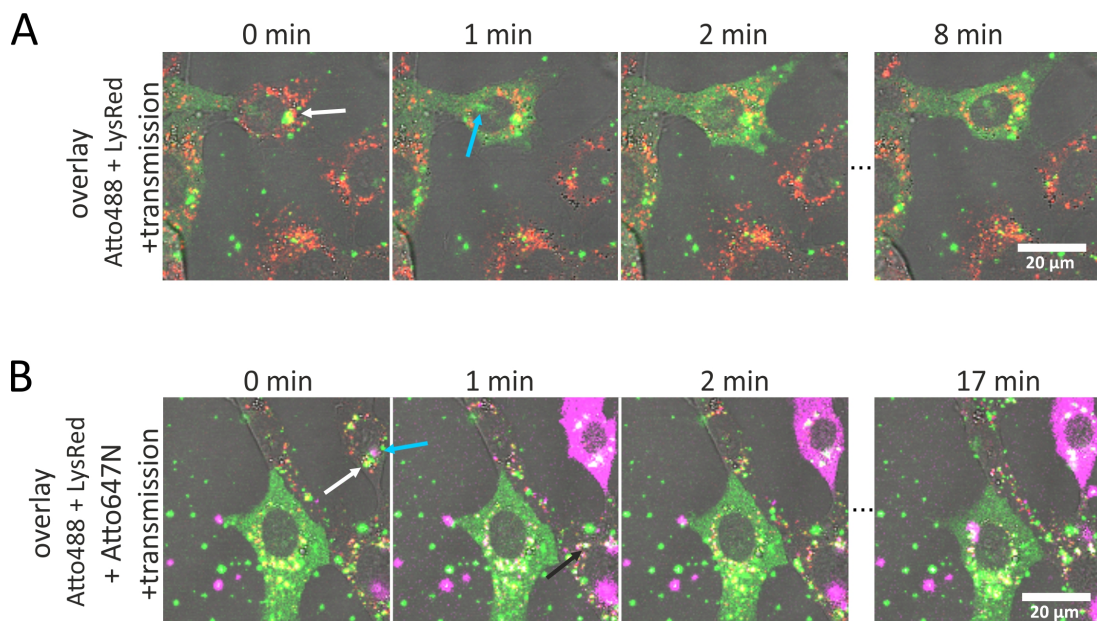


**Figure 3.34: Release of Atto488/— and —/Atto647N siRNA.** RBE4 cells transfected with Atto488/— siRNA (A) and re-transfection with —/Atto647N siRNA under live cell imaging conditions. Lysosomes are stained by LysoTracker<sup>®</sup> Red. At each time point data was acquired in sequential scans with  $\sim 0.85$  sec delay time. (A) Atto488/— siRNA signal (green) and lysosome (red) are shown in an overlay with the transmission channel. Images depict a release event 29 min after the addition of the transfection mixture. White arrow indicates the potential release site and blue arrow an influx into the nucleus. (B) Re-transfection of Atto488/— transfected cells with —/Atto647N siRNA 4 h 20 min after the first transfection. Sequence shows the beginning release of Atto647N-siRNA (blue arrow) at 4 h 26 min in 1 min intervals. White arrow depict Atto488/— and lysosomal colocalization and the black arrow a colocalization of both siRNA types in a lysosome.

into the cytosol or changings in cellular localization of siRNA. Due to cellular stress, caused by an additional transfection, it was assumed that already transfected lipoplexes, located in cellular organelles, might get a trigger for the release of their siRNA payload into the cytosol or released siRNA might be relocated. To test this feature RBE4 cells, already transfected with Atto488/— siRNA, were subjected to an additional round of transfection with —/Atto647N siRNA 4 h 20 min after the first transfection (see Figure 3.34 B). However, the hypothesis could so far not be confirmed. No additional releases of green fluorescence could be observed and only the already released siRNA signal remained. In two repetitions of the experiment only few first release events and none second release of Atto488/— or even an import or reimport of Atto488/— into the nucleus were observed. As in later experiments, however, more than 20 release events per region could be observed, these initial experiments with re-transfection need to be further investigated to discard or confirm the hypothesis of transfection stress triggering release or nuclear import of siRNA.

So far the re-transfection experiment showed, however, that the release of a second siRNA can occur independent from earlier transfected siRNA populations still present inside the cell. Figure 3.34 B depicts an example in which the described re-transfection with Atto647N siRNA leads to a release of —/Atto647N siRNA into the cytoplasm without a stimulation of an Atto488/— siRNA release. The start of the release was visualized by a blurred magenta signal as indicated by the blue arrow in Figure 3.34 B. In the example one cell, that already displayed Atto488 fluorescence when the —/Atto647N transfection mix was administered, showed no distribution changes over time. The colocalization with the red labeled lysosome is in this representation difficult, but the highlighted spot also shows a lysosome being present (see also Appendices J.24). The costaining with lysotracker also identified lysosomes that contained either one or two different siRNA species. The white arrow indicates a lysosome that only contains Atto488/— siRNA from the first transfection (yellow color in overlay), whereas the black arrow highlights a lysosome that contains both Atto488 and Atto647N siRNA (overlay color white).

The observations lead to the conclusion that a transfection with cation lipids leads to the uptake of siRNA into the cell by endocytosis with transport into lysosomes. Additionally, different transfections and thus uptake events result in different loaded lysosomes or other cellular structures from which siRNA might be released into the cytoplasm. A simultaneous release of two different labeled siRNA populations from the same lysosomes was not observed so far.

The results of the re-transfection experiment were confirmed by another transfection experiment where Atto488/— and —/Atto590 siRNA were separately complexed with cationic lipid and then simultaneously administered to the cells. Figure 3.35 illustrates



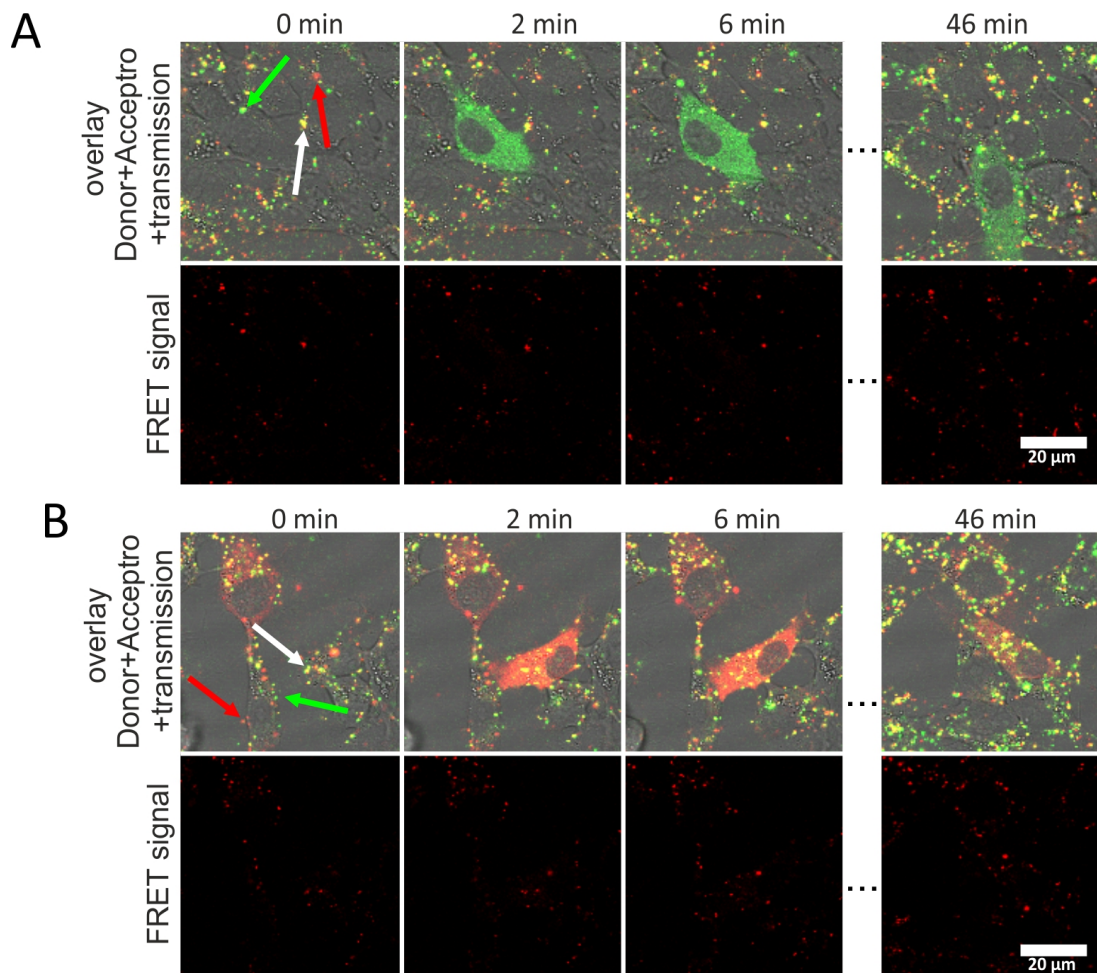


**Figure 3.35: RBE4 cells co-transfected with Atto488/— siRNA and —/Atto590 siRNA.** siRNA was complexed separately to prevent homogenous lipoplexes. At each time point data was acquired in the acceptor mode at 2 min intervals resulting in the donor, FRET, transmission and acceptor channel. Arrows indicate delivered lipoplexes with both types of siRNA (white), only Atto488/— siRNA (green) and only —/Atto590 siRNA (red). (A) Release event of Atto488/— siRNA (green) in overlay with acceptor channel and transmission (1<sup>st</sup> row) compared with FRET signal (2<sup>nd</sup> row). Image sequence depicts a release event 36 min after the addition of the transfection mixture. (B) Release event of —/Atto590 siRNA (red; acceptor channel) in overlay with donor channel and transmission (1<sup>st</sup> row) compared with FRET signal (2<sup>nd</sup> row). Image sequence depicts a release event 38 min after the addition of the transfection lipoplexes.

two release events 30 min after transfection at different regions of the monitored 2x2 tile-scan (for detailed channel data Appendices K.26). The FRET control channel, at 488 nm excitation, shows no signal, indicating no FRET siRNA involved in the release. In both observed regions, lipoplexes can be monitored inside cells that consist of only the Atto488/— siRNA, —/Atto590 siRNA or both siRNAs (indicated by colored arrows before the release events in Figure 3.35 A+B). The original source of the released siRNA could hardly be determined as one scanning sequence later the complete cytosol showed strong fluorescence in the respective siRNA fluorescence. In conclusion, only a single labeled siRNA was released as otherwise also a high FRET signal would have been detected.

The experiment also demonstrates a similar release behavior of both single labeled siRNA species. After the release, the fluorescence is mainly localized in the cytoplasm

with no strong signal in the nucleus, which can again be seen as gray, round shaped area in the overlay. On the basis of the manual segmentation (see Figure 3.32) and the observations of single labeled siRNA one can also try to segment the nucleus by the different distribution of the fluorescence signal inside the cell as supporting information to the transmission signals. In order to verify of this hypothesis fluorescent and transmission channels were inspected and the nucleus was manually segmented (see Appendices J.25). The manually segmented nuclei, on the basis of the transmission signal, showed similar results as a segmentation on the basis of fluorescence signals of the released siRNA.

For this reason it was finally decided to use no additional nuclear stain, which could influence the cellular distribution behavior, and to observe distribution changes by manual inspection of the cells.

### **3.4.3.2 Live cell transfection with double labeled Atto488/Atto590 siRNA**

In a next step the optimized FRET labeled Atto488/Atto590 siRNA was transfected and observed over time.

In Figure 3.36 snapshots of a 6 h transfection experiment with Atto488/Atto590 siRNA in the advanced imaging mode are shown. The complete transfection and uptake of siRNA into the cell was monitored in this experimental setup. The sequence showed impressively the high number of monitored release events by displaying multiple different cells in red and green color during the whole observation time. Cells that display a release event are highlighted by green arrows. After 30 min seven cells in the observed region showed an orange fluorescence in the cytosol whereas the nucleus seems to show a higher donor signal and thus green signal in the donor/FRET overlay. The time-dependent changes have to be mentioned as well. 120 min after transfection five cells lost the fluorescence signal in the cytosol (red mark indicates depletion), whereas in two cells the fluorescence persisted (orange arrow). Additionally, new releases could be monitored (green arrows). The last image of the sequence, after 330 min of incubation showed again depletion in seven cells, two new releases and additionally a second release of siRNA in two cells.

The R/G analysis (depicted in the R/G-ratio images in Figure 3.36) indicate that the monitored fluorescence can be assigned in most cases to populations of intact or partly intact siRNA ( $R/G > 0.5 \hat{=} 80\%$  intact siRNA in the population).

The major observation made in this live cell experiment is that release and persistence of siRNA in the cell, i.e. free in cytoplasm and/or nucleus, is not synchronized in different cells. The release seems to occur randomly concerning place and time. The progression inside the cell shows different behavior over time, as well. Thus a detailed analysis of single release events is necessary to understand the process of siRNA being released into



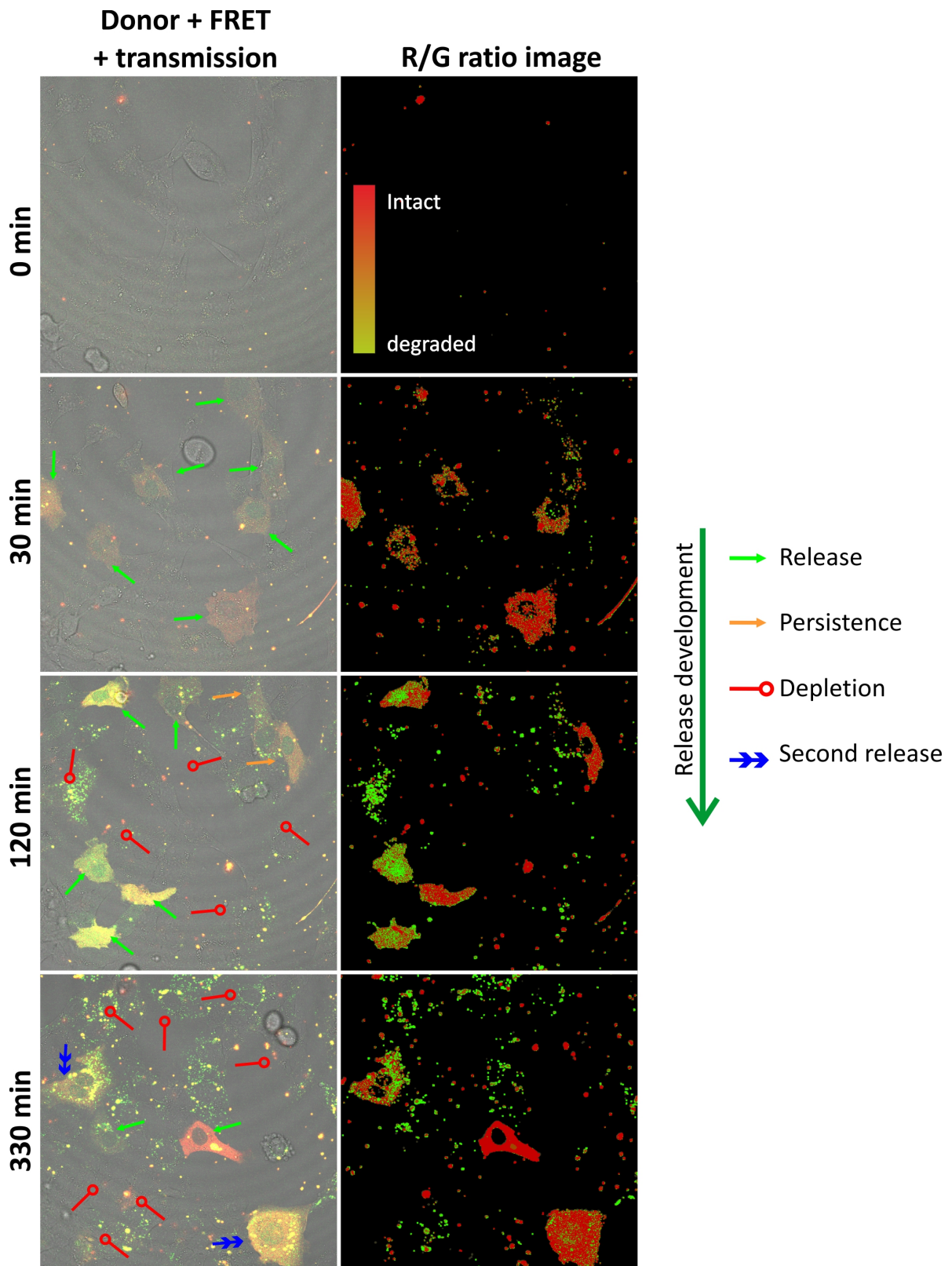


**Figure 3.36: R/G processing in living RBE4 cells after transfection with Atto488/Atto590 siRNA.** Snapshots of a 350 min observation of live transfected RBE4 cells. Cells were imaged in the advanced imaging mode recording donor and FRET signal at two sensitivities in a 2x2 tile scan with each 5 z-slices, resulting in 1 min intervals. The first column depicts an overlay of the donor, FRET and transmission channel. In the second column the R/G ratio image processed with R/G-settings setA is depicted. Release process and development is indicated for release (green arrow), persistent fluorescence (orange arrow), depletion of release (red mark) and second release in depleted cells (blue double-arrow).

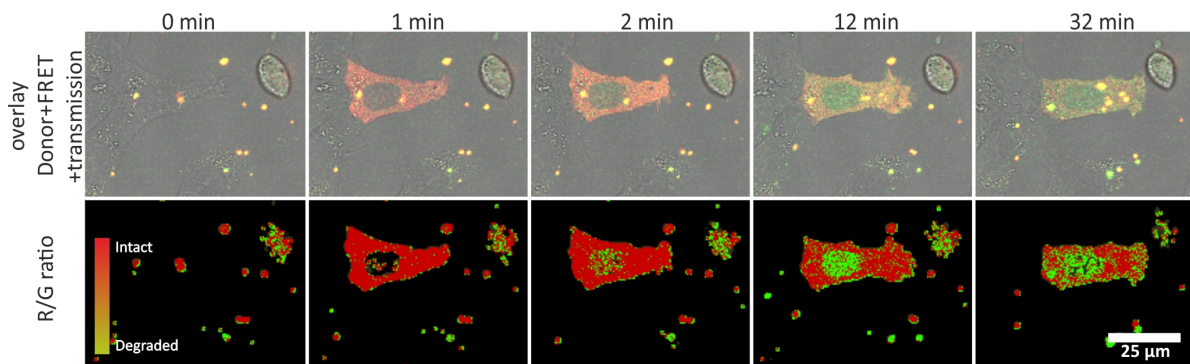


**Figure 3.37: R/G processing of digital magnified release event in RBE4 cells after transfection with Atto488/Atto590 siRNA.** The image sequence shows starting release and development over 32 min. Cells were imaged in the advanced imaging mode recording donor and FRET signal at two sensitivities in a 2x2 tile scan with each 5 z-slices, resulting in 1 min intervals. First row depicts an overlay of the donor, FRET and transmission channel. Second column the R/G ratio processed image with R/G-settings setA is shown.

the cytoplasm and being available for the cellular RNAi machinery.

In Figure 3.37 one release event of the image sequence shown in Figure 3.36 is given at a higher digital magnification. Similar to the experiments with single labeled siRNA, one can discriminate the cytoplasm and nucleus simply by looking at the fluorescence distribution pattern after a release event. The sequence shows a fast release within one scanning cycle of 1 min. One can see that first the cytoplasm and later the nucleus shows fluorescence. At the beginning intact siRNA is released into the cytosol and also inside the nucleus. The green fluorescence of the Atto488 labeled sense strand can be detected by looking at the single donor and FRET signal (see Appendices L.27). In the overlay the presence of the donor dye is visible by the orange color.

A close visual inspection of merged and R/G images indicates an accumulation of an siRNA population with lower integrity states in the nucleus. This means that the transfected and released siRNA enters the nucleus at some point. Inside the nucleus a light FRET signal can be detected indicated by the orange color in the overlay (see also Appendices L.27). Thereby the exclusive localization of free Atto488 dye or single stranded sense siRNA was ruled out. In consequence the detected signals inside the nucleus might originate from intact duplexes (in case of FRET) or the sense strand or the free dye (in case of the donor signal). The question whether only free dye or a complete single strand causes the detected signal can not be addressed by the two color FRET system as both will result in the same signal. Over time the intact siRNA was depleted from the cytoplasm detectable by lower fluorescence intensities and changing of the merged color from red to orange and to a greenish yellow color. Similar to the observation in the nucleus, the drop in R/G may be caused by degradation or active depletion of intact siRNA from the cytoplasm.

### 3.4.3.3 Influence of fixation

In Chapter 3.3.2 fixed cells were analyzed, but the question of comparability remained: Does the fixation arrest the situation inside a cell immediately or are processes induced that change the situation in fixed cells compared to living ones? To address this question a subsequent evaluation of the fixation process under the microscope was performed in real-time. For this purpose, transfected RBE4 cells were fixed in a live cell imaging experiment on the Leica STED microscope, observing the fixation process and possible changes over time. In Figure 3.38 the fixation and subsequent imaging over the following 15 min is shown.

The fixation was performed by addition of PBS-Formaldehyde solutions to final 4%. Formaldehyde penetrates cells very fast and cross-links free amino groups by formation of a methylene cross-links [256] and is thus suitable for instant fixation. In the presence of formaldehyde proteins are known to be cross-linked by bridging two free amino-groups. Nucleotides and other cellular macromolecules with free amino groups can form cross-links, as well [257]. In this arrested matrix the labeled siRNA is either

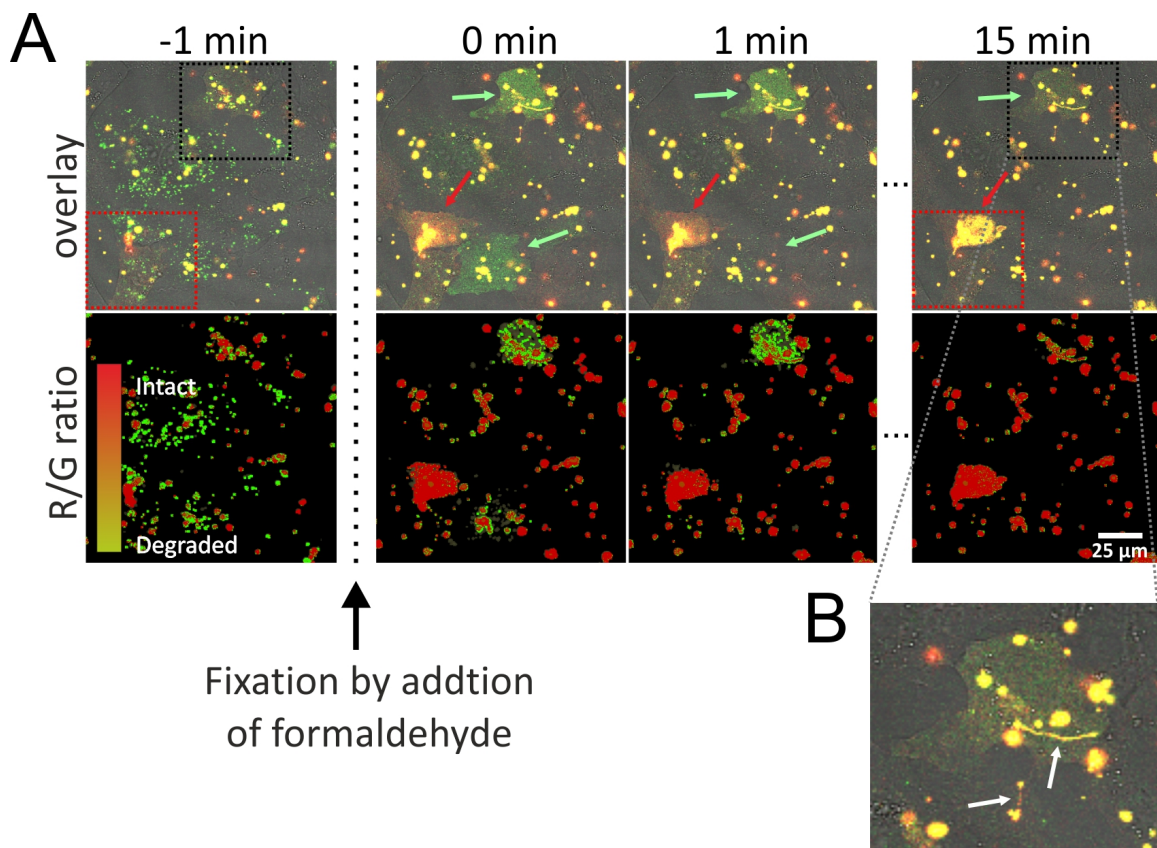


**Figure 3.38: Live cell imaging of the fixation process of transfected RBE4 cells with formaldehyde.** (A) After 6 hours of incubation ( $\Delta t = -1$  min) formaldehyde was added directly to the culture medium of an ongoing live cell observation. The overlay shows donor, FRET and transmission channel. R/G ratio was calculated using setA. Images were acquired in 1 min intervals for 15 min. The release of intact and degraded siRNA is indicated by red and light green arrows. Black and red box indicate cells with weak fluorescence before the addition of formaldehyde. (B) Digital magnification of the cell highlighted by black, dotted box at 15 min after fixation. White arrows indicate connection of cellular siRNA aggregates.

retained or directly cross-linked and preserved. An immediate arrest of cellular motion was detected indicating the immediate death by fixation (see Figure 3.38 A).

Furthermore, direct after the addition of the fixative, cells appeared that showed both green and orange fluorescence in the entire cell (red arrows for orange release and green arrows for green release processes). This indicates a release of siRNA from endo- or lysosomal foci that burst during the fixation process. This triggered release fades from the cells within minutes. The signal is lost again 15 min after addition of formaldehyde and the possible triggered release. Bleaching can be ruled out as verified in Section 3.3.1.2. Nevertheless, cells that showed weak fluorescence in the cytoplasm before fixation kept this fluorescence (red and black box in Figure 3.38 A). Additionally, the loss of fluorescent signal seems to be limited to the Atto488 signal. This might indicate a cleavage of the dye from the duplex or single strand by nuclease activity resulting in free dye that can diffuse within the cell. Nevertheless, Atto488 bears two amino group at the xanthene moiety which should be cross-link via the formaldehyde fixation.

The question why one fluorescence remains whereas the other vanishes cannot be answered and needs further investigation.

Comparing the cells before and after fixation one can detect stronger FRET signals in the fixed cells than in their living counterparts. This effect can especially be seen in the R/G ratio image (see Figure 3.38 A second row). A lot of speckles with green dominated color and thus degraded siRNA were classified at  $t = -1$  min. After fixation those speckles either vanished or turned into red dominated (in R/G ratio image) or orange dots (in the overlay), which contain intact siRNA populations. This might again support the idea of free Atto488, that masks the R/G ratio and is washed away by fixation to leave only complete siRNA duplexes or single stranded sense strands.

Similar to other experiments, sometimes connections or channels between two siRNA containing spots were seen. This was the case after the fixation, as well, as magnified in Figure 3.38 B. It seems that the labeled intact siRNA migrates from one aggregate to another. Thereby a tube is formed or the siRNA is transported along a cellular filament to another cellular compartment. This theory needs further investigation.

### **3.4.3.4 R/G ratio analysis in HeLa cells**

Apart from the investigation of Atto488/Atto590 siRNA in RBE4 cells, as the gold standard for the performed investigations, first experiments with FRET siRNA were performed in HeLa cells.

Similar to RBE4 cells, HeLa cells showed multiple release events after addition of lipoplexes containing cationic lipids and Atto488/Atto590 siRNA. In Figure 3.39 one release event of Atto488/Atto590 siRNA in a HeLa cells is shown. However, the manual segmentation of the nucleus of the HeLa cells was problematic, which was not the case



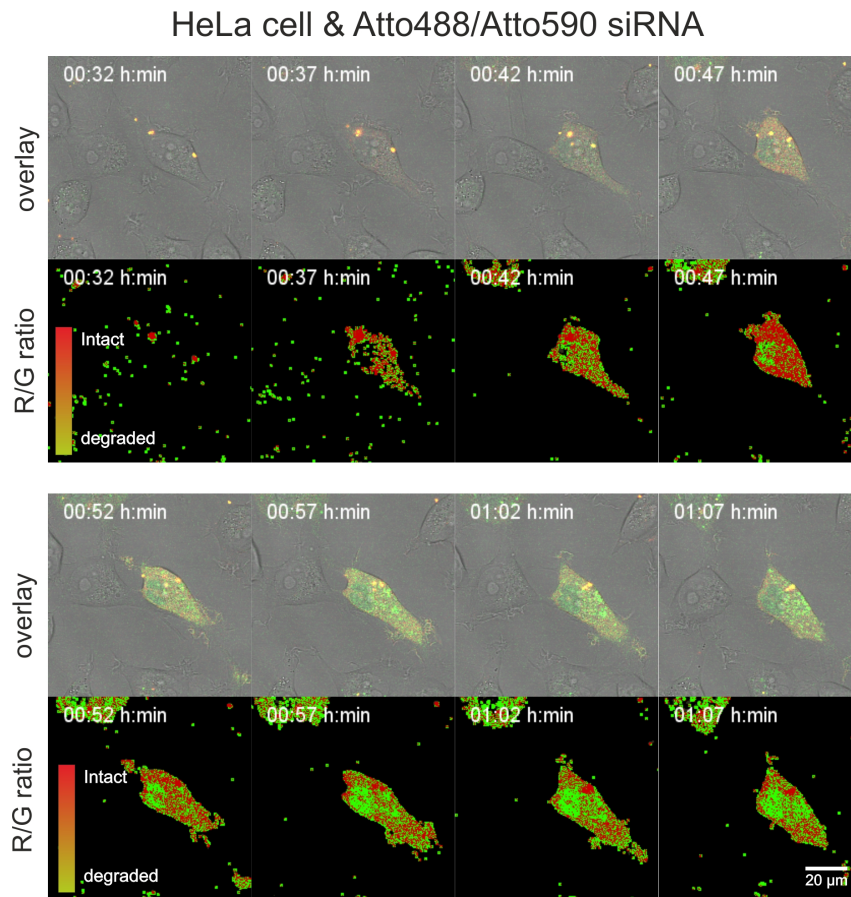


**Figure 3.39: HeLa cells transfected with Atto488/Atto590 and analyzed by the R/G algorithm.** Overlay depicts a merging of donor, FRET and transmission channel of Atto488/Atto590 transfected HeLa cells. The R/G ratio image row depicts R/G processed data with the R/G setting setA. Cells were imaged in the advanced imaging mode recording donor and FRET signal at two sensitivities in a 2x2 tile scan with each 5 z-slices, resulting in 1 min intervals

for the RBE4 cells. HeLa cells are rather compact with little cytoplasm which makes a good differentiation of cytosol and nucleus nearly impossible without additional staining. At the beginning one can see orange signals in the overlay channel indicating both FRET and donor signals. The R/G ratio shows that intact siRNA is observed. First red to orange fluorescence is detected after the release inside the cell (at 0 h 37 min) and later one can see a green dominated, kidney shaped area in the middle of the cell. This structure could be the nucleus and would thus confirm the observation in RBE4 cells, where the Atto488 labeled sense strand accumulates inside the nucleus.

Over time, cells show increasing green fluorescence indicating either free dye or strand separated duplexes, which mask the quenched donor signal of an intact FRET siRNA duplex.

The recorded data was analyzed via the R/G ratio algorithm with the same settings as for RBE4 cells. The results look similar to RBE4 data, but a more detailed evaluation of the R/G distribution in simulated integrity states is necessary to confirm comparability (compare RBE4 cells in Figure 3.23 or 3.24).

### 3.4.3.5 Test of an alternative FRET pair on siRNA - Alexa555/Atto647N

In Chapter 3.1.5 different FRET siRNA were presented and later evaluated *in vitro* via fluorometry. One of the systems was Alexa555/Atto647N siRNA which had already been used to evaluate protective effects of different nanoparticulate delivery systems against nucleases.

In a preliminary experiment, Alexa555/Atto647N siRNA was transfected under live conditions into RBE4 cells and the release of siRNA into the cytoplasm was observed. Figure 3.40 depicts the release of the FRET siRNA with additional R/G processing for a representative sample (a detailed representation of each channel can be found in Appendices L.28). For processing, the same settings as for Atto488/Atto590 siRNA were tested. The release process depicted shows similarities to the results from Atto488/Atto590 (see Figure 3.37): A fast release of intact siRNA into the cytosol and a subsequent weak signal originated from degraded or low integrity level siRNA in the nucleus. Over time the signals are again depleted.

The integrity analysis showed that the released siRNA in the cytoplasm has a high R/G value relating to an intact population of siRNA. Besides the intact siRNA in the cytoplasm, some aggregates with equally strong donor and FRET signal can be seen (white pixels in overlay). These aggregates contain an siRNA population that shows signals of degradation and are located on the right side of the nucleus in the perinuclear region.

In the surrounding cells mainly degraded siRNA is detected in aggregates distributed in the entire cells. A similar pattern is also seen with Atto488/Atto590.

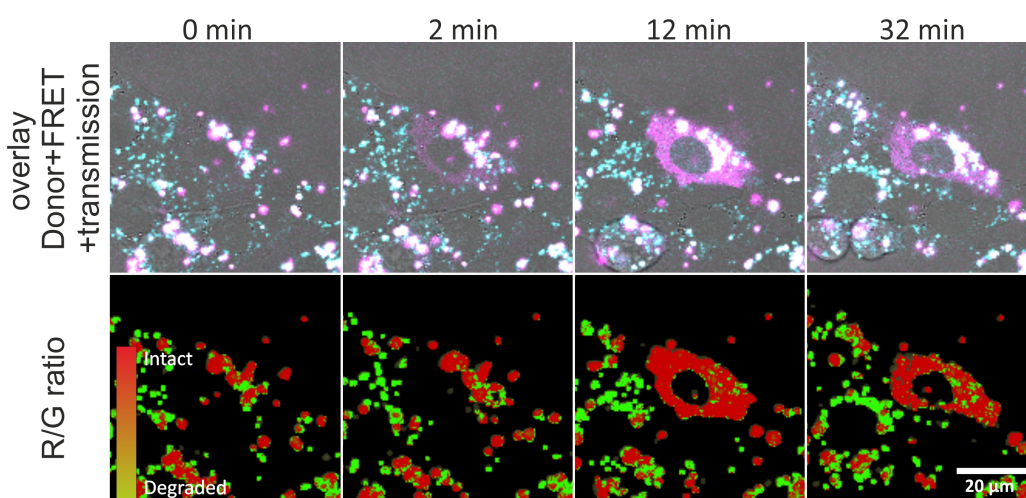


**Figure 3.40: Release of Alexa555/Atto647N siRNA.** RBE4 cells transfected with Alexa555/Atto647N siRNA under live conditions. Sequence depicts digital magnified release event of FRET siRNA into the cytoplasm. Overlay depicts donor signal (in cyan) and FRET signal (in magenta) with the recorded transmission. R/G processing with same settings as for Atto488/Atto590 siRNA, i.e. R/G setting setA, with red indicating intact and green degraded siRNA. Image sequence depicts starting release and development over 32 min. Cells were imaged in the the acceptor mode mode recording donor and FRET and acceptor signal in only one region with each 7 z-slices, resulting in 1 min intervals.

Two advantageous properties of the Alexa555/Atto590 construct are demonstrated: higher R/G values of intact siRNA and a larger dynamic range compared to Atto488/Atto590. Similar as in the cuvette the FRET occurring between Alexa555 and Atto647N is very dominant which results in a strong magenta colored overlays an a homogenous classification of intact siRNA via R/G. The R/G ratio image presented here is based on the settings for Atto488/Atto590 (setA:  $rg_{\min} = 0.5$  and  $RG_{\max} = 1.2$ ). While in case of Atto488/Atto590 siRNA an R/G of 0.5 would still indicate more than 80 % of intact siRNA, a classification via the calibration data in section 3.2.2 results in only 20 % intact siRNA for Alexa555/Atto647N. Transferring the threshold integrity states of Atto488/Atto590 to Alexa555/Atto647N the values for  $rg_{\min}$  and  $RG_{\max}$  need to be increased to 1.5 and 3, respectively.

The comparison of different sensitivities demonstrates that a further adaptation for the Alexa555/Atto647N siRNA for life cell application is essential.

### 3.4.4 Observations made during live cell imaging

The last three sections will again focus on Atto488/Atto590 transfected RBE4 cells under live conditions. In total, 11 similar experiments with RBE4 cells transfected with Atto488/Atto590 siRNA were performed. The observation of siRNA release events ranged from 350 min up to 500 min. Thereby different imaging setups, meaning advanced or acceptor mode (see Figure 3.33), were chosen. Nevertheless with all data sets the R/G processing was performed with R/G setting setA and for visualization one slice at a lower position was chosen to best represent the cellular state.

In the previous sections, release events have been mentioned and described (see e.g. Figure 3.34 and 3.35 for single labeled siRNA and Figure 3.37 and 3.40 for FRET siRNAs). Here a closer look at the release events and interesting observations made by screening the recorded movies will be presented.

#### 3.4.4.1 Uptake and release from lipoplexes

So far the release of Atto488/Atto590 siRNA was observed several times. In the total set of experiments, 328 single events in 54 scanned regions could be observed (see Table 3.14), but the origin of fluorescence could not exactly be localized. All observed cells contain more than one delivered lipoplex which makes a determination of the release source difficult. Additionally, the observed experiments can be grouped in two categories. First there are experiments that show a lot of release events, up to 30 events per scanned region, whereas in other experiments only 1 or 2 release events could be detected. For this reason the live cell experiments were classified in two categories. Category I contains experiments with less than three release events per region, whereas

**Table 3.14: Cellular release events**

	# of live transfections	scanned regions in total	observed cells in total*	cells showing release events	fraction of cells showing release of total (in %)	average release events per region
category I	5	24	1056	32	3.0	1.3
category II	6	30	1320	296	22.4	9.9
<b>total</b>	11	54	2376	328	13.8	6.1

\*: on basis of an average cell number of 44 cells per region and more than 60 analyzed regions

category II contains the experiments with more than three observed releases. In average category I experiments show  $\sim 1.3$  releases per region and category II experiments  $\sim 9.9$ . The source of this variability is not clear as all experiments were performed in a similar way and no system in the order of performed experiments could be found.

One particularly interesting event is shown in Figure 3.41. Over a period of 35 min the aggregate and cell approach and an uptake occurs (white arrows in Figure 3.41) followed by an immediate release of siRNA into the cytoplasm. The presented release of siRNA follows the same pattern as described earlier. In a rapid release process, i.e. between two scanning rounds with a 1 min interval, the cell shows fluorescence in the complete cytoplasm and with short time delay also in the nucleus. The R/G analysis reveals initial intact siRNA in the cytoplasm and partly degraded siRNA in the nucleus. Over time the cell shows bright green fluorescence with only the perinuclear region showing FRET signals. Due to the high donor signal the R/G analysis indicates mainly degraded or low level integrity siRNA.

This particular case of cellular release also demonstrates that strong fluorescence, as an indication for high levels of siRNA being released, is followed by stronger donor dominated fluorescence. This is due to the fact that donor dye without an acceptor shows much brighter fluorescence signal than the FRET based acceptor emission. Thus by overloading the cell with siRNA, the degradation and separation of siRNA duplexes superposes the signal of the remaining intact siRNA.

Nevertheless, the cell already contains other lipoplexes that contain intact or partly degraded siRNA. The fact that this one lipoplex approaches the cell, probably on basis of diffusion in the surrounding medium and finally on attraction of the positively charged lipoplex and negatively charged membrane of the cell, and a release directly after the uptake leads to the assumption that this lipoplex is the origin of the release. A general relation of the moment of uptake until the release event cannot be determined as, except for the presented event, no clear origin of the detected siRNA signal can be assigned. It rather looks like release processes occur randomly, sometimes directly after the uptake of an aggregate or after an indefinite time of the lipoplex being localized in endosomal or lysosomal structures.



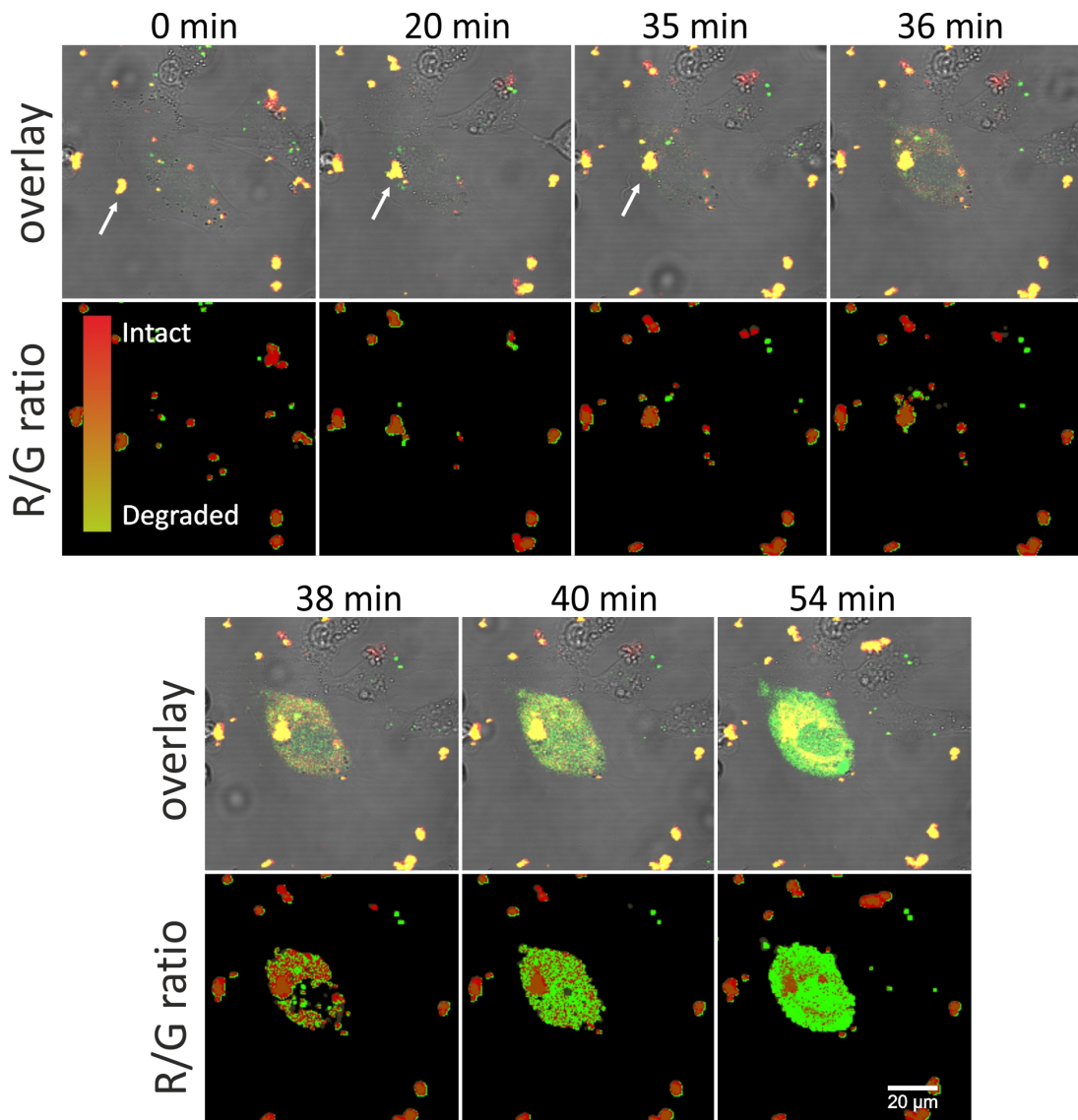


**Figure 3.41: Release of siRNA from lipoplex right after uptake into the cell.** RBE4 cells were transfected with Atto488/Atto590 siRNA and incubated for 4 h until the depicted event was observed. From 0 to 35 min the approaching and uptake is indicated by white arrows. In the following 20 min the release and cellular fate of the siRNA is shown. Image was acquired in the advanced mode at final 1 min intervals. Overlay consists of recorded donor, FRET and transmission signal. R/G ratio analysis was performed with R/G setA.

#### 3.4.4.2 Formation of siRNA aggregates during and after release

Another observation that was made during the process of analyzing the acquired live cell data was that after the depletion of siRNA from the cytoplasm bright green aggregates were detected inside the cell and especially in the perinuclear region.

Figure 3.42 depicts 5 examples of an siRNA release into the cytoplasm in both overlay and R/G ratio analysis, right after the release process and after depletion of the siRNA released. One can see that after the depletion green aggregates remain inside the cell seeming to group around the nucleus. In some cases these aggregates are close to each other forming a structure that might be related to the endoplasmic reticulum as they seem to be attached to the nuclear envelope. Additionally, comparing the aggregate

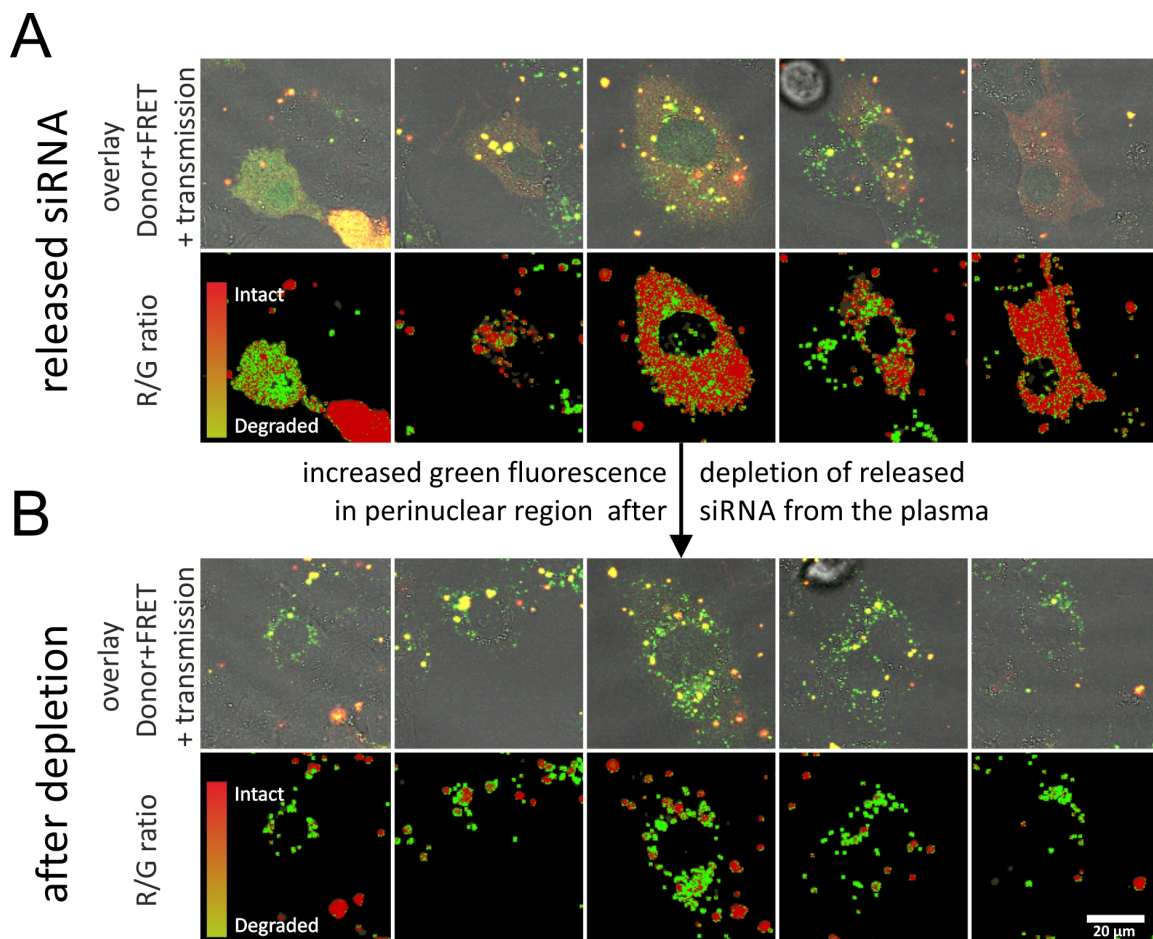


**Figure 3.42: Formation of speckles during release.** Examples of RBE4 cells that shows siRNA release and later depletion from cytoplasm. Cells are depicted in overlay of donor, FRET and transmission channel (top row) and after R/G processing (lower row). (A) Cells right after release of siRNA into the cytoplasm. R/G image classifies intact or partly intact siRNA populations. (B) Same cells after depletion of siRNA from cytoplasm. Green spots remain surrounding the nucleus and are classified as degraded siRNA.

number inside a cell before and after a release and depletion event, one notices an increase in the number of green accumulation sites differing in size. A first preliminary analysis of the siRNA integrity level inside these aggregation site indicated still fractions of intact siRNA.

An open question is how the siRNA is depleted from the cytoplasm and the nature of those accumulation foci formed. There are two possibilities imaginable concerning a cellular release of the FRET siRNA.

First, dyes are cleaved off the duplex by RNases present in the cytoplasm, which would lead to free dye and a strong Atto488-based signal, as shown in Figure 3.41 where a release of a large amount of siRNA leads to the formation of strong donor signals. The cleaved dyes might then be transported into lysosomes for cellular recycling processes. But a cleavage of just the dyes, the completed degradation of the duplex or strand separation would lead to a strong donor signal, which is not found for all cases. In fact, in most events observed the overall fluorescence of intact siRNA decreases inside the

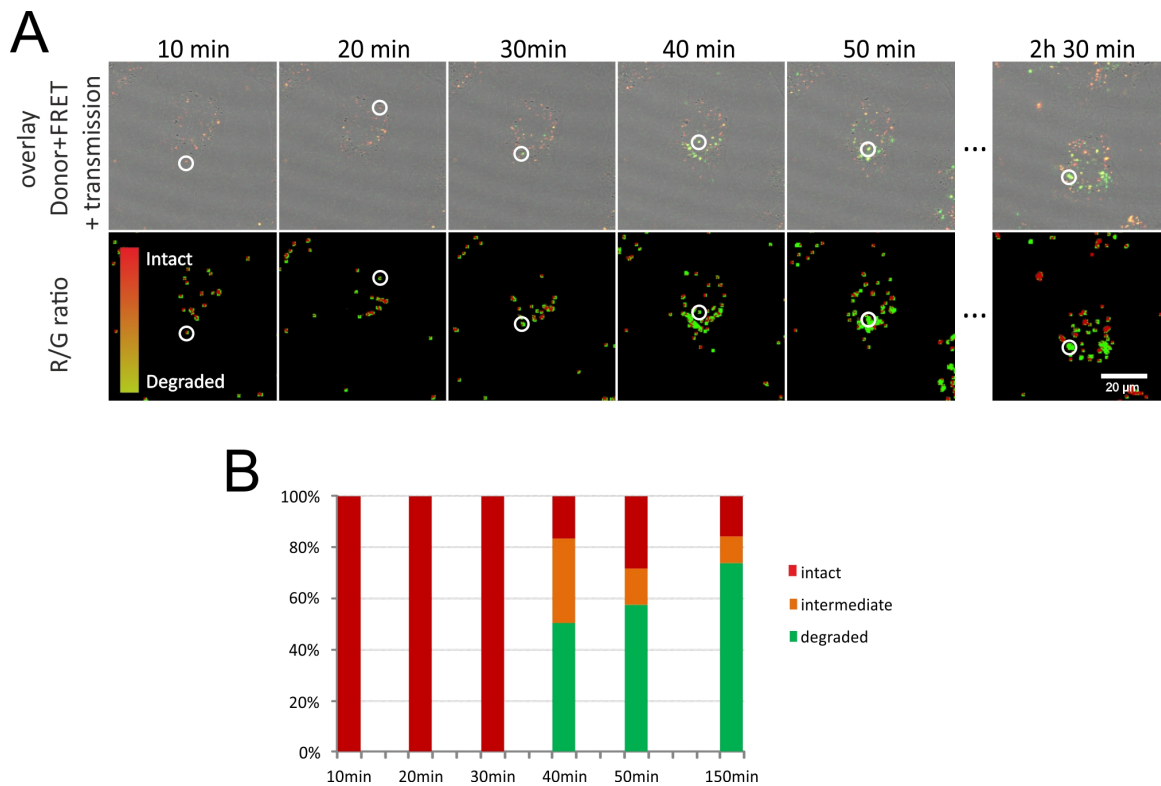


**Figure 3.43: Cellular aggregates of transfected lipoplexes over time.** RBE4 cell after transfection with Atto488/Atto590 that does not show any detectable release. (A) Over the observation time of 150 min the speckles change from first red to orange and green in the overlay image (top row). R/G analysis is performed with setA and depicted in second row. White circles indicate spots that were analyzed towards R/G value distribution. (B) R/G value distribution of highlighted spots. Thresholds for classification of degraded (intact), intermediate (orange) and intact (red) state were 0.7 and 1.5.

cytoplasm over time and no burst in donor signal was detected (e.g. see Figure 3.49 or 3.51 in following section). This indicates an active transport of intact siRNA from the cytoplasm into other organelles, a second possibility for depletion.

Assuming that the siRNA is depleted from the cytoplasm and transported into other organelles, the process of autophagy may be considered. In autophagy cellular molecules are surrounded by a bilayer, that is thought to be either originated from endoplasmic formed membrane vesicles or ER inversions that surround cytoplasm components and form vesicles (autophagosomes). Autophagosomes finally merge with lysosomes for recycling [258]. As this process might involve membrane parts of the ER the accumulations of labeled siRNA or parts close to the ER, meaning the perinuclear region, might be explained by this.

Additionally, the theory of autophagy would explain an increase of fluorescent organelles, meaning lysosomes, over time as new autophagosomes may form and merge with lysosomes that so far did not contain fluorescent dyes or labeled siRNA.

Besides the formation of new aggregates inside the cell, already internalized lipoplexes evolve over time. In the beginning delivered particles or aggregates are dominated by a measurable FRET signal and later the donor signal dominates in those aggregates.

In Figure 3.43 A a cell is depicted that in the beginning shows several weak, mainly red fluorescent spots. In the R/G analysis these spots are classified red with some green edge pixels. These edge pixels are a kind of artifact that occurs due to smoothing processes of the R/G algorithm at the edge of regions that display intensities just above a the detection threshold. Over time the spots observed change their color. In the beginning they contain mainly intact siRNA but over the observed time period more and more spots exhibit green dominated fluorescence indicating degraded siRNA. Nevertheless, a huge fraction of the spots visible still show a strong FRET signal and are thus classified as partly intact siRNA.

In an analysis of example spots (highlighted by white circles in Figure 3.43 A; Appendices L.29 displays single channel data) the R/G composition of each spot was determined (see Figure 3.43 B). The spot analysis shows the composition of the analyzed spot evolves from 100 % intact pixels towards 80 % degraded pixels after 150 min.

It is also important to mention that the analyzed spot at 150 min (showing bright green fluorescence) still contains some pixels with R/G ratios above 0.7, i.e. intact populations of siRNA.

This change in integrity of delivered lipoplexes over time indicate that the aggregates somehow undergo a maturation or degradation process. This might give a hint as to cellular localization. Lysosomes, for example, contain a large number of enzymes that are used in recycling cellular molecules. Assuming the aggregates are taken up by endocytosis, they end up in endosomes first and later in lysosomes. This would explain the degradation process, since in lysosomes the lipoplexes and siRNA would be decomposed over time. Nevertheless in other observations lipoplexes inside a cell can trigger a release even after hours from late endosomes or lysosomes.

### **3.4.4.3 2<sup>nd</sup> releases, cell death and cell division after release**

During the screening process of the live cell experiments performed with Atto488/Atto590 siRNA some other observations were made. A summary of these observation can be seen in Table 3.15. During the observation period, i.e. up to 8 hours after transfection, not only single release events in one cell were detected, but also a second or third release after depletion of the initially released siRNA. In total 11.6 % of all release events showed multiple releases. Simultaneous releases, or releases while there was still intact siRNA present could not be analyzed for obvious reasons. These events would lead to an prolonged siRNA circulation and thus longer duration of the initial event. An example of a secondary release event is shown in Figure 3.44 A.

Besides multiple releases in the same cell, cell death and cell division after a preceding release were also observed (for an example see Figure 3.44 B+C). Nevertheless, correlating these events to siRNA releases is difficult: Did the release occur due to stress



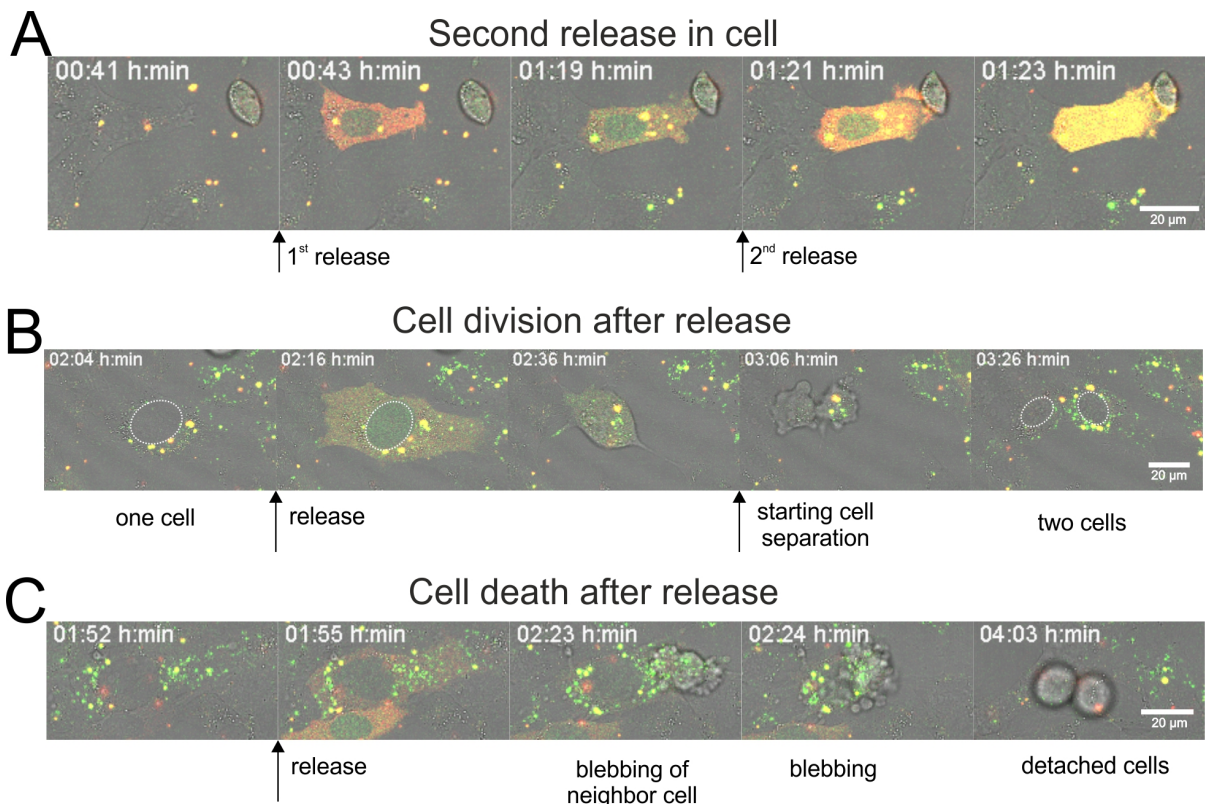


**Figure 3.44: 2<sup>nd</sup> release, cell division and cell death of transfected cells.** RBE4 cells transfected with Atto488/Atto590 siRNA observed over 5 hours by live cell imaging. (A) Release event of intact siRNA at 0:41 h:min followed by a depletion of the cellular signal and an additional release at 1:21 h:min. (B) cell division of a transfected cell that shows a release of siRNA. The nuclei before and after division are highlighted. (C) Apoptotic cell after the release of siRNA. Cell shows blebbing and finally detaches.

caused by an initiated apoptotic pathway or starting cell division? Or did a release trigger the induction of apoptosis? The number of all events (4 cell deaths after a release) indicate no connection of cell death and release events (~ 3% of all release events). The same is true for cell division, although 22 divisions after release processes were observed. Also cells that do not show any release but contain lipoplexes undergo mitosis thus indicating that cells are healthy and the stress due to imaging is minimal.

**Table 3.15:** Release events and more

	total releases	single release events	2 <sup>nd</sup> release after depletion	death after release	division after release	infection of neighbor cells
category I	32	32	0 ( 0 % )	4 ( 12.5 % )	1 ( 3.1 % )	4 ( 12.5 % )
category II	296	262	34 ( 13 % )	4 ( 1.5 % )	21 ( 8 % )	17 ( 6.5 % )
<b>total</b>	<b>328</b>	<b>294</b>	<b>34 ( 11.6 % )</b>	<b>8 ( 2.7 % )</b>	<b>22 ( 7.5 % )</b>	<b>21 ( 7.1 % )</b>

Numbers are absolute numbers; numbers in brackets indicate the fraction of total events in each category

#### 3.4.4.4 Transfer of siRNA into neighboring cells

A very interesting observation was a transport of released siRNA into neighboring cells. The event resembles an infection of the neighbor cell with labeled siRNA (see Figure 3.45 and Appendices L.30 for detailed signals of each channel).

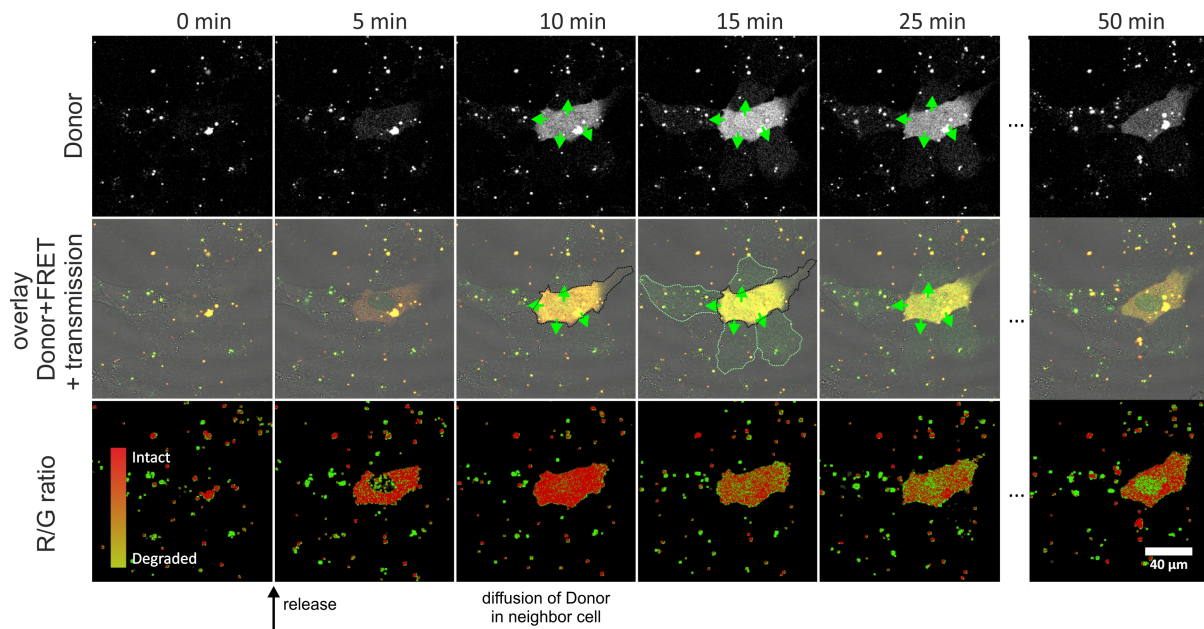


**Figure 3.45: Transfer of siRNA into neighboring cells.** RBE 4 cell transfected with Atto488/Atto590 siRNA showing release of intact siRNA transmitting green fluorescence in neighbor cells. After 160 min of transfection, the central cell shows release of intact siRNA. Depicted are the following 40 min with a detectable fluorescence in the the 4 surrounding cells. For better visualization donor channel is depicted as grayscale image besides the overlay (donor, FRET and transmission) and R/G ratio image. Green arrows at 10 min indicate a transfer of green fluorescence to 4 neighbor cells. At 15 min cell outline of mother cell (black) and daughter cell (light green) indicate a homogenous distribution of detected fluorescence.

One can see a central cell that shows no fluorescence at the beginning of the image sequence. After 5 min the release of intact siRNA into the cytoplasm is completed. After an additional 5 min, a release of green fluorescence into the four neighboring cells occurs (green arrows). The fluorescence is only detectable in the donor channel thus it is unclear whether the sense labeled siRNA or just the cleaved off dye has entered into the neighboring cell. As the signals are very weak a closer look at the R/G values does not give further insight as the intensities are below the R/G ratio algorithm thresholds used for classifying background and signal. In total 7.4% of all 328 observed cells showed such an infection, which makes an additional evaluation necessary.

In literature one can find reports of this behavior in plants, a process referred to as non-cell-autonomous or systemic RNAi [259–263]. In animal cells, reports from the early stages of RNAi research, report a cell-to-cell spread in *C.elegans* [8, 263, 264] and later first hints in mammalian [265, 266] or insect cells [267] were reported. So far no detailed insight into how a transfer in a neighbor cell occurs was made. Valiunas et al. [265] and Wolvetang et al. [266] refer to gap-junctions as possible sites of intercellular RNAi transport.

The data presented might be the first visual confirmation of siRNA or at least the sense strand being intercellular transported to neighboring cells and might give indication of non-cell-autonomous RNAi in mammalian cells. For confirmation whether a full length sense strand or just the label is transported an extension of the FRET siRNA

system might be necessary. By using so called triple FRET [268], a third dye is used to either act as a FRET donor for Atto488 or a potential FRET acceptor of Atto590 to result in interstrand FRET, whereas Atto488/Atto590 siRNA results in intrastrand FRET. Nevertheless a triple FRET system is much more complicated as three combinations of FRET pairs can be formed (see Figure 4.1 in Outlook, Chapter 4). In such a way degradation of one strand would lead to a collapse of the inter- and intrastrand FRET. A strand separation on the other hand would lead only to the collapse of the interstrand FRET.

#### 3.4.5 Detailed analysis of cellular release events

Most of the observations reported come from single experiments or events and do not give information on a whole population of cells. The presented events occur at different time points after transfection and show different fluorescence times of the labeled siRNA in the cytosol. The following section deals with general analysis of the observed release events (see Table 3.14).

##### 3.4.5.1 Starting release process

The first question that arises is the starting point of a cellular release after transfection and uptake. The recorded data made it impossible to narrow down the exact time point of uptake of the lipoplexes as within the first scanning sequences, fluorescent aggregates could be seen in each slices of the acquired z-stack and the entire cell population. This indicates an almost instant transfection or uptake of the the applied siRNA. Whether the detected fluorescence refers to lipoplexes on the surface of a cell or already delivered siRNA remains unclear.

The release processes were analyzed chronologically according to their appearance after the addition of the transfection mixture to the cells. Thus for all 328 release events the time of release after transfection and the duration of fluorescence being present in the cytosol of a cell was determined by visual inspection of the acquired data. Thereby a differentiation between category I and II was made (see Table 3.14).

Figure 3.46 A depicts a summary of the time points of release and duration of the 328 release events, by plotting lines for the presence of fluorescence inside the cytoplasm or entire cell. In Figure 3.46 B+C the same graphical representation is depicted for release events divided into category I and II (for the separate line plots of each single experiment see Appendices M.31). One can see a strong increase in the number of fluorescent cells within the first 35 min for the complete data set and the category II set. With a subsequent delay of 30 min a more moderate release rate could be detected. The length of events also differs and some cells show a secondary release indicated by

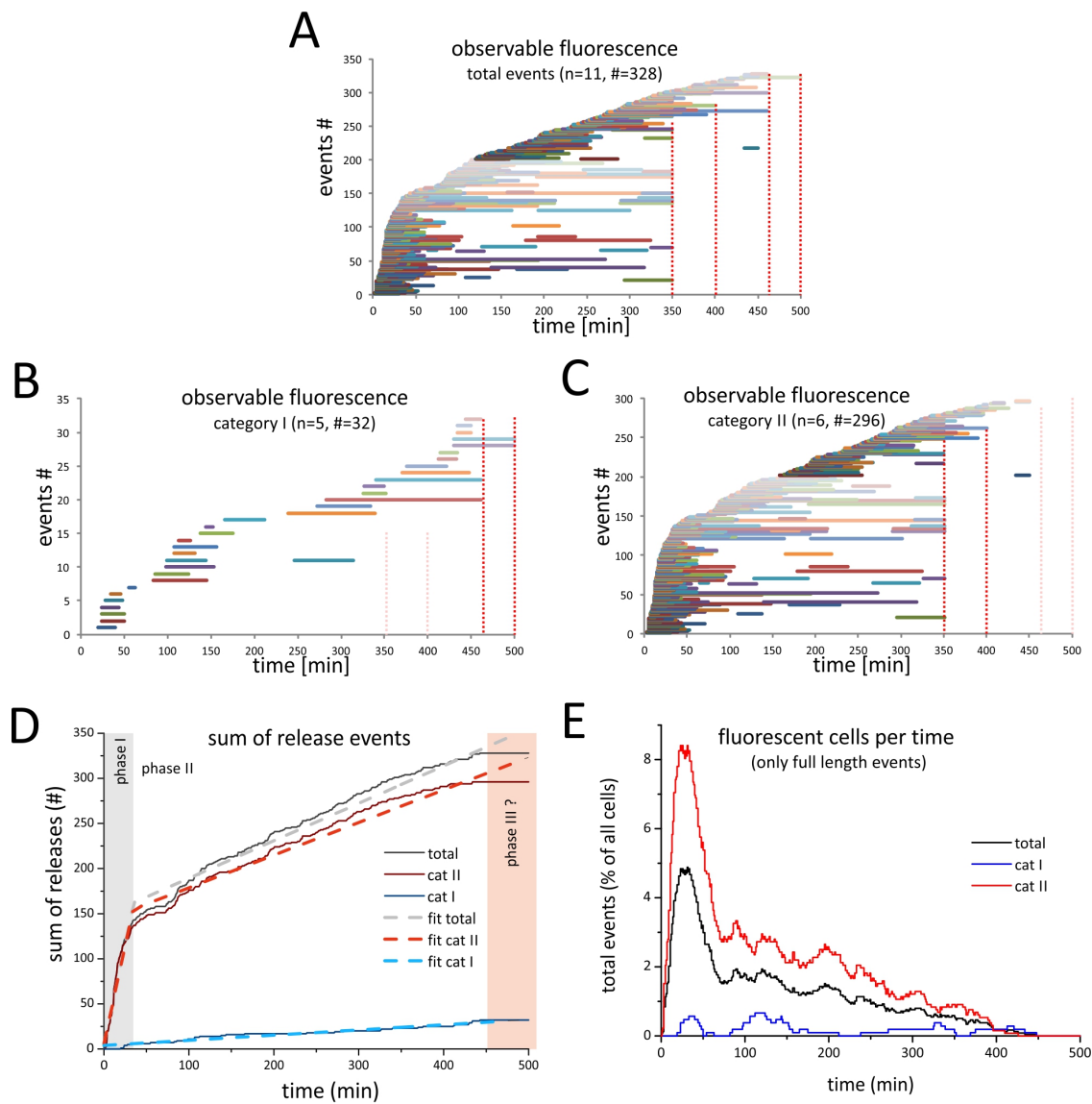


**Figure 3.46: Time point of release of siRNA into cytoplasm after transfection.** (A-C) line plots of release events, with each line representing one release events. Events were arranged in order of occurrence by increasing event number values (Y-axis). Red vertical lines indicate the termination of observations in some of the single experiments. (A) Summary of all 11 experiments with a total number of 328 release events. (B) Category I experiments (5 experiments with 32 release events) with only few observed events per experiment. Red lines at 460 and 500 min indicate stopped observations. (C) Line plot of category II experiments (6 experiments with 298 release events) with aborted experiments at 350 and 400 min. (D) Coverage curve of release time points, which corresponds to the envelope curve of (A-C), with a piecewise linear fit for category I (blue), category II (red) and total release events (gray). Shaded boxes indicate different release phases. (E) fraction of fluorescent cells per observed time point for total experiments, category I and category II experiments. Only full length events with depletion within the respective observation time were included.

**Table 3.16: Phases in cellular release after transfection**

	release		release rate per 100 cells [ 1/min]	
	phase I	phase II	phase I	phase II
category I		N/A		0.006
category II	0 - 34 min	34 - 450 min	0.33	0.12
total	0 - 35 min	35 -450 min	0.19	0.13

N/A: not applicable



interrupted lines referring to a depletion of fluorescence. The red dotted lines indicate the end of the observation time of the single live cell experiments.

For category I events a stronger increase in release events can be seen from 0-30 min and additionally 80-110 min. An additional release phase can be seen at 250 min with some releases until 410 min of incubation. At this point an additional increase in release events can be seen. In summary of all events this stepwise release could not be detected any more, neither can it be observed in category II events. This leads to the assumption that with many observed release events an averaging occurs that leads to finally only two phases which are dominated by category II events.

These two phases could also be confirmed by a closer look at the coverage curves (see Figure 3.46 D), which are simply the envelope curves of the line plots in Figure 3.46 A-C. A two phase linear model was fitted to the total number of release events and category II events. The interception point for the two parts is at 35 min for total events and 34 min for category II events. Thus one can distinguish two release phases, one initial with a strong release rate of  $0.33 \frac{\text{cells}}{\text{min} \cdot (100 \text{ observed cells})}$  for category II and a rate of  $0.19 \frac{\text{cells}}{\text{min} \cdot (100 \text{ observed cells})}$  (see Table 3.16) and a secondary phase with a release rate of 0.12 and  $0.13 \frac{\text{cells}}{\text{min} \cdot (100 \text{ observed cells})}$  for category II and total, respectively. As fewer cells seem to be released in the end ( $> 450$  min), one might assume a third phase with even less detectable releases. The distinction described could not be made for the experiments with less release events. For category I a release rate of only  $0.006 \frac{\text{cells}}{\text{min} \cdot (100 \text{ observed cells})}$  could be calculated for the complete observation time.

The last phase with less events in category II and the total plot might perhaps be related to the fact that some of the experiments were stopped before at 350 min and 400 min of observation. Thus less data was acquired in this potential last phase due to terminated experiments.

Additionally to the release starting point analysis, a closer look at the total amount of fluorescent cells per time point was made (see Figure 3.46 E). For this examination only full length release events were taken into account, meaning events that showed a complete depletion from the cytoplasm within the observed time frame.

The data confirms strong release rates at the beginning of the transfection with a maximum number of fluorescent cells at 25 min for category II, 32 min for total and 118 min for category I (see Table 3.17). This corresponds to a maximum of 0.7%

**Table 3.17: Maximal number of fluorescent cells**  
max number of coexisting fluorescent cells

	time point	number	[% of total]
category I	118 min	7	0.7
category II	25 min	111	8.4
total	32 min	116	4.9

fluorescent cells in case of category I, 8.4% fluorescent cells for category II and as average 4.9% of all cells in the observed region. Until the first experiments were aborted (350 & 400 min) category II experiments display at least 1% of fluorescent cells. For category I experiment the average fluorescent cell number ranges between 0 and 0.7% for the complete observation time. As less events were detected in category I, the total number of fluorescent cells is more constant compared to category II. With only few events in category I, the average fluorescent cell number for total events corresponds to approximately the half of the category II numbers.

Having a look at all events, including multiple releases and releases that might last longer than the observation time, higher fractions of fluorescent cells per time point were obtained at longer incubation times (for data of all different coverage curves see Appendices M.32). Nevertheless due to different observation times steps occur at the respective time in these representations.

### **3.4.5.2 Fluorescence time of siRNA in cytosol**

In addition to the starting point analysis for release events, the duration of each release process was determined. The duration of an event was determined by fluorescence time of the labeled siRNA in the cytoplasm. The event duration corresponds to the line length of each respective event in the event line plot in Figure 3.46 A-C. The analysis of the event length is depicted by a histogram in Figure 3.47 A.

Although an automated analysis of the histogram data by the Origin software suggested a binning size of 20 min, a bin size of 10 and 5 min was considered for a higher resolving analysis. On basis of finding local maxima in each histogram data, Gaussian populations were fit for each binning size. To compare the different fitted populations, a sum of curve was calculated and superposed with the histogram and single population fits. The 5 min bin size seems to best represent the data of the fluorescence time of siRNA inside the cytosol by assigning three different populations to the data sets (see Figure 3.47 B-D and Appendices M.33 for other bin sizes).

In Table 3.18 a summary of the average fluorescence time in the cytoplasm for three populations at bin size of 5 and one population at bin size of 20 can be found. The less detailed analysis at bin size of 20 resulted in an average fluorescence time inside the cytoplasm of 32 to 36 min for all three categories. The analysis with lower bin size of 5 resulted in only one population for category I, as too few events were detected in this class, whereas category II and total showed the three different populations mentioned earlier (pop I, II and III). Thereby the results for category II are more or less similar to the total data set, therefore in following only category I and II will be compared.

A closer look at these populations indicates that for all three classes a short duration population with an average fluorescence time of 24 to 27 min can be assigned (see Table

### 3.4 Observation of siRNA and integrity measurements in living cells

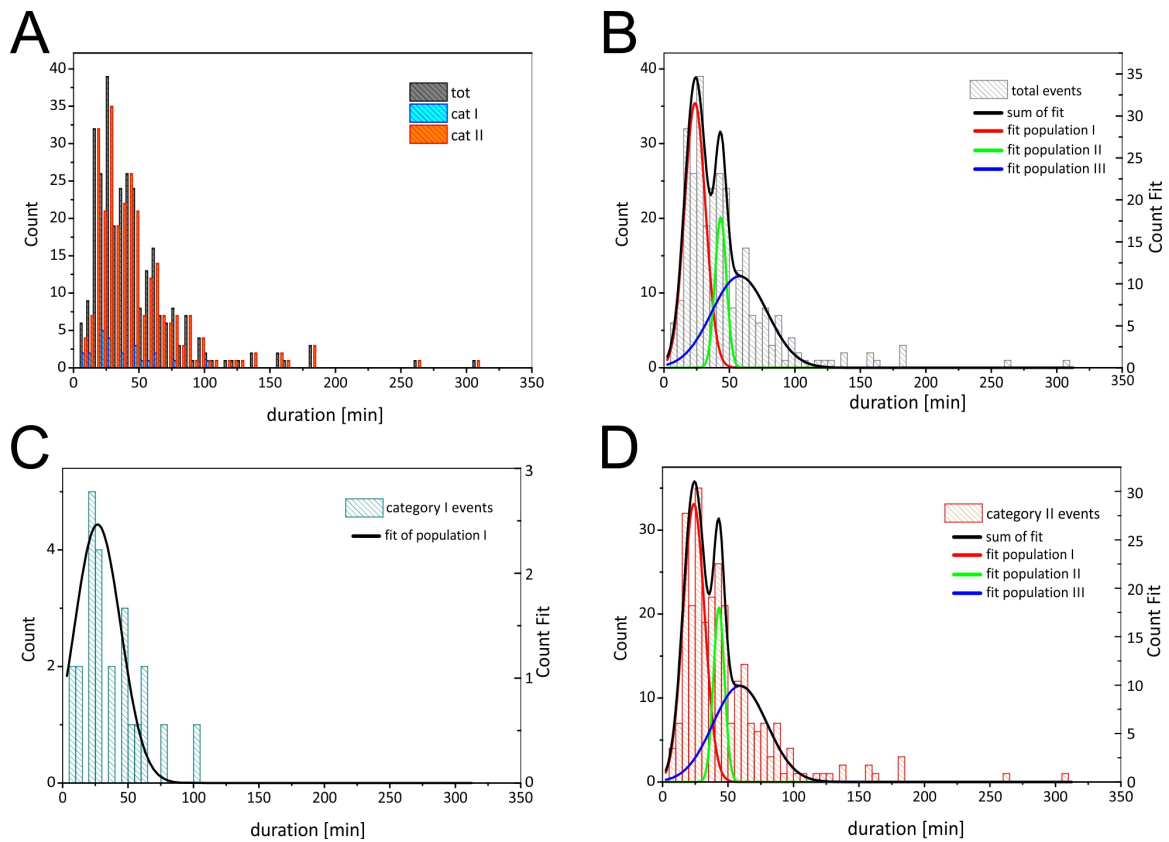


**Figure 3.47: Fluorescence time of released siRNA.** Fluorescence time in the cytosol of release events after transfection of Atto488/Atto590. Data is grouped in category I (blue in (A) and (C)), category II (red in (A) and (D)) and total (black in (A) and (B)). Histograms show fluorescence duration at a bin size of 5 min. Gaussian fits (B-D) for each population with a local maximum in the frequency distribution (population I = red; population II = green; population III = blue). On basis of each population of a category as sum of curve was calculated (black) (A) Summary of duration frequency of category I (blue), II (red) and total (gray) in one histogram. (B) Duration frequency of total events (gray columns), consisting of category I and II with three sub-populations (pop I-III; red, green, blue) and sum of curve (black). (C) Category I event duration frequency (blue columns) with the only fitted population I (black). (D) Category II event duration frequencies (red columns) with three sub-populations (pop I-III; red, green, blue) and summarizing envelope curve (black).

3.18). For category I this is the only population determined and the average fluorescent time is lower than in case of a bin size of 20. Besides this short duration population (pop I) additional populations with 43 min duration (pop II) and 59 min (pop III) were classified.

The analyzed populations with 24 and 43 min duration show a very narrow distribution, whereas population III with an average duration of 59 min shows a broad distribution (see Figure 3.47 B+D and Table 3.18). This indicates that population III is more

	mean fluorescence time in cytoplasm [min] *				% of covered data by fitted population			
	bin 5			bin 20	bin 5			bin 20
	pop I	pop II	pop III	pop 0	pop I	pop II	pop III	pop 0
cat I	26.7 (17.7)	NA	NA	32 (7)	100	NA	NA	100
cat II	23.9 (8.2)	43.1 (4.2)	59.2 (20.6)	35.7 (9.8)	46	15	40	100
total	23.7 (8)	43.3 (4.4)	57.7 (21.3)	35.4 (9.6)	45	14	41	100

\*: Numbers in brackets indicated absolute standard deviation; NA not applicable

inhomogeneous and contains release events with durations up to 300 minutes. These long fluorescence times might be related to multiple releases in one cells before a depletion of the fluorescence signal occurred.

For pop 0 in the 20 min bin size analysis the average fluorescence time of 36 min for cat II events corresponds approximately to the weighted average of the sub-population I, II and III obtained by the 5 min bin size analysis.

The question which of the presented analysis systems is the right or best is difficult to say. Both analysis address the same question, whereas one approach tries to provide a more detailed analysis. In consequence an average population pop 0 can be assigned which more or less splits in the different sub-populations I, II, III. Interestingly, when looking at the data covered for each sub-population, 45 % of the data lie within pop I, 15 % in pop II and 40 % in pop III. This indicates in general release events that get depleted faster or slower by yet to identify cellular mechanisms.

### **3.4.6 Single cell analysis of siRNA release**

In a final step a detailed analysis of the integrity state and fluorescence signals inside single cells was performed. Therefore each release event of one single live cell observation experiment, i.e. live-29 (see Appendices M.31, row 1, column 2), was subjected to a manual segmentation process for distinguishing nucleus and cytoplasm. In total 76 single events were so far segmented. On the basis of these regions, data for each time point were extracted resulting in a distinct profile for each cellular release event. In the following section the process of single cell analysis will be described and the current state of the analysis process specified.

#### **3.4.6.1 Workflow in single cell analysis**

An overview of the complete analysis process is depicted in Figure 3.48 and will be described shortly in following paragraphs. A more detailed description can be found in the method section 5.3.16.

After the acquisition of a 6D-image, which is actually an xy-scan (2D) with z-stacking (3D) over time (4D) with multiple channel detection (5D) at different positions (6D), separated TIFF-files for each channel were used to perform the R/G ratio analysis. In a next step xyz-t-stacks were constituted, including stacks for the RGB overlay of single channels, the R/G ratio images and R/G raw data with the calculated R/G values for each pixel (see Figure 3.48 D). The stacks were further subdivided into regions containing only one release event (event-ROI). After the manual selection of nucleus and cell outline for each release event the MFI values for donor, FRET and RAW-stack are measured. In an additional attempt the ratio of cellular R/G ratio pixels

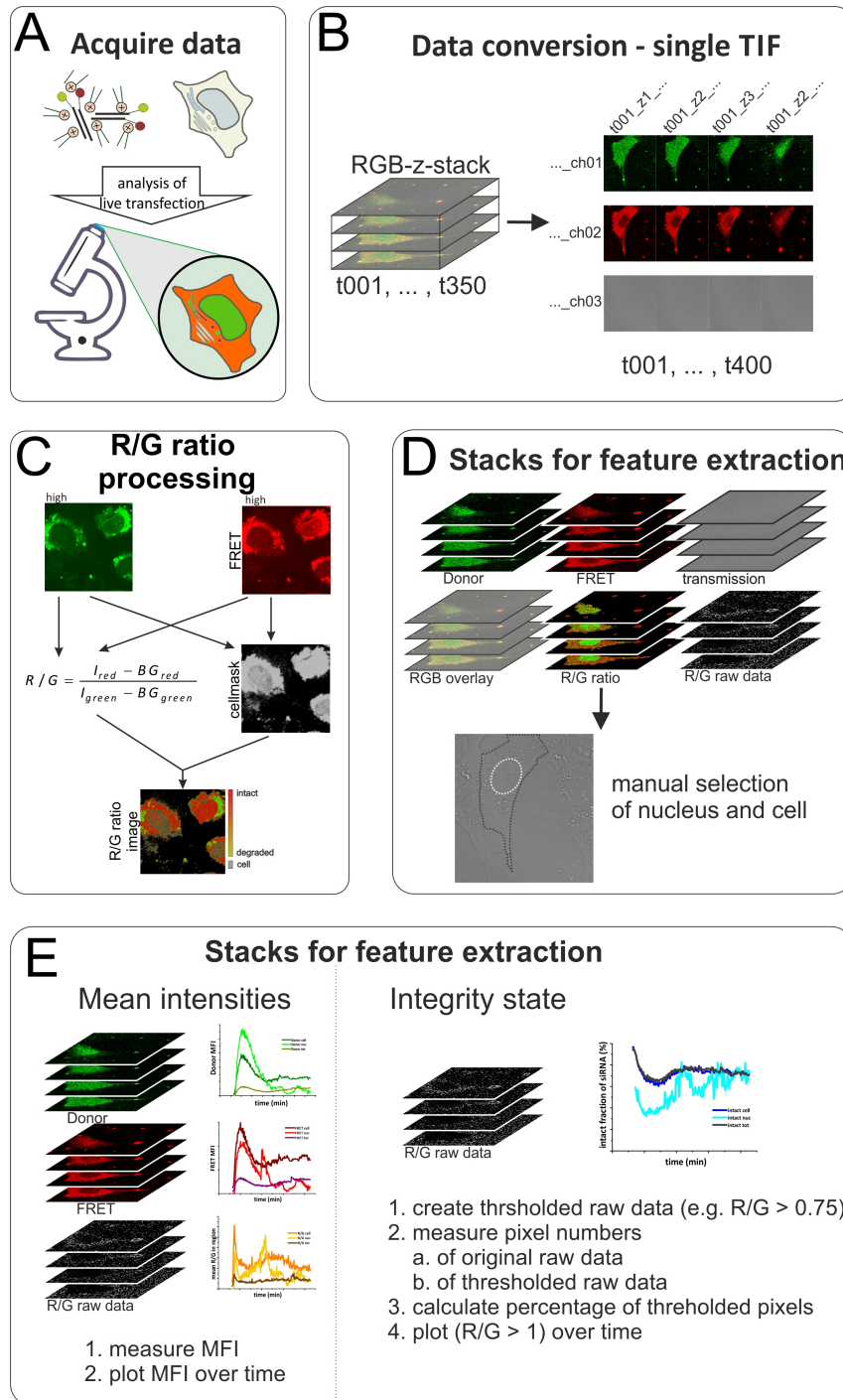


**Figure 3.48: Schematic representation of the workflow for single cell analysis.** (A) live cell observation of Atto488/Atto590 transfection with possibility of tile-scan and z-stacking. (B) Recorded data is separated in single TIFF-files with coding for recorded channels, z-position, tile-position and timeframe. (C) R/G ratio processing by calculating the R/G ratio on the basis of donor and FRET channel, resulting in R/G ratio image and an R/G raw data file. (D) For each signal, i.e. donor, FRET, transmission, R/G ratio image a xyzt-stack is built and used for merging the donor-FRET-transmission RGB overlay. Raw data is imported and also built to an xyzt-stack. For each release event a subregion of the original stack is cropped and used for further analysis (event-ROI). With help of the substacks segmentation of the nucleus and cell outline is performed. (E) *left side*: For nucleus, cell and total event-ROI MFI values are measured for each timeframe an z-slice. The final graph depicts z-averaged MFI or R/G value for a single event and fluorescence channel. (E) *right side*: Integrity measurement by thresholding Raw-stack and determining total pixel numbers and thresholded pixel numbers for nucleus, cell and total image. The ratio of thresholded to complete pixels numbers represents fraction of intact siRNA (integrity state above selected threshold value).

above a threshold of 0.75, which corresponds to siRNA with more than 85 % of intact siRNA (according to calibration data), to all cellular R/G ratio pixels was determined. This value was used for classifying pixels that are related to siRNA at an high integrity state.

### 3.4.6.2 Example of cellular release

A first screening of the detailed analysis of the 76 processed events revealed a similar initial release behavior for most cells. In Figure 3.49 a snapshot of an event is depicted that shows a longer fluorescence time in the cytosol (a detailed time-lapse representation can be found in Appendices N.34 & N.35). For this cell a release event can be observed approximately 3 h 36 min after transfection.

The overlay shows a strong FRET signal indicating intact siRNA in the cytoplasm which is confirmed by the R/G analysis. At 3 h 41 min only weak fluorescence is detected inside the nucleus which is also below the threshold of R/G analysis. As the experiment proceeds the cytosolic signal turns from deep red to orange, whereas the nuclear signal shows a green dominated fluorescence (3 h 46 min). The R/G ratio analysis confirms a population of intact siRNA at a high integrity level in the cytoplasm and a population with a lower integrity level in the nucleus. In a next step intact siRNA enters the nucleus at 3 h 51 min with an additional increase in overall fluorescence intensity of both channels. In the the next image (4 h 01 min) the overall fluorescence drops again and the nucleus shows again only decomposed siRNA. With ongoing observation until 5 h 11 min the fluorescence is almost completely depleted (complete depletion at 5 h 40 min) from the cytosol resulting in an overall event length of approximately 2 hours. Over the complete observation time intact siRNA, meaning FRET, could be detected.

The long fluorescence time of 2 hours makes this release event a member of the population III events (see Section 3.4.5.2). As mentioned population III might contain multiple release events which is difficult to identify in the presented event. Maybe one can identify a second release event at 3 h 51 min. At this time point an additional strong increase in fluorescence is detected. Nevertheless no further releases can be assigned until the final depletion after 2 h of observation.

This suggests different classes of release events tentatively classified in strong and weak releases. Here a strong release would lead to a longer detectable fluorescence in the cytosol whereas a weak release is depleted faster from the cytoplasm.

In Figure 3.50 A1-A4 the exact changes in fluorescence, R/G value and intact fraction of siRNA over time of the example release are depicted. The plot confirms the observation made by visual inspection of the image sequence. In the beginning the donor and FRET signal increases in both nucleus and cell. The shoulder at 225 min might

### 3.4 Observation of siRNA and integrity measurements in living cells

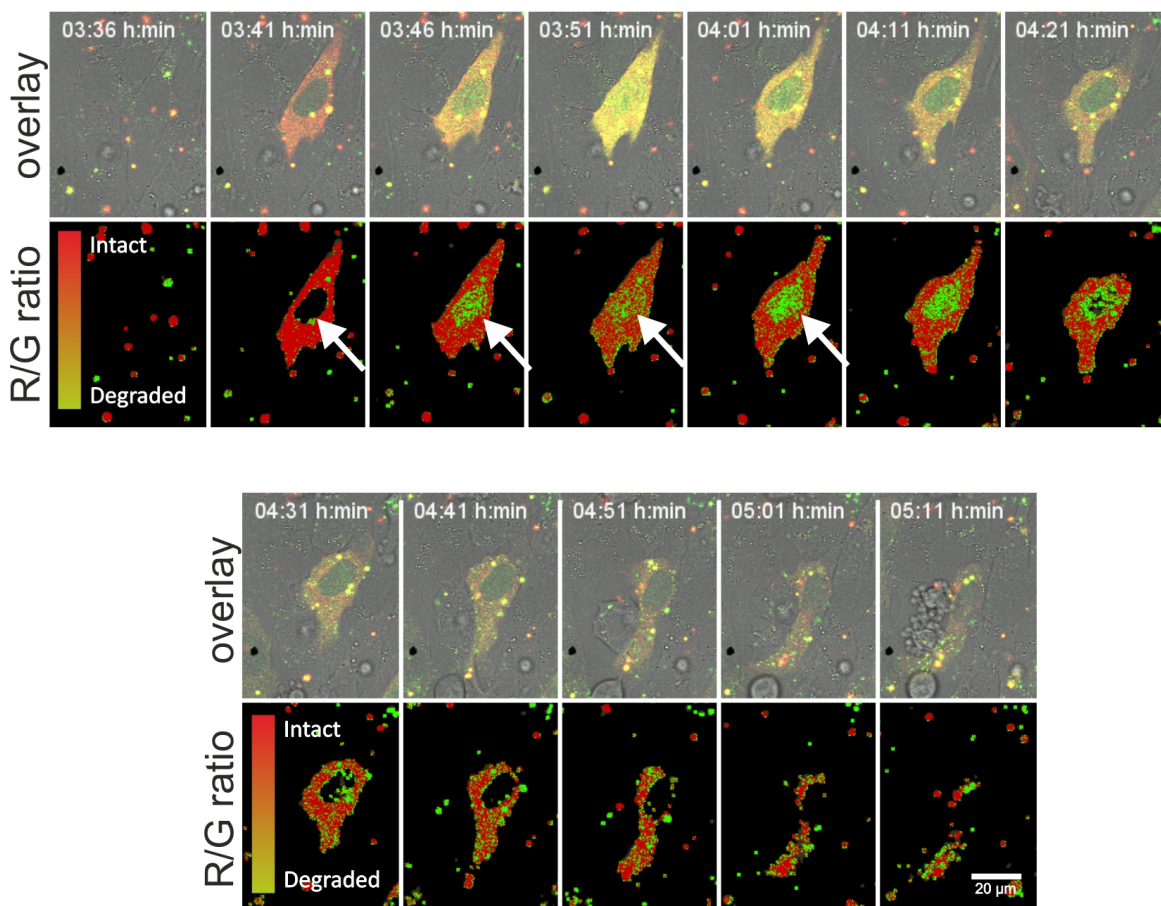


**Figure 3.49: One example of a long release event of Atto488/Atto590 siRNA in RBE4 cells.** Sequence depicts a release at 3 h 40 min after transfection. Displayed are the overlay of donor, FRET and transmission channel (first row) and the calculated R/G ratio image (setA). White arrows point to nucleus which first shows little fluorescence and later a changing integrity state according to the R/G analysis. Donor and FRET fluorescence can be detected up to 5h after transfection indicating a long persistence in the cytosol. Data represents a snapshot of a 1 min interval acquisition.

indicate the before mentioned second release. One can also see that in the beginning cell fluorescence is stronger for both donor and acceptor signal and relatively fast fluorescence increases inside the nucleus. In addition, the FRET signal drops faster below the cell value than the donor signal, again indicating degraded siRNA in the nucleus. The analysis of average R/G values show an average R/G higher than 2 for the complete cell over the complete time, representing on average intact siRNA inside the complete cell. The average nuclear R/G drops similarly as in the complete cell from a high value at the beginning to an average R/G of 1 at around 240 min, corresponding to the time point when most pixels were classified green in the R/G ratio image. The following rise is probably caused by a reduction of classified pixels and thus a boosting of the average ratio.

At around 280 min most of the fluorescence is already depleted from the cytoplasm and nucleus. An MFI of 10 in the nucleus and 25 in the cell can be determined compared to a maximal MFI higher than 60 for the cell and 100 for the nucleus, which is true for

both donor and FRET signal. Later the data is more prone to fluctuations due to less classified pixels.

A look at the fraction of intact siRNA in the nucleus and cell showed a larger fraction of intact siRNA in the cell as expected from the image data, but also in nucleus (which is colored green in the R/G image) contains still 45 % of pixels with a integrity level higher than 80 %. The data after 280 min again shows more fluctuations due to less pixels with intensities (and thus R/G values) over the background threshold.

To summarize, until 280 min the depicted MFI, R/G and fraction of intact siRNA can be used to describe the release event. With longer incubation, meaning depletion and thus further lowering of the mean fluorescence signals, more pixels are not taken into account for R/G calculation as the signal is below the background threshold and stronger fluctuation is observed, with strong increase in integrity over time. This rise can be caused by remaining intact, internalized lipoplexes that mask the signal of cytosolic siRNA.

### **3.4.6.3 Example of nuclear import**

Another observation made during screening single cell data was nuclear accumulation of intact siRNA at later time points. In Figure 3.51 the snapshot of a release event with later nuclear import of intact siRNA is depicted (a detailed time-lapse representation can be found in Appendices N.36 & N.37). The example shows no import of intact siRNA into the nucleus in the beginning. A clear separation of intact siRNA in the cytoplasm and degraded siRNA in the nucleus can be seen until 1 h 31 min. At 1 h 41 min a sudden strong FRET signal inside the nucleus can be observed with extranuclear siRNA showing more signs of degradation. With ongoing observation, total fluorescence decreases further and the integrity state in the cytoplasm seems to increase again (more red pixels in R/G ratio image).

The intact siRNA in the nucleus displays a kind of aggregation in small nuclear foci as earlier described (see Section 3.3.5.1 and 3.4.1.3). As this observation was made in different experiments, closer investigation of these foci should be performed to identify these structures.

The example chosen represents a longer lasting release event as in pop I or II no similar changes in cellular distribution could be observed so far.

The detailed analysis in Figure 3.50 B1-B4 depicts the described release behavior shown in Figure 3.51. Similar to other observed release events a fast initial increase in overall fluorescence is followed by a continuous decrease in fluorescence. In this second example the average FRET fluorescence inside the nucleus is much lower than the overall cellular fluorescence, whereas the donor signal shows a stronger signal in the nucleus over a certain time period. At around 100 min a sudden increase of the FRET



### 3.4 Observation of siRNA and integrity measurements in living cells

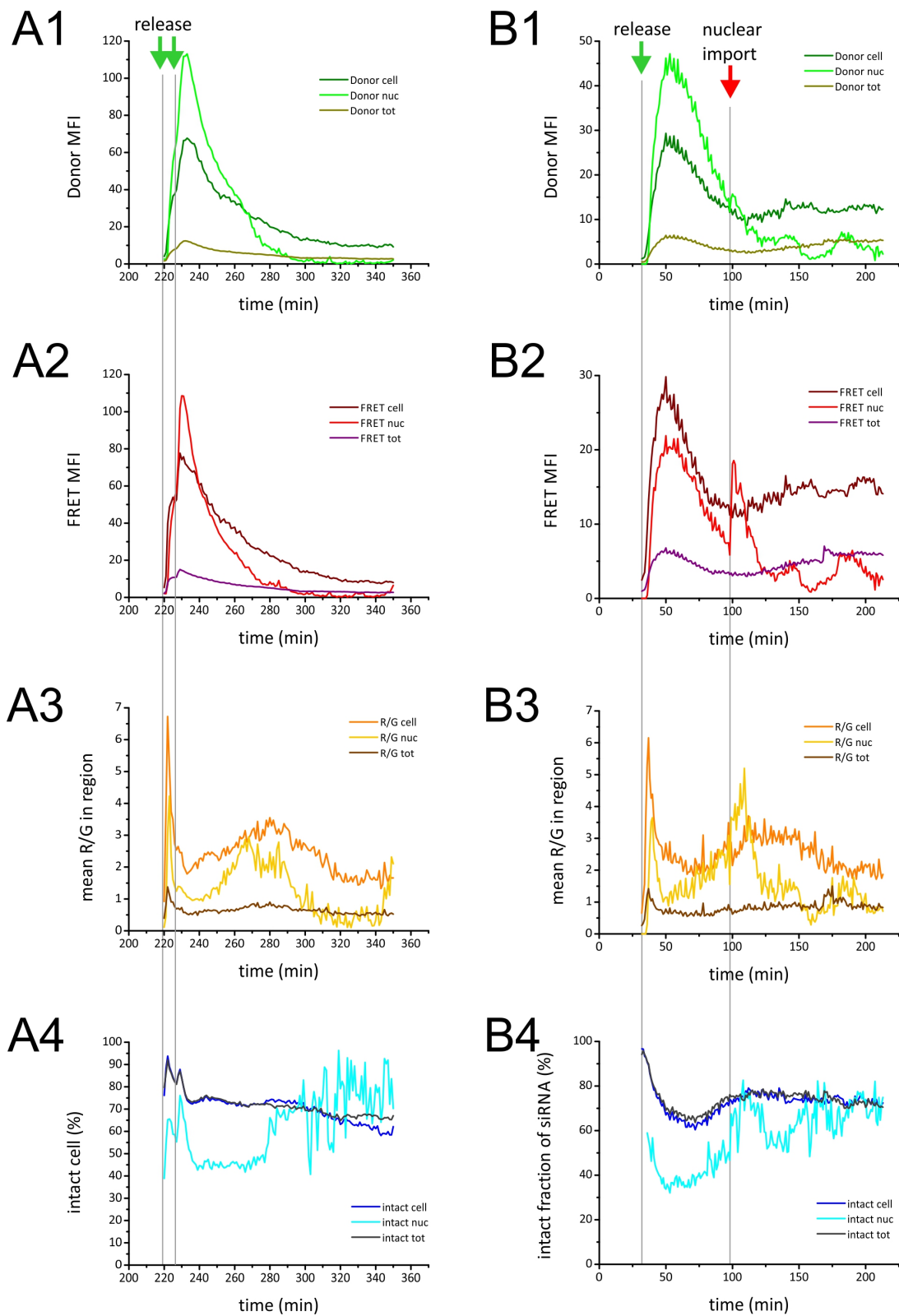


**Figure 3.50: Single cell analysis data of siRNA release.** Data of two release events in two different cells (AX and BX). The MFI values for the donor (graph X1) and FRET signal (graph X2) are shown for the nucleus, cell and the total analyzed region including non-cell pixels (tot). The averaged R/G value can be found in graph X3 including only values above the R/G background threshold. In the last row (graph X4) the fraction of intact siRNA pixels is depicted. In column 1 (AX) the gray lines indicate the different releases. In column 2 (BX) the gray line indicates the cellular release (green arrow) and the import of intact siRNA into the nucleus (red arrow).

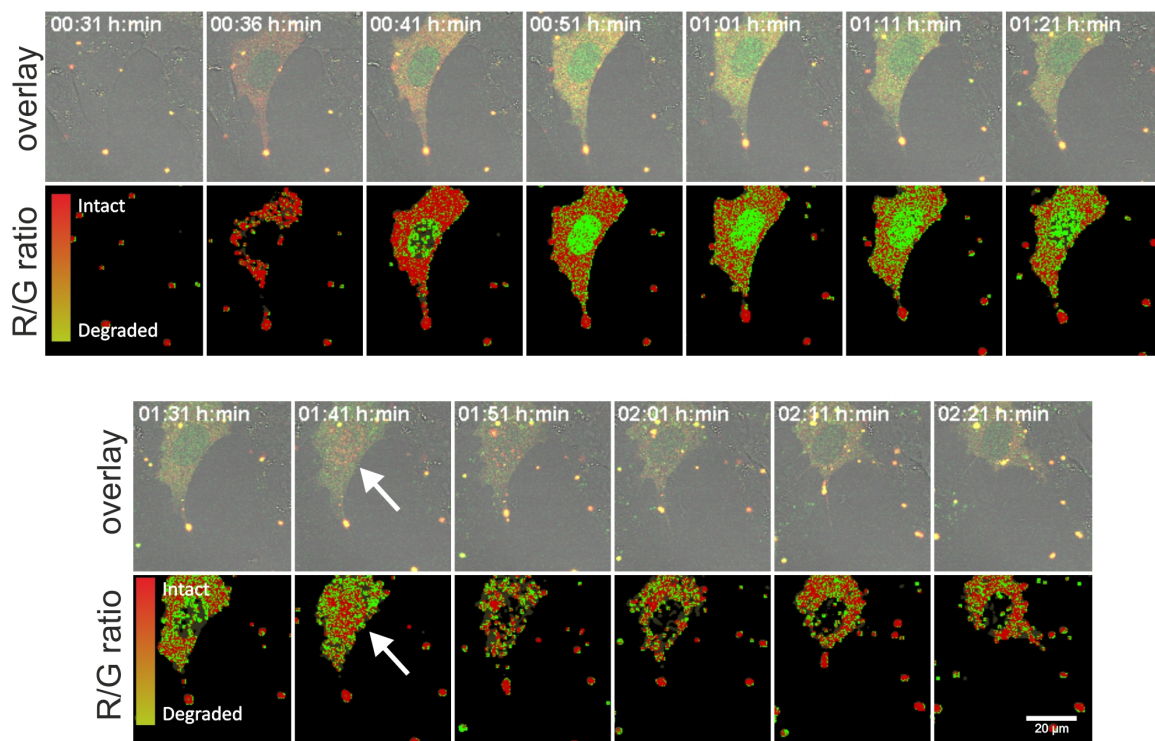


**Figure 3.51:** Release event that shows a later import of intact siRNA into the nucleus. Sequence depicts a release at 0:35 h:min after transfection. Displayed are the overlay of donor, FRET and transmission channel (first row) and the calculated R/G ratio image. White arrow at 1:41 h:min points to import of intact siRNA into the nucleus. Donor and FRET fluorescence can be detected up to 2h 40 min after transfection indicating a long persistence in the cytosol.

fluorescence inside the nucleus could be observed. This increase also leads to a higher average R/G ratio, as visible by more red pixels in the R/G ratio image, and a rise of the overall fraction of intact siRNA in the nucleus. Though in the beginning the R/G ratio image depicts only green pixels inside the nucleus still 40% of the pixel are assigned with an R/G ratio that is higher than 0.75. The amount of intact siRNA in the cytoplasm lies in a range of 70-80% (similar to the first release example).

In summary the single cell analysis shows a fast increase of donor and FRET signal with subsequent depletion of both signals. The lower the overall release intensity, the shorter the duration of the event. This indicates an active depletion process of the siRNA released. The shape of the declining fluorescence resembles an exponential decay which should be investigated further by trying to fit a model to the fluorescence decay determining the half-life of siRNA in the cytosol.

Second releases result in an additional strong increase in both fluorescence signals. Intersection points of nucleus and cell curves might represent interesting time points for future screening for changes in cellular distribution.

Spikes in the respective fluorescence curves either indicate the sudden decomposition of the siRNA (spike in donor signals) or the accumulation of an intact siRNA population (spike in FRET signal).

The analysis of the average R/G ratio might not be necessary or useful as pixel with

rather high values (R/G values over 10 are calculated) will superimpose the lower values. The approach of thresholding R/G raw data might be extended to different integrity states creating the possibility to get a impression of the integrity distribution over time. Nevertheless the large changes in later time points of the release events is probably caused by a drop of the original fluorescence below the R/G signal threshold used for calculation the R/G ratio. In consequence this approach is not valid below a certain level of fluorescence or R/G classified pixels.



# 4 Conclusion & Outlook

## 4.1 Conclusion

In the work presented here a new FRET pair for the measurements of siRNA duplexes integrity has been successfully evaluated and used for *in vitro* applications in both the cuvette and in living cells.

### New FRET siRNA systems

The Atto488/Atto590 siRNA system showed enhanced photophysical properties, regarding resistance to photobleaching, compared to FL/TMR FRET siRNA. While FL was bleached within minutes, Atto488 showed strong fluorescence even after 10 hours of permanent excitation in the cuvette. The microscopic analysis showed no severe bleaching within the range of performed time-lapse analysis. In addition, the Atto488/Atto590 showed no spectral shifts as detected for FL/TMR over long time excitation. Due to a better spectral separation less cross-talk, i.e. bleed-through and cross-excitation, occurs which makes Atto488/Atto590 siRNA the gold standard for ongoing live cell imaging observations.

Additional FRET siRNA systems have been evaluated and proven suitable for integrity measurements. They are located in the blue, i.e. Atto390/Atto550, or red, i.e. Alexa555/Atto647N, range of the visible light spectrum (see Figure 3.9 and 3.10). In addition, a direct replacement of FL/TMR, i.e. Alexa488/Atto550, was tested which displayed a higher FRET efficiency and thus attenuates the effects of crosstalk compared to the FL/TMR system. A final interesting system is based on Atto390/Atto647N, in which the donor and acceptor dyes are placed at both edges of the visible spectrum, which would allow to use additional dyes between the FRET pair spectra.

The evaluated FRET siRNA displayed a dynamic range that allows a sensitive quantification of the integrity states of siRNA samples down to level of 80 % of intact siRNA (see Figure 3.13). At lower integrity levels inaccuracies may occur. For low integrity levels the Alexa555/Atto647N siRNA displayed a better dynamic range (down to 50 %), which makes this construct suitable for evaluation studies in the cuvette to test RNase protection of new delivery systems.

With the help of FRET siRNA, a monitoring of the formulation process of nanoparticulate siRNA can be performed, as described for the entrapping of siRNA in liposomes by DAC. The survey showed a successful encapsulation of intact siRNA and the system can be used to monitor degradation processes that might occur upon storage of the formulated siRNA samples. In consequence the FRET siRNA can be used to evaluate potentially new delivery systems with regard to their compatibility with siRNA, which is susceptible to decomposition upon harsh treatment (e.g. pH, temperature and contaminations with RNases). The performed evaluation of different delivery systems classified liposomes, one type of nanohydrogel and cationic peptides as optimal for protection of siRNA against nucleases (see Figure 3.18) and several other tested systems with medium or little protective effects (see Table 3.8). Nevertheless, besides protection, a release of the complexed or formulated siRNA at the target site is also essential for therapeutic purpose. In a next step the release of siRNA from the evaluated nanoparticles needs to be investigated, which is done by [REDACTED] at the moment. By a heparin displacement assay the release capability is determined and a gene silencing assay addresses the potential for delivering active siRNA into cells.

The presented siRNA FRET systems allow to choose a FRET system that best fits the spectral requirement for a certain experiment or experimental setup.

### **FRET siRNA in fixed cells**

The Atto488/Atto590 system proved superior to FL/TMR in fixed cells, as no crosstalk, i.e. bleed-through and cross-excitation, was detected in the respective controls. Whereas the FL/TMR system displayed crosstalk signals of around 35-40% the optimized Atto488/Atto590 siRNA showed crosstalk values below 5% (see Section 3.3.2). This behavior makes Atto488/Atto590 ideal for imaging as detected signals in the FRET channel are caused by FRET between donor and acceptor and not due to bleed-through or cross-excitation of the respective donor or acceptor.

Additional studies, concerning the bleaching resistance of Atto488/Atto590 in cells, resulted in only moderate bleaching rates over a shorter time, which would allow to detect released siRNA for at least 6-8 h. In this simulated time frame (by rapid excitation cycles in a small ROI) fixed cells lost around 40% of the initial detected fluorescence. The acquired data suggests that even longer observation times are possible, without a complete loss in fluorescence due to bleaching.

With this information an adaptation of the R/G ratio algorithm for Atto488/Atto590 was performed, allowing to discriminate between intact, partly degraded and degraded siRNA. With the R/G thresholds adapted to 0.5 and 1.2, siRNA populations with an integrity level above 95% are colored red and siRNA populations with an integrity state

below 80 % are colored green. Partly degraded siRNA with integrity levels between 80-95 % are visualized in colors ranging from green to red in the R/G ratio image. This allows an easy way to recognize populations that contain a higher amount of intact siRNA.

The assessment of integrity inside cells shows, that though a degradation of transfected siRNA might occur, the transfected samples display a R/G ratio distribution that match the theoretical integrity level.

In a final analysis of fixed cells transfected with FL/TMR siRNA, before the optimized Atto488/Atto590 siRNA was established, temporal changes in cellular distribution were investigated. The data, based on approximately 50 analyzed cells for each timepoint showed, however, no significant changes in cellular distribution in the investigated time range of 0.5 h to 48 h (see Section 3.3.5). The observed nuclear accumulation of intact siRNA could not be assigned to one incubation time but seemed to be a random process in an inhomogeneous cell population. This observation of a random release process was later confirmed by live cell studies.

## **FRET siRNA in living cells**

The live cell observation of transfected cells represents an optimal technique to investigate the uptake and release process of siRNA. Thereby, the use of Atto488/Atto590 labeled siRNA allows to determine the integrity level in real-time. So far, no cellular costaining for lysosomes, ER, Golgi or nucleus was included in the long-term observation studies due to compatibility problems of the used dyes and potential costains. The Atto488/Atto590 siRNA requires costains that emit in the far-red range like the mentioned LysoTracker Deep-Red. The costaining for different cellular organelles is indispensable for a correct assignment of siRNA population to a certain organelle. The usage of Alexa555/Atto647N siRNA might offer the possibility to use green stains, which are available for almost every organelle, instead of the few far-red stains that can be combined with Atto488/Atto590.

The costaining attempts performed so far, showed compatibility of the LysoTracker dyes with single labeled siRNA in short-time observations but over time the signal of the costaining got diluted or bleached. An evaluation of the respective costains for long-term imaging was not yet done.

The live cell transfection of RBE4 cells showed cellular releases of transfected lipoplexes resulting in strong signals of intact siRNA inside the complete cytosol of a cell. The release occurred very fast, meaning within one scanning cycle of 1 min the entire cytoplasm was already colored by the released siRNA. The signal increased to maximum intensity within a few minutes before a depletion of cytosolic siRNA occurred, leaving

small aggregation sites inside the perinuclear region. First preliminary results indicate the presence of small fractions of intact siRNA in these accumulation sites. So far the process for depletion remains unclear but autophagy or lysosomal recycling mechanisms might be involved. On basis of the bleaching data in fixed cells, bleaching can be ruled out, leaving only an active cellular process responsible for the clearance of cellular released siRNA.

The start of release could, so far, not be narrowed down to a certain time point after transfection or uptake (see Section 3.4.5.1). What could be observed was an initial fast release phase direct after transfection, followed by a moderated release rate. These initial frequent releases might be related to stress-based uptake by the applied cationic lipids which attenuates over time.

The overall duration of free siRNA being present in the cytosol differs among the observed release events. A detailed analysis revealed three different populations of release events with average fluorescence times of 24, 43 and 57 min (see Section 3.4.5.2). Nevertheless, release events lasting for up to three hours were also observed. In case of these long release events, an additional investigation might be necessary to confirm these releases as single or multiple release events. In addition, releases that depict an initial strong release of siRNA seem to display longer fluorescence time in the cytosol, which would confirm a constant depletion mechanisms.

A nuclear accumulation of siRNA, as earlier observed in fixed cells, could be observed in living cells, too (see Section 3.4.6). In the beginning of most release events, intact siRNA could be seen inside the nucleus whereas over time the integrity level decreases. It remains unclear whether the detected donor dominated signals are caused by ss sense siRNA or by free dye that had been cleaved from the duplex.

Another observation that faces the same problem was a transfer of green fluorescence to neighbor cells (see Section 3.4.4.4). Again free dye, or the intact sense strand can be responsible for the observations. Literature reports this non-cell-autonomous or systemic RNAi but so far no visual observation in mammalian cells was made.

During the screening of many live cell imaging data nuclear accumulation sites of intact siRNA or cytoplasmic connection of delivered siRNA aggregates have been observed in some cells but the numbers are probably too low to be generalized.



## 4.2 Outlook

The presented FRET siRNA systems proved their suitability in investigating siRNA integrity. With the help of FRET labeled siRNA the formulation of new potential delivery systems can be evaluated and tested towards RNase protection. In cell studies single releases of Atto488/Atto590 have been analyzed but a huge set of data needs to be further analyzed. Therefore, a bioinformatical approach using automated or semi-automated algorithms to segment cells and analyze the fluorescence distribution is necessary. This way a robust statement on the release behavior of delivered siRNA can be made.

In addition to cationic lipids the uptake mechanisms of other delivery systems need to be compared to the presented and future results. By usage of endocytosis inhibitors, like amiloride (macropinocytosis [269]), chlorpromazin (clathrin dependent endocytosis [270]), genistein (caveolae dependent endocytosis [271] or other inhibitors [272]), the uptake pathway for the respective formulation can be determined or narrowed down. To address the question whether the free dye or an intact ss sense siRNA is detected by strong donor signals, a triple FRET system might be used (see Figure 4.1). By attaching an additional dye in the middle or other end of one strand of the FRET siRNA duplex, intrastrand FRET would confirm the integrity of the respective strand, whereas interstrand FRET confirms the duplex integrity.

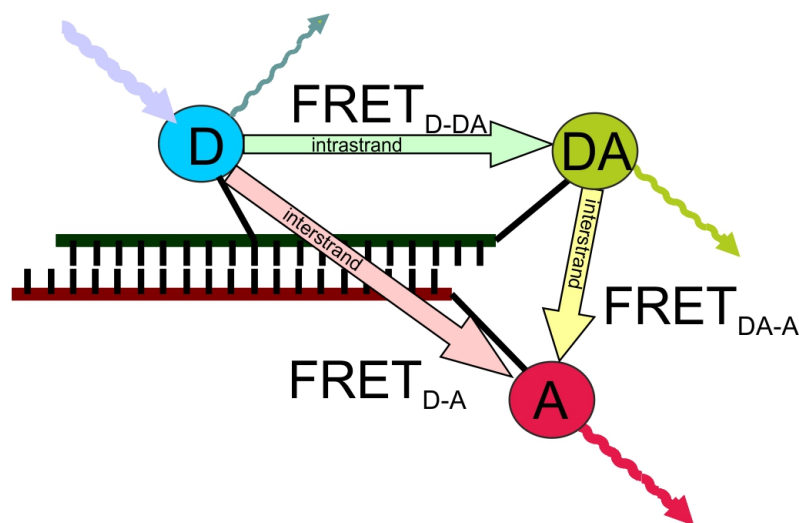


**Figure 4.1: Triple FRET system.** Scheme of a possible triple FRET construct with one donor dye (D), one dye that can act as donor or acceptor dye, respectively (DA) and a final acceptor (A). FRET can occur between D and DA ( $\text{FRET}_{\text{D-DA}}$ ), DA and A ( $\text{FRET}_{\text{DA-A}}$ ) and D and A ( $\text{FRET}_{\text{D-A}}$ ).

The use of a pro-dye concept, as it is at the moment established in the Helm lab by [REDACTED] as “*First contact imaging*”, that triggers fluorescence upon uptake and contact with cellular enzymes might solve the question of the origin of a release event. In this system a non-fluorescent pro-dye, which is actually a functionalized and thereby inactivated fluorophore, is attached to either siRNA or nanoparticle and upon cleavage of the functionalization the fluorophore is restored. This would allow to image the point of uptake or the release site into the cytosol.

Especially the observed speckles inside the nucleus or the connection of cellular aggregates containing siRNA need a further analysis to clarify their purpose and function in the cellular machinery and RNAi. The introduction of FP-tagged proteins as selective organelle costainings might give insight in this phenomenon.

The hypothesis of transfection stress itself triggers a release or change in nuclear localization could so far not be verified. The attempt of a second transfection with another population of labeled siRNA resulted in only few release events not allowing to draw a conclusion. Therefore additional live cell observation of the transfection process including a second transfection need to be performed.

Atto488/Atto590 proved as a versatile tool for investigating the whereabouts of delivered siRNA. First observations were made but an extensive analysis and further studies are necessary to elucidate the cellular fate of siRNA.

# 5 Materials & Methods

## 5.1 Materials

### 5.1.1 Chemicals, enzymes, reagents, ready-to-use buffers and media

Acetic acid	Merck (Darmstadt, Germany)
Ammonium persulfate (APS)	Carl Roth
Ampicillin	Carl Roth (Karlsruhe, Germany)
bFGF, human recombinant	Invitrogen (Karlsruhe, Germany)
Bromphenol Blue	Sigma-Aldrich (St. Louis, USA)
Cholesterol	Sigma-Aldrich
Collagen, Type I, from rat tail #C3867	Sigma-Aldrich
DAKO fluorescent mounting medium #S3023	DAKO Cytomation (Hamburg, Germany)
4',6-diamidino-2-phenylindole (DAPI)	Sigma Aldrich
Dimethyl sulfoxide (DMSO)	Fluka (Buchs, Germany)
Disodium hydrogen phosphate (Na <sub>2</sub> HPO <sub>4</sub> )	Carl Roth
D-MEM indicator free with HEPES #21063	Gibco
D-MEM, #61965	Gibco (Invitrogen)
D-MEM:F-12 (1:1) indicator free, #11039	Gibco
D-PBS, #14190	Gibco
Ethylenediaminetetraacetic acid (EDTA)	Carl Roth
EndoFree Plasmid Maxi Kit	Qiagen (Hilden, Germany)
Ethanol, absolute	Carl Roth
Fetal bovine Serum, #10500	Gibco
Formaldehyde 36,5 %	Carl Roth
Formamide	Sigma-Aldrich
GelRED	Biotium (Hayward, USA)
Glycerol	Sigma-Aldrich
Ham's F-10, #41550	Gibco
Hellmanex®	Hellma (Müllheim, Germany)
HEPES	Sigma Aldrich
Hoechst 33342	Sigma Aldrich
Hydrochloric acid (HCL)	VWR (Darmstadt, Germany)
Hydrogen peroxide (H <sub>2</sub> O <sub>2</sub> )	Carl Roth
Hydrogenated egg phosphatidylcholin (EPC3)	Lipoid (Ludwigshafen, Germany)
Isopropanol	AppliChem (Darmstadt, Germany)

## Materials & Methods

---

Kanamycin	Fluka
LB-Agar (Lennox)	Sigma-Aldrich
LB-Broth (Lennox)	Carl Roth
Lipid mixture EPC3 : Cholesterol (55:45)	Lipoid
Lipofectamine 2000	Invitrogen
LysoTracker®Blue	Molecular Probes (Invitrogen)
LysoTracker®Green	Molecular Probes
LysoTracker®Red	Molecular Probes
Magnesium chloride (MgCl <sub>2</sub> )	Merck
Monosodium phosphate (Na <sub>3</sub> HPO <sub>4</sub> )	Carl Roth
MPEG-2000-DSPE	Lipoid
Oligofectamine	Invitrogen
OptiMem, #31985	Gibco
PAGE buffer, denaturing #3050.1	Carl Roth
PAGE concentrate 25 %, denaturing #3043.1	Carl Roth
PAGE diluent, denaturing #3047.1	Carl Roth
PAGE concentrate 19:1, 40 % #3030.1	Carl Roth
Penicillin-Streptomycin liquid, #15140	Gibco
Potassium chloride (KCl)	AppliChem
Potassium dihydrogen phosphate (KH <sub>2</sub> PO <sub>4</sub> )	Carl Roth
RedDot™1	Biotium
RNase V1, 0.1 U/μL, #AM2275	Invitrogen
RPMI 1640, #61870	Gibco
RPMI 1640, indicator free #61835	Gibco
Sodium chloride (NaCl)	Carl Roth
Sodium pyruvate 100mM, #11360	Gibco
Stains-All	Sigma-Aldrich
Sulfuric acid (H <sub>2</sub> SO <sub>4</sub> )	Merck
TBE 10x buffer #3061.1	Carl Roth
TEMED	Carl Roth
Tris-Base	Carl-Roth
Tris-HCl	Carl-Roth
Trisodium phosphate (Na <sub>3</sub> HPO <sub>4</sub> )	Carl Roth
Trypsin EDTA 0.05 %, # 25300	Gibco
Xylene Cyanol	Sigma Aldrich

All chemicals and solvents not included in the list were provided by the institute's chemical store (1<sup>st</sup> floor, Staudingerweg 5, 55128 Mainz).

### 5.1.2 Disposables for cell culture, microscopy and *in vitro* tests

12-well plate, tissue culture treated	Greiner Bio-One (Frickenhause, Germany)
24-well plate, tissue culture treated	Greiner Bio-One
8-well chamber, μ-slide	Ibidi (Martinsried, Germany)
Centrisart II, MWCO 100000	Sartorius (Göttingen, Germany)

Cell culture flask, 75cm <sup>2</sup> / 175cm <sup>2</sup> , ventilated cap, tissue culture treated	Sarstedt (Nümbrecht, Germany)
Ceramic beads, 0.6 - 0.8 mm #9607-53	Sigmund Lindner (Warmensteinach, Germany)
Cover slips, round 18 mm diameter	Carl Roth
Cover slips, round 12 mm diameter	Carl Roth
Disposable plastic macro cuvettes	Sarstedt
FACS tubes, round-bottom #352052	Becton Dickinson (Franklin Lake San Jose, USA)
Filter top vacuum bottles, PES, pore:0.2 μm 250 ml or 500 ml, #83.1822.101/#831 823 101	Sarstedt
Glass beads, 1 mm diameter #4901001	Marienfeld (Lauda Königshofen, Germany)
Pipet tips, with filter, sterile RNase/DNase free, 10μL #771288, 20μL #774288, 200μL #739288, 1000 μL #740288	Greiner Bio-One
Polyethylen foil, 0.2 mm	Neolab (Heidelberg, Germany)
Reaction tube, 1.5 ml and 2.0 ml, #7080.1, #CK06.1	Carl Roth
Serological pipettes, sterile, disposable 5, 10, 25 ml	Sarstedt
Syringe filters units, cellulose, pore: 0.2 μm	Carl Roth
Screw cap vials, 0.65 or 2.0 ml, #T601.1/#T604.1	Carl Roth
Suprasil quartz glass cuvette, 15 μl, 1.5mm light pass	Hellma

### 5.1.3 Buffers & media

All buffers and media were prepared by using MilliQ-water. Stock salt solutions were diluted to the final concentration with MilliQ water. If necessary, pH was adjusted with indicated acids or bases and pH-value verified with the FiveEasy<sup>TM</sup> FE20 pH-meter (Mettler-Toledo, Gießen, Germany). For short-term storage, buffers were kept at room temperature and media at 4°C. In case of long-term storage, buffers or aliquots were stored frozen at -20°C.

#### Filtered buffers, media & solutions:

##### **PBS 10x:**

1.4 M NaCl, 27 mM KCl, 15 mM KH<sub>2</sub>PO<sub>4</sub>, 80.6 mM Na<sub>2</sub>HPO<sub>4</sub> in H<sub>2</sub>O, resulting in pH of 6.8

##### **PBS-acidic 10x:**

1.4 M NaCl, 27 mM KCl, 15 mM KH<sub>2</sub>PO<sub>4</sub>, 80.6 mM NaH<sub>2</sub>PO<sub>4</sub> in H<sub>2</sub>O, resulting in a pH of 3.88

##### **PBS-basic 10x:**

1.4 M NaCl, 27 mM KCl, 15 mM KH<sub>2</sub>PO<sub>4</sub>, 80.6 mM Na<sub>3</sub>PO<sub>4</sub> in H<sub>2</sub>O, resulting in a pH of 11.58

##### **PBS 1x (pH 7.4):**

dilution of PBS 10x with sterile water resulted in a pH of 7.4. With final 140 mM NaCl, 2.7 mM KCl, 1.5 mM KH<sub>2</sub>PO<sub>4</sub>, 8.06 mM Na<sub>2</sub>HPO<sub>4</sub>. pH was adjusted with NaOH or HCl

##### **PBS-acidic 1x:**

dilution of PBS-acidic 10x with sterile water resulted in a pH of ≈11.8

## Materials & Methods

---

### **PBS-basic 1x:**

dilution of PBS-basic 10x with sterile water resulted in a pH of  $\approx 4.5$

### **PBS 1x (pH X):**

PBS 10x, PBS-acidic 10x and PBS-basic 10x were combined to result in the desired pH X. Final adjustment of the PBS 1x (pH X) was done with PBS-acid 1x, PBS-basic 1x or NaOH and HCl for pH 3.5 and 12, respectively.

### **RBE growth medium, standard (RBE std med):**

45 % v/v D-MEM, 45 % v/v HAM's F-10, 10 % v/v FBS, 100  $\mu\text{g/ml}$  Pen/Strep, 1 ng/ml bFGF

### **RBE pre-transfection medium (RBE pre TF med):**

RBE4 std med without Pen/Strep

### **RBE transfection medium (RBE TF med):**

RBE std med without Pen/Strep and without FBS

### **RBE freezing medium:**

35 % v/v D-MEM, 35 % v/v Ham's F-10, 20 % v/v FBS, 10 % v/v DMSO

### **RBE transfection medium for live cell microscopy (RBE TF mic medium):**

100 % v/v D-MEM:F-12 indicator free, 25 mM HEPES

### **RBE standard medium for live cell microscopy (RBE std mic medium):**

90 % v/v D-MEM:F-12 indicator free, 10 % v/v FBS, 25 mM HEPES

### **HEK/HeLa growth medium, standard (HEK std med):**

90 % v/v D-MEM, 10 % v/v FBS, 100  $\mu\text{g/ml}$  Pen/Strep

### **HEK/HeLa pre-transfection medium (HEK pre TF med):**

HEK std med without Pen/Strep

### **HEK/HeLa transfection medium (HEK TF med):**

HEK std med without Pen/Strep and without FBS

### **HEK/HeLa freezing medium:**

70 % v/v D-MEM, 20 % v/v FBS, 10 % v/v DMSO

### **HEK/HeLa transfection medium, live cell microscopy (HEK TF mic medium):**

100 % v/v D-MEM indicator free with HEPES

### **HEK/HeLa standard medium for live cell microscopy (HEK mic medium):**

90 % v/v D-MEM indicator free with HEPES, 10 % v/v FBS

All mentioned buffers, media and stock solutions were filtered sterile with syringe filters or filter top vacuum bottles.

### Buffers & solutions not filtered before usage:

#### **15% denaturing PAGE mixture**

10% v/v PAGE buffer denaturing, 60% v/v PAGE concentrate denaturing (25%), 30% v/v PAGE diluent denaturing

#### **15% non-denaturing PAGE mixture**

10% v/v TBE 10x, 37.5% v/v PAGE concentrate (40%), 52.5% v/v water

**APS solution**

10% m/v Ammoniumpersulfate dissolved in MilliQ water

**Collagen coating solution:**

1% v/v collagen solution ( $38 \frac{\mu\text{g}}{\text{ml}}$ ) in sterile distilled water

**Degradation buffer 2x:**

80 mM Tris-HCL pH 7.5 at 25°C, 80 mM NaCl, 20 mM MgCl<sub>2</sub>

**Cuvette cleaning solution**

2% Hellmanex in water

**Piranha solution**

3 : 1 mixture of conc. H<sub>2</sub>SO<sub>4</sub> : H<sub>2</sub>O<sub>2</sub> 30%. Hydrogen peroxide was carefully added dropwise in the ice cooled sulfuric acid. Extreme heat development might lead to foaming or boiling. Special acid gloves, protection of face and eyes are required. Piranha was prepared fresh and later inactivated by excessive dilution.

**Fixation buffer:**

4 % Formaldehyde in PBS 1x

**LB medium**

20 g LB-Broth mix (containing 5 g yeast extract, 5 g NaCl, 10 g tryptone) was added to final 1 L distilled water before autoclaving.

**LB agar**

17.5 g LB-agar mix (containing 2.5 g yeast extract, 2.5 g NaCl, 5 g tryptone, 7.5 g agar-agar) was added to final 500 mL water before autoclaving

**LB medium with kanamycin (LB<sup>Kan</sup>)**

Autoclaved LB medium was supplemented with kanamycin to final  $100 \frac{\text{mg}}{\text{mL}}$ .

**LB agar with kanamycin (LB<sup>Kan</sup> agar)**

Autoclaved LB agar, supplemented with kanamycin to final  $100 \frac{\text{mg}}{\text{mL}}$ .

**PAGE loading buffer 10x, non-denaturing, colorless**

50% v/v Glycerol, 10% v/v TBE 10x in water.

**PAGE loading buffer 2x, non-denaturing, colorless**

10% v/v Glycerol, 10% v/v TBE 10x in water.

**PAGE loading buffer, non-denaturing, blue color**

10% v/v Glycerol, 10% v/v TBE 10x, 0.1% Xylene Cyanol, 0.1% Bromphenol Blue in water.

**PAGE loading buffer, denaturing, colorless**

90% v/v Formamide, 10% v/v TBE 10x in water.

**PAGE loading buffer, denaturing, blue color**

90% v/v Formamide, 10% v/v TBE 10x, 0.1% Xylene Cyanol, 0.1% Bromphenol Blue in water.

**StainsAll-Staining**

Freshly prepared staining solution composed of 10% v/v, 0.1% m/v StainsAll in Formamide, 25% v/v isopropanol, 65% v/v TBE 1x.

**StainsAll-Destain**

25% v/v isopropanol and 75% v/v TBE 1x.

All stock salt solutions used, were sterile filtered before preparations of buffers or reaction mixtures.

## 5.1.4 Plasmids and oligonucleotides

### 5.1.4.1 EGFP plasmids

#### pEGFP-N1

The EGFP coding plasmid pEGFP-N1 (GenBank Accession #U55762) was a kind gift from [REDACTED] (*Hygiene-Institut, Abteilung Hygiene und Medizinische Mikrobiologie, Im Neuenheimer Feld 324, Heidelberg, Germany*).

For transformation and selection, the plasmid contains the kanamycin/neomycin resistance gene.

### 5.1.4.2 siRNA

siRNA single strands were purchased from IBA GmbH (Göttingen, Germany). The labels are attached to the oligonucleotides (ON) via a phosphate group and linker (see Appendices B.4) and can be grouped in :

**Donor-dyes** : Atto390, FL, Atto488, Alexa488 or Alexa555

**Acceptor-dyes**: TMR, Atto550, Atto590 or Atto647N

The siRNA sequence is directed against the sequence of enhanced green fluorescent protein (EGFP) (GenBank Accession #U55762) with the sense strand (s): 5'-GCAAGCUGACCCUGAAGUUCAU-3' and antisense strand (as): 5'-GCCGUUCGACUGGGACUUCAAG-3'.

Purchased oligos were stored in aqueous solution at a concentration of 100  $\mu$ M at -20°C. Duplexes were named by *label on 3'-sense/label on 5'-antisense strand*, meaning **donor/acceptor** in general, or Atto488/Atto590 as an example. Unlabeled strands were indicated by the place holder —, like —/**acceptor** or **donor**/— for antisense acceptor labeled or sense donor labeled siRNA duplexes, respectively. The nomenclature implies the double stranded siRNA duplex form.

With 3'-donor-labeling on the sense strand (s) and 5'-acceptor-labeling on the antisense strand different double stranded siRNA constructs could be designed with dyes and combinations based on Table 3.1:



**unlabeled (—/—)**

s: 5'-GCAAGCUGACCCUGAAGUUCAU-3'  
 as: 3'-GCCGUUCGACUGGGACUUCAAG-5'

**single sense labeled duplex (donor/—)**

s: 5'-GCAAGCUGACCCUGAAGUUCAU-3'- Donor  
 as: 3'-GCCGUUCGACUGGGACUUCAAG-5'

**single antisense labeled duplex(—/acceptor)**

s: 5'-GCAAGCUGACCCUGAAGUUCAU-3'  
 as: 3'-GCCGUUCGACUGGGACUUCAAG-3'- Acceptor

**double labeled duplex (donor/acceptor)**

s: 5'-GCAAGCUGACCCUGAAGUUCAU-3'-Donor  
 as: 3'-GCCGUUCGACUGGGACUUCAAG-3'-Acceptor

**5.1.5 Nanoparticulate delivery systems**

The evaluated nanoparticulate delivery systems were kind gifts of our collaborators:

**nanohydrogels** [redacted] (*Institut für Organische Chemie, Universität Mainz*)

**magnetic core-shell particles** [redacted] (*Institut für Anorganische Chemie, Universität Mainz*)

**poly-L-lysine brush** [redacted] (*Institut für Physikalische Chemie, Universität Mainz*)

**cationic peptides** [redacted] (*Institute of Pharmaceutica Science, King's College, London*)

**5.1.6 Cell lines**

Cell line data bases like DSMZ (Deutsche Sammlung von Mikroorganismen und Zellkulturen) [273] or HyperCLDB (Cell line data base) [274] provide information about most common cell lines.

**5.1.6.1 RBE4**

RBE4 cells are an immortalized cell line derived from Rat Brain Endothelial Cells [236]. The endothelial cells express high levels of p-glycoprotein which can be found in the blood brain barrier. The cell line has a clear visible nucleus surrounded by a large volume

of cytoplasm.

The cells were provided by Prof. G. Fricker (*IPMB, Abt. Pharmazeutische Technologie, Im Neuenheimer Feld 366, 69120 Heidelberg, Germany*) at passage 28.

### 5.1.6.2 293T

HEK 293T or just 293T (DSMZ no. ACC635) cells are a variation of HEK 293. The human embryonal kidney cells were established from a human primary embryonal kidney transformed by adenovirus type 5 (Ad 5). The variation 293T includes the SV40 large T-antigen, that allows the episomal replication and expression of transfected plasmids containing the SV40 origin of replication.

The cells were a kind gift from Prof. A. Dalpke, at passage 6.

### 5.1.6.3 HeLa

HeLa cells are an immortal cell line established from a epitheloid cervix carcinoma (DSMZ no. ACC 57) of a female in 1951. Later they were classified as adenocarcinoma derived.

HeLa cells are a standard cell line for *in vitro* experiments and one of the oldest cultured cell lines [275] and used for many studies.

The cells were a kind gift from the Prof B. Epe (*IPB, Abt. Pharmakologie und Toxikologie, Staudingerweg 5, 55128 Mainz, Germany*)

### 5.1.6.4 *E.coli*

*Escherichia coli* is a Gram-negative bacterium. *E.coli* is easy to cultivate and allows the expression of proteins coded on plasmids that are delivered into the bacterial cell by transformation.

DH5 $\alpha$  is an *E.coli* strain (DSMZ no. 6897), that can be used for plasmid preparation [276], and is easy transformable via chemical transformation method.

## 5.2 Instruments & software

### 5.2.1 Standard laboratory equipment

All pipetting was performed with the variable single-channel micropipettes Discovery Comfort from Abimed (Langenfeld, Germany), with volume ranges from: 0.5-2  $\mu$ l, 0.5-10  $\mu$ l, 2-20  $\mu$ l, 20-200  $\mu$ l and 100-1000  $\mu$ l.

Serological pipettes were used with the PIPETBOY acu from IBS-Integra (Fernwald, Germany).

For centrifugation the Sigma 1-15PK refrigerated centrifuge (Sigma Laborzentrifugen, Osterode am Harz, Germany), the Eppendorf Centrifuge 5810R (Eppendorf, Hamburg, Germany) or the Hettich EBA 20S (Hettich, Tuttlingen, Germany) were used. For evaporating or concentrating liquids, the Eppendorf Concentrator Plus (Eppendorf) was used.

For incubation of samples, temperature controlled incubators, like the Eppendorf Thermoshaker Plus (Eppendorf) or the BIOER ThermoCell (BIOER, Hangzhou, China), were used.

### 5.2.2 Gel electrophoresis & detection

PAGE was performed using the CBS LSG-400-20 NA adjustable vertical electrophoresis device (C.B.S. Scientific, San Diego, USA) and a power supply that can provide constant wattage, like the Pharmacia 3501XL or 3500XL (formerly Amersham Bioscience now GE Healthcare, Buckinghamshire, UK) or the Consort EV232 (Consort, Turnhout, Belgium). Agarose electrophoresis was performed using the PerfectBlue Gelsystem (PeqLab, Erlangen, Germany) horizontal electrophoresis chamber.

For scanning of the different gels the Typhoon 9600 with blue laser unit (formerly Amersham Bioscience now GE Healthcare) was used. The device is equipped with 457/488/532/633 nm laser lines, 560/580/630 nm beamsplitter and a set of emission filters (526SP, 520BP40, 555BP20, 580BP30, 610BP30, 670BP30 and 560LP).

### 5.2.3 Liposome preparation

Liposomes were prepared by using the Dual Asymmetric Centrifuge provided by [REDACTED] (Department of Clinical Research, Tumor Biology Center, Freiburg, Germany). The device was a test system and not yet commercially available. Alternatively a SpeedMixer<sup>TM</sup> from Hauschild (Hamm, Germany) can be used [229].

Liposomal size was determined on the Zetasizer Nano (Malvern, Herrenberg, Germany) provided by the group of Prof. P. Langguth (IPB, Mainz).

### 5.2.4 Bacterial cell culture

*E.coli* cells were incubated in the Incutex K30-30 incubator (Axon, Kaiserslautern, Germany). For sterile working, the CaptairBio fume hood with BioCup (Erlab, Köln, Germany) was used or working near a flame was performed to guarantee sterile working conditions. For plasmid quantification the NanoDrop ND-2000 (PeqLab) was used.

### 5.2.5 Mammalian cell culture

The cells were incubated in a HeraCell 150 (Heraeus<sup>®</sup>, by ThermoFisher Scientific, Waltham, USA) incubator and handled under a Heraeus<sup>®</sup>LaminAir<sup>®</sup>HB-2472 (ThermoFisher Scientific) flow bench. For centrifugation a Heraeus<sup>®</sup>Labofuge<sup>®</sup>400R (ThermoFisher Scientific) was used. All prepared buffers and solutions for the cell culture were either autoclaved or sterile filtered. For cell counting a Neubauer Improved counting chamber (Marienfeld) was used.

### 5.2.6 Fluorimetry

Spectral measurements in the cuvette (i.e. emission profiles and degradation) were performed on the FP-6500 Fluorimeter (JASCO, Tokyo, Japan) equipped with ETC-273T temperature controller, a peltier element for heating cooling and a HAAKE<sup>®</sup>WKL26 cooling unit (ThermoFisher Scientific).

### 5.2.7 FACS

The FACS measurements for analyzing the EGFP knockdown were performed on the flow cytometer FACSCanto or LSR-FortessaSORP(both BD Biosciences, Franklin lakes, USA). For acquisition and analysis the FACSDiva Software (BD Biosciences) was used. The FACSCanto was kindly provided by Prof. Dalpke and the LSR-FortessaSORP by the *Cytometry Core Facility of the Institute of Molecular Biology (IMB)* (Mainz, Germany).

### 5.2.8 Microscopy

Four different microscopes were used:

**Leica DM IRBE TCS** In the beginning fixed cells were imaged on the DM IRBE TCS MP1 confocal microscope (Leica, Wetzlar, Germany) with an 63x oil immersion objective. The microscope was equipped with a 488 nm and 543 nm laser, a triple dichroic mirror (488/544/633) as beamsplitter and the Leica spectral detection system without filter cubes. For acquisition the LCS software (Leica) was used. The Leica DM IRBE TCS was provided by the group of Prof. G. Fricker.

**Zeiss LSM510-UV** Live Cell imaging was first performed on the inverted confocal microscope LSM510-UV operated with the ZEN acquisition software (Zeiss, Oberkochen, Germany). For temperature control the microscope was equipped with a stage top heating system (Ibidi). The microscope was equipped with a 63x oil immersion objective (N.A. 1.4), a MBS 488/543/633 beamsplitter, the Zeiss

META scanning unit for splitting the visible light in 32 spectral detection channels and four lasers lines (Argon-UV laser: 351/364 nm; Argon laser: 458/488 nm; HeliumNeon laser green: 543 nm; HeliumNeon laser red: 633 nm). For data inspection, the Zeiss LSM Image Browser was used.

The Leica LSM5 was provided by the Confocal Laser Scanning Microscope Core Facility of the Forschungszentrum für Immununologie (FZI), Universtitätsmedizin der Johannes Gutenberg-Universität (Mainz, Germany).

**Leica TCS SP5** In the end, single cell images of living or fixed cells were mainly acquired on the Leica TCS SP5 confocal. The TCS SP5 was equipped with 4 laser lines (405/488/561/633nm), a 63x oil immersion objective (N.A. 1.4), a fast resonance scanner and the Leica filter free detection system (Acousto Opticla tunable excitation filter (AOTF), Acousto-Optical Beam Splitter (AOBS) and spectrophotometer detection system). Images were acquired using the Leica Application Suite (LAS AF) and the free LAS AF lite was used to inspect the images. The TCS SP5 was provided by the Microscopy Core Facility of the IMB.

**Leica TCS STED CW** Live cell imaging was mainly done on the Leica STED CW. The microscope was a modified TCS SP5 and similarly equipped. Instead of the 405 nm laser, the STED system is included. In addition to the TCS SP5, the TCS STED was equipped with an adaptive Focus Control system (AFC), 2 HyD detectors and an incubation box for live cell conditions. Images were acquired using the Leica Application Suite (LAS AF) and the free LAS AF lite was used to inspect the images. The TCS SP5 was provided by the Microscopy Core Facility of the IMB.

### 5.2.9 Software for data processing

Besides the provided software from the manufacturer of the respective instrument the following software was used to analyze and process data:

**spreadsheet analysis** For standard spreadsheet analysis Microsoft Excel 2007 (Microsoft, Redmont, USA) was used.

**$IC_{50}$  calculation** The determination of  $IC_{50}$  was done with the Prism software (GraphPad Software, La Jolla, USA).

**Graphic creation** All prepared figures were assembled in the vector graphics editor CorelDraw (Corel, Ottawa, Canada).

**Model fitting** Data analysis, plotting and model fitting was performed with the OriginPro software (OriginLab, Northampton, USA).

**Image processing** Image processing, meaning segmentation, intensity measurements and merging of channels, was performed with open source software ImageJ (developed at the National institute of health, USA) [250].

## 5.3 Methods

### 5.3.1 Working with RNA

RNA is prone to degradation caused by RNases that are omnipresent on the human skin. To prevent degradation, RNA samples should be treated with special care avoiding contaminations. One possibility is to decontaminate equipment and solutions with DEPC. The other method is to avoid samples and equipment getting into contact with skin and other body fluids. Therefore, fresh clean gloves should be worn when touching equipment and working with RNA samples.

RNA samples should be kept on ice to prevent degradation and should be stored frozen. Gentle thawing of frozen samples is recommended.

A good way to prevent unwanted contaminations, is to use a special set of pipettes, only used for working with RNA.

The RNA working place should be strictly separated from locations where cell culture, eukaryotic or bacterial, is performed.

If these precautions are followed, unwanted degradation of RNA sample can be avoided.

### 5.3.2 siRNA duplex formation

For the formation of siRNA duplexes as indicated above, the corresponding single stranded siRNA ON were mixed with 10x PBS and MilliQ-water to final 5  $\mu\text{M}$  or 40  $\mu\text{M}$  sense strand concentration and 1x PBS. The antisense strand was added in the optimal ratio. The mix was incubated for 1 minute at 90°C (denaturing strands) followed by 1 hour annealing at 37°C. The prepared duplex siRNA can be stored at -20°C.

siRNA concentrations higher than 40  $\mu\text{M}$  were obtained by concentrating the siRNA stock in the vacuum concentrator. Concentrations always refer to the sense strand concentration if not other specified.

**Hybridization ratios** The optimal ratios for labeled sense and antisense strand were determined by hybridizing ratios of sense:antisense strand ranging from 2:1 to 1:2 with a final concentration of the sense strand of 5  $\mu\text{M}$ . The respective hybridization ratios are depicted in Table 3.2.

Hybridized siRNA duplexes were analyzed on non-denaturing PAGE and by fluorescence emission scan prior to usage.

**Integrity simulation** siRNA different integrity states of siRNA duplexes was simulated by mixing different fractions of double labeled donor/acceptor siRNA (dsDA) and single labeled donor/— (dsD) and —/acceptor (dsA) siRNA duplexes. The different mixes contained the same overall concentration of donor and acceptor dye, respectively. Mixtures were always prepared fresh to avoid rehybridization.

$$X\% \text{ intact} = X\% \text{ dsDA} + (100 - X)\% \text{ dsD} + (100 - X)\% \text{ dsA} \quad (\text{Eq. 5.1})$$

### 5.3.3 PAGE

Polyacrylamide gel electrophoresis (PAGE) was the method of choice to analyze nucleic acids. Denaturing PAGE, containing 8 M urea, and formamide loading buffers break down hydrogen bonds guaranteeing single stranded DNA or RNA samples on the gel. In case of non-denaturing PAGE no urea was used letting hydrogen bonds intact and allowing to analyze hybridized probes such as siRNA duplexes. Glycerol was used in the loading buffer to increase the density of the sample.

**Casting** To cast a PAGE gel, glass plates (20x30 cm) are thoroughly washed with detergent and ethanol. Dried plates are silanized on the inner face with 2% dichlorodimethylsilane in chloroform. The glass plates and spacers (1 mm) were assembled and fixed with clamps to prevent leakage. For casting 100 ml of 15% PAGE mix (non-denaturing or denaturing) were supplemented with 1 ml (non-denat) or 400  $\mu\text{L}$  (denat) APS solution and mixed thoroughly. The addition of 60  $\mu\text{L}$  TEMED started the polymerization process and the gel should be cast immediately. After inserting the comb, the gel has to polymerize for at least one hour.

**Sample analysis** Polymerized PAGE was fixed in the vertical PAGE apparatus and pockets were washed with TBE 1x buffer. Samples were mixed with equal parts of color free loading buffer. Samples were loaded into pockets with colored loading buffer as reference in empty lanes. Denaturing PAGE was run for 2-3 hours at constant 20-25 Watt, non-denaturing for 3-4 hours at around 10-13 Watt. siRNA duplexes and single strands run approximately in between bromphenol blue and xylene cyanol. In case of non-denaturing PAGE a fan was used to prevent strong heating.

**Detection** For detection of fluorescently labeled siRNA, PAGE was directly scanned on the Typhoon 9600, whereas unlabeled strands were visualized by 20 min staining with GelRED (0.3x solution in TBE 1x) or by 10-15 min staining with StainsAll-Staining solution followed by 2 h destaining with StainsAll-Destaining solution. To accelerate

destaining paper tissue, that absorbs the dye molecules, were placed in the destaining solution.

The scanning settings for fluorescent labeled siRNA and stains can be seen in Table 5.1. Scans of fluorescently labeled siRNA duplexes were performed by scanning each dye directly according to Table 5.1. In case of FRET siRNA the FRET channel was recorded simultaneously with the donor dye in a first scan and in the second scan the acceptor dye is scanned.

Acquired data was analyzed and merged with ImageJ.

**Table 5.1: Settings for PAGE analysis**

dye	direct excitation [nm]	FRET excitation [nm]	emission filter
GelRED	532	N/A	610BP30
StainsAll	532	N/A	580BP30/610BP30/670BP30/LP560
FL, Atto488, Alexa488	488	N/A	520BP40
TMR, Atto550, Alexa555	532	488	580BP30
Atto590	532	488	670PB30
Atto647N	633	488/532	670BP30

N/A: not applicable; BP: band pass filter, LP: long pass filter, FL: Fluorescein, TMR: Tetramethylrhodamine.

### 5.3.4 Plasmid preparation

The EGFP containing plasmid was transformed in chemically competent *E.coli* cells (strain: DH5 $\alpha$  from Invitrogen). The transformation was performed according to the manufacturer's instructions.

For selection transformed cells were plated on LB<sup>Kan</sup>-plates and incubated at 37°C. Liquid LB<sup>Kan</sup>-cultures were afterward grown to an OD<sub>600</sub> of 1.5 and the amplified plasmid was isolated with the EndoFree Plasmid Maxi Kit (Qiagen) to remove endotoxins.

### 5.3.5 Liposomal preparation

Liposomes containing siRNA were prepared by using DAC as described earlier by Hirsch et al. [229].

**Lipid films** The phospholipid mixtures for sterically stabilized liposomes (SL; EPC3/Chol/MPEG-2000-DSPE mixture in 56.9 : 37.9 : 5.2 molar ratio) were prepared by dissolving the components in pure EtOH followed by air-drying under vacuum. For a 50 mg batch size, 17.5 mg of the phospholipid mix was prepared directly in 0.65 ml screw cap vials.

**DAC** The liposomal preparation was performed by the addition of 32.5 $\mu$ L of 40  $\mu$ M siRNA or PBS 1x solution resulting in a mass ratio of 35 : 65 and additional 250 mg of



0.6 mm ceramic beads (500 % of batch size). After 10 min of incubation, 20 min of dual asymmetric centrifugation (DAC) at 2500 rpm was performed. The obtained vesicular phospholipid gel (VPG) was redispersed by diluting 1 : 3 with PBS 1x (100  $\mu$ L) and 2x2 min of redispersion in the DAC.

**Purification** For purification liposomal mixtures were adjusted to 2.5 ml with PBS 1x and filtered twice with inverted spin filters, centriscart II MWCO 100000, to remove free siRNA. The concentration of entrapped compound was determined via fluorometric quantification of liposomes that have been cracked.

**Cracking** The addition of final 1% Triton X-100 led to a disruption of the liposomal bilayer, by formation of micelles with the lipid components and a release of the entrapped compounds.

**Size measurements** The size of the liposomes was determined by dynamic light scattering using the Zetasizer. Therefore 1  $\mu$ L of the liposomal solution was added to 1 mL PBS 1x in plastic cuvettes. Sample was measured in triplicates and the diameter averaged.

### 5.3.6 Complexation of siRNA with delivery systems

Liposomes were separately prepared and stored at 4°C until usages. The other delivery systems were complexed at the adequate siRNA:particle mass:mass ratio before usage. Complexation was performed at final 1x PBS at room temperature for 20 min.

Different siRNA:particles ratios were complexed and analyzed on 15x15 cm agarose gels (1% in TBE 1x; comb placed in the middle of the gel) by constant 100 V for approximately 1 h. Free siRNA migrates to the anode whereas complexed or free particles remain in the pocket or migrate in the opposite direction to the cathode.

### 5.3.7 Fluorescence emission scans

Fluorescence emission scans were performed in a 15  $\mu\text{L}$  cuvette on the fluorimeter. Before the experiment, an auto-zero with closed excitation shutter and open emission shutter was performed. The auto-zero was repeated when changings in emission, excitation or sensitivity were made. For each experiment a blank consisting of buffer only was recorded and subtracted from each recorded spectrum or data-set.

The cuvettes were cleaned with water and ethanol between each measurement. For intensive cleaning, the cuvette was incubated for 2 h in 2% Hellmanex solution at room temperature.

**Spectral profiling** For the spectral analysis (*spectral measurements* in fluorimeter software) the siRNA constructs and mixtures of different constructs (in case of the R/G-simulation) were diluted with 1x PBS to final 1  $\mu\text{M}$  of the sense strand. 20  $\mu\text{l}$  of each sample were analyzed in a 15  $\mu\text{l}$  cuvette at 25°C.

The excitation of the samples was performed according to excitations wavelength for the cuvette in Table 3.2 with a band width of 3 nm. The emission was detected from 5 nm higher than the excitation wavelength to 750 nm at 1 nm data pitch, 0.5 sec response time, scanning speed of 1000 nm/min, 3 nm emission bandwidth and spectral correction for PMT (emission) and illumination lamp (excitation).

**Bleaching experiments** Single or double labeled siRNA duplexes or single strands were diluted to final 0.1  $\mu\text{M}$  in PBS 1x. Excitation was performed at 488 nm or 561 nm at 10 nm bandwidth (different to spectral profiling) to guarantee sufficient bleaching. Samples were analyzed either at a single wavelength for 10 h in 5 s intervals (*Dual wavelength time course measurement* in fluorimeter software) or the whole emission spectrum at 30 s intervals for 2 h (*Interval scan measurements* in fluorimeter software). For long-term analysis, emission was recorded at 520 or 590 nm according to R/G ratio values (see Table 3.3). Based on the 2 h spectral analysis, traces for 520 and 590 nm were extracted.

### 5.3.8 Analysis of fluorimetry data

**R/G calculation** The R/G ratio was calculated from corrected spectral data as a ratio of acceptor emission to donor emission. A list of wavelength used to calculate the R/G ratio of different dye combinations can be found in Table 3.3, with:

$$R/G = \frac{I_{\text{Acceptor}}}{I_{\text{Donor}}} = \frac{I_A}{I_D} \quad (\text{Eq. 5.2})$$

**Calculation of spectral cross-talk factors** The cross-excitation factor  $C_f$  and bleed-through factor  $B_f$  were calculated according to (Eq. 5.3) and (Eq. 5.4) on basis of the respective emission profiles.

$$C_f = \frac{A_D(dsA)}{A_D(dsDA)} \quad (\text{Eq. 5.3})$$

$$B_f = \frac{A_D(dsD)}{A_D(dsDA)} \quad (\text{Eq. 5.4})$$

With dsA referring to **—/acceptor**, dsD to **donor/—** and dsDA to **donor/acceptor** siRNA.  $A_D$  refers to acceptor (variable A) emission at donor excitation (subscribed  $D$ ), see also 3.5 for visualization of  $C_f$  and  $B_f$ . For respective emission wavelength of D and A see Table 3.3.

**Integrity simulation** R/G values of different integrity levels were calculated and normalized to the 100 % intact siRNA sample and plotted against the integrity state.

**Fitting a model for siRNA integrity** The model for the quantification of siRNA samples in the cuvette was fitted with Origin 8. In order to fit a model that best simulates the integrity progression, the degradation level of each sample was used, with:

$$X\% \text{ degraded} = 100\% - X\% \text{ intact} \quad (\text{Eq. 5.5})$$

The fitting was done using a second order exponential decay (with  $y$  = degradation level;  $x$  = normalized R/G.)

$$y = A_1 * e^{-\frac{x}{t_1}} + A_2 * e^{-\frac{x}{t_2}} + y_0 \quad (\text{Eq. 5.6})$$

The fitted parameters were further used to calculate the degradation levels of unknown samples. The degradation levels can be similarly converted to integrity levels according to (Eq. 5.5). Parameters of the fit models were listed in the respective graphs.

### 5.3.9 Degradation by RNase V1

For integrity measurements of the duplex siRNA or nanoparticle complexed with siRNA, a 1 : 1 mixture of 1  $\mu\text{M}$  sample and degradation buffer was prepared resulting in final 0.5  $\mu\text{M}$  siRNA. For reducing inter-assay variability at different days, a reference degradation of free siRNA was performed on every test day. The emission profiles were acquired as described in Section 5.3.7.

**Degradation** Emission spectra were recorded before and after the addition of RNase V1. 10 mU of RNase V1 ( $10 \frac{\text{mU}}{\mu\text{L}}$ ) were added to the sample by mixing a part of the sample outside of the cuvette with the RNase and immediately pipetting it back. The degradation was monitored over 2 hours direct (0 s) and after 20 s, 40 s, 60 s, 90 s, 2 min, 2.5 min, 3 min, 4 min, 5 min, 6 min, 7 min, 8 min, 10 min, 12 min, 15 min, 20 min, 25 min, 35 min, 45 min, 60 min, 90 min, 120 min of incubation with V1. Between the measurement of different samples the cuvette was thoroughly washed with water, ethanol and Hellmanex solution. For inactivating the RNase, the cuvette was incubated with *Piranha* for at least 2 hours.

**Data analysis** On the basis of recorded data, the R/G ratio was calculated and normalized to the initial R/G value of the intact reference siRNA sample. The reference siRNA sample was normalized to its initial R/G value. Normalized data sets, i.e. normalized reference sample (free siRNA) and normalized particle complexed siRNA, were used to calculate degradation levels according to the R/G model converting the integrity in degradation levels and using (Eq. 5.5) and (Eq. 5.6).

After reconverting into integrity levels the data was standardized with the reference siRNA degradation. Therefore the calculated reference siRNA integrity before degradation was set to 100% and the integrity after 2 h to 0%. The other samples were harmonized by using the *TREND*-Function of Microsoft Excel.

For visualization data was plotted in an integrity-time-plot and an exponential decay model was fitted (based on (Eq. 5.6)).

### 5.3.10 Cell culture

For all cells the same protocols were used with the respective medium for each cell type. After recultivation of frozen cells, cells were cultivated up to one month or  $\sim 10$  passages before recultivating another aliquot.

All media and buffers were sterile (autoclaved or sterile filtered) and prewarmed to 37°C before using.

#### 5.3.10.1 Basic cell culture routines

**Thawing** Cells pellets were stored in liquid nitrogen. For recultivation cells were thawed by rapidly adding warm std med and centrifuged (at 250 xg, 5 min; standard for pelleting cells). The pellet was resuspended and cultivated in 15 ml of the appropriate standard medium in 75 cm<sup>2</sup> culture flasks at 37°C, high humidity and 5 % CO<sub>2</sub>.

**Passaging** Cells in culture were passaged 2 - 3 times per week (depending on confluency). At 70 - 80 % confluency cells were trypsinated for 5 min with 3 ml of Trypsin/EDTA, followed by inactivation of Trypsin by FBS (adding 7 ml of std med), centrifugation and resuspension in std med or pre TF med. Usually, 1/5 to 1/10 of the cell suspension was further cultivated for maintaining the cell line, the rest was either used for experiments, stored or discarded.

**Counting** Accurate cell densities were manually determined by using a Neubauer counting chamber.

**Freezing** For storage cells were placed in freezing medium and first cooled down to -80°C (to prevent cell damage by too fast freezing) before storing in liquid nitrogen.

#### 5.3.10.2 Seeding cells for experimental usage

**Knockdown experiments** One day prior to the knockdown experiments, 40k HEK 293T cells were seeded in 500  $\mu$ l of pre TF med in 24-well plates. This seeding density led to 50 % confluency for the transfection and about 90 % confluency on the day of FACS analysis.

**Imaging of fixed cells** For imaging of fixed cells, cells were seeded one day prior to transfection on collagen coated coverslips ( $\varnothing$ 18 mm) in pre TF med. The collagen coating was obtained by adding 1 mL of the collagen coating solution to the cover slip in a 12-well plate and incubating for 2 h at 37°C. Coating solution was discarded and coverslips were dried under UV-light in the flow bench. The coated coverslips, in 12-well plates, can be stored in the fridge.

Before seeding the coverslips were placed for around 20 min under UV-light and washed once with 1x PBS to remove unbound collagen. Per well of a 12-well plate, 50k RBE4 cells were seeded in 1 ml of the respective pre TF med. These cell numbers resulted in a minimum of 40 % to a maximum of 90 % confluency after the incubation of 2 h to 48 h. For the smaller cover slips (12 mm) in 24-well plates all volumes and numbers were halved.

**Imaging of living cells** One day prior to the experiments 10k - 20k RBE4 or Hela cells were seeded in 250  $\mu$ l of pre TF med in the well of a Ibidi 8-well  $\mu$ -slide chamber resulting in about 40 % confluency during live-imaging.

### 5.3.11 Knockdown studies

One day before transfection, cells were seeded as described and transfected by cotransfection of siRNA and EGFP-plasmid.

**Cotransfection** For cotransfection the desired amount of siRNA (0.01 fmol up to 20 pmol) and 400 ng of pEGFP-N1 were diluted with OptiMem to a final volume of 50  $\mu$ l. After addition of 1  $\mu$ l lipofectamine diluted in 50  $\mu$ l OptiMem, the 100  $\mu$ l transfection mix was incubated for 15 min at room temperature to form lipoplexes. After incubation the transfection mix was added dropwise to the prepared cells and incubated for 24 h before detection by FACS.

Transfection without siRNA and/or pEGFP-N1 and siRNA alone serve as controls.

**FACS analysis** After 1 day of incubation cells had to be resuspended in 300  $\mu$ l 1x PBS by simply pipetting up and down as HEK cells easily detach.

Resuspended cells were transferred in FACS-tubes and analyzed by FACS. Forward (FSC) and side scatter (SSC) were adjusted to see the whole spectrum in the FSC-SSC-Plot (Population P0).

Populations referring to living cells were gated (P1) and further analyzed. The living population was analyzed in the FITC-channel (histogram mode) by compensating untreated cells to lower intensity ranges. With help of positive controls the gate of EGFP positive cells was determined.

After compensation each sample was measured until a total amount of 30k events was detected in P0.

**Data processing** For determining the EGFP signal of a transfection X, the product of EGFP-intensity ( $I_{EGFP}$ ) and normalized number of EGFP transfected cells ( $cells_{EGFP}$ , normalized to cell numbers in P0 and P1 of respective pos control, +co) was calculated:

$$EGFP(X) = \frac{I_{EGFP}(X) \times cells_{EGFP}(X)}{I_{EGFP}(+co) \times cells_{EGFP}(+co)} \times 100\% \quad (\text{Eq. 5.7})$$

All data was normalized to the positive control and the knockdown efficiency KD was determined by:

$$KD(X) = 100 - EGFP(X) \quad (\text{Eq. 5.8})$$

The  $IC_{50}$  values were calculated with GraphPad Prism and the asymmetric (5-parameter) dose-respnd model [277].

### 5.3.12 Transfection for imaging

One day before transfection cells were prepared as described.

**Fixed cells** For transfections with oligofectamine the medium was exchanged to 364  $\mu\text{l}$  of TF med before adding the transfection mix (TF mix).

The mix consisted of (A) 25 pmol siRNA (6  $\mu\text{l}$  of a 5  $\mu\text{M}$  stock) diluted with 100  $\mu\text{l}$  OptiMem mixed with (B) 6  $\mu\text{l}$  Oligofectamine diluted with 24  $\mu\text{l}$  OptiMem. After 15 min of incubation of (A+B) at room temperature the transfection mix (136  $\mu\text{l}$ ) was added dropwise to the cells resulting in a total volume of 500  $\mu\text{l}$  per well.

The cells were incubated at 37°C until fixation or second transfection. After 4 h medium was replaced by std med.

After incubation, the coverslips with the cells were washed once in 1x PBS and placed for 10 min in 500  $\mu\text{l}$  fixation solution. After three washing steps with 1x PBS the coverslips were mounted with one drop of DAKO mounting medium on microscope slides. The slides were stored at 4°C for at least one day before imaging.

**Living cells** For imaging of living cells, cells were transfected with oligofectamine in Ibidi  $\mu$ -slides in real-time under the microscope.

The TF mix consisting of (A) 8 pmol siRNA (1.6  $\mu\text{l}$ ) diluted with 29  $\mu\text{l}$  TF mic medium mixed with (B) 1.7  $\mu\text{l}$  Oligofectamine diluted with 7  $\mu\text{l}$  TF mic medium. The mix (A+B) was incubated for 15 min before adding to the cells. Prior adding of the 39.4  $\mu\text{l}$  TF mix, the culture medium was replaced by 105.6  $\mu\text{l}$  TF mic medium.

The transfection, i.e. the addition of the mix, was in general performed directly under the microscope.

Living cells can be costained with DAPI or Hoechst (final 1.7  $\frac{\mu\text{g}}{\text{ml}}$ ), RedDot 1 (final 1x) or LysoTracker (final 100 nM) for 30 min at 37°C. The staining solution was replaced by fresh medium prior to the addition of the TF mix.

### 5.3.13 Confocal imaging

Imaging was performed on different microscopes. The Leica IM DBRE and Zeiss LSM5 were mainly used for FL/TMR and the setting up of live-cell imaging. The Leica SP5 and STED became the main microscopes for imaging Atto488/Atto590 siRNA. The settings for imaging of the main analyzed siRNA are depicted in Table 5.2. Other dyes were analyzed using similar settings with altered excitation and emission wavelength according to Table 5.3,

**Table 5.2: Microscopy parameters for FRET imaging**

	Leica DM IRBE	Zeiss LSM5	Leica SP5	Leica STED
image size (pixel x pixel)	512x512	512x512	512x512	512x512
pixel depth	8 bit	8 bit	8 bit	8 bit
zoom	1	1	1	1
focus control	no	yes	no	yes
Objective	63x oil	63x oil	63x oil	63x oil
pinhole (diameter/airy units)	228 $\mu\text{m}$ / 1.5 AU	64.5 / 1.4 AU	131.8 $\mu\text{m}$ / 1.4 AU	131.8 $\mu\text{m}$ / 1.4 AU
section thickness	unknown	1 $\mu\text{m}$	1 $\mu\text{m}$	1 $\mu\text{m}$
pixel size	310 nm	260 nm	481.5 nm	481.5 nm
type	fixed	fixed/live	fixed/live	live
siRNA	FL/TMR	Atto488/Atto590	Atto488/Atto590	Atto488/Atto590
excitation donor/FRET [nm]	488	488	488	488
excitation acceptor [nm]	543	543	561	561
laser power donor [%]	50	10	15	15
laser power acceptor [%]	50	10	15	15
emission donor [nm]	510-540	510-540	510-540	510-540
emission FRET/acceptor [nm]	570-600	605-635	605-635	605-635
PMT gain [V]	830/750/600/(500)	830/700/600/(500)	830/700/600/(500)	N/A
HyD gain [%]	N/A	N/A	N/A	100/10%
transmission	yes	yes	yes	yes

N/A: not applicable; AU: airy unit;

**Table 5.3: Parameters for different dyes and stains**

stain	excitation	emission
Hoechst/DAPI	405	430-480
lysotracker Blue	405	430-480
lysotracker Green	488	510-540
lysoTracker Red	543/561	580-610
RedDot 1	561/633	700-730
FL/Atto488	488	510-540
TMR/Alexa555	543/561	570-600
Atto590	543/561	605-635
Atto647N	633	660-700

**Confocal bleaching** For analyzing the bleaching behavior of free siRNA, 1  $\mu\text{M}$  siRNA was added to 2% agarose in PBS 1x prior to cooling and pipetted into the live-cell imaging chamber slides. siRNA in agarose and fixed transfected cells were bleached with the same setting as used for live-cell imaging. To speed-up the procedure, the scanning area was reduced to 64x64 pixels by a simultaneous 8-fold zoom and same pixel size, increasing scanning speed by the factor 8. The area was bleached by performing 1000 scans. Before and after bleaching, a normal single image scan was performed.



**Single image acquisition** For single image acquisition sequences with different PMT gains and donor or acceptor or stain excitation were recorded as no time limitation exists. Acquisition was performed by room temperature.

Fixed FL/TMR samples were analyzed by acquiring at least three different PMT gains (high/medium/low) including the acceptor signal by TMR excitation and the transmission channel. It was tried to distribute the scanned areas equally throughout the coverslip by screening the specimen meander-shaped.

For overlay of the single channels ImageJ was used.

**Live-cell imaging** For live-cell imaging almost exclusively Atto488/Atto590 siRNA was analyzed on the Leica STED by acquiring 6D-image data.

At least one hour before imaging the incubation unit of the microscope was set to 37°C. Prior to live-cell imaging the CO<sub>2</sub> saturated air-flow was switched on and the oil-immersion objective selected and one drop of immersion oil applied.

The untransfected cells were placed in the chamber-slide holder, place on top of the stage and the air-flow-lid was installed. The transfection mix was prepared and in the meanwhile the settings adjusted.

First untransfected cells were screened to find an area with approximately 10-20 cells. The surrounding was also scanned to get in each single region of the used 4x4 tile-scan field an adequate number of cells. The settings were loaded and z-sectioning was adjusted by starting the z-slices right above the cover slip (visible by scattering and interference circles on the phase interface). In total 5 z-slices at 1  $\mu\text{m}$  thickness were recorded resulting in a scanning range of 4  $\mu\text{m}$ . The time-lapse interval was set to maximum and the focus control to be conducted one time in every scanning cycle. The total imaging time ranged up to 8 hours with up to 500 scan cycles at an interval time of  $\sim 1$  min.

A short time-lapse scan of two acquisitions was performed prior to transfection to determine the approximate interval and a working tile-scan, z-sectioning. The exact combination of scanned channels and approximate interval times can be seen in Table 3.13 and Figure 3.33.

#### 5.3.14 Analysis of confocal data

Acquired microscopy data was exported in TIFF-images by the respective acquisition software and separated in subfolders containing all recorded channels of one condition (meaning data of one time-point, z-slice and tile-position). RGB merging was done by using the *Image>Color>merge channels...* function of ImageJ.

**Microscopic bleaching** The microscopy bleaching data was analyzed by determining the average mean fluorescence intensities (MFI) of the scanned region with the *Analyze>Measure* function of ImageJ . Data was plotted against scan-number. R/G values were calculated by using the respective MFI values and (Eq. 5.2).

**Segmentation of cellular regions** On basis of the transmission channel and the fluorescence data, the nucleus and cell outline were manually selected and the region stored as ImageJ ROI zip-file in the respective subfolder. Besides the nucleus and cell (for live cell data), the perinuclear region was selected in fixed cell images. The perinuclear region contains the nucleus and the highly structured region around it. In fixed cells this also corresponds to the strong fluorescent area around the nucleus.

Nuclear stains segmentation: In a first step, the image was smoothed with the built-in ImageJ smoothing function *Process>Smooth* to get a blurred and homogeneous image of the nucleus. Finally, a binarization, using the built-in function *Process>Binary>Make Binary*, resulted in a nuclear outline by using the wand tool *Edit>Options>Wand Tool...* of ImageJ.

Manual segmentation: On basis of the contrast in the transmission channel and the recorded fluorescence, the nuclear outline was manually drawn according to descriptions in Section 3.4.1.4.

Similarly the highly structured region surrounding the nucleus was segmented in fixed cells, representing the perinuclear region.

**Colocalization** A rudimentary colocalization with cellular costainings was visualized by simple overlay studies. Colocalization resulted in yellow spots in a red/green merge image. The use of special colocalization tools, i.e. plugins in ImageJ, was not pursued.

### 5.3.15 R/G algorithm analysis

The algorithm for R/G-ratio-processing was kindly provided by [REDACTED] and [REDACTED] (Biomedical Computer Vision Group, Department of Bioinformatics, IPMB University of Heidelberg, Germany) and developed with [REDACTED] and adjusted in the my previous master thesis (both members of the Helm group). An in-detail illustration can be found Appendices H.16 according to [2–4].

The green (G) and red (R) channel images (meaning donor and FRET images) for each setting (time, z-position and region) were input via a processing loop in the Linux console to the R/G-algorithm using the settings specified in Table 3.11. If not other indicated, setA was used for the analysis of Atto488/Atto590 and set1 for the analysis of FL/TMR.

**Ratio image** The green and red channel images (meaning donor and FRET) were used to calculate background values as the mean intensities of the red ( $R_{BG}$ ) and green ( $G_{BG}$ ) channel, respectively.

Using the pixel intensities of donor and FRET image, the R/G ratio was calculated according to the equation:

$$R/G = \frac{R - R_{BG}}{G - G_{BG}} \quad (\text{Eq. 5.9})$$

Starting from the data set obtained at highest PMT gain, R/G values from pixel pairs reaching saturation in either channel were substituted with the corresponding values from unsaturated pixel pairs from data sets obtained at lower PMT gains (see Figure 3.22).

**Ratio mask** The ratio mask was used as a filter to get rid of R/G values that were calculated from intensities that were rather background noise than real signals. The mask was calculated by creating a threshold image that was based on a sum of red and green pixel values. This sum image was used to calculate a threshold for each pixel as a sum of mean and standard deviation.

The ratio mask consists of all intensities of the sum image that are above the threshold. Pixels values below the calculated threshold were assigned the value 0 in the corresponding mask.

**Cell mask** In a similar way a cell mask is calculated by separately thresholding the green and red image with their respective sum of mean and standard-deviation. After addition of both thresholded images and smoothing by mean- and median-filter an additional thresholding removes gray values below 10 by setting these values to 0.

**R/G visualization - R/G ratio image** Based on the ratio image, the ratio mask and the cell mask the output image (R/G ratio image) was calculated in the following way: pixels whose counterpart in both cell and ratio mask were 0 were assigned a value of 0. In case only the cell mask counterpart was positive, the respective value of the cell mask pixels was assigned as gray scale value. In all other cases, where both the ratio and cell mask value were positive, the ratio image value was kept and a color code according to  $rg_{\min}$  and  $RG_{\max}$  range was assigned, with  $rg_{\min}$  set to green and  $RG_{\max}$  to red (for respective threshold values see Table 3.11). Intermediate colors range from green, over yellow to red.

**R/G histogram analysis** On basis of the R/G ratio image and the ratio image (no masking), the corresponding R/G values are binned with a bin size of 0.1 and stored in a separate data tables. Data was used to create histogram with R/G distributions. The

thresholds for the different classes, meaning intact, intermediate and degraded siRNA, can be seen in 3.12.

R/G analysis of selected ROIs or speckles was achieved by creating a histogram with the ImageJ function *Analysis>Histogram* of the respective region of the raw-data file (for details on raw-data import see Methods 5.3.16.2).

**Output files** Processed R/G ratio images (with integrity color coding; File: *maskedratio.tif*), the raw data (corresponds to ratio image; File: *rawratio.raw*) and distribution table of R/G values (File: *histRoi.log*) were stored in the respective subfolder and used for further analysis.

### 5.3.16 Single cell analysis

#### 5.3.16.1 MFI in fixed cells

On basis of the segmented regions, the MFI values of each respective region were calculated using the *Analyze>Measure* function of ImageJ, by loading each region with the *ROI Manager* and measuring the MFI, area and integrated area (INT). Data was extracted from donor, FRET, acceptor and merged donor/FRET image (RGB) by using for each segmented cell the ROI for the nucleus (nuc), nucleus+perinuclear (nuc+per) and nucleus+perinuclear+cytoplasm (nuc+per+plas=cell). MFI values for perinuclear only (per) and cytoplasm only (plas) were calculated by subtracting the respecting regions:

$$INT_{area} = MFI \cdot area$$

$$MFI(per) = \frac{INT_{area}(nuc + peri) - INT_{area}(nuc)}{area(nuc + peri) - area(nuc)}$$

(Eq. 5.10)

$$MFI(plas) = \frac{INT_{area}(cell) - INT_{area}(nuc + per)}{area(cell) - area(nuc + per)}$$

$$MFI(per + plas) = \frac{INT_{area}(cell) - INT_{area}(nuc + per)}{area(cell) - area(nuc + per)}$$

In a next step the data was normalized to the overall cell fluorescence of the cell. The data of all analyzed fixed cells was plotted as box and whisker plots. Average values are plotted with standard deviations.

### 5.3.16.2 MFI and R/G in living cells

**Stack creation** The source and analyzed image data (TIFF-files of donor, FRET, transmission, R/G ratio image, raw data) were copied in folders for each channel or type. In a next step, single TIFF-files were imported in ImageJ by using the *File>Import>Image Sequence...* function to create xyzt-stacks of each type (donor, FRET, transmission, R/G ratio image). Donor, FRET and transmission channel were converted into 8-bit stacks for further processing and merged into RGB overlays. The raw data has to be imported by the *File>Import/Raw...* function choosing *Little-endian byte order*, *64-bit REAL* and *Open all files in folder*. The raw data stack can now be saved as TIFF-stack (raw data) and used to read out the correct R/G values (Part D in Figure 3.48).

**Sub-ROI stack creation** In a subsequent step the stacks of each signal was cropped to a rectangular ROI in which one cellular release was completely covered (sub-ROI or ROI-stack). These ROI-stacks were used to select the nucleus and cell outline.

**Feature extraction** Similar to fixed cells the MFI, area and integrated area was measured for each region in the donor, FRET, RGB, raw data tz-stack. In living cell,s only nucleus, cell and cytoplasm are distinguished, which can be used to calculate the MFI of the cytoplasm only (plas):

$$MFI(plas) = \frac{INT_{area}(cell) - INT_{area}(nuc)}{area(cell) - area(nuc)} \quad (\text{Eq. 5.11})$$

For analysis of the integrity state, the raw-stack was first thresholded to separate intact from partly degraded pixels by usage of an R/G threshold of 0.75 (corresponds to  $\sim 90\%$  of intact siRNA). The pixel number corresponds to the measured area as pixel values of 0 are ignored. To determine the fraction of intact pixels the total pixel numbers of thresholded and source image were set into relationship for each cell region.

$$\text{intact fraction} = \frac{area(thresholded)}{area(total)} \cdot 100\% \quad (\text{Eq. 5.12})$$

**Visualization** In a final step the extracted values were averaged over all z-stacks and plotted over time. The resulting graphs depict the change in fluorescence or integrity in the analyzed cell over time (see part E Figure 3.48).

### 5.3.17 Event analysis

All performed live-cell observations were manually inspected and analyzed by determining the start point of a release event and the fluorescence time inside the cytosol. Thereby, second or third release events before complete depletion from the cytoplasm were seen as one long fluorescence persistence time.

The live cell experiments were classified in two groups with many and few release events. Each category and the complete set was analyzed in the same way. The events were furthermore sorted according to their time of release and numbered. The data was represented in a plot in which each numbered event was assigned a horizontal line in the length of the fluorescence time inside the cytosol.

**Release time analysis** The total number of cells showing or having showed a release at an earlier time point corresponds to the envelope curve of the dwell time plot. The slope of the increase in this envelope curve corresponds to the release rate at a certain time. With Origin a piece-wise linear curve fitting was performed.

**Event duration analysis** The fluorescence time of the events was plotted in a frequency histogram with different bin sizes. Gaussian populations were fit by finding local maxima and fitting a Gaussian model using the *Peak Analyzer* tool of the Origin software. Fitted populations were plotted in the histogram plot.

# Collaborations





# Bibliography

- [1] M. Hirsch, D. Strand, and M. Helm. Dye selection for live cell imaging of intact siRNA. *Biol Chem*, 393(1-2):23–35, 2012.
- [2] A. Jarve, J. Muller, I. H. Kim, K. Rohr, C. MacLean, G. Fricker, U. Massing, F. Eberle, A. Dalpke, R. Fischer, M. F. Trendelenburg, and M. Helm. Surveillance of siRNA integrity by FRET imaging. *Nucleic Acids Res*, 35(18):e124, 2007.
- [3] M. Hirsch, I.-H. Kim, A. Järve, R. Fischer, M. F. Trendelenburg, U. Massing, K. Rohr, and M. Helm. Tracing of siRNAs inside cells by FRET imaging. In S. Q. Harper, editor, *RNA Interference Techniques*, pages 141–157. Springer, New York, Heidelberg, London, 2011.
- [4] I. H. Kim, A. Jarve, M. Hirsch, R. Fischer, M. F. Trendelenburg, U. Massing, K. Rohr, and M. Helm. FRET imaging of cells transfected with siRNA/liposome complexes. *Methods in Molecular Biology*, 606:439–55, 2010.
- [5] F. Crick. Central dogma of molecular biology. *Nature*, 227(5258):561–563, 1970.
- [6] M. Thattai. Using topology to tame the complex biochemistry of genetic networks. *Philosophical Transactions of the Royal Society A: Mathematical, Physical and Engineering Sciences*, 371(1984), 2013.
- [7] U. Ozomaro, C. Wahlestedt, and C. B. Nemeroff. Personalized medicine in psychiatry: problems and promises. *BMC medicine*, 11(1):132, 2013.
- [8] A. Fire, S. Xu, M. K. Montgomery, S. A. Kostas, S. E. Driver, and C. C. Mello. Potent and specific genetic interference by double-stranded RNA in caenorhabditis elegans. *Nature*, 391(6669):806–11, Feb 19 1998.
- [9] V. Mittal. Improving the efficiency of RNA interference in mammals. *Nat Rev Genet*, 5(5):355–65, May 2004.
- [10] H. Cerutti and J. A. Casas-Mollano. On the origin and functions of RNA-mediated silencing: from protists to man. *Current genetics*, 50(2):81–99, 2006.
- [11] S. M. Elbashir, J. Harborth, W. Lendeckel, A. Yalcin, K. Weber, and T. Tuschl. Duplexes of 21-nucleotide RNAs mediate RNA interference in cultured mammalian cells. *Nature*, 411(6836):494–8, May 24 2001.
- [12] S. M. Elbashir, J. Harborth, K. Weber, and T. Tuschl. Analysis of gene function in somatic mammalian cells using small interfering RNAs. *Methods*, 26(2):199–213, Feb 2002.
- [13] G. Hutvagner and M. J. Simard. Argonaute proteins: key players in RNA silencing. *Nat Rev Mol Cell Biol*, 9(1):22–32, Jan 2008.
- [14] C. Ender and G. Meister. Argonaute proteins at a glance. *Journal of cell science*, 123(11):1819–1823, 2010.
- [15] P. C. Zamecnik and M. L. Stephenson. Inhibition of rous sarcoma virus replication and cell transformation by a specific oligodeoxynucleotide. *Proceedings of the National Academy of Sciences*, 75(1):280–284, 1978.
- [16] J.-R. Bertrand, M. Pottier, A. Vekris, P. Opolon, A. Maksimenko, and C. Malvy. Comparison of antisense oligonucleotides and siRNAs in cell culture and in vivo. *Biochemical and biophysical*

- research communications*, 296(4):1000–1004, 2002.
- [17] M. Jinek and J. A. Doudna. A three-dimensional view of the molecular machinery of RNA interference. *Nature*, 457(7228):405–412, 2009.
- [18] D. J. Obbard, K. H. Gordon, A. H. Buck, and F. M. Jiggins. The evolution of RNAi as a defence against viruses and transposable elements. *Philosophical Transactions of the Royal Society B: Biological Sciences*, 364(1513):99–115, 2009.
- [19] V. N. Kim, J. Han, and M. C. Siomi. Biogenesis of small RNAs in animals. *Nature reviews Molecular cell biology*, 10(2):126–139, 2009.
- [20] E. Bernstein, A. A. Caudy, S. M. Hammond, and G. J. Hannon. Role for a bidentate ribonuclease in the initiation step of RNA interference. *Nature*, 409(6818):363–366, 2001.
- [21] K. Morris and J. Rossi. Lentiviral-mediated delivery of siRNAs for antiviral therapy. *Gene therapy*, 13(6):553–558, 2006.
- [22] D. Moazed. Small RNAs in transcriptional gene silencing and genome defence. *Nature*, 457(7228):413–420, 2009.
- [23] B. A. Janowski, K. E. Huffman, J. C. Schwartz, R. Ram, R. Nordsell, D. S. Shames, J. D. Minna, and D. R. Corey. Involvement of AGO1 and AGO2 in mammalian transcriptional silencing. *Nature structural & molecular biology*, 13(9):787–792, 2006.
- [24] V. N. Kim. MicroRNA biogenesis: coordinated cropping and dicing. *Nature reviews Molecular cell biology*, 6(5):376–385, 2005.
- [25] H. Siomi and M. C. Siomi. On the road to reading the RNA-interference code. *Nature*, 457(7228):396–404, 2009.
- [26] C.-Y. Chu and T. M. Rana. Small RNAs: regulators and guardians of the genome. *Journal of cellular physiology*, 213(2):412–419, 2007.
- [27] R. W. Carthew and E. J. Sontheimer. Origins and mechanisms of miRNAs and siRNAs. *Cell*, 136(4):642–655, 2009.
- [28] C. D. Malone and G. J. Hannon. Small RNAs as guardians of the genome. *Cell*, 136(4):656–668, 2009.
- [29] C. Klattenhoff and W. Theurkauf. Biogenesis and germline functions of piRNAs. *Development*, 135(1):3–9, 2008.
- [30] M. C. Siomi, K. Sato, D. Pezic, and A. A. Aravin. PIWI-interacting small RNAs: the vanguard of genome defence. *Nature reviews Molecular cell biology*, 12(4):246–258, 2011.
- [31] J. Brennecke, A. A. Aravin, A. Stark, M. Dus, M. Kellis, R. Sachidanandam, and G. J. Hannon. Discrete small RNA-generating loci as master regulators of transposon activity in drosophila. *Cell*, 128(6):1089–1103, 2007.
- [32] R. F. Ketting. The many faces of RNAi. *Developmental Cell*, 20(2):148–61, Feb 15 2011.
- [33] K. Bohmert, I. Camus, C. Bellini, D. Bouchez, M. Caboche, and C. Benning. AGO1 defines a novel locus of arabidopsis controlling leaf development. *The EMBO journal*, 17(1):170–180, 1998.
- [34] J. Höck and G. Meister. The argonaute protein family. *Genome Biol*, 9(2):210, 2008.
- [35] I. A. Drinnenberg, D. E. Weinberg, K. T. Xie, J. P. Mower, K. H. Wolfe, G. R. Fink, and D. P. Bartel. RNAi in budding yeast. *Science*, 326(5952):544–550, 2009.
- [36] K. Gavrilov and W. M. Saltzman. Therapeutic siRNA: principles, challenges, and strategies. *The Yale Journal of Biology and Medicine*, 85(2):187, 2012.
- [37] S. Shukla, C. S. Sumaria, and P. Pradeepkumar. Exploring chemical modifications for siRNA therapeutics: a structural and functional outlook. *ChemMedChem*, 5(3):328–349, 2010.
- [38] J.-B. Ma, K. Ye, and D. J. Patel. Structural basis for overhang-specific small interfering RNA recognition by the PAZ domain. *Nature*, 429(6989):318–322, 2004.

- [39] S. M. Elbashir, W. Lendeckel, and T. Tuschl. RNA interference is mediated by 21- and 22-nucleotide RNAs. *Genes & development*, 15(2):188–200, 2001.
- [40] M. Nowotny and W. Yang. Structural and functional modules in RNA interference. *Current opinion in structural biology*, 19(3):286–293, 2009.
- [41] A. S. Peek and M. A. Behlke. Design of active small interfering RNAs. *Curr Opin Mol Ther*, 9(2):110–8, 2007.
- [42] S. Seidu-Larry, B. Krieg, M. Hirsch, M. Helm, and O. Domingo. A modified guanosine phosphoramidite for click functionalization of RNA on the sugar edge. *Chem Commun (Camb)*, 48(89):11014–6, Nov 18 2012.
- [43] J. Liu, M. A. Carmell, F. V. Rivas, C. G. Marsden, J. M. Thomson, J. J. Song, S. M. Hammond, L. Joshua-Tor, and G. J. Hannon. Argonaute2 is the catalytic engine of mammalian RNAi. *Science*, 305(5689):1437–41, Sep 3 2004.
- [44] T. A. Rand, S. Petersen, F. Du, and X. Wang. Argonaute2 cleaves the anti-guide strand of siRNA during RISC activation. *Cell*, 123(4):621–9, Nov 18 2005.
- [45] D. S. Schwarz, G. Hutvagner, T. Du, Z. Xu, N. Aronin, and P. D. Zamore. Asymmetry in the assembly of the RNAi enzyme complex. *Cell*, 115(2):199–208, 2003.
- [46] D. S. Schwarz, G. Hutvagner, B. Haley, and P. D. Zamore. Evidence that siRNAs function as guides, not primers, in the drosophila and human RNAi pathways. *Mol Cell*, 10(3):537–48, 2002.
- [47] J. B. Preall, Z. He, J. M. Gorra, E. J. Sontheimer, et al. Short interfering RNA strand selection is independent of dsRNA processing polarity during RNAi in drosophila. *Current biology*, 16(5):530–535, 2006.
- [48] J.-B. Ma, Y.-R. Yuan, G. Meister, Y. Pei, T. Tuschl, and D. J. Patel. Structural basis for 5'-end-specific recognition of guide RNA by the a. fulgidus Piwi protein. *Nature*, 434(7033):666–670, 2005.
- [49] J. S. Parker, S. M. Roe, and D. Barford. Structural insights into mRNA recognition from a piwi domain–siRNA guide complex. *Nature*, 434(7033):663–666, 2005.
- [50] K. Miyoshi, H. Tsukumo, T. Nagami, H. Siomi, and M. C. Siomi. Slicer function of drosophila argonautes and its involvement in RISC formation. *Genes Dev*, 19(23):2837–48, Dec 1 2005.
- [51] C. Matranga, Y. Tomari, C. Shin, D. P. Bartel, and P. D. Zamore. Passenger-strand cleavage facilitates assembly of siRNA into Ago2-containing RNAi enzyme complexes. *Cell*, 123(4):607–20, Nov 18 2005.
- [52] P. J. Leuschner, S. L. Ameres, S. Kueng, and J. Martinez. Cleavage of the siRNA passenger strand during RISC assembly in human cells. *EMBO Rep*, 7(3):314–20, Mar 2006.
- [53] S. L. Ameres, J. Martinez, and R. Schroeder. Molecular basis for target RNA recognition and cleavage by human RISC. *Cell*, 130(1):101–112, 2007.
- [54] G. Hutvagner and P. D. Zamore. A microRNA in a multiple-turnover RNAi enzyme complex. *Science*, 297(5589):2056–2060, 2002.
- [55] A. Stark, J. Brennecke, R. B. Russell, and S. M. Cohen. Identification of drosophila microRNA targets. *PLoS biology*, 1(3):e60, 2003.
- [56] K. A. Whitehead, R. Langer, and D. G. Anderson. Knocking down barriers: advances in siRNA delivery. *Nature reviews Drug discovery*, 8(2):129–138, 2009.
- [57] J. C. Burnett, J. J. Rossi, and K. Tiemann. Current progress of siRNA/shRNA therapeutics in clinical trials. *Biotechnology journal*, 6(9):1130–1146, 2011.
- [58] J. C. Burnett and J. J. Rossi. RNA-based therapeutics: current progress and future prospects. *Chemistry & biology*, 19(1):60–71, 2012.
- [59] E. Wagner. Biomaterials in RNAi therapeutics: quo vadis? *Biomater. Sci.*, 1:804–809, 2013.
- [60] A. L. Jackson and P. S. Linsley. Recognizing and avoiding siRNA off-target effects for target

- identification and therapeutic application. *Nature reviews Drug discovery*, 9(1):57–67, 2010.
- [61] A. L. Jackson, S. R. Bartz, J. Schelter, S. V. Kobayashi, J. Burchard, M. Mao, B. Li, G. Cavet, and P. S. Linsley. Expression profiling reveals off-target gene regulation by RNAi. *Nature biotechnology*, 21(6):635–637, 2003.
- [62] A. L. Jackson, J. Burchard, J. Schelter, B. N. Chau, M. Cleary, L. Lim, and P. S. Linsley. Widespread siRNA "off-target" transcript silencing mediated by seed region sequence complementarity. *RNA*, 12(7):1179–1187, 2006.
- [63] L. Aagaard and J. J. Rossi. RNAi therapeutics: principles, prospects and challenges. *Advanced drug delivery reviews*, 59(2):75–86, 2007.
- [64] A. Reynolds, E. M. Anderson, A. Vermeulen, Y. Fedorov, K. Robinson, D. Leake, J. Karpilow, W. S. Marshall, and A. Khvorova. Induction of the interferon response by siRNA is cell type–and duplex length–dependent. *RNA*, 12(6):988–993, 2006.
- [65] G. R. Stark, I. M. Kerr, B. R. Williams, R. H. Silverman, and R. D. Schreiber. How cells respond to interferons. *Annu Rev Biochem*, 67:227–64, 1998.
- [66] V. Hornung, M. Guenthner-Biller, C. Bourquin, A. Ablasser, M. Schlee, S. Uematsu, A. Noronha, M. Manoharan, S. Akira, A. de Fougères, et al. Sequence-specific potent induction of IFN- $\alpha$  by short interfering RNA in plasmacytoid dendritic cells through TLR7. *Nature medicine*, 11(3):263–270, 2005.
- [67] R. L. Kanasty, K. A. Whitehead, A. J. Vegas, and D. G. Anderson. Action and reaction: the biological response to siRNA and its delivery vehicles. *Molecular Therapy*, 20(3):513–524, 2012.
- [68] K. A. Whitehead, J. E. Dahlman, R. S. Langer, and D. G. Anderson. Silencing or stimulation? siRNA delivery and the immune system. *Annual Review of Chemical and Biomolecular Engineering*, 2:77–96, 2011.
- [69] G. J. Hannon. RNA interference. *Nature*, 418(6894):244–51, Jul 11 2002.
- [70] J. D. Heidel, S. Hu, X. F. Liu, T. J. Triche, and M. E. Davis. Lack of interferon response in animals to naked siRNAs. *Nature biotechnology*, 22(12):1579–1582, 2004.
- [71] T. Dowler, D. Bergeron, A.-L. Tedeschi, L. Paquet, N. Ferrari, and M. J. Damha. Improvements in siRNA properties mediated by 2'-deoxy-2'-fluoro- $\beta$ -D-arabinonucleic acid (FANA). *Nucleic acids research*, 34(6):1669–1675, 2006.
- [72] D. Bumcrot, M. Manoharan, V. Kotliansky, and D. W. Sah. RNAi therapeutics: a potential new class of pharmaceutical drugs. *Nat Chem Biol*, 2(12):711–9, Dec 2006.
- [73] J. Harborth, S. M. Elbashir, K. Vandeburgh, H. Manninga, S. A. Scaringe, K. Weber, and T. Tuschl. Sequence, chemical, and structural variation of small interfering RNAs and short hairpin RNAs and the effect on mammalian gene silencing. *Antisense Nucleic Acid Drug Dev*, 13(2):83–105, Apr 2003.
- [74] H. Vornlocher, T. Zimmermann, M. Manoharan, K. Rajeev, I. Roehl, and A. Akinc. Nuclease-resistant double-stranded RNA for RNA interference. Patent: WO2005115481, 2005.
- [75] A. D. Judge, V. Sood, J. R. Shaw, D. Fang, K. McClintock, and I. MacLachlan. Sequence-dependent stimulation of the mammalian innate immune response by synthetic siRNA. *Nature biotechnology*, 23(4):457–462, 2005.
- [76] M. Terrazas and E. T. Kool. RNA major groove modifications improve siRNA stability and biological activity. *Nucleic acids research*, 37(2):346–353, 2009.
- [77] S. M. Elbashir, J. Martinez, A. Patkaniowska, W. Lendeckel, and T. Tuschl. Functional anatomy of siRNAs for mediating efficient RNAi in drosophila melanogaster embryo lysate. *The EMBO journal*, 20(23):6877–6888, 2001.
- [78] F. Graham and A. Van der Eb. A new technique for the assay of infectivity of human adenovirus 5

- DNA. *Virology*, 52(2):456–467, 1973.
- [79] W. A. Keown, C. R. Campbell, and R. S. Kucherlapati. Methods for introducing DNA into mammalian cells. *Methods Enzymol*, 185:527–37, 1990.
- [80] D. Liu, E. F. Chiao, and H. Tian. Chemical methods for DNA delivery: an overview. *Methods Mol Biol*, 245:3–24, 2004.
- [81] M. E. Davis. Non-viral gene delivery systems. *Curr Opin Biotechnol*, 13(2):128–31, Apr 2002.
- [82] O. Boussif, F. Lezoualc'h, M. A. Zanta, M. D. Mergny, D. Scherman, B. Demeneix, and J. P. Behr. A versatile vector for gene and oligonucleotide transfer into cells in culture and in vivo: polyethylenimine. *Proc Natl Acad Sci U S A*, 92(16):7297–301, Aug 1 1995.
- [83] M. X. Tang, C. T. Redemann, and F. C. Szoka. In vitro gene delivery by degraded polyamidoamine dendrimers. *Bioconjugate chemistry*, 7(6):703–714, 1996.
- [84] Y. Omid, A. J. Hollins, M. Benboubetra, R. Drayton, I. F. Benter, and S. Akhtar. Toxicogenomics of non-viral vectors for gene therapy: a microarray study of lipofectin-and oligofectamine-induced gene expression changes in human epithelial cells. *Journal of drug targeting*, 11(6):311–323, 2003.
- [85] M. Overhoff and G. Sczakiel. Phosphorothioate-stimulated uptake of short interfering RNA by human cells. *EMBO Rep*, 6(12):1176–81, Dec 2005.
- [86] A. Detzer, M. Overhoff, A. Mescalc'hin, M. Rompf, and G. Sczakiel. Phosphorothioate-stimulated cellular uptake of siRNA: a cell culture model for mechanistic studies. *Curr Pharm Des*, 14(34):3666–73, 2008.
- [87] E. Neumann, M. Schaefer-Ridder, Y. Wang, and P. H. Hofschneider. Gene transfer into mouse lyoma cells by electroporation in high electric fields. *Embo J*, 1(7):841–5, 1982.
- [88] M. Graessmann and A. Graessmann. Microinjection of tissue culture cells. *Methods Enzymol*, 101:482–92, 1983.
- [89] S. J. Reich, J. Fosnot, A. Kuroki, W. Tang, X. Yang, A. M. Maguire, J. Bennett, and M. J. Tolentino. Small interfering RNA (siRNA) targeting vegf effectively inhibits ocular neovascularization in a mouse model. *Mol Vis*, 9(5):210–216, 2003.
- [90] R. Alvarez, S. Elbashir, T. Borland, I. Toudjarska, P. Hadwiger, M. John, I. Roehl, S. S. Morskaya, R. Martinello, J. Kahn, et al. RNA interference-mediated silencing of the respiratory syncytial virus nucleocapsid defines a potent antiviral strategy. *Antimicrobial agents and chemotherapy*, 53(9):3952–3962, 2009.
- [91] M.-S. Martina, V. Nicolas, C. Wilhelm, C. Ménager, G. Barratt, and S. Lesieur. The in vitro kinetics of the interactions between peg-ylated magnetic-fluid-loaded liposomes and macrophages. *Biomaterials*, 28(28):4143–4153, 2007.
- [92] F. Alexis, E. Pridgen, L. K. Molnar, and O. C. Farokhzad. Factors affecting the clearance and biodistribution of polymeric nanoparticles. *Molecular pharmaceutics*, 5(4):505–515, 2008.
- [93] D. T. Auguste, K. Furman, A. Wong, J. Fuller, S. P. Armes, T. J. Deming, and R. Langer. Triggered release of siRNA from poly (ethylene glycol)-protected, pH-dependent liposomes. *Journal of Controlled Release*, 130(3):266–274, 2008.
- [94] M. Schaefer-Ridder, Y. Wang, and P. H. Hofschneider. Liposomes as gene carriers: efficient transformation of mouse L cells by thymidine kinase gene. *Science*, 215(4529):166–8, Jan 8 1982.
- [95] S. D. Patil, D. G. Rhodes, and D. J. Burgess. DNA-based therapeutics and DNA delivery systems: a comprehensive review. *Aaps J*, 7(1):E61–77, 2005.
- [96] M. R. Mozafari. Liposomes: an overview of manufacturing techniques. *Cell Mol Biol Lett*, 10(4):711–9, 2005.
- [97] D. Grimm, K. L. Streetz, C. L. Jopling, T. A. Storm, K. Pandey, C. R. Davis, P. Marion, F. Salazar,

- and M. A. Kay. Fatality in mice due to oversaturation of cellular microRNA/short hairpin RNA pathways. *Nature*, 441(7092):537–541, 2006.
- [98] Y. Gao, X.-L. Liu, and X.-R. Li. Research progress on siRNA delivery with nonviral carriers. *International journal of nanomedicine*, 6:1017, 2011.
- [99] V. Hughes. Therapy on trial. *Nature medicine*, 13(9):1008–1009, 2007.
- [100] K. A. Howard, U. L. Rahbek, X. Liu, C. K. Damgaard, S. Z. Glud, M. Ø. Andersen, M. B. Hovgaard, A. Schmitz, J. R. Nyengaard, F. Besenbacher, et al. RNA interference in vitro and in vivo using a chitosan/siRNA nanoparticle system. *Molecular Therapy*, 14(4):476–484, 2006.
- [101] J. K. Lam, W. Liang, Y. Lan, P. Chaudhuri, M. Y. Chow, K. Witt, L. Kudsiova, and A. J. Mason. Effective endogenous gene silencing mediated by pH responsive peptides proceeds via multiple pathways. *Journal of Controlled Release*, 158(2):293–303, 2012.
- [102] S. E. Andaloussi, T. Lehto, I. Mäger, K. Rosenthal-Aizman, I. I. Oprea, O. E. Simonson, H. Sork, K. Ezzat, D. M. Copolovici, K. Kurrikoff, et al. Design of a peptide-based vector, PepFect6, for efficient delivery of siRNA in cell culture and systemically in vivo. *Nucleic acids research*, 39(9):3972–3987, 2011.
- [103] A. Zintchenko, A. Philipp, A. Dehshahri, and E. Wagner. Simple modifications of branched PEI lead to highly efficient siRNA carriers with low toxicity. *Bioconjugate chemistry*, 19(7):1448–1455, 2008.
- [104] T. D. Schladt, K. Koll, S. Prüfer, H. Bauer, F. Natalio, O. Dumele, R. Raidoo, S. Weber, U. Wolfrum, L. M. Schreiber, et al. Multifunctional superparamagnetic MnO<sub>2</sub> core/shell nanoparticles and their application for optical and magnetic resonance imaging. *Journal of Materials Chemistry*, 22(18):9253–9262, 2012.
- [105] M. L. Patil, M. Zhang, S. Betigeri, O. Taratula, H. He, and T. Minko. Surface-modified and internally cationic polyamidoamine dendrimers for efficient siRNA delivery. *Bioconjugate chemistry*, 19(7):1396–1403, 2008.
- [106] K. Kataoka, A. Harada, and Y. Nagasaki. Block copolymer micelles for drug delivery: design, characterization and biological significance. *Advanced drug delivery reviews*, 64, Supplement(0):37–48, 2012.
- [107] J. H. Jeong, H. Mok, Y.-K. Oh, and T. G. Park. siRNA conjugate delivery systems. *Bioconjugate chemistry*, 20(1):5–14, 2008.
- [108] J. Soutschek, A. Akinc, B. Bramlage, K. Charisse, R. Constien, M. Donoghue, S. Elbashir, A. Geick, P. Hadwiger, J. Harborth, M. John, V. Kesavan, G. Lavigne, R. K. Pandey, T. Racie, K. G. Rajeev, I. Rohl, I. Toudjarska, G. Wang, S. Wuschko, D. Bumcrot, V. Kotliansky, S. Limmer, M. Manoharan, and H. P. Vornlocher. Therapeutic silencing of an endogenous gene by systemic administration of modified siRNAs. *Nature*, 432(7014):173–8, Nov 11 2004.
- [109] C. Dohmen, T. Fröhlich, U. Lächelt, I. Röhl, H.-P. Vornlocher, P. Hadwiger, and E. Wagner. Defined folate-peg-siRNA conjugates for receptor-specific gene silencing. *Molecular Therapy-7Nucleic Acids*, 1(1):e7, 2012.
- [110] A. Muratovska and M. R. Eccles. Conjugate for efficient delivery of short interfering RNA (siRNA) into mammalian cells. *FEBS letters*, 558(1):63–68, 2004.
- [111] M. Oishi, Y. Nagasaki, K. Itaka, N. Nishiyama, and K. Kataoka. Lactosylated poly(ethylene glycol)-siRNA conjugate through acid-labile  $\beta$ -thiopropionate linkage to construct pH-sensitive polyion complex micelles achieving enhanced gene silencing in hepatoma cells. *Journal of the American Chemical Society*, 127(6):1624–1625, 2005.
- [112] J. O. McNamara, E. R. Andrechek, Y. Wang, K. D. Viles, R. E. Rempel, E. Gilboa, B. A. Sullenger, and P. H. Giangrande. Cell type-specific delivery of siRNAs with aptamer-siRNA chimeras. *Nature*

- biotechnology*, 24(8):1005–1015, 2006.
- [113] C.-F. Xia, R. J. Boado, and W. M. Pardridge. Antibody-mediated targeting of siRNA via the human insulin receptor using avidin- biotin technology. *Molecular pharmaceuticals*, 6(3):747–751, 2008.
- [114] A. Akinc, M. Thomas, A. M. Klibanov, and R. Langer. Exploring polyethylenimine-mediated DNA transfection and the proton sponge hypothesis. *The journal of gene medicine*, 7(5):657–663, 2005.
- [115] D. N. Nguyen, S. C. Chen, J. Lu, M. Goldberg, P. Kim, A. Sprague, T. Novobrantseva, J. Sherman, S. Shulga-Morskaya, A. de Fougères, et al. Drug delivery–mediated control of RNA immunostimulation. *Molecular Therapy*, 17(9):1555–1562, 2009.
- [116] T. S. Zimmermann, A. C. Lee, A. Akinc, B. Bramlage, D. Bumcrot, M. N. Fedoruk, J. Harborth, J. A. Heyes, L. B. Jeffs, M. John, A. D. Judge, K. Lam, K. McClintock, L. V. Nechev, L. R. Palmer, T. Racie, I. Rohl, S. Seiffert, S. Shanmugam, V. Sood, J. Soutschek, I. Toudjarska, A. J. Wheat, E. Yaworski, W. Zedalis, V. Kotliansky, M. Manoharan, H. P. Vornlocher, and I. MacLachlan. RNAi-mediated gene silencing in non-human primates. *Nature*, 441(7089):111–4, May 4 2006.
- [117] A. Akinc, A. Zumbuehl, M. Goldberg, E. S. Leshchiner, V. Busini, N. Hossain, S. A. Bacallado, D. N. Nguyen, J. Fuller, R. Alvarez, et al. A combinatorial library of lipid-like materials for delivery of RNAi therapeutics. *Nature biotechnology*, 26(5):561–569, 2008.
- [118] M. E. Davis, J. E. Zuckerman, C. H. Choi, D. Seligson, A. Tolcher, C. A. Alabi, Y. Yen, J. D. Heidel, and A. Ribas. Evidence of RNAi in humans from systemically administered siRNA via targeted nanoparticles. *Nature*, 464(7291):1067–70, Apr 15 2010.
- [119] H. Lv, S. Zhang, B. Wang, S. Cui, and J. Yan. Toxicity of cationic lipids and cationic polymers in gene delivery. *Journal of Controlled Release*, 114(1):100–109, 2006.
- [120] R. Kedmi, N. Ben-Arie, and D. Peer. The systemic toxicity of positively charged lipid nanoparticles and the role of toll-like receptor 4 in immune activation. *Biomaterials*, 31(26):6867–6875, 2010.
- [121] S. Dokka, D. Toledo, X. Shi, V. Castranova, and Y. Rojanasakul. Oxygen radical-mediated pulmonary toxicity induced by some cationic liposomes. *Pharmaceutical research*, 17(5):521–525, 2000.
- [122] O. M. Merkel, A. Beyerle, B. M. Beckmann, M. Zheng, R. K. Hartmann, T. Stöger, and T. H. Kissel. Polymer-related off-target effects in non-viral siRNA delivery. *Biomaterials*, 32(9):2388–2398, 2011.
- [123] E. Koller, S. Propp, H. Murray, W. Lima, B. Bhat, T. P. Prakash, C. R. Allerson, E. E. Swayze, E. G. Marcusson, and N. M. Dean. Competition for RISC binding predicts in vitro potency of siRNA. *Nucleic acids research*, 34(16):4467–4476, 2006.
- [124] J. Nguyen and F. C. Szoka. Nucleic acid delivery: the missing pieces of the puzzle? *Accounts of Chemical Research*, 45(7):1153–1162, 2012.
- [125] A. Sharma and U. S. Sharma. Liposomes in drug delivery: progress and limitations. *International Journal of Pharmaceutics*, 154(2):123–140, 1997.
- [126] M. Gooding, L. P. Browne, F. M. Quinteiro, and D. L. Selwood. siRNA delivery: From lipids to cell-penetrating peptides and their mimics. *Chemical Biology & Drug Design*, 80(6):787–809, 2012.
- [127] C.-Y. Jiao, D. Delaroche, F. Burlina, I. D. Alves, G. Chassaing, and S. Sagan. Translocation and endocytosis for cell-penetrating peptide internalization. *Journal of Biological Chemistry*, 284(49):33957–33965, 2009.
- [128] U. Massing and S. Fuxius. Liposomal formulations of anticancer drugs: selectivity and effectiveness. *Drug Resist Updat*, 3(3):171–177, Jun 2000.
- [129] L. W. Seymour. Passive tumor targeting of soluble macromolecules and drug conjugates. *Crit Rev Ther Drug Carrier Syst*, 9(2):135–87, 1992.
- [130] A. Gabizon and D. Papahadjopoulos. Liposome formulations with prolonged circulation time in

- blood and enhanced uptake by tumors. *Proc Natl Acad Sci U S A*, 85(18):6949–53, Sep 1988.
- [131] R. K. Jain. Transport of molecules in the tumor interstitium: a review. *Cancer Res*, 47(12):3039–51, Jun 15 1987.
- [132] S. Lopez and C. Arias. How viruses hijack endocytic machinery. *Nature Education*, 3(9):16–23, 2010.
- [133] S. Mayor and R. E. Pagano. Pathways of clathrin-independent endocytosis. *Nature reviews Molecular cell biology*, 8(8):603–612, 2007.
- [134] S. Falcone, E. Cocucci, P. Podini, T. Kirchhausen, E. Clementi, and J. Meldolesi. Macropinocytosis: regulated coordination of endocytic and exocytic membrane traffic events. *Journal of cell science*, 119(22):4758–4769, 2006.
- [135] M. Kirkham and R. G. Parton. Clathrin-independent endocytosis: new insights into caveolae and non-caveolar lipid raft carriers. *Biochimica et Biophysica Acta (BBA)-Molecular Cell Research*, 1745(3):273–286, 2005.
- [136] S. Mousavi, L. Malerd, T. Berg, and R. Kjekken. Clathrin-dependent endocytosis. *Biochem. J*, 377:1–16, 2004.
- [137] R. G. Parton and K. Simons. The multiple faces of caveolae. *Nature reviews Molecular cell biology*, 8(3):185–194, 2007.
- [138] N. Nelson, N. Perzov, A. Cohen, K. Hagai, V. Padler, and H. Nelson. The cellular biology of proton-motive force generation by V-ATPases. *Journal of Experimental Biology*, 203(1):89–95, 2000.
- [139] A.-T. Dinh, C. Pangarkar, T. Theofanous, and S. Mitragotri. Understanding intracellular transport processes pertinent to synthetic gene delivery via stochastic simulations and sensitivity analyses. *Biophysical journal*, 92(3):831–846, 2007.
- [140] M. A. Welte. Bidirectional transport along microtubules. *Current Biology*, 14(13):R525–R537, 2004.
- [141] J.-P. Behr. The proton sponge: a trick to enter cells the viruses did not exploit. *CHIMIA International Journal for Chemistry*, 51(1-2):1–2, 1997.
- [142] N. D. Sonawane, F. C. Szoka, and A. Verkman. Chloride accumulation and swelling in endosomes enhances DNA transfer by polyamine-DNA polyplexes. *Journal of Biological Chemistry*, 278(45):44826–44831, 2003.
- [143] Y. Xu and F. C. Szoka. Mechanism of DNA release from cationic liposome/DNA complexes used in cell transfection. *Biochemistry*, 35(18):5616–5623, 1996.
- [144] I. Hafez, N. Maurer, P. Cullis, et al. On the mechanism whereby cationic lipids promote intracellular delivery of polynucleic acids. *Gene therapy*, 8(15):1188–1196, 2001.
- [145] O. Zelphati and F. C. Szoka. Mechanism of oligonucleotide release from cationic liposomes. *Proceedings of the National Academy of Sciences*, 93(21):11493–11498, 1996.
- [146] S. C. Semple, A. Akinc, J. Chen, A. P. Sandhu, B. L. Mui, C. K. Cho, D. W. Sah, D. Stebbing, E. J. Crosley, I. M. Hafez, et al. Rational design of cationic lipids for siRNA delivery. *Nature biotechnology*, 28(2):172–176, 2010.
- [147] H. Valadi, K. Ekström, A. Bossios, M. Sjöstrand, J. J. Lee, and J. O. Lötvall. Exosome-mediated transfer of mRNAs and microRNAs is a novel mechanism of genetic exchange between cells. *Nature cell biology*, 9(6):654–659, 2007.
- [148] L. Weinmann, J. Hock, T. Ivacevic, T. Ohrt, J. Mutze, P. Schwille, E. Kremmer, V. Benes, H. Urlaub, and G. Meister. Importin 8 is a gene silencing factor that targets argonaute proteins to distinct mRNAs. *Cell*, 136(3):496–507, Feb 6 2009.
- [149] L. Sinkkonen, T. Hugenschmidt, W. Filipowicz, and P. Svoboda. Dicer is associated with ribosomal



- DNA chromatin in mammalian cells. *PLoS one*, 5(8):e12175, 2010.
- [150] T. A. Rand, K. Ginalski, N. V. Grishin, and X. Wang. Biochemical identification of argonaute 2 as the sole protein required for RNA-induced silencing complex activity. *Proc Natl Acad Sci U S A*, 101(40):14385–9, Oct 5 2004.
- [151] R. Parker and U. Sheth. P bodies and the control of mRNA translation and degradation. *Molecular cell*, 25(5):635–646, 2007.
- [152] A. Eulalio, I. Behm-Ansmant, D. Schweizer, and E. Izaurralde. P-body formation is a consequence, not the cause, of RNA-mediated gene silencing. *Molecular and cellular biology*, 27(11):3970–3981, 2007.
- [153] D. J. Gibbings, C. Ciaudo, M. Erhardt, and O. Voinnet. Multivesicular bodies associate with components of miRNA effector complexes and modulate miRNA activity. *Nature Cell Biology*, 11(9):1143–1149, 2009.
- [154] Y. S. Lee, S. Pressman, A. P. Andress, K. Kim, J. L. White, J. J. Cassidy, X. Li, K. Lubell, D. H. Lim, I. S. Cho, et al. Silencing by small RNAs is linked to endosomal trafficking. *Nature Cell Biology*, 11(9):1150–1156, 2009.
- [155] L. Stalder, W. Heusermann, L. Sokol, D. Trojer, J. Wirz, J. Hean, A. Fritzsche, F. Aeschmann, V. Pfanzagl, P. Basselet, et al. The rough endoplasmic reticulum is a central nucleation site of siRNA-mediated RNA silencing. *The EMBO journal*, 32:1115–1127, 2013.
- [156] D. W. Bartlett and M. E. Davis. Insights into the kinetics of siRNA-mediated gene silencing from live-cell and live-animal bioluminescent imaging. *Nucleic acids research*, 34(1):322–333, 2006.
- [157] M. HATTORI, A. TUGORES, L. VELOZ, M. KARIN, and D. A. BRENNER. A simplified method for the preparation of transcriptionally active liver nuclear extracts. *DNA and cell biology*, 9(10):777–781, 1990.
- [158] T. E. Tjelle, A. Brech, L. K. Juvet, G. Griffiths, and T. Berg. Isolation and characterization of early endosomes, late endosomes and terminal lysosomes: their role in protein degradation. *Journal of cell science*, 109(12):2905–2914, 1996.
- [159] Y. Hayashida, T. Nishibu, K. Inoue, and T. Kurokawa. A useful approach to total analysis of risc-associated RNA. *BMC research notes*, 2(1):169, 2009.
- [160] N. M. Christensen, K. J. Oparka, and J. Tilsner. Advances in imaging RNA in plants. *Trends in plant science*, 15(4):196–203, 2010.
- [161] O. Shimomura, F. H. Johnson, and Y. Saiga. Extraction, purification and properties of aequorin, a bioluminescent protein from the luminous hydromedusa, aequorea. *Journal of cellular and comparative physiology*, 59(3):223–239, 1962.
- [162] R. Heim, A. B. Cubitt, and R. Y. Tsien. Improved green fluorescence. *Nature*, 373:663–664, 1995.
- [163] S. Tyagi. Imaging intracellular RNA distribution and dynamics in living cells. *natuRe methods*, 6(5):331–338, 2009.
- [164] E. Bertrand, P. Chartrand, M. Schaefer, S. M. Shenoy, R. H. Singer, and R. M. Long. Localization of ASH1 mRNA particles in living yeast. *Molecular cell*, 2(4):437–445, 1998.
- [165] N. Daigle and J. Ellenberg.  $\lambda$ n-GFP: an RNA reporter system for live-cell imaging. *Nature methods*, 4(8):633–636, 2007.
- [166] A. Calapez, H. M. Pereira, A. Calado, J. Braga, J. Rino, C. Carvalho, J. P. Tavanez, E. Wahle, A. C. Rosa, and M. Carmo-Fonseca. The intranuclear mobility of messenger RNA binding proteins is ATP dependent and temperature sensitive. *The Journal of cell biology*, 159(5):795–805, 2002.
- [167] O. Rackham and C. M. Brown. Visualization of RNA–protein interactions in living cells: FMRP and IMP1 interact on mRNAs. *The EMBO journal*, 23(16):3346–3355, 2004.
- [168] T. Ozawa, Y. Natori, M. Sato, and Y. Umezawa. Imaging dynamics of endogenous mitochondrial

- RNA in single living cells. *Nature methods*, 4(5):413–419, 2007.
- [169] G. S. Wilkie and I. Davis. *Drosophila* wingless and pair-rule transcripts localize apically by dynein-mediated transport of RNA particles. *Cell*, 105(2):209–219, 2001.
- [170] C. Y. Jao and A. Salic. Exploring RNA transcription and turnover in vivo by using click chemistry. *Proceedings of the National Academy of Sciences*, 105(41):15779–15784, 2008.
- [171] F. A. Tanious, J. M. Veal, H. Buczak, L. S. Ratmeyer, and W. D. Wilson. DAPI (4', 6-diamidino-2-phenylindole) binds differently to DNA and RNA: minor-groove binding at at sites and intercalation at au sites. *Biochemistry*, 31(12):3103–3112, 1992.
- [172] Q. Li, Y. Kim, J. Namm, A. Kulkarni, G. R. Rosania, Y.-H. Ahn, and Y.-T. Chang. RNA-selective, live cell imaging probes for studying nuclear structure and function. *Chemistry & biology*, 13(6): 615–623, 2006.
- [173] D. J. Arndt-Jovin and T. M. Jovin. Fluorescence labeling and microscopy of DNA. *Methods Cell Biol*, 30:417–448, 1989.
- [174] P. Vader, L. J. van der Aa, J. F. Engbersen, G. Storm, and R. M. Schiffelers. A method for quantifying cellular uptake of fluorescently labeled siRNA. *Journal of Controlled Release*, 148(1):106–9, Nov 20 2010.
- [175] T. Ohrt, D. Merkle, K. Birkenfeld, C. J. Echeverri, and P. Schwill. In situ fluorescence analysis demonstrates active siRNA exclusion from the nucleus by exportin 5. *Nucleic Acids Res*, 34(5): 1369–80, 2006.
- [176] K. Raemdonck, K. Remaut, B. Lucas, N. N. Sanders, J. Demeester, and S. C. De Smedt. In situ analysis of single-stranded and duplex siRNA integrity in living cells. *Biochemistry*, 45(35): 10614–23, Sep 5 2006.
- [177] A. Jagannath and M. J. Wood. Localization of double-stranded small interfering RNA to cytoplasmic processing bodies is Ago2 dependent and results in up-regulation of GW182 and Argonaute-2. *Molecular Biology of the Cell*, 20(1):521–9, Jan 2009.
- [178] D. P. Bratu, B.-J. Cha, M. M. Mhlanga, F. R. Kramer, and S. Tyagi. Visualizing the distribution and transport of mRNAs in living cells. *Proceedings of the National Academy of Sciences*, 100(23): 13308–13313, 2003.
- [179] J. S. Paige, K. Y. Wu, and S. R. Jaffrey. RNA mimics of green fluorescent protein. *Science*, 333 (6042):642–646, 2011.
- [180] D. M. Chudakov, M. V. Matz, S. Lukyanov, and K. A. Lukyanov. Fluorescent proteins and their applications in imaging living cells and tissues. *Physiological Reviews*, 90(3):1103–1163, 2010.
- [181] A. D. Ellington and J. W. Szostak. In vitro selection of RNA molecules that bind specific ligands. *Nature*, 346(6287):818–822, 1990.
- [182] J. S. Mattick and M. B. Clark. RNA lights up. *Nature biotechnology*, 29(10):883–884, 2011.
- [183] J. S. Paige, T. Nguyen-Duc, W. Song, and S. R. Jaffrey. Fluorescence imaging of cellular metabolites with RNA. *Science*, 335(6073):1194–1194, 2012.
- [184] H. Hong, Y. Zhang, and W. Cai. In vivo imaging of RNA interference. *Journal of Nuclear Medicine*, 51(2):169–172, 2010.
- [185] G. G. Stokes. On the change of refrangibility of light. *Philosophical Transactions of the Royal Society of London*, 142:463–562, 1852.
- [186] B. Valeur and M. N. Berberan-Santos. A brief history of fluorescence and phosphorescence before the emergence of quantum theory. *Journal of Chemical Education*, 88(6):731–738, 2011.
- [187] S. E. Braslavsky et al. Glossary of terms used in photochemistry, (iupac recommendations 2006). *Pure and applied chemistry*, 79(3):293–465, 2007.
- [188] H. C. Ishikawa-Ankerhold, R. Ankerhold, and G. P. Drummen. Advanced Fluorescence Microscopy

- Techniques - FRAP, FLIP, FLAP, FRET and FLIM. *Molecules*, 17(4):4047–4132, 2012.
- [189] M. Kasha. Characterization of electronic transitions in complex molecules. *Discussions of the Faraday Society*, 9:14–19, 1950.
- [190] T. Förster. Zwischenmolekulare energiewanderung und fluoreszenz. *Annalen der physik*, 437(1-2): 55–75, 1948.
- [191] S. Padilla-Parra and M. Tramier. FRET microscopy in the living cell: different approaches, strengths and weaknesses. *Bioessays*, 34(5):369–376, 2012.
- [192] P. Held. An introduction to fluorescence resonance energy transfer (FRET) technology and its application in bioscience, June 2005. [Online] URL: <http://micro.magnet.fsu.edu/index.html>, accessed 2013-08-01.
- [193] J. R. Lakowicz. *Principles of fluorescence spectroscopy*. Springer, 2009.
- [194] L. Stryer. Fluorescence energy transfer as a spectroscopic ruler. *Annual review of biochemistry*, 47(1):819–846, 1978.
- [195] P. Wu and L. Brand. Resonance energy transfer: methods and applications. *Anal Biochem*, 218(1): 1–13, Apr 1994.
- [196] M.-C. Chirio-Lebrun and M. Prats. Fluorescence resonance energy transfer (FRET): theory and experiments. *Biochemical Education*, 26(4):320–323, 1998.
- [197] L. Ying, M. I. Wallace, S. Balasubramanian, and D. Klenerman. Ratiometric analysis of single-molecule fluorescence resonance energy transfer using logical combinations of threshold criteria: a study of 12-mer DNA. *The Journal of Physical Chemistry B*, 104(21):5171–5178, 2000.
- [198] A. Miyawaki, J. Llopis, R. Heim, J. M. McCaffery, J. A. Adams, M. Ikura, and R. Y. Tsien. Fluorescent indicators for  $Ca^{2+}$  based on green fluorescent proteins and calmodulin. *Nature*, 388(6645): 882–887, 1997.
- [199] M. Hengesbach, F. Voigts-Hoffmann, B. Hofmann, and M. Helm. Formation of a stalled early intermediate of pseudouridine synthesis monitored by real-time FRET. *RNA*, 16(3):610–620, 2010.
- [200] C. Holzhauser, R. Liebl, A. Goepferich, H.-A. Wagenknecht, and M. Breunig. RNA "Traffic Lights": An Analytical Tool to Monitor siRNA Integrity. *ACS chemical biology*, 8(5):890–894, 2013.
- [201] B. S. Watson, T. L. Hazlett, J. F. Eccleston, C. Davis, D. M. Jameson, and A. E. Johnson. Macromolecular arrangement in the aminoacyl-tRNA.elongation factor tu.GTP ternary complex. A fluorescence energy transfer study. *Biochemistry*, 34(24):7904–7912, 1995.
- [202] J. W. Nichols and R. E. Pagano. Resonance energy transfer assay of protein-mediated lipid transfer between vesicles. *Journal of Biological Chemistry*, 258(9):5368–5371, 1983.
- [203] O. Heimstädt. Das Fluoreszenzmikroskop. *Zeitschrift für Mikroskopie*, 28:330, 1911.
- [204] P. D. Andrews, I. S. Harper, and J. R. Swedlow. To 5D and beyond: quantitative fluorescence microscopy in the postgenomic era. *Traffic*, 3(1):29–36, 2002.
- [205] M. Minsky. Microscopy apparatus, December 19 1961. US Patent 3,013,467.
- [206] E. Abbe. On the Estimation of Aperture in the Microscope. *Journal of the Royal Microscopical Society*, 1(3):388–423, 1881.
- [207] G. B. Airy. On the diffraction of an object-glass with circular aperture. *Transactions of the Cambridge Philosophical Society*, 5:283, 1835.
- [208] E. Stelzer. Contrast, resolution, pixelation, dynamic range and signal-to-noise ratio: fundamental limits to resolution in fluorescence light microscopy. *Journal of Microscopy*, 189(1):15–24, 1998.
- [209] K. R. Spring, T. J. Fellers, and M. W. Davidson. Resolution and contrast in confocal microscopy, 2009. [Online] URL: <http://www.olympusconfocal.com/theory/resolutionintro.html>, accessed 2013-07-30.

- [210] J. C. Waters. Accuracy and precision in quantitative fluorescence microscopy. *The Journal of cell biology*, 185(7):1135–1148, 2009.
- [211] U. authors of the Center for Microscopy and I. A. of the University of Zurich. Practical introduction to light microscopy, July 2012. [Online] URL: <http://www.zmb.uzh.ch/resources/download/Lightmicroscopy.pdf>, accessed 2013-08-02.
- [212] T. T. Tan, C. Khaw, and M. M. Ng. Challenges and recent advances in live cell bioimaging. In A. Méndez-Vilas and Díaz, editors, *Microscopy: Science, Technology, Applications and Education*, pages 1495–1505. Formatex Research Center, 2010.
- [213] M. M. Frigault, J. Lacoste, J. L. Swift, and C. M. Brown. Live-cell microscopy—tips and tools. *Journal of Cell Science*, 122(6):753–767, 2009.
- [214] A. Oller, C. Buser, M. Tyo, and W. Thilly. Growth of mammalian cells at high oxygen concentrations. *Journal of Cell Science*, 94(1):43–49, 1989.
- [215] R. S. Fischer, Y. Wu, P. Kanchanawong, H. Shroff, and C. M. Waterman. Microscopy in 3D: a biologist’s toolbox. *Trends in cell biology*, 21(12):682–691, 2011.
- [216] I. Rasnik, S. A. McKinney, and T. Ha. Nonblinking and long-lasting single-molecule fluorescence imaging. *Nature Methods*, 3(11):891–893, 2006.
- [217] M. M. Knight, S. R. Roberts, D. A. Lee, and D. L. Bader. Live cell imaging using confocal microscopy induces intracellular calcium transients and cell death. *American Journal of Physiology-Cell Physiology*, 284(4):C1083–C1089, 2003.
- [218] K. Bacia, S. A. Kim, and P. Schwille. Fluorescence cross-correlation spectroscopy in living cells. *Nature methods*, 3(2):83–89, 2006.
- [219] D. C. Youvan, C. M. Silva, E. J. Bylina, W. J. Coleman, M. R. Dilworth, and M. M. Yang. Calibration of fluorescence resonance energy transfer in microscopy using genetically engineered GFP derivatives on nickel chelating beads. *Biotechnology*, 3:1–18, 1997.
- [220] F. S. Wouters, P. I. Bastiaens, K. W. Wirtz, and T. M. Jovin. FRET microscopy demonstrates molecular association of non-specific lipid transfer protein (nsl-TP) with fatty acid oxidation enzymes in peroxisomes. *The EMBO journal*, 17(24):7179–7189, 1998.
- [221] H. Wallrabe and A. Periasamy. Imaging protein molecules using FRET and FLIM microscopy. *Current opinion in biotechnology*, 16(1):19–27, 2005.
- [222] F. Eberle, K. Giessler, C. Deck, K. Heeg, M. Peter, C. Richert, and A. H. Dalpke. Modifications in small interfering RNA that separate immunostimulation from RNA interference. *J Immunol*, 180(5):3229–37, Mar 1 2008.
- [223] S. A. Marras, F. R. Kramer, and S. Tyagi. Efficiencies of fluorescence resonance energy transfer and contact-mediated quenching in oligonucleotide probes. *Nucleic acids research*, 30(21):e122–e122, 2002.
- [224] M. Hirsch. Tracing fluorescent labeled siRNA - activity, delivery, integrity. master thesis, Ruprecht-Karls Universität Heidelberg, Heidelberg, Germany, 2009.
- [225] S. Shah and S. H. Friedman. Tolerance of RNA interference toward modifications of the 5’ antisense phosphate of small interfering RNA. *Oligonucleotides*, 17(1):35–43, 2007.
- [226] N. Kitsera, A. Khobta, and B. Epe. Destabilized green fluorescent protein detects rapid removal of transcription blocks after genotoxic exposure. *Biotechniques*, 43(2):222, 2007.
- [227] A. Jaerve. Surveillance of siRNA integrity by FRET. master thesis, Ruprecht-Karls Universität Heidelberg, Heidelberg, Germany, 2006.
- [228] ATTO-TEC GmbH, Siegen, Germany. [Online] URL: <http://www.atto-tec.com/index.php?id=65&L=0>, accessed 2013-08-15.
- [229] M. Hirsch, V. Zirolì, M. Helm, and U. Massing. Preparation of small amounts of sterile

- siRNA-liposomes with high entrapping efficiency by dual asymmetric centrifugation (DAC). *Journal of Controlled Release*, 135(1):80–8, Apr 2 2009.
- [230] A. M. Hofmann, F. Wurm, E. Huehn, T. Nawroth, P. Langguth, and H. Frey. Hyperbranched polyglycerol-based lipids via oxyanionic polymerization: toward multifunctional stealth liposomes. *Biomacromolecules*, 11(3):568–574, 2010.
- [231] E. M. Sletten and C. R. Bertozzi. Bioorthogonal chemistry: fishing for selectivity in a sea of functionality. *Angewandte Chemie International Edition*, 48(38):6974–6998, 2009.
- [232] L. Nuhn, M. Hirsch, B. Krieg, K. Koynov, K. Fischer, M. Schmidt, M. Helm, and R. Zentel. Cationic nanohydrogel particles as potential siRNA carriers for cellular delivery. *ACS Nano*, 6(3):2198–214, Mar 27 2012.
- [233] M. Sahl, S. Muth, R. Branscheid, K. Fischer, and M. Schmidt. Helix–coil transition in cylindrical brush polymers with poly-l-lysine side chains. *Macromolecules*, 45(12):5167–5175, 2012.
- [234] T. D. Schladt, K. Schneider, H. Schild, and W. Tremel. Synthesis and bio-functionalization of magnetic nanoparticles for medical diagnosis and treatment. *Dalton Transactions*, 40(24): 6315–6343, 2011.
- [235] S. Duhr and D. Braun. Why molecules move along a temperature gradient. *Proceedings of the National Academy of Sciences*, 103(52):19678–19682, 2006.
- [236] F. Roux, O. Durieu-Trautmann, N. Chaverot, M. Claire, P. Mailly, J. M. Bourre, A. D. Strosberg, and P. O. Couraud. Regulation of gamma-glutamyl transpeptidase and alkaline phosphatase activities in immortalized rat brain microvessel endothelial cells. *J Cell Physiol*, 159(1):101–13, Apr 1994.
- [237] J. J. Rossi. RNAi and the P-body connection. *Nature cell biology*, 7(7):643–644, 2005.
- [238] S. Guang, A. F. Bochner, D. M. Pavelec, K. B. Burkhart, S. Harding, J. Lachowicz, and S. Kennedy. An argonaute transports siRNAs from the cytoplasm to the nucleus. *Science*, 321(5888):537–41, Jul 25 2008.
- [239] T. Ohrt, J. Mutze, W. Staroske, L. Weinmann, J. Hock, K. Crell, G. Meister, and P. Schwill. Fluorescence correlation spectroscopy and fluorescence cross-correlation spectroscopy reveal the cytoplasmic origination of loaded nuclear RISC in vivo in human cells. *Nucleic Acids Research*, 36(20):6439–49, Nov 2008.
- [240] A. I. Lamond and D. L. Spector. Nuclear speckles: a model for nuclear organelles. *Nature Reviews Molecular Cell Biology*, 4(8):605–612, 2003.
- [241] O. Pontes and C. S. Pikaard. siRNA and miRNA processing: new functions for Cajal bodies. *Current opinion in genetics & development*, 18(2):197–203, 2008.
- [242] K. Brasch and R. L. Ochs. Nuclear bodies (NBs): a newly "rediscovered" organelle. *Experimental cell research*, 202(2):211–223, 1992.
- [243] A. Zimmer, Q.-D. Nguyen, C. Gerspach, et al. Nuclear bodies and compartments: functional roles and cellular signalling in health and disease. *Cellular signalling*, 16(10):1085, 2004.
- [244] D. L. Spector. Nuclear domains. *Journal of Cell Science*, 114(16):2891–2893, 2001.
- [245] Y. L. Chiu and T. M. Rana. RNAi in human cells: basic structural and functional features of small interfering RNA. *Mol Cell*, 10(3):549–61, Sep 2002.
- [246] K. Omi, K. Tokunaga, and H. Hohjoh. Long-lasting RNAi activity in mammalian neurons. *FEBS Letters*, 558(1-3):89–95, Jan 30 2004.
- [247] D. W. Bartlett and M. E. Davis. Effect of siRNA nuclease stability on the in vitro and in vivo kinetics of siRNA-mediated gene silencing. *Biotechnology and Bioengineering*, 97(4):909–21, Jul 1 2007.
- [248] N. S. Petrova Kruglova, M. I. Meschaninova, A. G. Venyaminova, M. A. Zenkova, V. V. Vlassov, and E. L. Chernolovskaya. 2'-O-methyl-modified anti-MDR1 fork-siRNA duplexes exhibiting high nuclease resistance and prolonged silencing activity. *Oligonucleotides*, 20(6):297–308, Dec 2010.

- [249] W. R. Strapps, V. Pickering, G. T. Muiru, J. Rice, S. Orsborn, B. A. Polisky, A. Sachs, and S. R. Bartz. The siRNA sequence and guide strand overhangs are determinants of in vivo duration of silencing. *Nucleic Acids Research*, 38(14):4788–97, Aug 2010.
- [250] C. A. Schneider, W. S. Rasband, and K. W. Eliceiri. Nih image to imagej: 25 years of image analysis. *Nat Methods*, 9(7):671–675, 2012.
- [251] M. Dominska and D. M. Dykxhoorn. Breaking down the barriers: siRNA delivery and endosome escape. *J Cell Sci*, 123(Pt 8):1183–9, 2010.
- [252] S. Guo and L. Huang. Nanoparticles escaping res and endosome: challenges for siRNA delivery for cancer therapy. *Journal of Nanomaterials*, 2011:11, 2011.
- [253] T. Soldati and M. Schliwa. Powering membrane traffic in endocytosis and recycling. *Nature Reviews Molecular Cell Biology*, 7(12):897–908, 2006.
- [254] A. H. Wyllie. Cell death: the significance of apoptosis. *Int. Rev. Cytol.*, 68:251, 1980.
- [255] O. T. Fackler and R. Grosse. Cell motility through plasma membrane blebbing. *The Journal of cell biology*, 181(6):879–884, 2008.
- [256] J. A. Kiernan. Formaldehyde, formalin, paraformaldehyde and glutaraldehyde: what they are and what they do. *Microscopy Today*, 1:8–12, 2000.
- [257] R. Geoffrey. Fixation and fixatives (2) - factors influencing chemical fixation, formaldehyde and glutaraldehyde, March 2012. [Online] URL: <http://www.leicabiosystems.com/pathologyleaders/fixation-and-fixatives-2-factors-influencing-chemical-fixation-formaldehyde-and-glutaraldehyde/>, accessed 2013-06-14.
- [258] G. Juhasz and T. P. Neufeld. Autophagy: a forty-year search for a missing membrane source. *PLoS biology*, 4(2):e36, 2006.
- [259] Q. Xie and H.-S. Guo. Systemic antiviral silencing in plants. *Virus research*, 118(1):1–6, 2006.
- [260] O. Voinnet. Non-cell autonomous RNA silencing. *FEBS letters*, 579(26):5858–5871, 2005.
- [261] M. N. Uddin and J.-Y. Kim. Non-cell-autonomous RNA silencing spread in plants. *Botanical Studies*, 52(2):129–136, 2011.
- [262] K. Kalantidis, H. T. Schumacher, T. Alexiadis, and J. M. Helm. RNA silencing movement in plants. *Biology of the Cell*, 100(1):13–26, 2008.
- [263] D. H. Chitwood and M. C. Timmermans. Small RNAs are on the move. *Nature*, 467(7314):415–419, 2010.
- [264] L. Timmons and A. Fire. Specific interference by ingested dsRNA. *Nature*, 395(6705):854–854, 1998.
- [265] V. Valiunas, Y. Polosina, H. Miller, I. Potapova, L. Valiuniene, S. Doronin, R. Mathias, R. Robinson, M. Rosen, I. Cohen, et al. Connexin-specific cell-to-cell transfer of short interfering RNA by gap junctions. *The Journal of physiology*, 568(2):459–468, 2005.
- [266] E. J. Wolvetang, M. F. Pera, and K. S. Zuckerman. Gap junction mediated transport of shRNA between human embryonic stem cells. *Biochemical and biophysical research communications*, 363(3):610–615, 2007.
- [267] G. Attarzadeh-Yazdi, R. Fragkoudis, Y. Chi, R. W. Siu, L. Ülper, G. Barry, J. Rodriguez-Andres, A. A. Nash, M. Bouloy, A. Merits, et al. Cell-to-cell spread of the RNA interference response suppresses semliki forest virus (sfv) infection of mosquito cell cultures and cannot be antagonized by sfv. *Journal of virology*, 83(11):5735–5748, 2009.
- [268] E. Haustein, M. Jahnz, and P. Schwille. Triple FRET: A tool for studying long-range molecular interactions. *ChemPhysChem*, 4(7):745–748, 2003.
- [269] M. Koivusalo, C. Welch, H. Hayashi, C. C. Scott, M. Kim, T. Alexander, N. Touret, K. M. Hahn, and S. Grinstein. Amiloride inhibits macropinocytosis by lowering submembranous pH and preventing

- Rac1 and Cdc42 signaling. *The Journal of cell biology*, 188(4):547–563, 2010.
- [270] L.-H. Wang, K. G. Rothberg, and R. Anderson. Mis-assembly of clathrin lattices on endosomes reveals a regulatory switch for coated pit formation. *The Journal of cell biology*, 123(5):1107–1117, 1993.
- [271] D. Vercauteren, R. E. Vandembroucke, A. T. Jones, J. Rejman, J. Demeester, S. C. De Smedt, N. N. Sanders, and K. Braeckmans. The use of inhibitors to study endocytic pathways of gene carriers: optimization and pitfalls. *Molecular Therapy*, 18(3):561–569, 2009.
- [272] I. A. Khalil, K. Kogure, H. Akita, and H. Harashima. Uptake pathways and subsequent intracellular trafficking in nonviral gene delivery. *Pharmacological reviews*, 58(1):32–45, 2006.
- [273] H. Drexler, W. Dirks, R. MacLeod, H. Quentmeier, K. Steube, and C. Uphoff. DSMZ catalogue of human and animal cell lines, 2001. Leibniz Institute DSMZ-German Collection of Microorganism and Cell Cultures, [Online] URL: <http://www.dsmz.de/catalogues/catalogue-human-and-animal-cell-lines.html>, accessed 2013-08-08.
- [274] P. Romano, A. Manniello, O. Aresu, M. Armento, M. Cesaro, and B. Parodi. Cell Line Data Base: structure and recent improvements towards molecular authentication of human cell lines. *Nucleic acids research*, 37(suppl 1):D925–D932, 2009. Webpage of hyperCLDB, URL: [<http://bioinformatics.istge.it/cldb/indexes.html>], accessed 2013-08-08.
- [275] W. F. Scherer, J. T. Syverton, and G. O. Gey. Studies on the propagation in vitro of poliomyelitis viruses iv. Viral multiplication in a stable strain of human malignant epithelial cells (strain HeLa) derived from an epidermoid carcinoma of the cervix. *The Journal of experimental medicine*, 97(5):695–710, 1953.
- [276] R. G. Taylor, D. C. Walker, and R. McInnes. E. coli host strains significantly affect the quality of small scale plasmid DNA preparations used for sequencing. *Nucleic acids research*, 21(7):1677, 1993.
- [277] J. Giraldo, N. M. Vivas, E. Vila, and A. Badia. Assessing the (a)symmetry of concentration-effect curves: empirical versus mechanistic models. *Pharmacol Ther*, 95(1):21–45, Jul 2002.





# Publications

1. **M. Hirsch**, V. Ziroli, M. Helm, and U. Massing. Preparation of small amounts of sterile siRNA-liposomes with high entrapping efficiency by dual asymmetric centrifugation (DAC). *Journal of Controlled Release*, 135(1):80-8, Apr 2 2009
2. I. H. Kim, A. Järve, **M. Hirsch**, R. Fischer, M. F. Trendelenburg, U. Massing, K. Rohr, and M. Helm. Fret imaging of cells transfected with siRNA/liposome complexes. *Methods in Molecular Biology*, 606:439-55, 2010
3. **M. Hirsch**, I.-H. Kim, A. Järve, R. Fischer, M. F. Trendelenburg, U. Massing, K. Rohr, and M. Helm. Tracing of sirnas inside cells by fret imaging. In S. Q. Harper, editor, *RNA Interference Techniques*, pages 141-157. Springer, New York, Heidelberg, London, 2011
4. **M. Hirsch**, D. Strand, and M. Helm. Dye selection for live cell imaging of intact siRNA. *Biol Chem*, 393(1-2):23-35, 2012
5. L. Nuhn, **M. Hirsch**, B. Krieg, K. Koynov, K. Fischer, M. Schmidt, M. Helm, and R. Zentel. Cationic nanohydrogel particles as potential siRNA carriers for cellular delivery. *ACS Nano*, 6(3):2198-214, Mar 27 2012
6. S. Seidu-Larry, B. Krieg, **M. Hirsch**, M. Helm, and O. Domingo. A modified guanosine phosphoramidite for click functionalization of RNA on the sugar edge. *Chem Commun (Camb)*, 48(89):11014-6, Nov 18 2012



# Appendices



## A Introduction

Donor	Acceptor	Donor Excitation $\lambda_{\max}$ (nm)	Acceptor Emission $\lambda_{\max}$ (nm)	Donor QY (-)	Acceptor $\epsilon$ ( $M^{-1}cm^{-1}$ )	Förster Distance (nm)
Fluorescent protein FRET pairs						
BFP	DsRFP	380	586	0.18	72,500	3.1–3.3
EBFP2	mEGFP	383	507	0.56	57,500	4.8
CFP	GFP	433	509	0.40	21,000	4.7–4.9
CFP	YFP	433	526	0.40	77,000	~ 5.0
Cerulean	YFP	440	526	0.62	77,000	–
ECFP	EYFP	440	527	0.40	83,400	4.9
Cerulean	Venus	440	528	0.62	92,200	5.4
MiCy	mKO	472	559	0.90	51,600	5.3
GFP	YFP	475	526	0.77	77,000	5.5–5.7
GFP	mRFP	475	579	0.77	50,000	~ 4.7
CyPet	YPet	477	530	0.51	104,000	5.1
TFP1	mVenus	492	528	0.85	92,200	5.1
EGFP	mCherry	507	510	0.60	72,000	5.1
Venus	mCherry	528	610	0.57	72,000	5.7
Venus	tdTomato	528	581	0.57	138,000	5.9
Venus	mPlum	528	649	0.57	41,000	5.2
Fluorescent protein-dye FRET pairs						
EGFP	Alexa Fluor 555	484	568	0.6	155,000	6.3
EGFP	Alexa Fluor 546	484	573	0.6	112,000	5.7
EGFP	Alexa Fluor 594	484	618	0.6	92,000	5.3
EGFP	Alexa Fluor 568	484	603	0.6	88,000	5.4
Dye and dye-biofluorochrome FRET pairs						
Cy2	Cy3	489	570	> 0.12	150,000	5.0–6.0
Cy3	Cy5	550	670	> 0.15	250,000	> 5.0
Cy5	Cy5.5	649	694	> 0.28	250,000	> 8.0
Fluorescein	Tetramethylrhodamine	487 <sup>1</sup>	574	0.93 <sup>2</sup>	~ 87,000	4.9–5.5
FITC	TRITC	494	572	0.92	100,000	5.4
Phycocerythrin	APC <sup>3</sup>	(546), 565	660	0.98	700,000	4.0–11.0
Europium	APC	340	660	–	700,000	9.0
Tryptophan	Dansyl	280	525	0.01–0.35 <sup>4</sup>	4050	2.1
Dansyl	FITC	335	519	< 0.035 <sup>5</sup>	77,000	3.3–4.1
Dansyl	Octadecylrhodamine	335	625	< 0.035	106,000	4.3
Europium	Cy5	340	670	–	250,000	7.0
Atto 488	Atto 647N	501	670	0.8	150,000	5.1
Atto 488	Atto 590	501	621	0.8	120,000	6.0
Atto 550	Atto 647N	554	670	0.8	150,000	6.5
Atto 550	Atto 655	554	684	0.8	125,000	6.4
Atto 590	Atto 655	594	684	0.8	125,000	7.3
Alexa 405	Alexa 430	401	541	–	16,000	–
Alexa 488	Alexa 514	495	542	0.92	80,000	–
Alexa 488	Alexa 532	495	554	0.92	81,000	–
Alexa 488	Alexa 546	495	573	0.92	104,000	6.4
Alexa 488	Alexa 610	495	628	0.92	138,000	–
Alexa 647	Alexa 680	650	702	0.33	184,000	–
Alexa 647	Alexa 700	650	723	0.33	192,000	–
Alexa 647	Alexa 750	650	780	0.33	240,000	–
Non-fluorescent acceptor pairs						
Rhodamine 6G	Malachite Green (Abs 628 nm)	526	NF	0.95	76,000	6.1
Alexa 488	QSY 35 (Abs 475 nm)	495	NF	0.92	23,000	4.4
Alexa 488	Dabcyl (Abs 453 nm)	495	NF	0.92	32,000	4.9
Alexa 647	QSY 21 (Abs 661 nm)	650	NF	0.33	90,000	6.9

**Figure A.1: Overview of FRET pairs.** Example of common FRET pairs, including FP-FP FRET pairs, dye-dye FRET pairs, FP-dye FRET pairs and dye-quencher pairs. Excerpted from from Ishikawa-Ankerhold et al. [188].

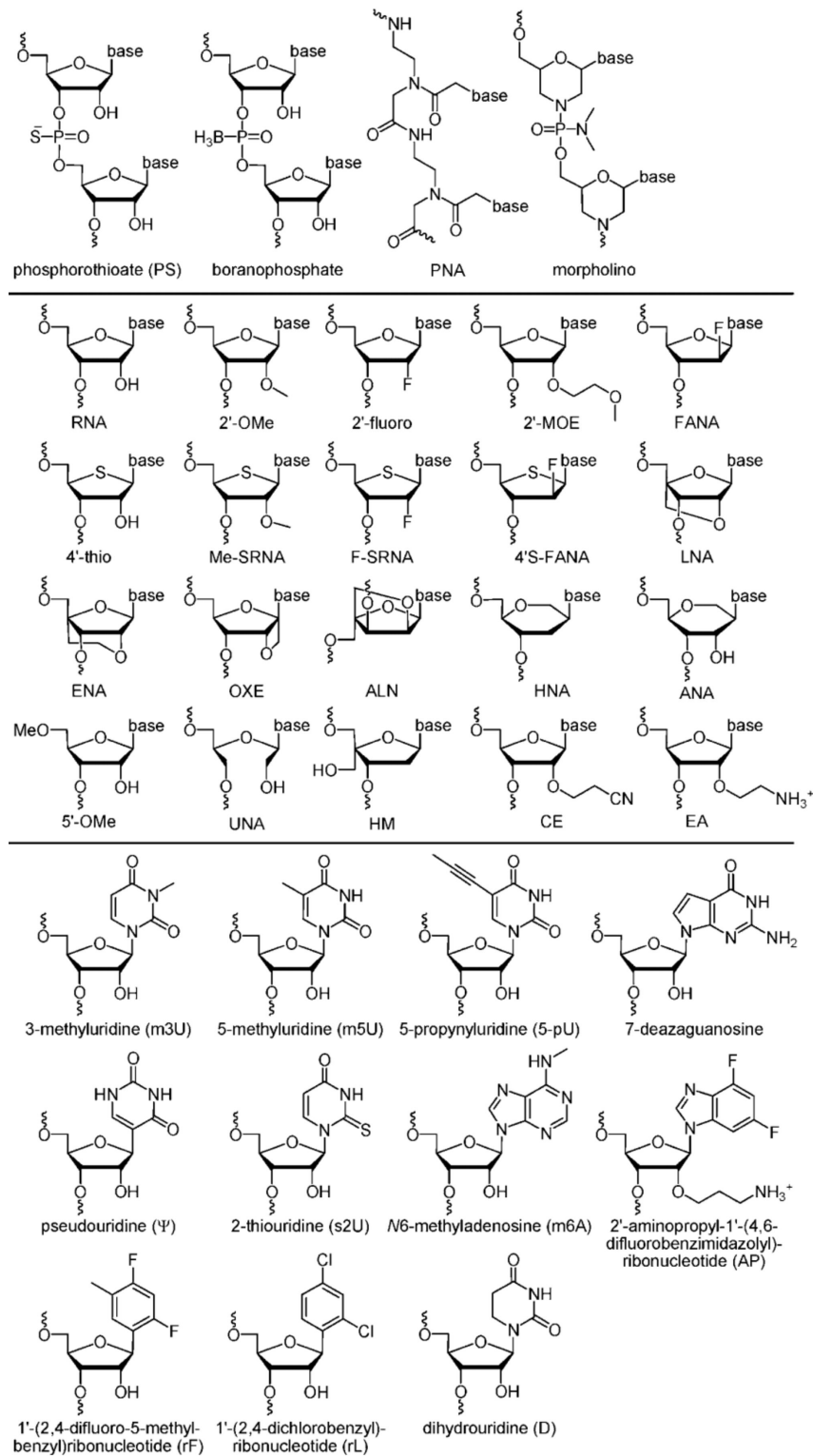


**Figure A.2: siRNA modifications.** Overview of siRNA modifications tested for enhancing silencing capability, stability (RNase, hybridization) and reduction of Off-target effects and immunostimulative potential. Upper part shows backbone modifications, middle part sugar modifications and lower part base modifications. Excerpt of Shukla et al. [37].

## B siRNA &amp; dyes

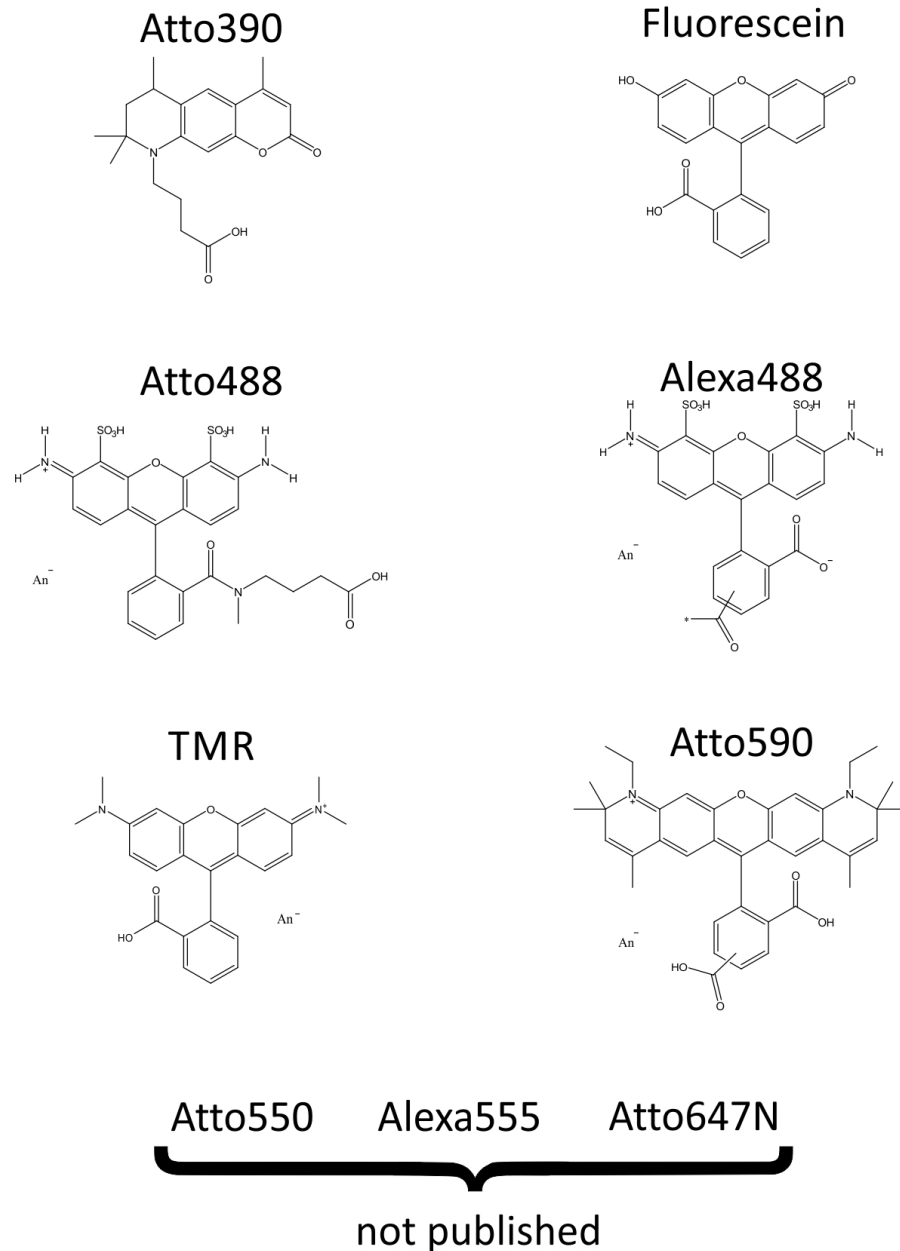


**Figure B.3: Structure of fluorescent dyes.** Chemical structure of fluorescent dyes that are attached to either the sense or antisense strand

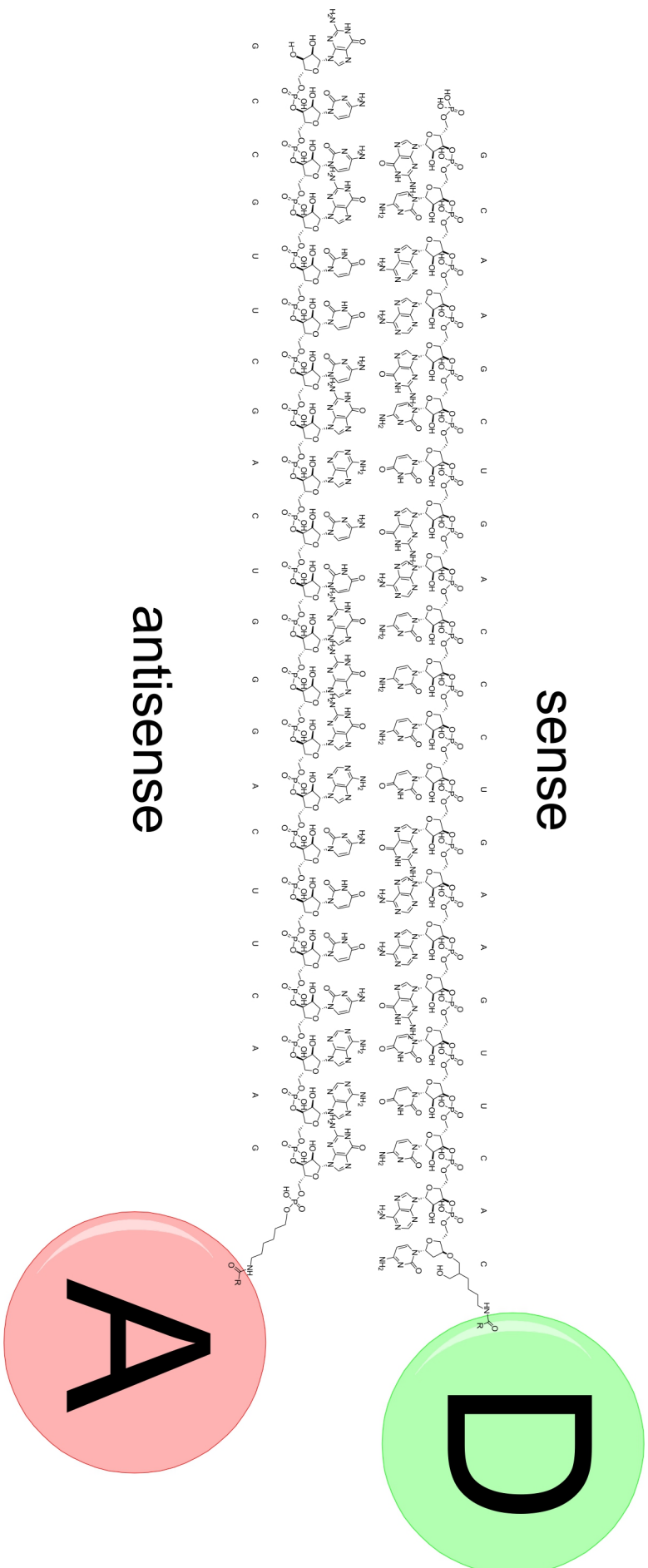
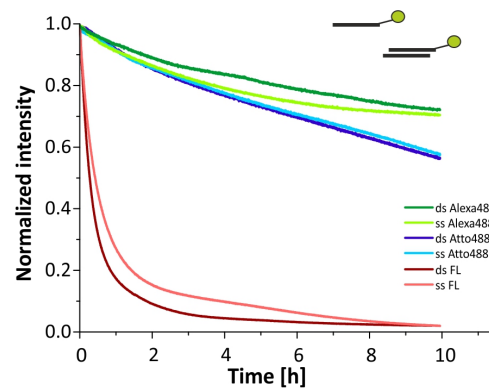


Figure B.4: siRNA structure. Chemical structure of siRNA duplex with linker for attached donor and acceptor dyes.



## C Photostability



**Figure C.5: Photostability of ss and ds siRNA.** Photostability of fluorescently labeled ss and ds siRNA, carrying a FL-analog, in the cuvette. siRNA constructs were excited permanently over 10 h. Normalized emission at 520 nm emission over 10 h by 488 nm excitation.

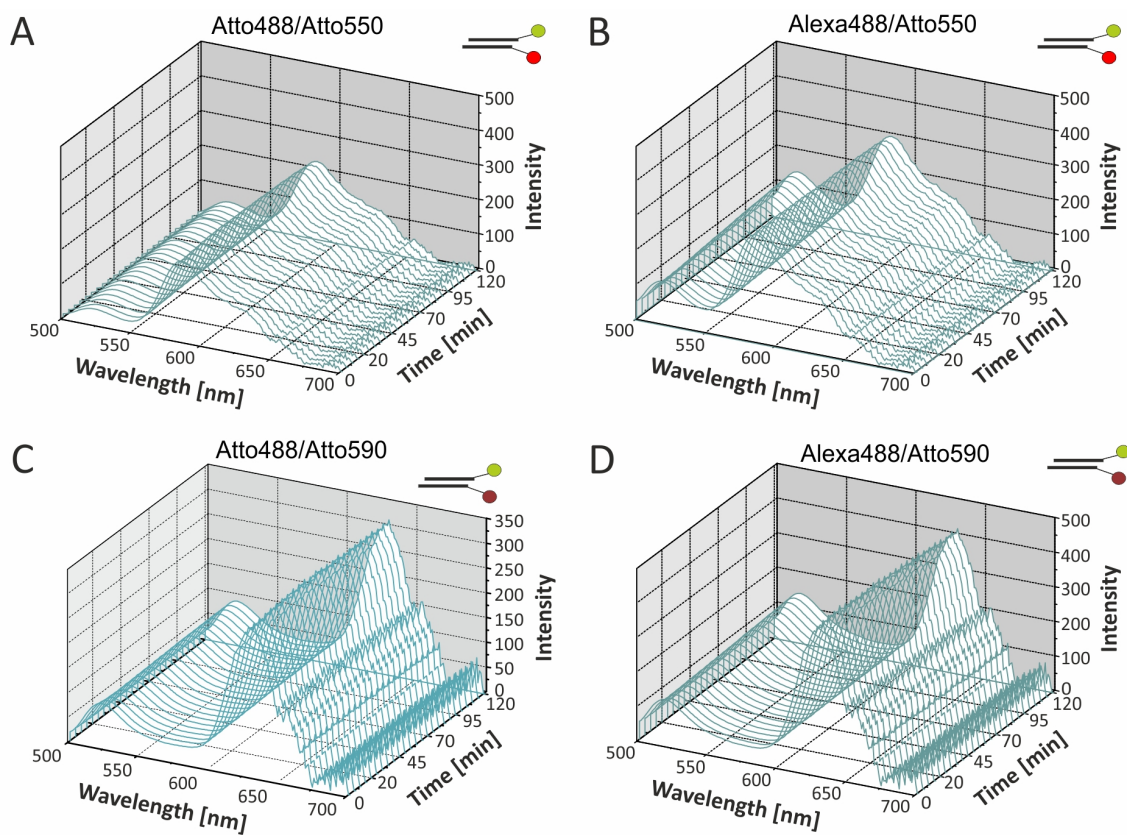


**Figure C.6: Bleaching of Atto488 and Alexa488 FRET pairs.** Photostability of double-labeled siRNA constructs containing photostable FL-analogs. Emission spectra of Atto488/Atto550 (A), Alexa488/Atto550 (B), Atto488/Atto590 (C) and Alexa488/Atto590 (D) siRNA at continuous excitation at 488 nm over 120 min.

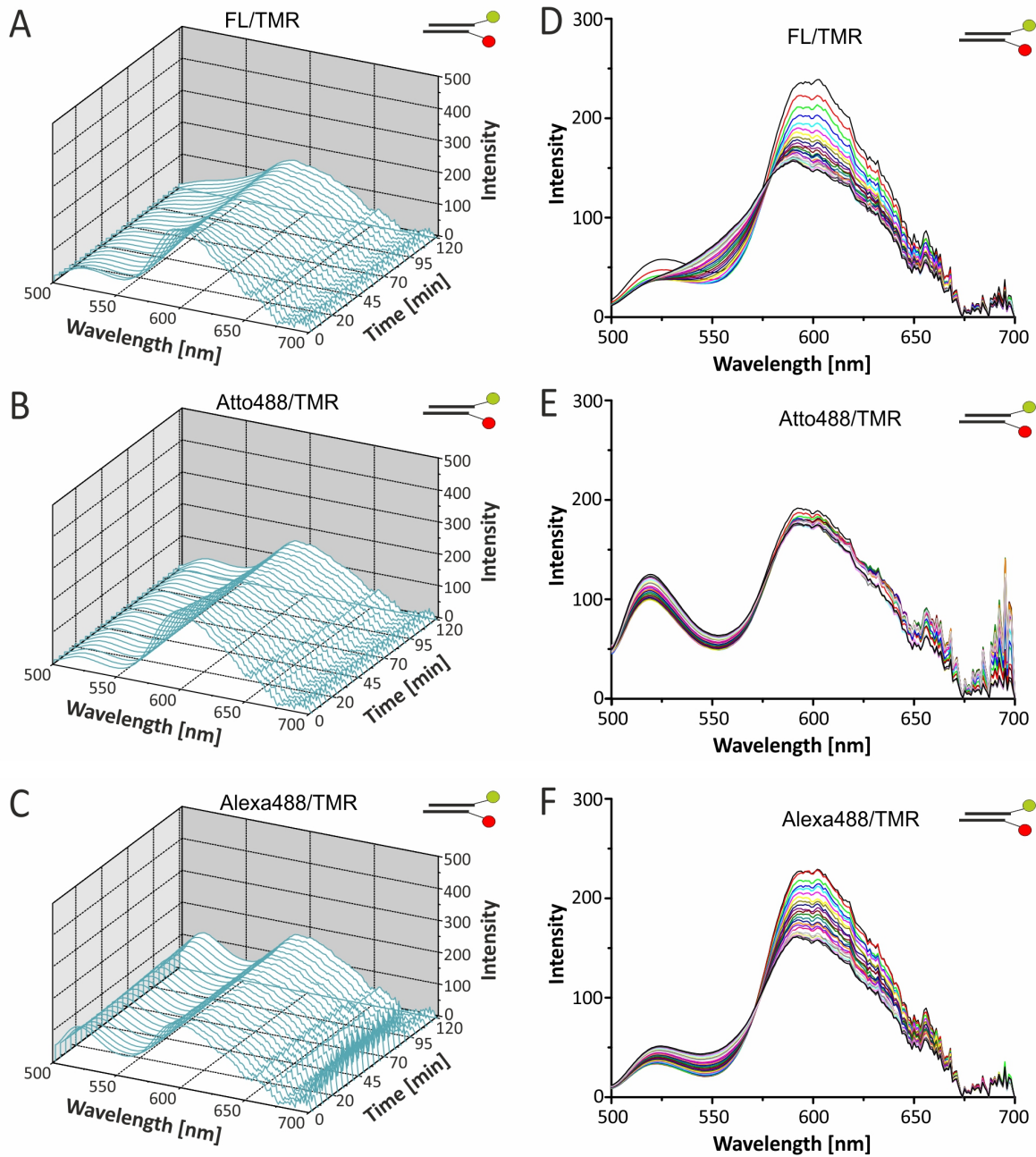


**Figure C.7: Bleaching of donor/TMR FRET pairs.** Photostability of double-labeled siRNA constructs containing TMR. Emission spectra of FL/TMR (A), Atto488/TMR (B) and Alexa488/TMR (C) siRNA at continuous excitation at 488 nm over 120 min. Data is visualized in a 3D- (A, B, C; left) and 2D-representation (D, E, F; right). Published in Hirsch et al. [1]

# D R/G calibration

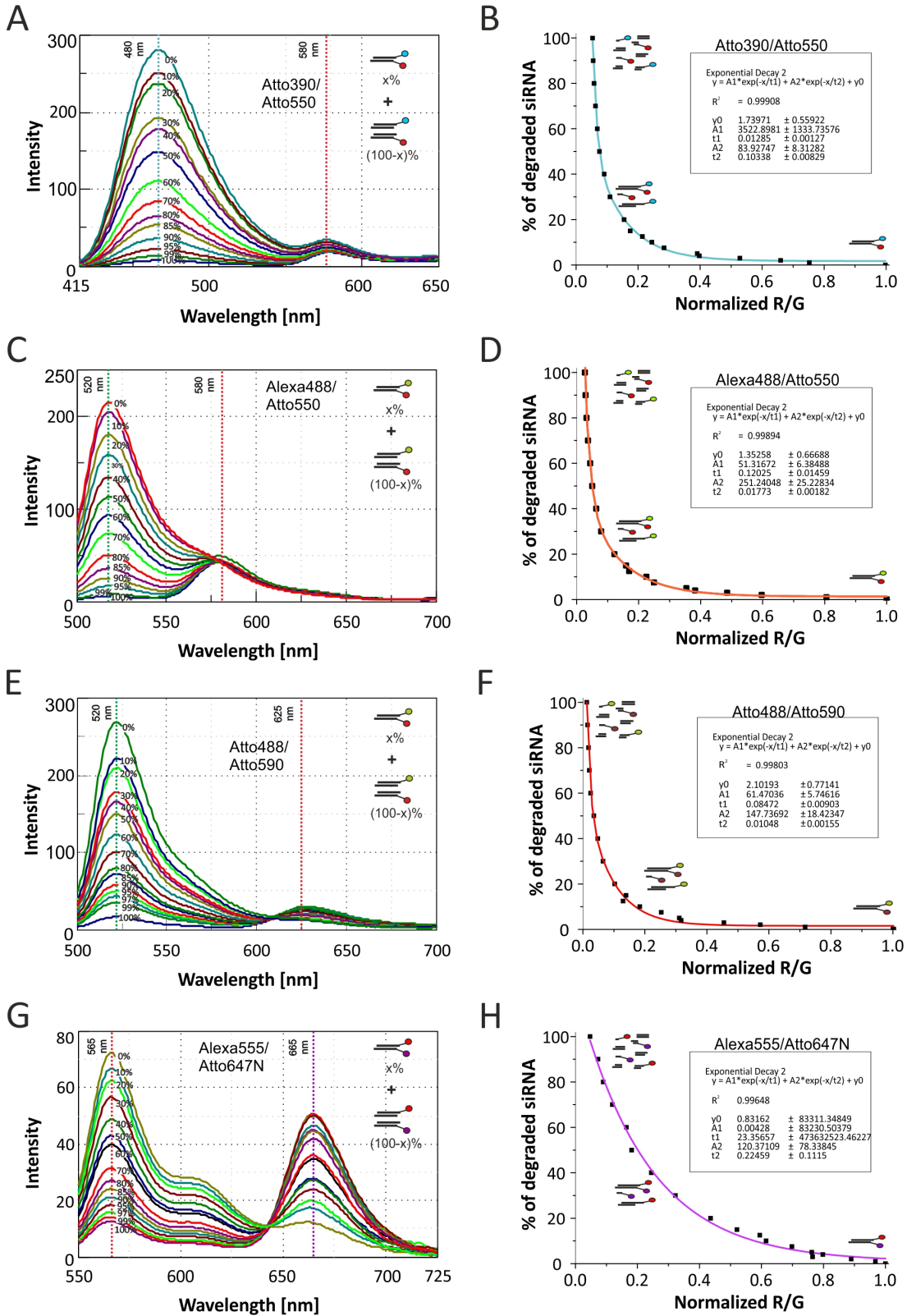
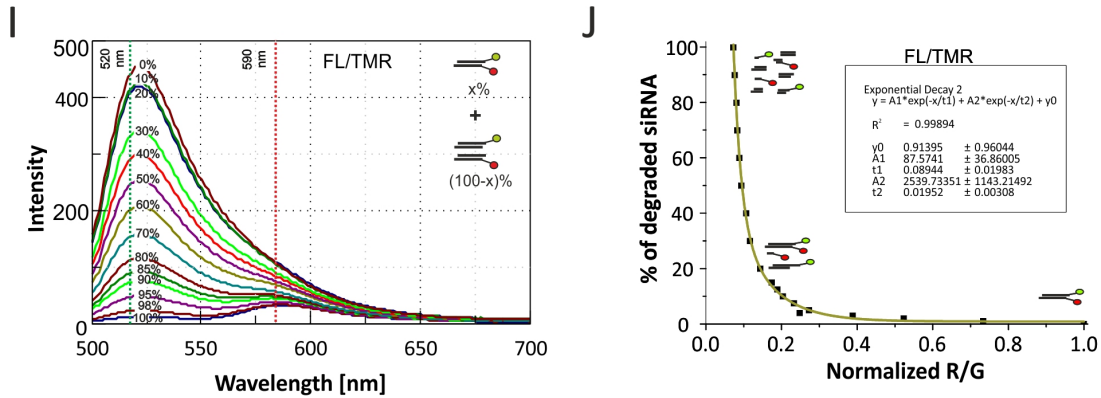
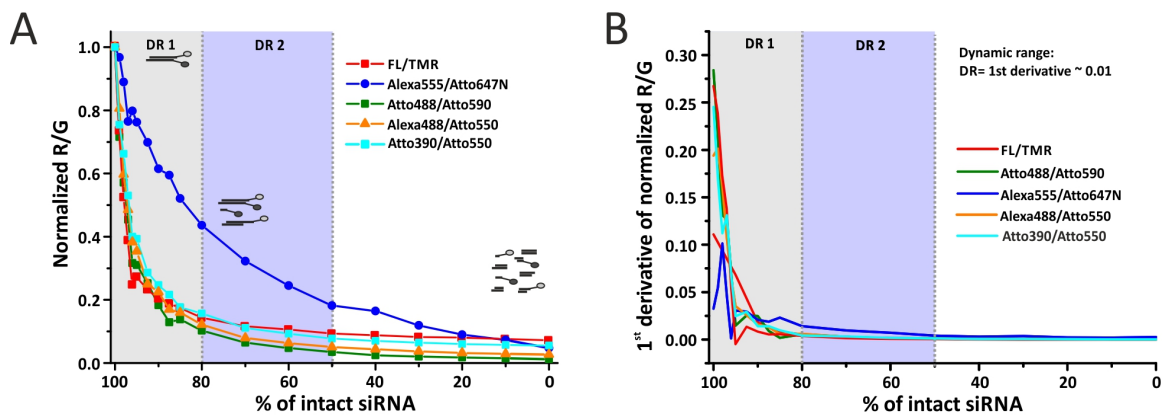


Figure continuous on next page



**Figure D.8: Calibration data of the different siRNA systems for the purpose of integrity calculation.** On the left side: emission spectra of samples with different integrity levels of the Atto390/Atto550 (A), Alexa488/Atto550 (C), Atto488/Atto590 (E), Alexa555/Atto647N (G) and FL/TMR (I) siRNA system. Emission wavelength of donor and acceptor that are used for calculating the respective R/G value are indicated. Numbers indicate fraction of intact siRNA and thus the integrity level. On the right side: Model fit on basis of the R/G values and corresponding degradation levels that allows to classify unknown samples for Atto390/Atto550 (B), Alexa488/Atto550 (D), Atto488/Atto590 (F), Alexa555/Atto647N (H) and FL/TMR (J) siRNA.



**Figure D.9: R/G calibration and dynamic range of different siRNA systems.** Comparison of the different evaluated FRET siRNAs, i.e. FL/TMR (red), Atto488/Atto590 (green), Alexa488/Atto550 (orange) and Alexa555/Atto647N (blue). (A) Normalized R/G values with dynamic range. (B) First derivative of R/G value changes, as indicator for determination of the dynamic range. First derivative larger than 0.01 was basis for DR 1 ranging from 100 % to 80 % (gray box) and DR 2 ranging from 100 % to 50 % (gray and blue box).



## E Degradation of FRET siRNA

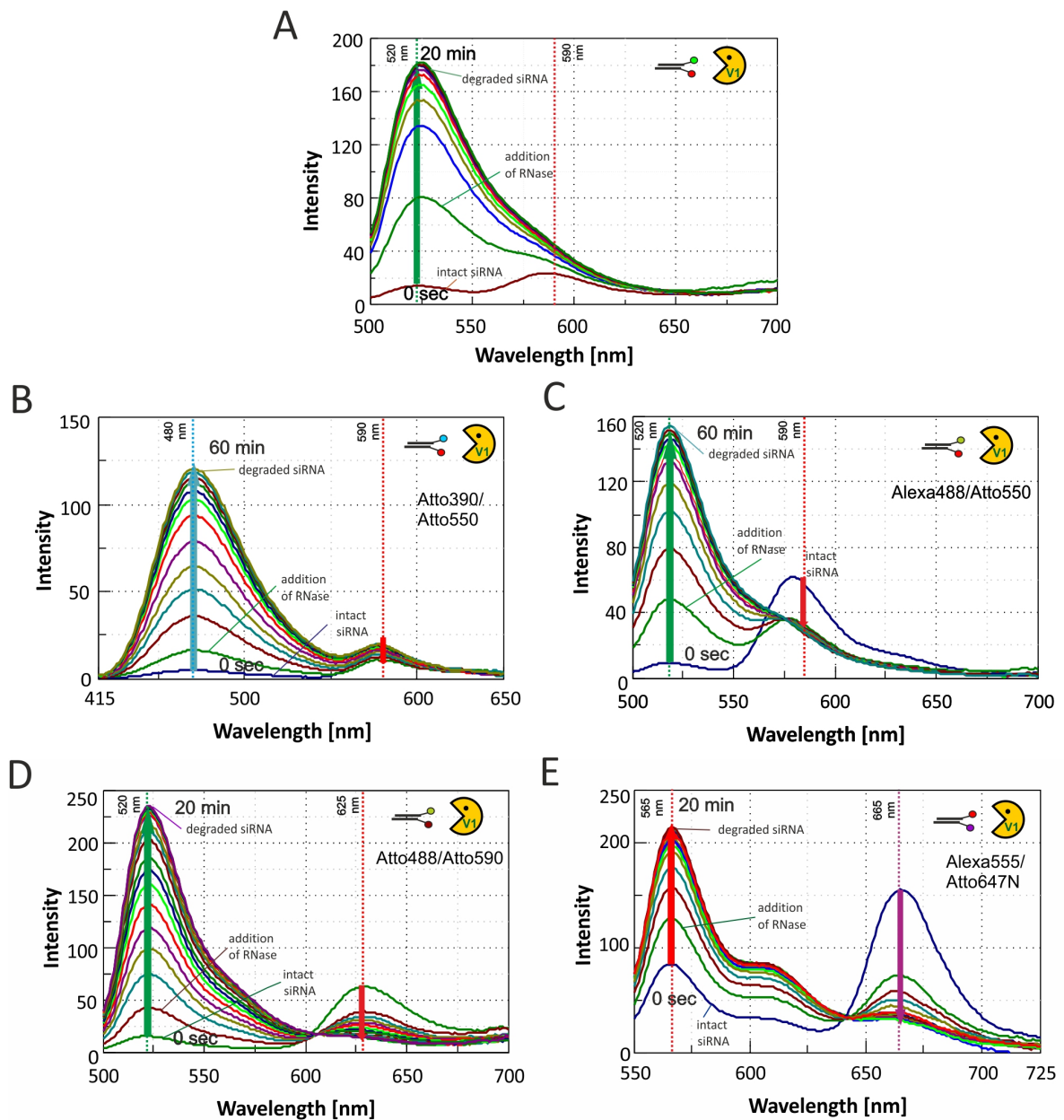


**Figure E.10: Degradation of FRET siRNA.** Degradation of FL/TMR (A), Atto390/Atto550 (B), Alexa488/Atto550 (C), Atto488/Atto590 (D) and Alexa555/Atto647N (E) siRNA by RNase V1 at donor excitation. Recorded donor and acceptor wavelength and time point at which no further changes in emission occurs are indicated.

## F Liposomes

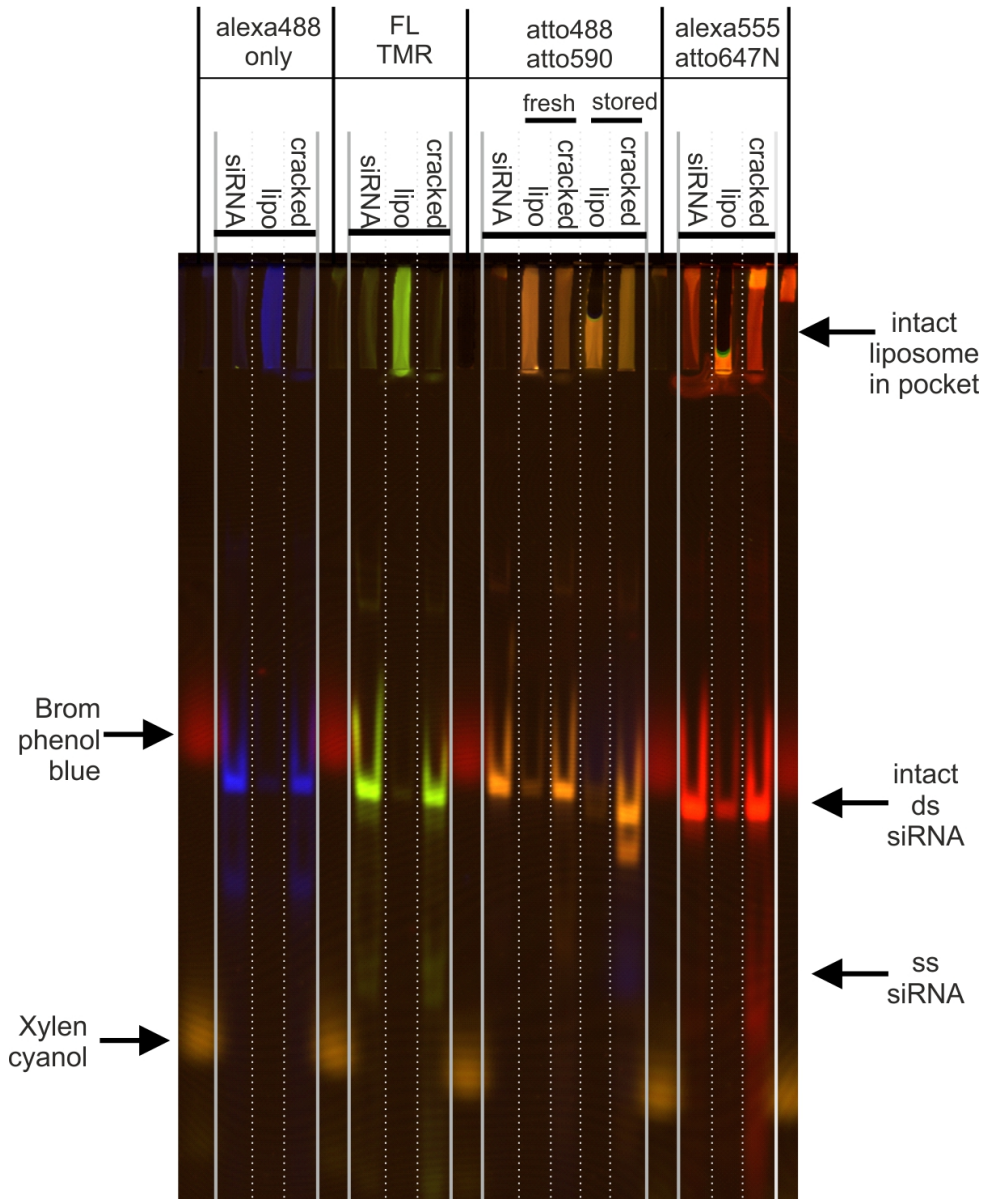


**Figure F.11: PAGE analysis of liposomes.** Purified liposomes containing Alexa488— (blue bands), FL/TMR (light green bands), Atto488/Atto590 (orange bands) and Alexa555/Atto647N (red bands) analyzed on non-denaturing PAGE. For each liposomal preparation siRNA, intact liposomes and cracked liposomes were loaded. Scan represents a merged color representation of a direct scan of Alexa488 (ex488/em520BP in blue) and the acceptor dyes, TMR (ex532/em580BP in green), Atto590 (ex532/em610BP in yellow) and Atto647N (ex633/em670BP in red).

## G Particle evaluation

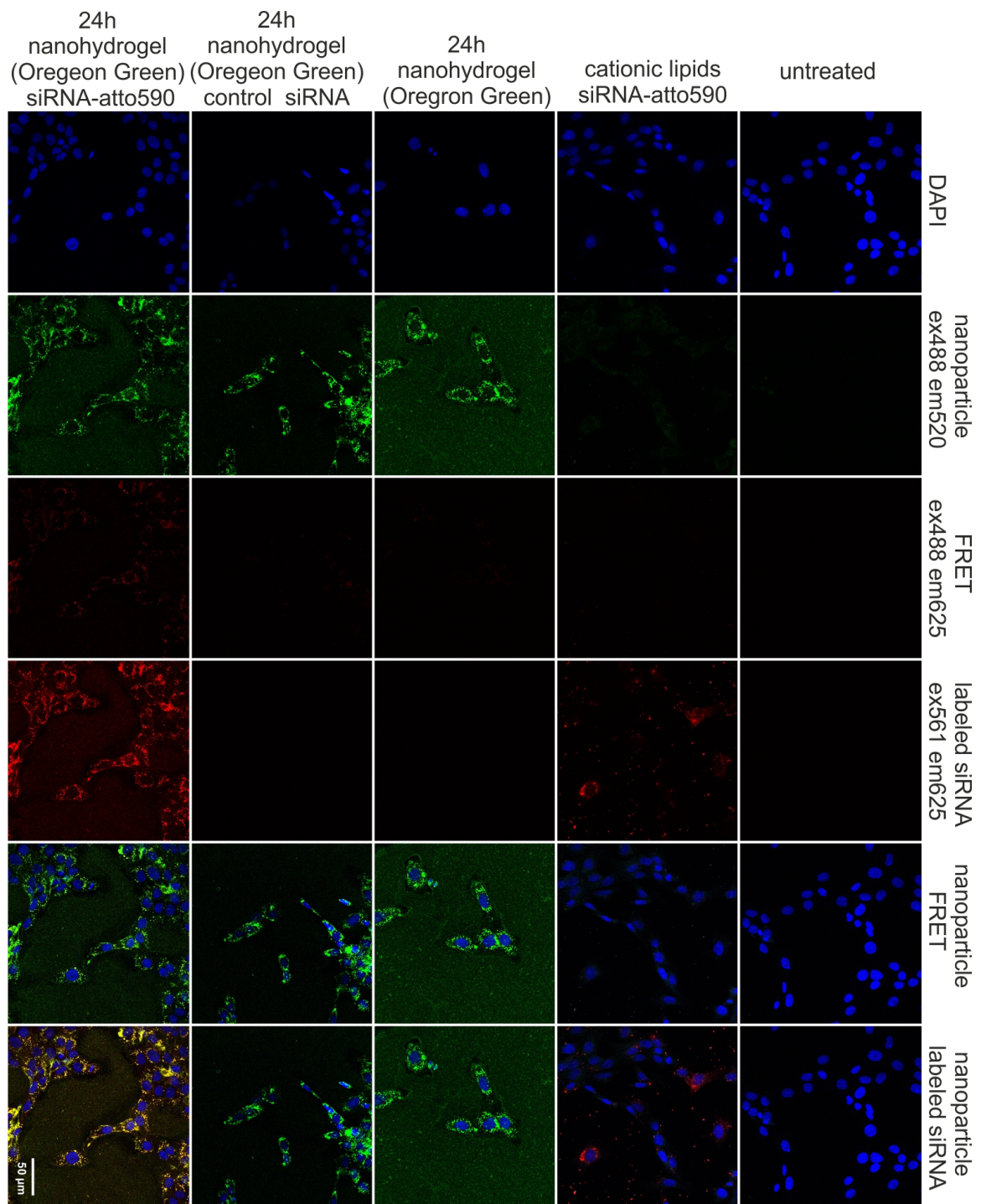


**Figure G.12: Nanohydrogel uptake into cells.** Uptake of OregonGreen labeled nanohydrogels complexed with —/Atto590 siRNA into RBE4 cells. Nuclear counterstain (blue channel), nanoparticles (green channel), potential FRET (red), siRNA signal (red) and RGB merge of FRET/particle/DAPI and siRNA/particle/DAPI (top to bottom rows). Columns depict particle+Atto590-siRNA, particle+unlabeled-siRNA, particle only, Atto590-siRNA only and untreated cells (from left to right). Cells are fixated after 24 h of incubation with respective samples. Data already published in Nuhn et al. [232].

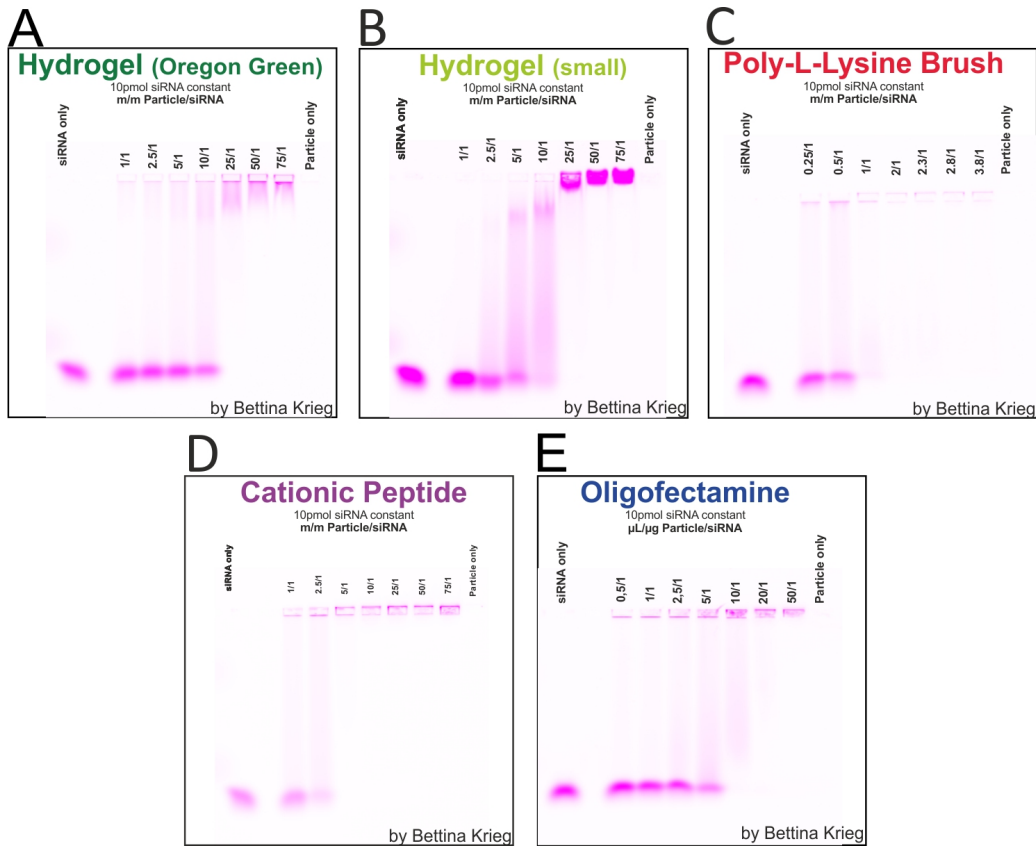


**Figure G.13: Complexation study part I.** Complexation study of Hydrogel containing (A), small hydrogel (B), poly-L-lysine brush (C), cationic peptide (D) and oligofectamine (E) with Alexa555/Atto647N siRNA. siRNA to particle ratios for complexation are indicated. Free siRNA and pure nanoparticles serve as controls. Date kindly provided by [REDACTED]

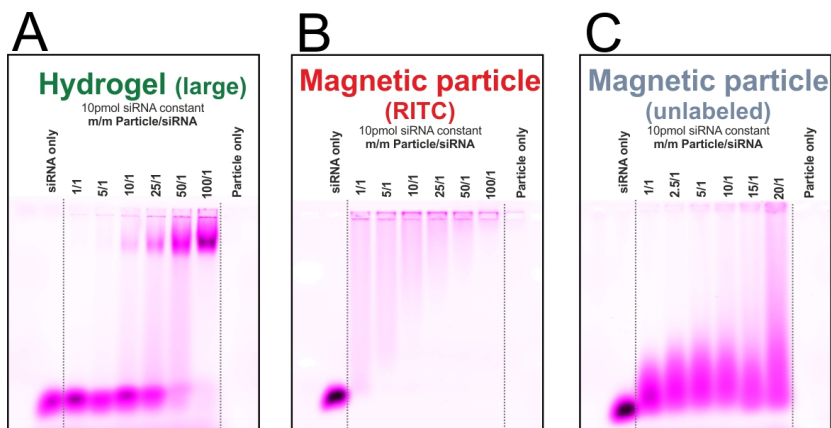


**Figure G.14: Complexation study part II.** Complexation study of large Hydrogel (A), magnetic particle containing RITC (B) and unlabeled magnetic particle with Alexa555/Atto647N siRNA. siRNA to particle ratios for complexation are indicated. Free siRNA and pure nanoparticles serve as controls.



## H Microscopy parameter and R/G algorithm

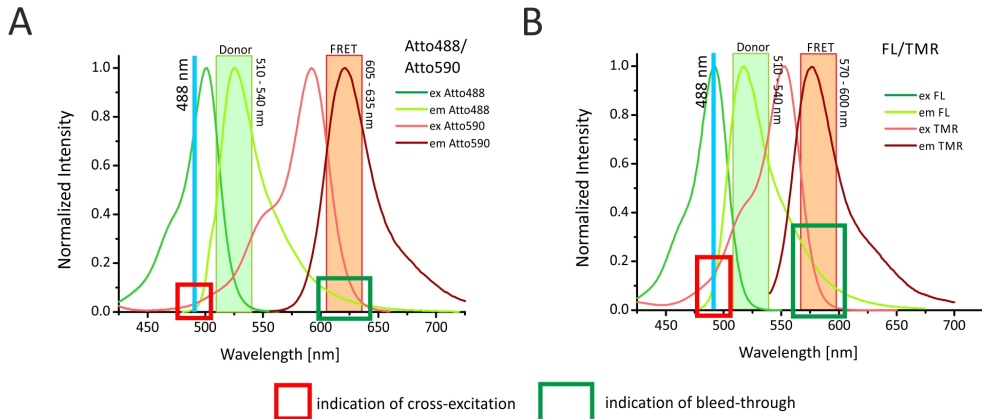


**Figure H.15: Scheme of cross-talk & bleed-through by CLSM.** Theoretical excitation and emission spectra of Atto488/Atto590 (A) and FL/TMR (B) siRNA with indication of CLSM excitation wavelength and recorded emission band. Potential cross-excitation and bleed-through are marked by boxes.

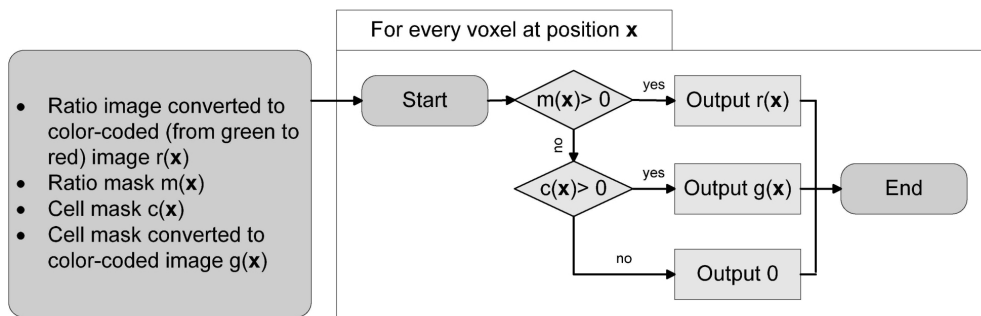
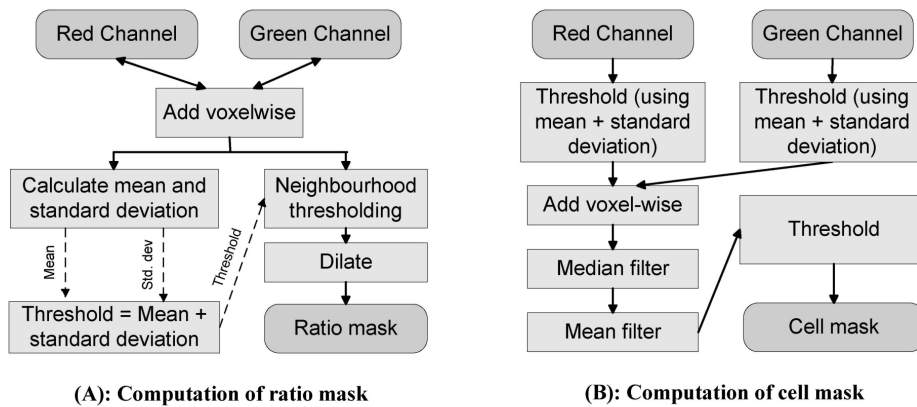


**Figure H.16: Schematics of R/G ratio algorithm.** Details of R/G ratio algorithm with calculation workflows for the ratio mask (A), cell mask (B) and R/G ratio image (C). (As published by Kim et al. [4])

## I siRNA in fixed cells

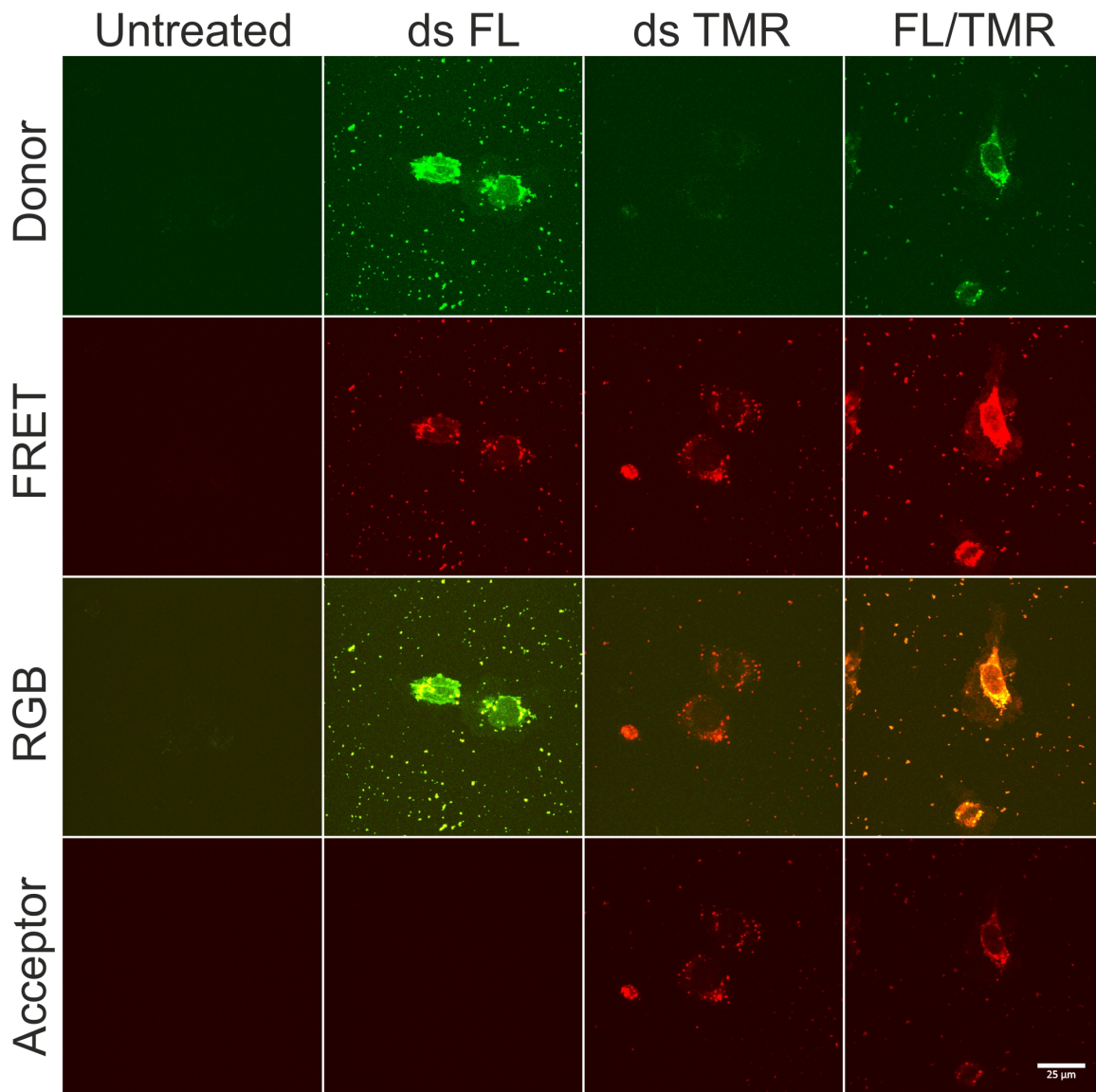


**Figure I.17: Suitability of FL/TMR for microscopy.** RBE4 cells transfected with FL/— (2<sup>nd</sup> column), —/TMR (3<sup>rd</sup> column) and FL/TMR siRNA (4<sup>th</sup> column) to verify cross-talk and bleed-through. Untreated cells (1<sup>st</sup> column) are shown as reference. Cells were excited at 488 nm and emission recorded for donor signal at 510-540 nm (1<sup>st</sup> row) and FRET signal at 570-600 nm (2<sup>nd</sup> row). 3<sup>rd</sup> row depicts an overlay of donor and FRET signal. The last row represents the acceptor signal at 561 nm excitation and emission at 570-600 nm.

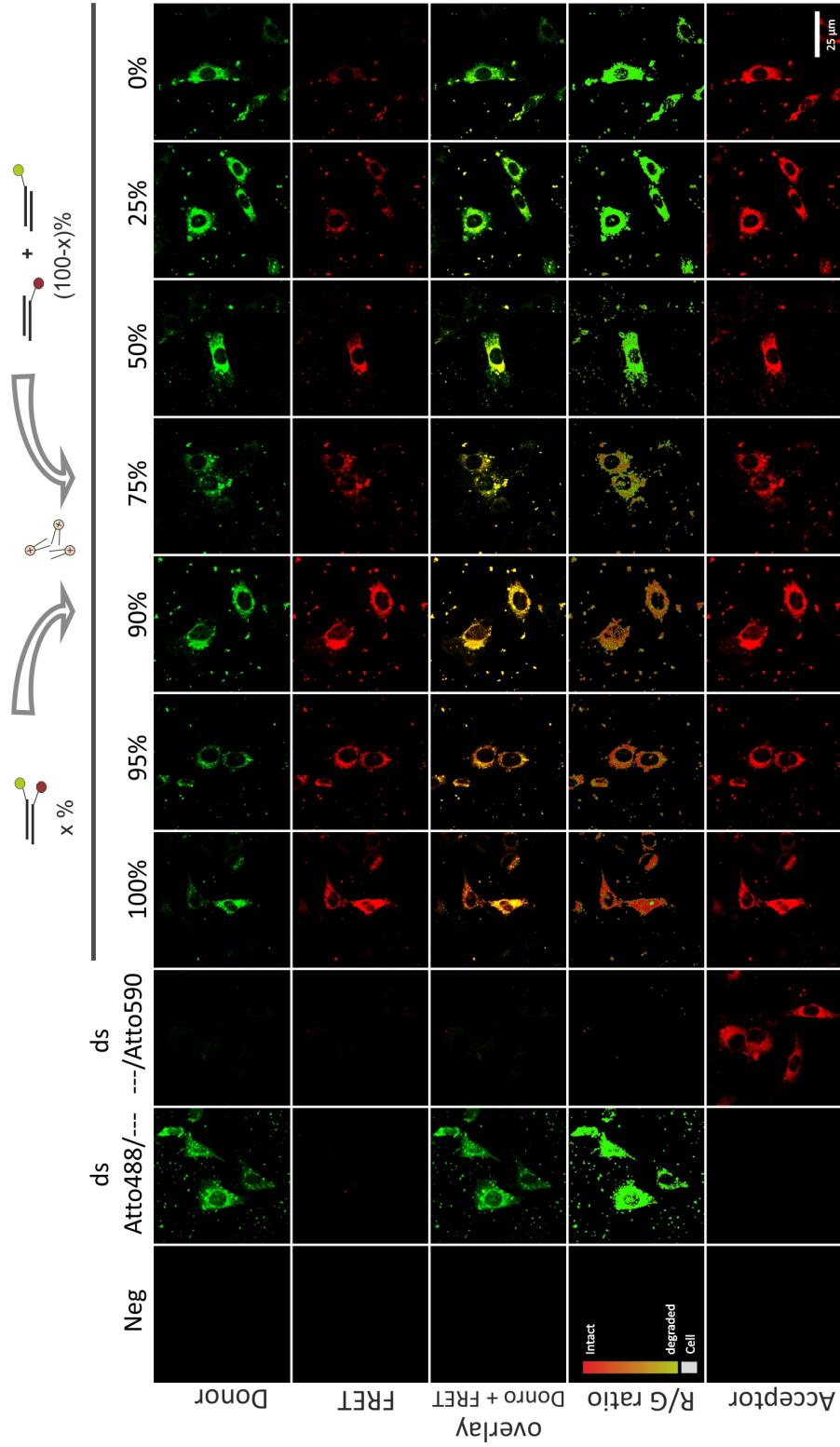


**Figure I.18: Integrity simulation and R/G processing inside fixed cells with Atto488/Atto590.** Depicted are the donor, FRET, donor/FRET-overlay, R/G ratio and acceptor signal of RBE4 cells transfected with samples referring to different siRNA integrity states of Atto488/Atto590 siRNA. The samples referring to 100 %, 95 %, 90 %, 75 %, 50 %, 25 % and 0 % intact siRNA are obtained by mixing different amounts of single labeled duplexes (simulating degraded siRNA) and double labeled (referring to intact siRNA) duplexes.

## MFI of Donor / FRET overlay

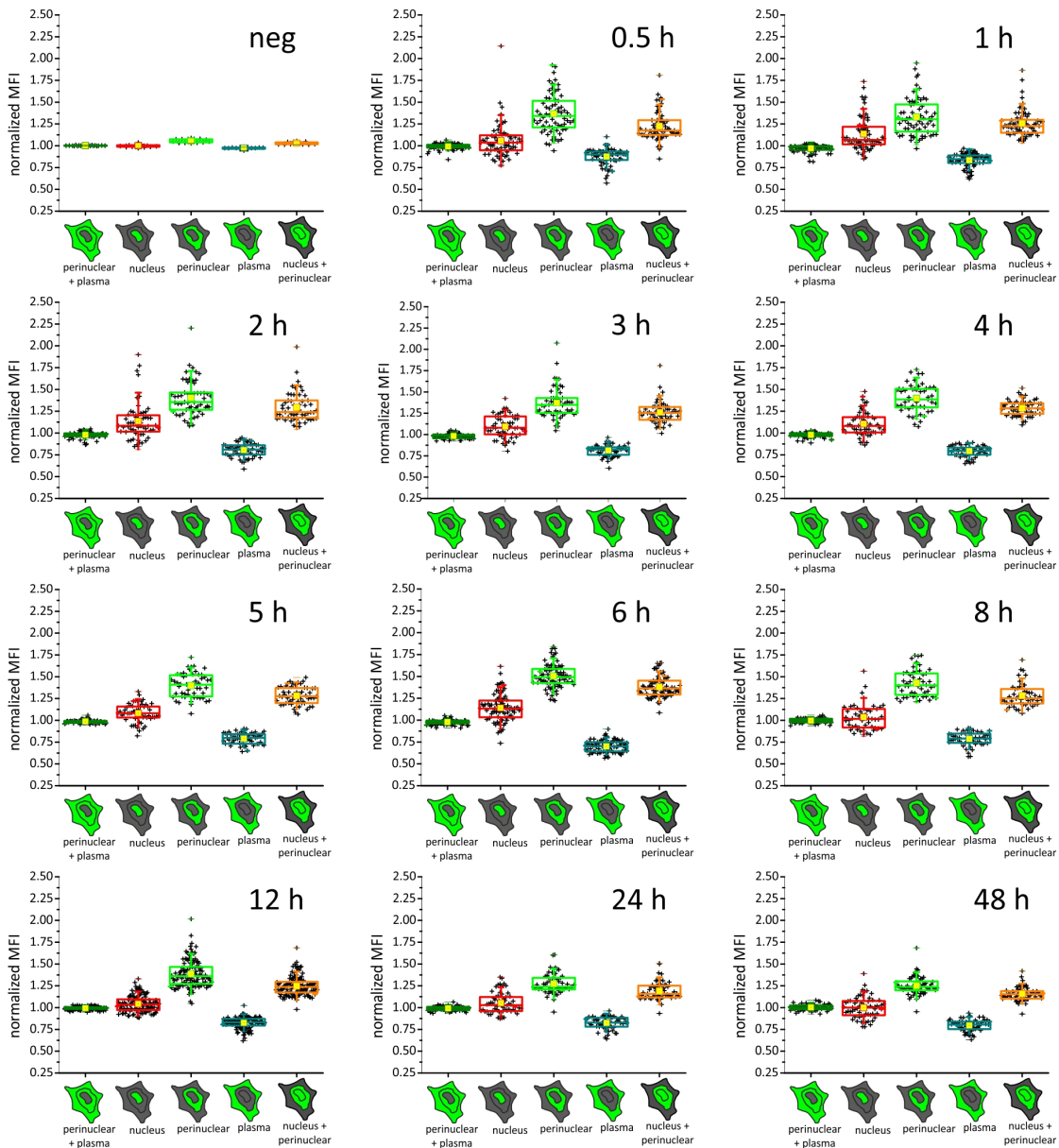


**Figure I.19: Box-whisker analysis of FL/TMR.** RBE4 cells transfected with FL/TMR and incubated for different time points before fixation, were manually segmented into nucleus, perinuclear, perinuclear&plasma, plasma and perinuclear&nucleus. For each ROI of an cell the MFI value was determined and normalized to the overall cell fluorescent. In average each data set contains at least 50 analyzed cells from around 30 different scanning areas. Box whisker analysis for control and incubation ranging from 0.5 h to 48 h incubation after transfection. Box represent upper and lower quartile, the line inside the box the median value and the whiskers the standard deviation. In yellow the mean value is depicted and in black all measured data points.

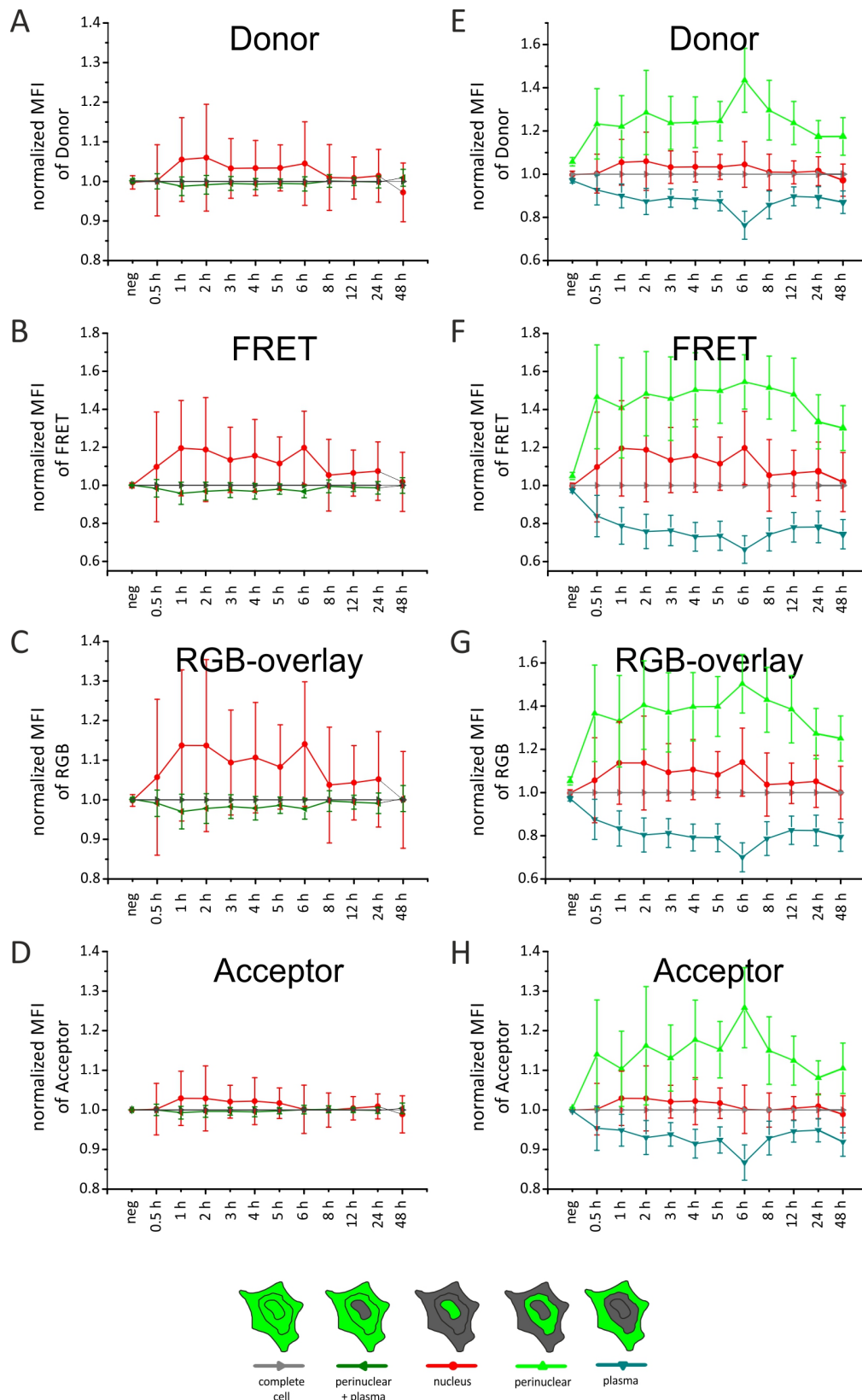


**Figure I.20: Temporal changes in ROI of FL/TMR.** RBE4 cells transfected with FL/TMR and incubated for different time points before fixation and segmentation into nucleus, perinuclear, perinuclear&plasma, plasma and perinuclear&nucleus. For each ROI of a cell the MFI value was determined and normalized to the overall cell fluorescent ( $n > 50$ ). Normalized MFI values compared over time, ranging from 0.5 h to 48 h. Depicted are nuclear ROI (red) and extranuclear (dark green) ROI (A, B, C, D). (E, F, G, H) show nuclear (red), perinuclear (light green) and plasma (blue-gray) ROI. (A+E) depict donor data, (B+F) FRET data, (C+G) RGB-overlay data and (D+H) acceptor data.



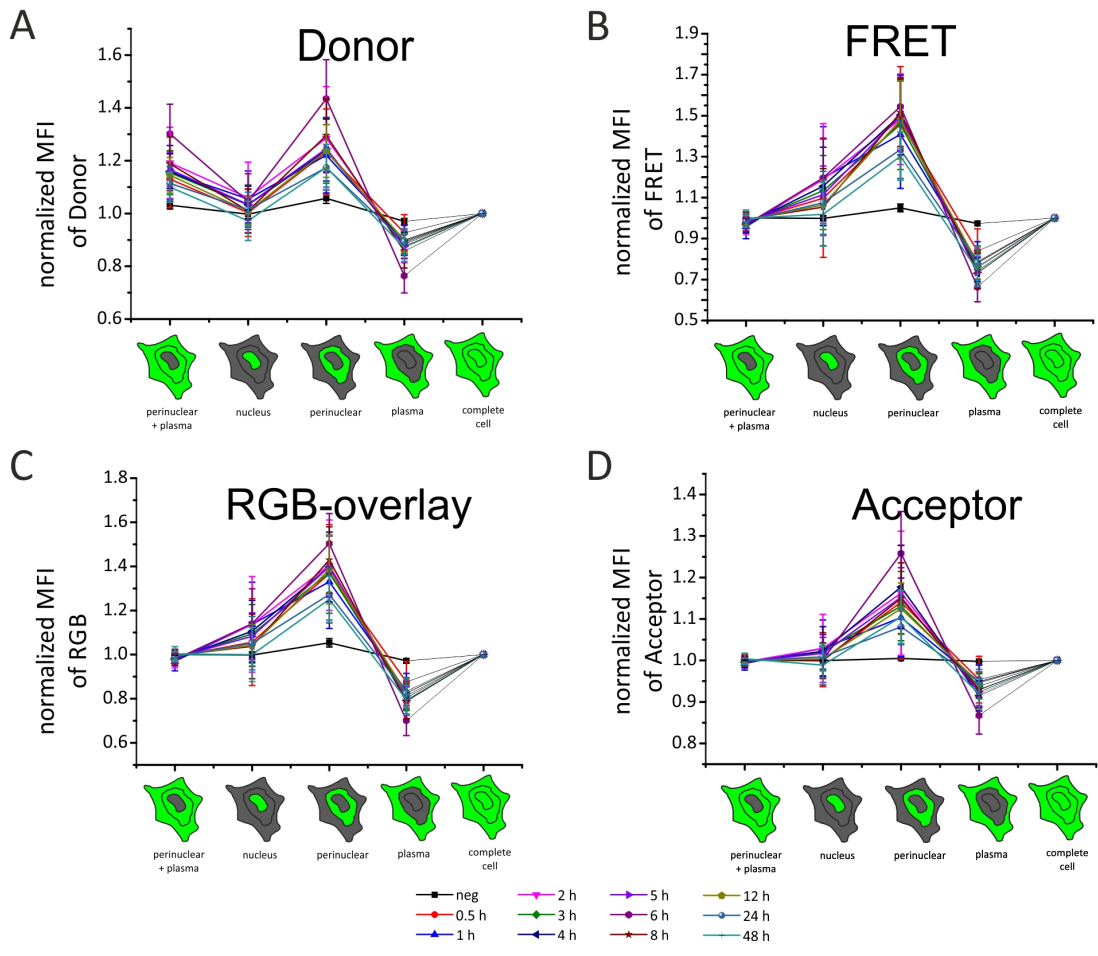


**Figure I.21: Localization of FL/TMR.** RBE4 cells transfected with FL/TMR and incubated for different time points before fixation and segmentation into nucleus, perinuclear, perinuclear&plasma, plasma and perinuclear&nucleus. For each ROI of an cell the MFI value was determined and normalized to the overall cell fluorescent (n>50). Normalized MFI values in different cellular ROIs based on donor (A), FRET (B), RGB-overlay (C) and acceptor (D) data. Each graph represents one incubation time.

## J Costaining of cellular organelles

### nuclear stain RedDot & Atto488/Atto590

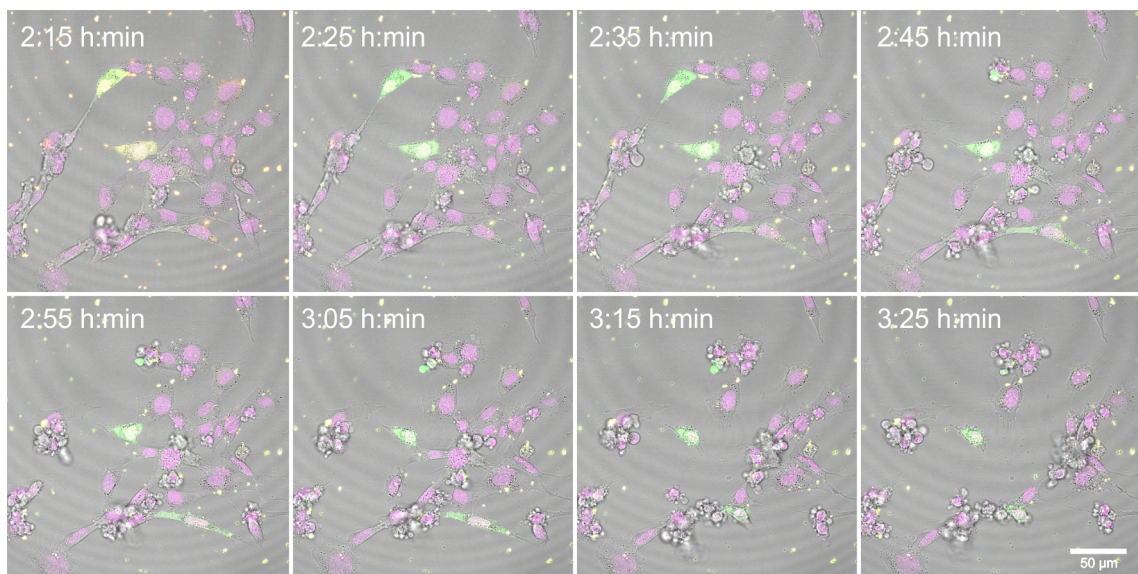


**Figure J.22: Nuclei of RBE4 cells stained by RedDot™ 1 in long-term incubation.** Sequence depicts RBE4 2 hours and 15 minutes after nuclear staining with RedDot™ 1. Cells are imaged over 70 minutes at 1 min intervals and shown as a sequence snapshot with 10 min intervals. Dying cells showing blebbing can be seen.

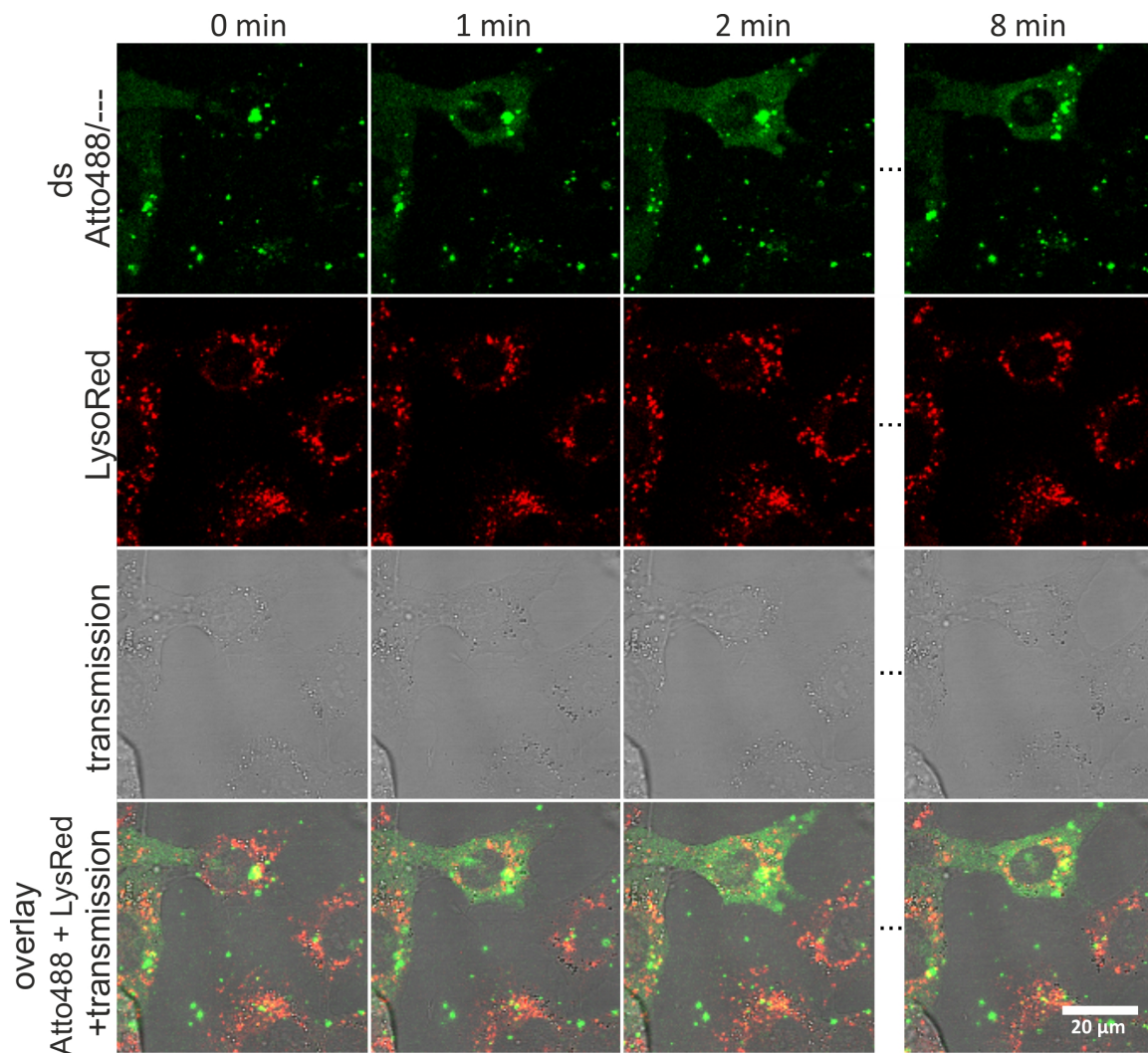


**Figure J.23: RBE4 cells transfected with Atto488— siRNA under live cell imaging conditions.** Lysosomes are stained by LysoTracker<sup>®</sup> Red. At each time point data was acquired in sequential scans with ~0.85 sec delay time. Atto488— siRNA signal (green), lysosome (red), transmission (gray) and merged color images are shown. Images depict a release event 29 min after the addition of the transfection lipoplexes.



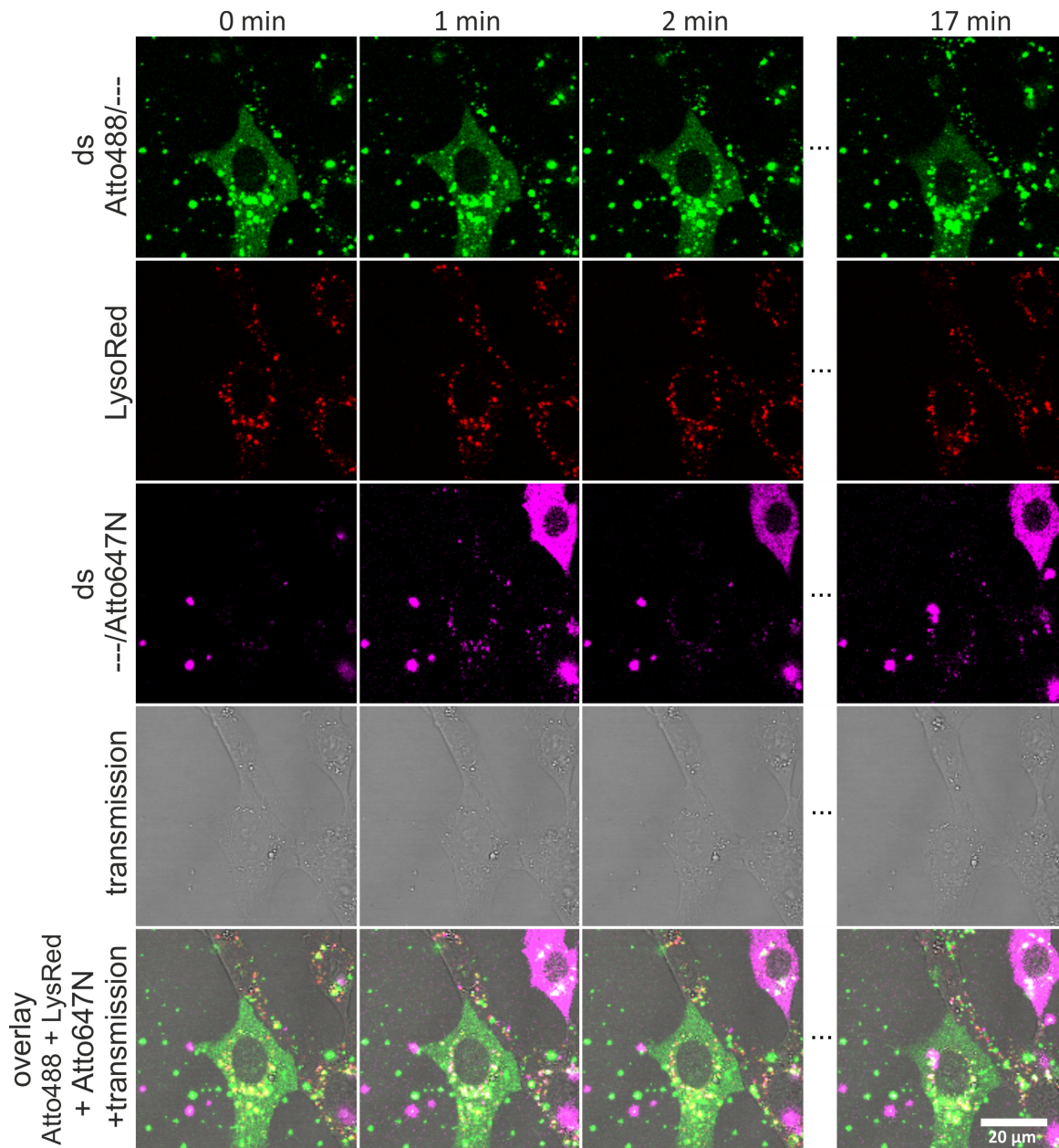


**Figure J.24: RBE4 cells transfected with Atto488/— siRNA are re-transfected with —/Atto647N siRNA under live cell imaging conditions.** Lysosomes are stained by LysoTracker<sup>®</sup> Red. At each time point data was acquired in sequential scans with ~0.85 sec delay time. Atto488/— siRNA (green), lysosome (red), —/Atto647N siRNA, transmission (gray) and color merged images are shown. Images depict a release event of the re-transfection of Atto488/— transfected cells with —/Atto647N siRNA 4:20 h:min after the first transfection. Sequence shows the beginning release of Atto647N-siRNA (blue arrow) at 4:26 h:min in 1 min intervals. White arrow depict Atto488/— and lysosomal colocalization and the black arrow a colocalization of both siRNA types in a lysosome.

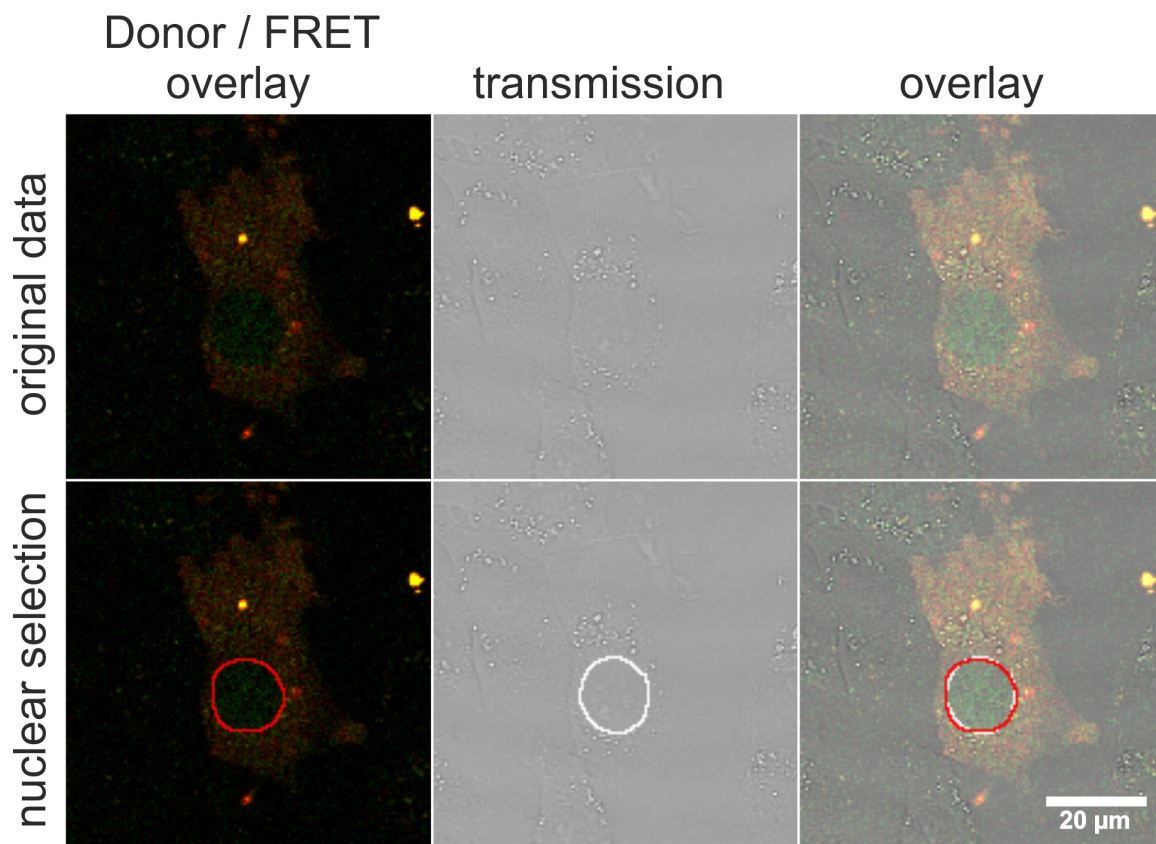


**Figure J.25: RBE4 cells transfected with FRET siRNA for nuclear segmentation.** Donor/FRET overlay (first column) shows a green, round shape area in the middle which corresponds to the nuclear segmentation on basis of the transmission channel (second column). The overlay of both images (third column) shows a similar segmentation of the nucleus by siRNA fluorescence and transmission signal.

## K Single labeled siRNA in cells

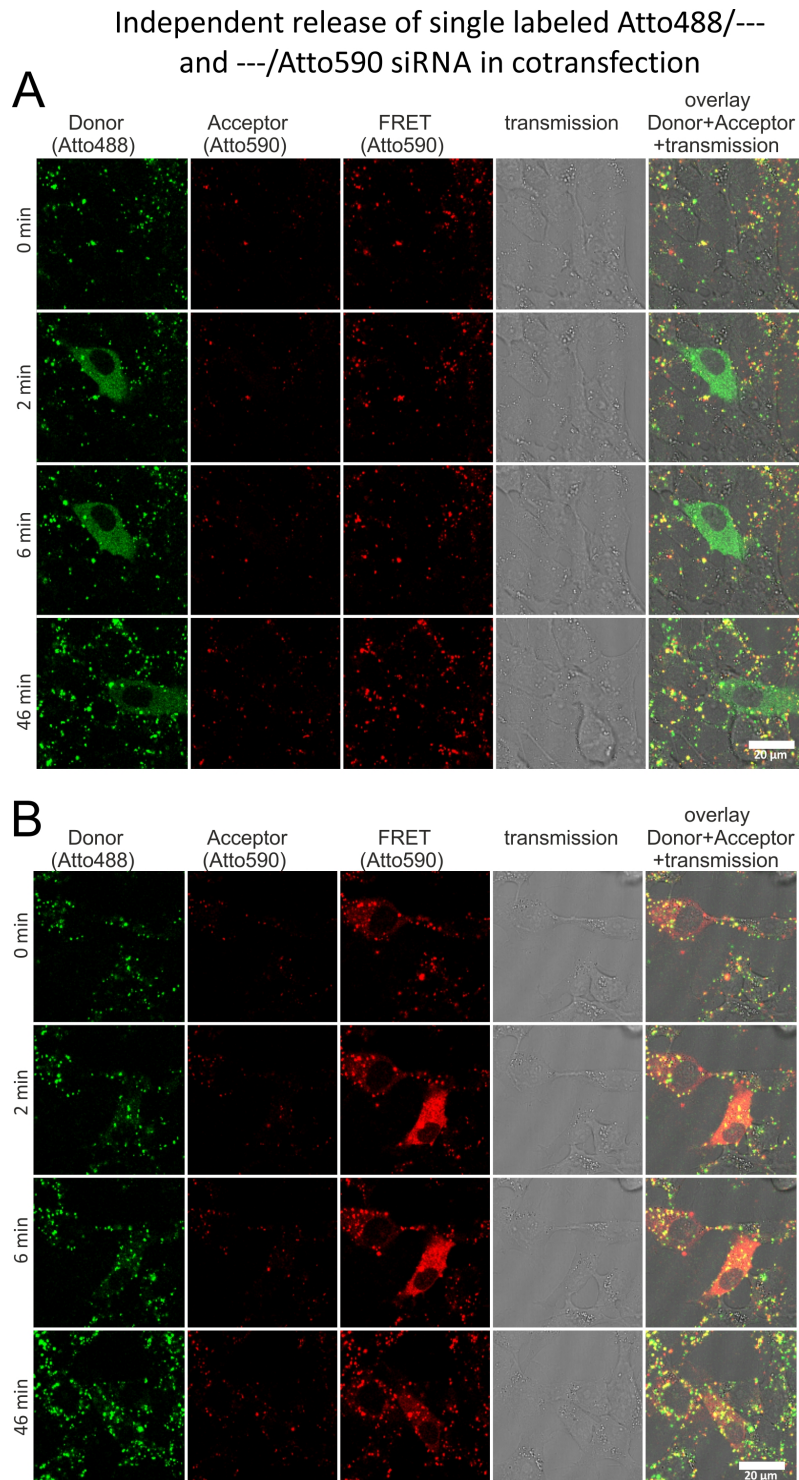


**Figure K.26: Co-transfection of single labeled siRNA.** RBE4 cells co-transfected with Atto488/— siRNA (A) and —/Atto590 siRNA (B). siRNA was complexed separately to prevent homogenous lipoplexes. At each time point data was acquired in the acceptor mode at 2 min intervals resulting in the donor, FRET, acceptor and transmission signal. Image data represents donor, FRET, acceptor, transmission and donor-acceptor-transmission overlay image (from top). (A) Atto488/— release 36 min after transfection. (B) —/Atto590 release 38 min after transfection.



## L Double labeled FRET siRNA in cells

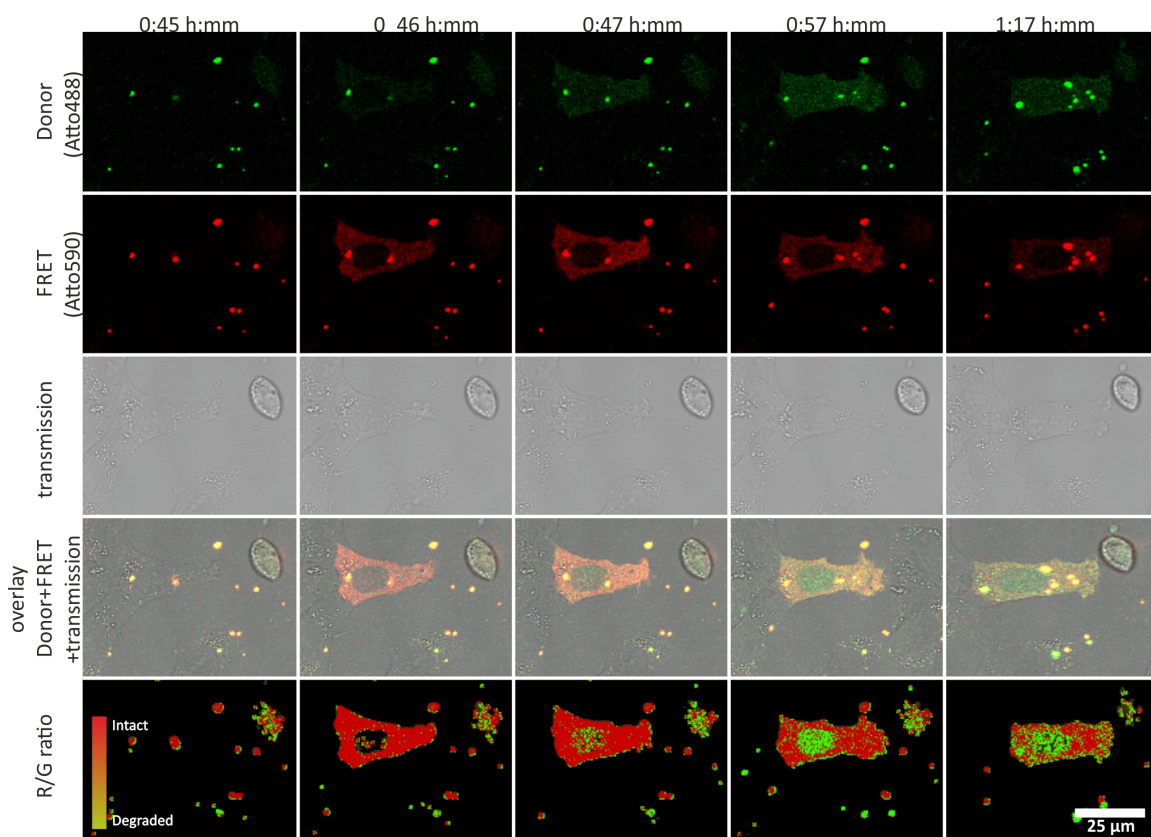


**Figure L.27: Release event of Atto488/Atto590 in RBE4.** R/G processing of digital magnified release event in RBE4 cells after transfection with Atto488/Atto590 siRNA. Image sequence depicts starting release and development over 32 min. Cells were imaged in the advanced imaging mode recording donor, FRET and transmission channel in a 2x2 tile scan with each 5 z-slices, resulting in 1 min intervals. In addition to single channel data, an overlay of the donor, FRET and transmission channel and the R/G ratio image with setA is depicted.

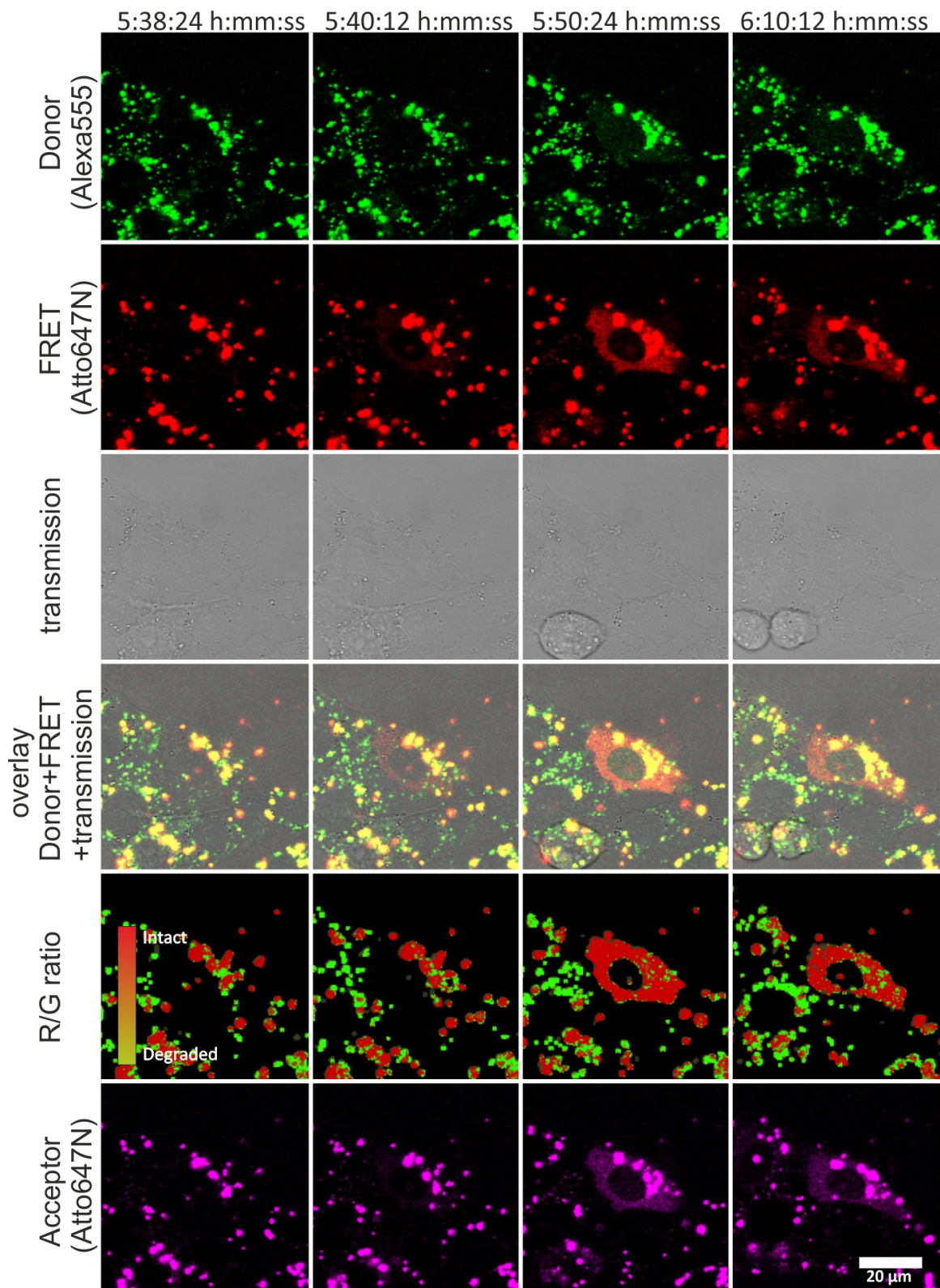


**Figure L.28: RBE4 cells transfected with Alexa555/Atto647N siRNA under live conditions.** Sequence depicts digital magnified release event of FRET siRNA into the cytoplasm. Besides donor (green), FRET (red), transmission (gray), acceptor (magenta), R/G ratio image and donor-fret-transmission overly is depicted. Data was recorded similar to the acceptor mode with adjusted emission bands in only one region at 1 min intervals. R/G processing with same settings as for Atto488/Atto590 siRNA, i.e. R/G setting setA, with red indicating intact and green degraded siRNA. Image sequence depicts starting release and development over 32 min.

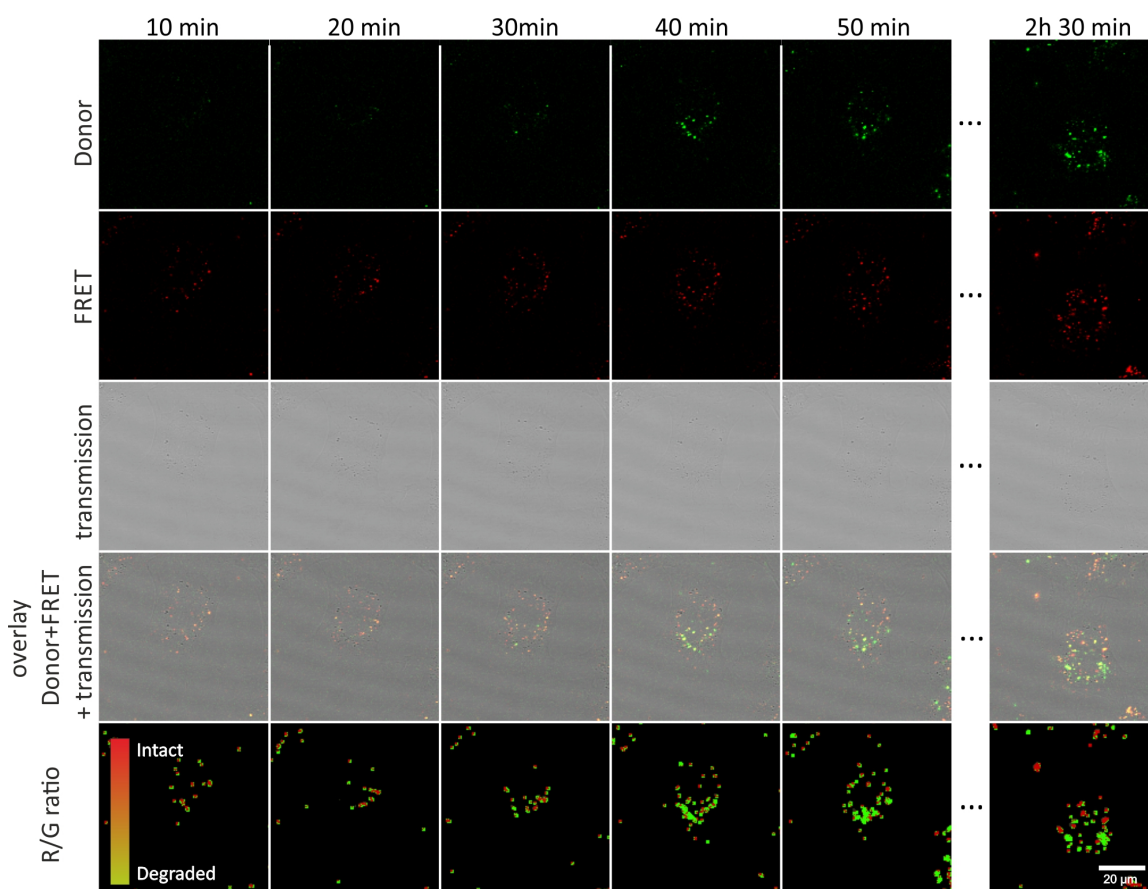


**Figure L.29: Cellular aggregates showing no release over time.** RBE4 cell after transfection with Atto488/Atto590 that does not show any detectable release. Data depicts donor, FRET, transmission, donor-FRET-transmission overlay and R/G ratio image (from top). R/G analysis is performed with setA.



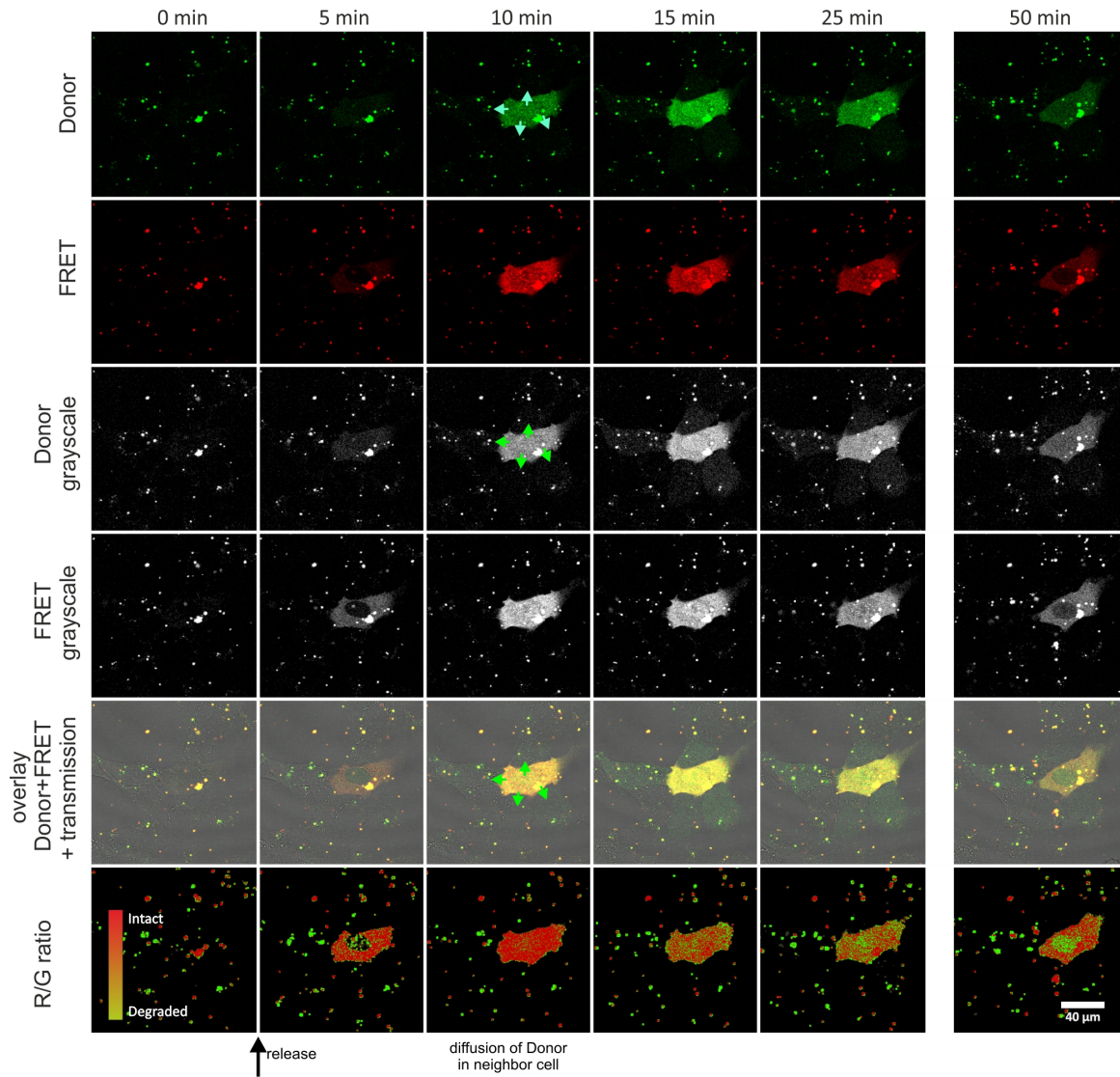


**Figure L.30: Transfer of siRNA into neighboring cells.** RBE 4 cell transfected with Atto488/Atto590 siRNA showing release of intact siRNA transmitting green fluorescence in neighbor cells. After 160 min of transfection, the central cell shows release of intact siRNA. Depicted are the following 40 min with a detectable fluorescence in the the 4 surrounding cells. For better visualization donor and FRET channel are also depicted as grayscale image besides the overlay (donor, FRET and transmission) and R/G ratio image. Green arrows at 10 min indicate a transfer of green fluorescence to 4 neighbor cells.

## M Detail analysis of release events

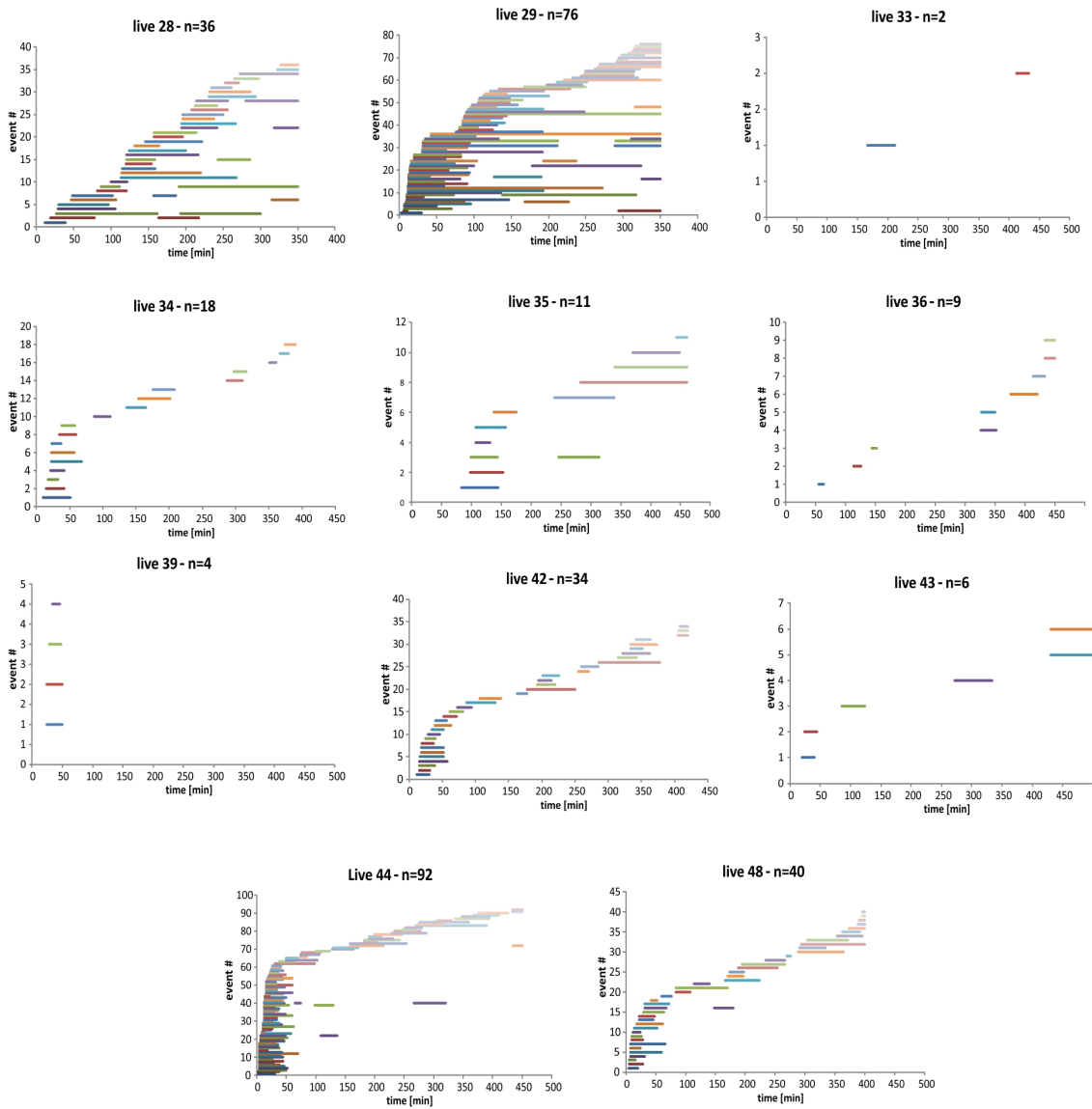


**Figure M.31: Time point of release of single experiments.** Time point of release of siRNA into cytoplasm after transfection for 11 live cell imaging observations. Line plots of release events, with each line representing one release events. Events were arranged in order of occurrence by increasing event number values (Y-axis).



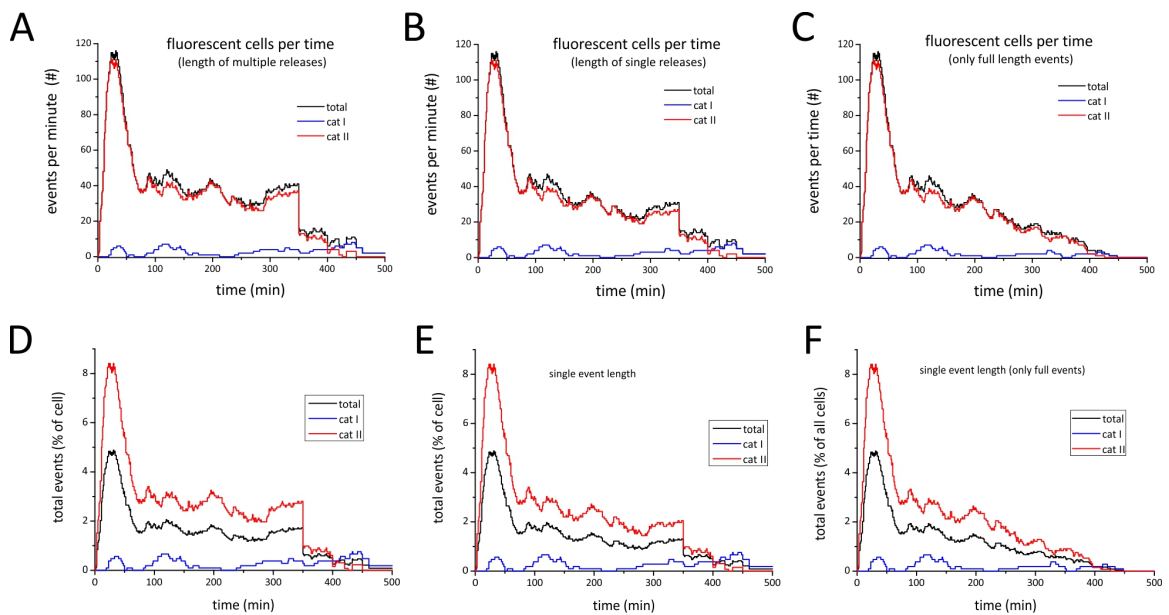


**Figure M.32: Fluorescent cells per time point.** Fraction of fluorescent cells per observed time point for total experiments, category I and category II experiments. (A-C) absolute cell numbers and (D-F) percentage of fluorescent cells per time point. (A+D) representation of all events, including multiple releases. (B+E) representation for only single release events. (C+F) Only full length events with depletion within the respective observation time.

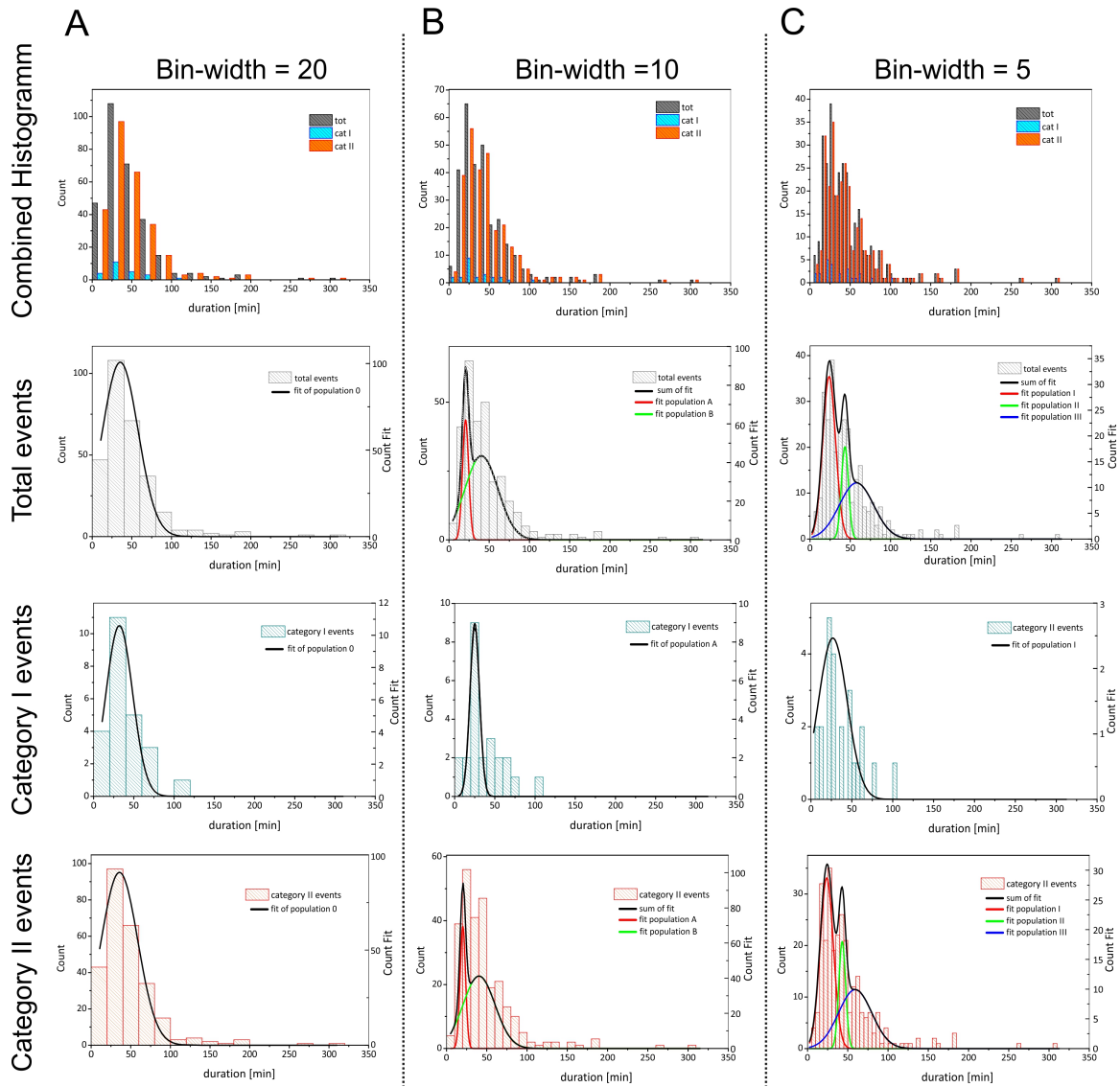


**Figure M.33: Fluorescence time of released siRNA.** Fluorescence time in the cytosol of release events after transfection of Atto488/Atto590. Data is grouped in category I (blue), category II (red) and total (black). Histograms show fluorescence duration at a bin size of 20 min (A), 10 min (B) 5 min (C). Gaussian fits for each population with a local maximum in the frequency distribution with one population at bin size 20 min, two populations at bin size 10 min and three populations at bin size 5 min. On basis of each population of a category as sum of curve was calculated.

## **N Single cell analysis**

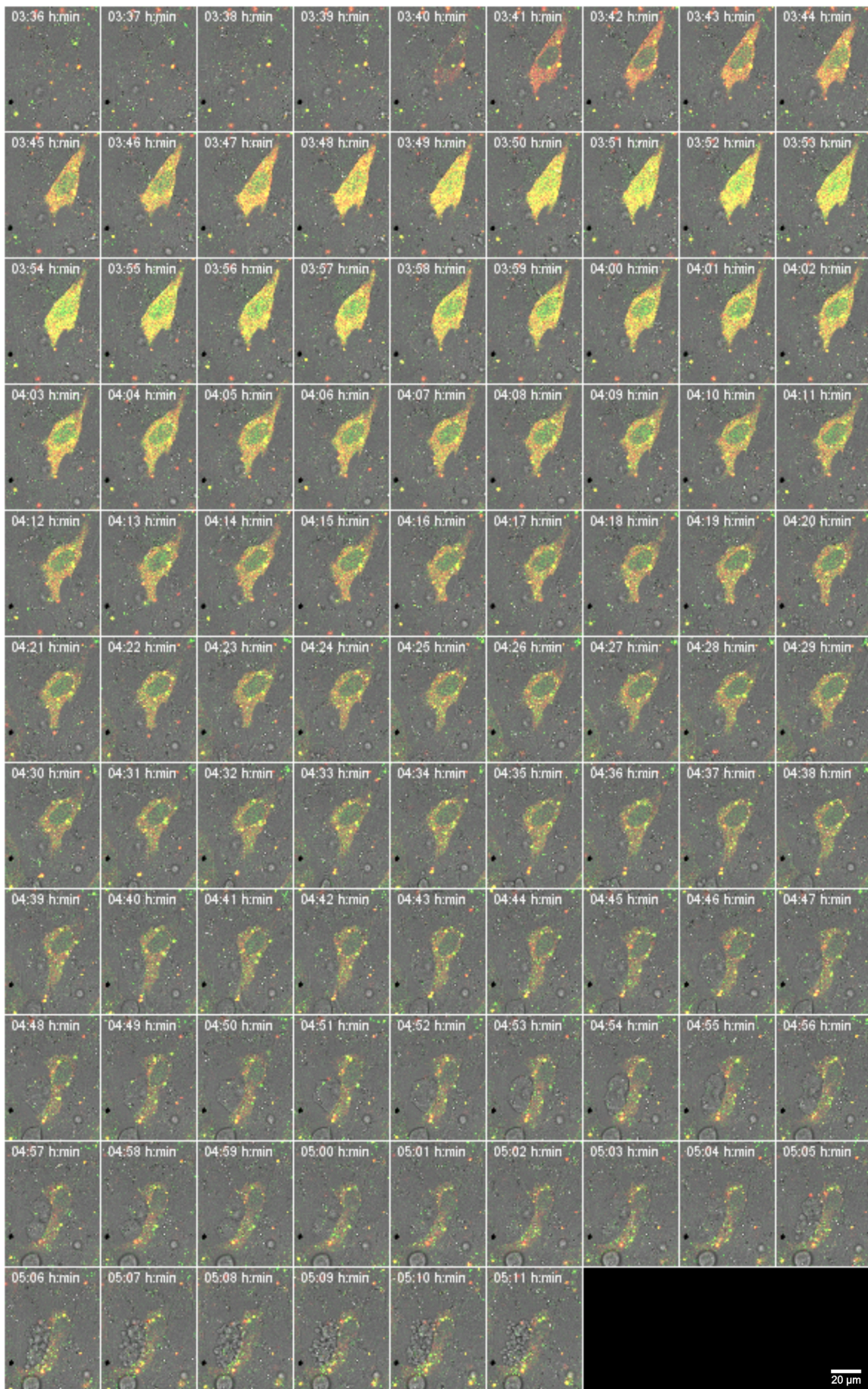


**Figure N.34: Example release event of Atto488/Atto590 - overlay.** One example of a long release event of Atto488/Atto590 siRNA in RBE4 cells. Sequence depicts a release at 3:40 h:min after transfection. Displayed are the overlay of donor, FRET and transmission channel. R/G ratio (setA) is depicted in Figure N.35



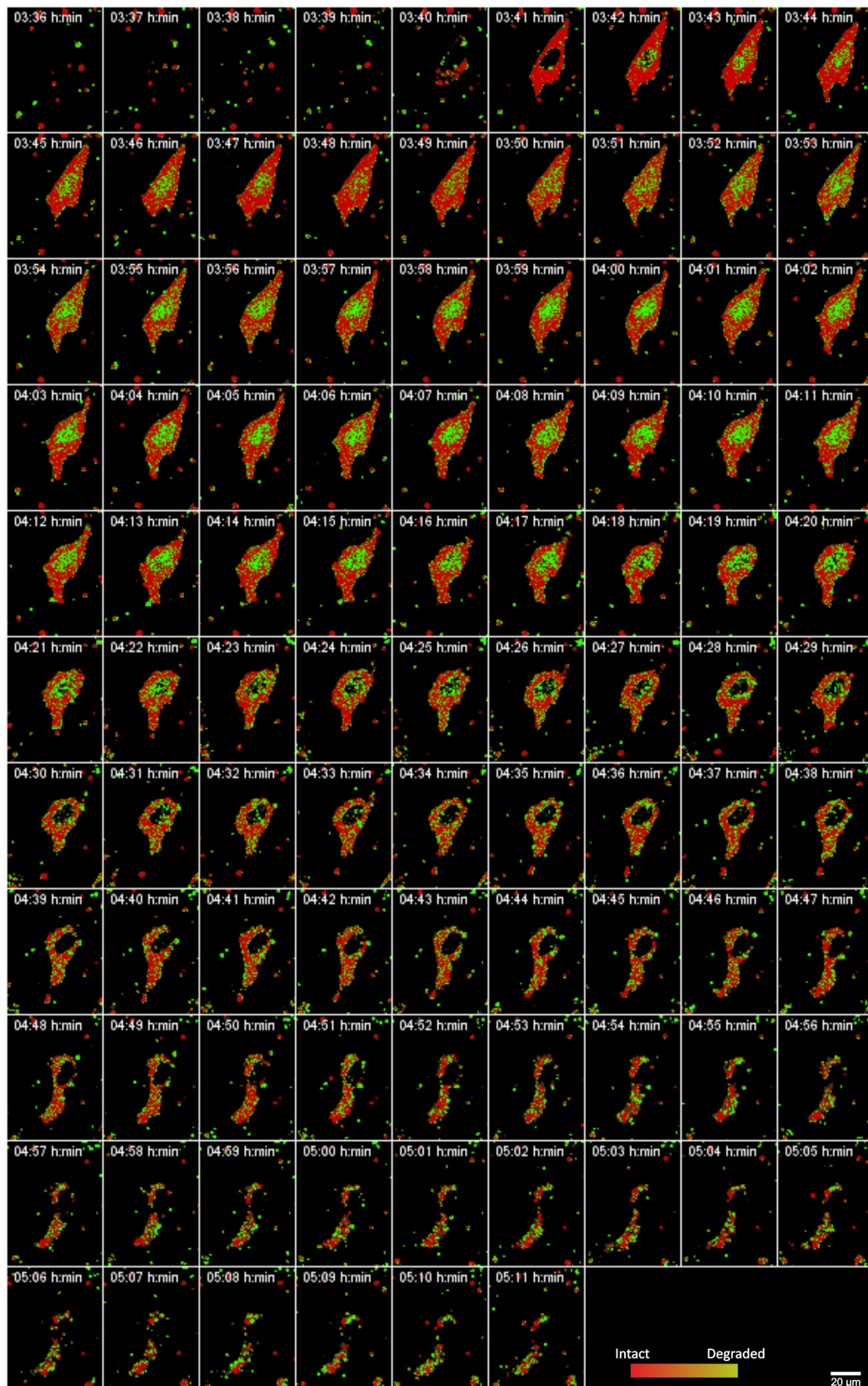


**Figure N.35:** Example release event of Atto488/Atto590 - R/G-ratio. One example of a long release event of Atto488/Atto590 siRNA in RBE4 cells. Sequence depicts a release at 3:40 h:min after transfection. Displayed is the R/G ratio image (set A).



**Figure N.36: Nuclear import of intact siRNA in detail - overlay.** Release event that shows a later import of intact siRNA into the nucleus. Sequence depicts a release at 0:35 h:min after transfection. Displayed are the overlay of donor, FRET and transmission channel. The calculated R/G ratio image (setA) can be found in Figure N.37.



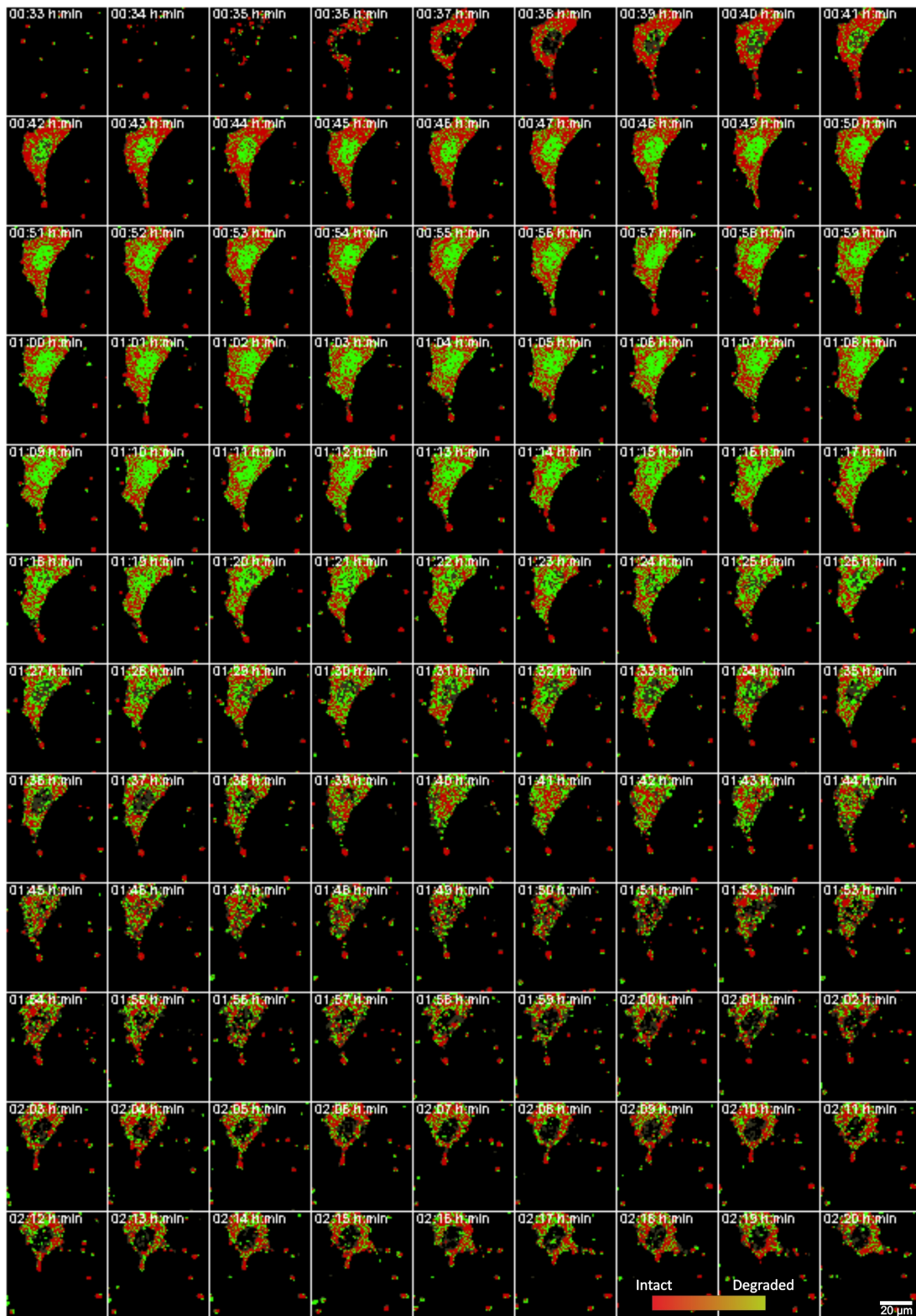


**Figure N.37: Nuclear import of intact siRNA in detail - R/G ratio.** Release event that shows a later import of intact siRNA into the nucleus. Sequence depicts a release at 0:35 h:min after transfection. Displayed are the R/G images (setB).





